



## PhD thesis

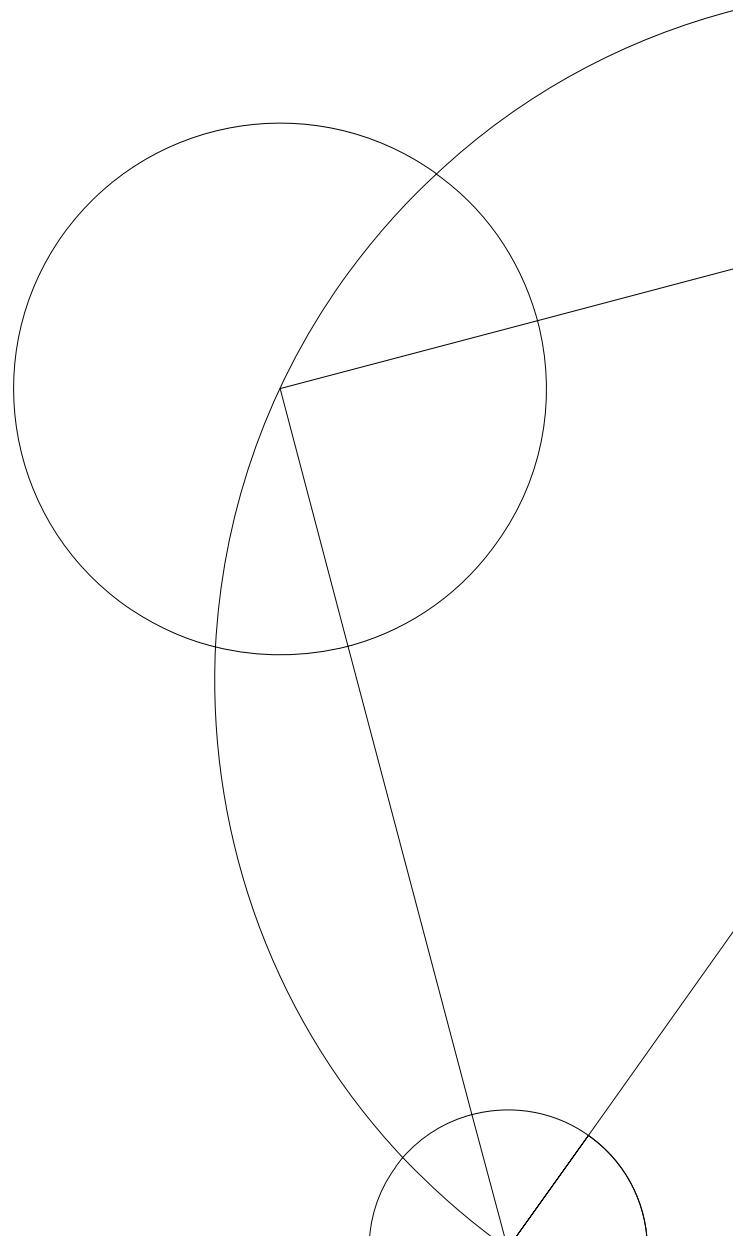
Nicholas Mossor Rathmann

# Nonlinear fluid dynamics

Studies on the dynamics of ice sheet deformation and the turbulent energy cascade

Advisor: Christine S. Hvidberg, Niels Bohr Institute

This thesis has been submitted to the PhD School of  
The Faculty of Science, University of Copenhagen, 2018.





# Abstract

Nonlinear fluid motion occurs naturally in central components of the climate system. Studying such motion is instrumental for improving the accuracy and realism of models of climate components, which has important implications for future climate projections. This thesis presents four studies on the topic of nonlinear fluid dynamics addressing two subjects: the dynamics of ice sheet deformation and the dynamics of the turbulent energy cascade.

The first study investigates the controlling mechanisms of the observed 2016 seasonal speed-up of Zachariae and Nioghalvfjerdingsfjorden outlet glaciers in north-east Greenland, which drain a significant part of the Greenland ice sheet. From surface imagery made available by the newest generation of satellites, state-of-the-art velocity maps are derived, and the timings of processes potentially impacting the speed-up are estimated. By combining observations with numerical modelling, it is shown that the subglacial environment exerts an important control over the ice discharge rate of the region, which has implications for estimating the region's contribution to near-term sea level rise.

The second study investigates the influence of strong single-maximum fabrics on the transient deformation of internal layers within ice sheets. By using a new Lagrangian numerical ice flow model, it is shown that discrete, strong single-maximum layers — which may account for suppressed shearing along nonbasal crystallographic planes — are a plausible candidate for explaining the disturbed flow observed from ice-penetrating radar transects. The results have potential implications for interpreting ice-core stratigraphies and chronologies, as well as understanding of how internal disturbances might influence surrounding flow fields.

The third and fourth study address the origin of the transfer direction of kinetic energy between scales of motion (upscale/downscale) in fully developed turbulence using the spectral-helical decomposition of the velocity field. In this decomposition, the nonlinear term in the Navier–Stokes equation becomes to a sum over eight distinct types of three-wave interactions. In the third study, a simple model (a shell model) is introduced to investigate the behaviour of the eight types of nonlinear interactions, which is compared to a linear stability analysis, finding a fair agreement. In the fourth study, a subset of the three-wave interactions are shown to conserve a new positive-definite quadratic quantity in addition to kinetic energy, which cause the interactions to contribute to a reverse transfer of energy in three dimensions (small to large scales) in analogy to two-dimensional turbulence. Understanding the energy transfer directionality, and possible ties between two- and three-dimensional turbulence, has implications for geophysical flows such as the free atmosphere and oceans where vertical motion in many places is suppressed, thereby affecting predictability time scales and the transport of energy and momentum in climate.



# Resumé

I centrale dele af klimasystemet finder ulineære væskestrømninger naturligt sted, og komplicerer klimamodellers forudsigelser. For at øge nøjagtigheden af klimamodelberegninger er det vigtigt at studere disse væsker, da modelbeskrivelsen af de enkelte komponenter i klimasystemet derved kan forbedres. Denne afhandling består af fire studier under temaet ulineære væskestrømninger, delt i to emner: den dynamiske beskrivelse af iskappers flydning, samt den dynamik, der kontrollerer transporten af energi i turbulente strømninger.

Det første studie undersøger hvilke mekanismer, der kontrollerer de observerede hastighedsændringer i 2016 ved udløbsgletsjere Zachariæ and Nioghalvfjærdsfjorden i det nordøstlige Grønland, som er et udløbsområde, der dræner en betydelig del af den Grønlandske indlandsis. Ud fra satellitbilleder undersøger studiet afledte hastighedskort, og sammenholder dem med igangsættelsen af bestemte processer, der er kendt for at kunne påvirke isens flydehastighed. I kombination med numeriske modelberegninger peger studiet på, at koblingen mellem is og grundfjeld (der er påvirket af processer som f.eks. afsmeltningen af is) kan have en betydelig indflydelse på iseksporten. Dette har konsekvenser for regionens estimerede bidrag til havvandsstigninger.

Det andet studie undersøger forholdet mellem de stærkt anisotropiske iskrystalstrukturer, der findes i iskapper, og den tidsafhængige udvikling af dybe interne lag i iskapper. Ved at gøre brug af en ny Lagransk isflydemodel viser studiet, at diskrete interne lag med stærkt anisotropiske egenskaber — der kan bremse isdeformationen hvis iskrystaller er orienteret ugunstigt — er et plausibelt bud på, hvorfor dybe interne lag i iskapper kan have dramatiske forstyrrelser i flydemønstret. Dette resultat har konsekvenser for både fortolkningen af stratigrafier og kronologier i iskerner, men også for forståelsen af, hvordan flydningen af den øvrige ismasse påvirkes.

Det tredje og fjerde studie beskæftiger sig med overførelsen af kinetisk energi i turbulente strømninger mellem forskellige karakteristiske størrelser af bevægelse ved at benytte den spektral-heliske dekomposition af hastighedsfeltet. I denne dekomposition reduceres det ulinære led i Navier—Stokes ligningen til en sum over otte forskellige typer tre-bølge interaktioner. I det tredje studie introduceres en simpel skalmodel for at undersøge opførelsen af de otte typer interaktioner, og det viser sig, at de til dels er i overensstemmelse med en lineær stabilitetsanalyse. Det fjerde studie tager udgangspunkt i en delmængde af mulige tre-bølge interaktioner, og det konkluderes at disse bevarer en ny positiv-definit kvadratisk størrelse udover bevarelsen af den kinetiske energi. Denne nye invariant muliggør en energioverførelse fra små til større karakteristiske størrelser af bevægelse (dvs. et inverst bidrag til energioverførelsen) i tredimensional turbulens i analogi med todimensional turbulens. Både retningen af energitransporten, samt hvilke bånd, der findes mellem to- og tredimensional turbulens, spiller en vigtig rolle for de bevægelser, der finder sted i eksempelvis atmosfæren og oceanerne. I disse hydrodynamiske fluider, hvor vertikal bevægelse flere steder er undertrykt, kan retningen på energioverførelsen have indflydelse på væskebevægelsens forudsigelighed samt transporten af energi og impuls i klimasystemet.



# Preface

This PhD thesis is based on work by Nicholas Mossor Rathmann and was carried out during 2015–2018 at the Niels Bohr Institute, Faculty of Science, University of Copenhagen. The work was supervised by Christine S. Hvidberg, and was funded by the Niels Bohr institute and the European Research Council under the European Community’s Seventh Framework Programme (FP7/2007-2013)/ERC grant agreement 610055 as part of the ice2ice project.

The work presented here is original, while part of it has been already published in the following research publications:

Rathmann, N., Hvidberg, C., Solgaard, A., Grinsted, A., Gudmundsson, G. H., Langen, P. L., Nielsen, K., and Kusk, A. Highly temporally resolved response to seasonal surface melt of the Zachariae and 79N outlet glaciers in northeast Greenland. *Geophysical Research Letters*, 44(19):9805–9814, 2017

Rathmann, N. M. and Ditlevsen, P. D. Pseudo-invariants contributing to inverse energy cascades in three-dimensional turbulence. *Physical Review Fluids*, 2(5): 054607, 2017

Rathmann, N. M. and Ditlevsen, P. D. Role of helicity in triad interactions in three-dimensional turbulence investigated by a new shell model. *Physical Review E*, 94(3):033115, 2016

This version of the thesis is a revised version based on feedback/critique from reviewers (and opponents at the defence) Ralf Greve, Edwin Waddington, and Joachim Mathiesen.



# Acknowledgements

First and foremost, I wish to thank my thesis advisor, Christine S. Hvidberg, whose door was always open whenever I had questions or wished to reflect upon ideas. She consistently steered me in the right direction with her broad knowledge on ice flow dynamics and relevant literature, and supported my pursuit of own research ideas. For that I am incredibly grateful, leading to three very motivating years in my scientific research career filled with stimulating discussions and exciting opportunities.

Secondly, I equally wish to thank my MSc thesis supervisor, Peter D. Ditlevsen, for continued collaboration on my side projects on turbulence theory, and whose sense for detail has led to many stimulating discussions influencing how I approach my research today.

In addition, I would like to thank Aslak Grinsted and Hilmar Gudmundsson whose knowledge of glaciology and technical experience provided valuable help on many occasions, and co-supervisor Dorthe Dahl-Jensen whose ideas led me to study anisotropic ice-flow dynamics.

Furthermore, I wish to thank my office colleagues Christian T. Holme, Marius F. Simonsen, Diana Vladimirova, and the staff at the Center for Ice and Climate for useful discussions and reflections throughout my studies.

As part of my fieldwork in 2017 and 2018 at the east Greenland ice core project camp (EastGRIP camp), I sincerely wish to thank Trevor J. Popp and Steffen B. Hansen for the opportunity to participate in the deep ice-core drilling and for patiently mentoring Marius F. Simonsen and myself on the subject.

As part of my stay abroad at the University of Bergen, I wish to thank Kerim Nisancioglu, Eystein Jansen, Trond Dokken, Jørund Strømsøe, and others from the Norwegian part of ice2ice, for hosting me and for a fruitful stay.

Finally, I wish to thank family and friends for their support and patience.



# Contents

<b>1</b>	<b>Introduction</b>	<b>13</b>
1.1	Ice sheet dynamics . . . . .	15
1.2	Turbulent cascade dynamics . . . . .	16
1.3	Structure . . . . .	17
1.4	Notation . . . . .	18
<b>2</b>	<b>Continuous matter</b>	<b>19</b>
2.1	Incompressibility and the momentum balance . . . . .	19
2.2	Constitutive relations . . . . .	21
<b>I</b>	<b>Ice sheet dynamics</b>	<b>23</b>
<b>3</b>	<b>Creep of polycrystalline ice</b>	<b>25</b>
3.1	Steady state creep . . . . .	28
3.2	Glen’s isotropic flow law . . . . .	30
3.3	Inverse constitutive equation . . . . .	34
3.4	Block flow . . . . .	34
3.5	Drag over hard beds . . . . .	35
<b>4</b>	<b>Study #1</b>	<b>37</b>
4.1	Introduction . . . . .	37
4.2	The paper . . . . .	41
4.3	Outlook . . . . .	64
<b>5</b>	<b>Study #2</b>	<b>65</b>
5.1	Introduction . . . . .	65
5.2	Transversely isotropic creep . . . . .	67
5.2.1	Inverse two-dimensional constitutive equation . . . . .	70
5.2.2	Phenomenology of two-dimensional flow law . . . . .	72
5.3	The model . . . . .	74
5.3.1	Weak formulation . . . . .	77
5.4	Model setup and experiments . . . . .	79
5.5	Results . . . . .	81

5.6	Discussion and outlook . . . . .	87
<b>II</b>	<b>Turbulent cascade dynamics</b>	<b>91</b>
<b>6</b>	<b>Hydrodynamical turbulence</b>	<b>93</b>
6.1	Real-space invariants . . . . .	94
6.2	Spectral-space dynamics . . . . .	96
6.3	Spectral–helical decomposition . . . . .	98
6.4	Shell models . . . . .	103
<b>7</b>	<b>Study #3</b>	<b>107</b>
7.1	Introduction . . . . .	107
7.2	The paper . . . . .	108
7.3	Outlook . . . . .	123
<b>8</b>	<b>Study #4</b>	<b>125</b>
8.1	Introduction . . . . .	125
8.2	The paper . . . . .	126
8.3	Outlook . . . . .	135

# Chapter 1

## Introduction

Nonlinear fluid motion occurs naturally in central components of the climate system across a large range of spatial and temporal scales. While the degree of nonlinearity may vary from having subordinate influence on the larger-scale fluid motion to being principal for the flow, studying the behaviour of nonlinear flows has important implications for future projections of the climate system.

Depending on their type, flow nonlinearities can cause a significant departure from steady, laminar flow regimes by the formation of instabilities and symmetry breaking, and can lead to complicated internal stress fields affecting the response to external influences in a nontrivial way. As a result, nonlinearities can severely complicate theoretical pursuits by not allowing central quantities to be expressed in closed forms, or by introducing terms with exponents that complicate the search for solutions even in simple, idealized cases. Investigating nonlinear flows numerically can likewise be troublesome, or resource intensive at best, due to the governing equations being dynamically stiff (requiring accurately resolving the smallest naturally occurring time scales) or having to approximate solutions iteratively.

Nonetheless, studying nonlinear flows theoretically, numerically, and in practice is instrumental for improving the accuracy and realism of models of central components in the climate system.

This thesis is a collection of four studies addressing two different kinds of nonlinear fluid motion occurring in the climate system: the deformation of ice sheets (main body of work), and the turbulent flows in e.g. the atmosphere and oceans. In particular, the four studies consider the three phenomena shown in figure 1.1: the response of marine-terminating glaciers subject to spatio-temporal variable forcings (top), the disturbed flow of internal layers deep within ice sheets (middle), and the dynamics of the turbulent energy cascade in large inertial-range flows (large range of scales of motion) such as in the atmosphere and oceans (bottom).

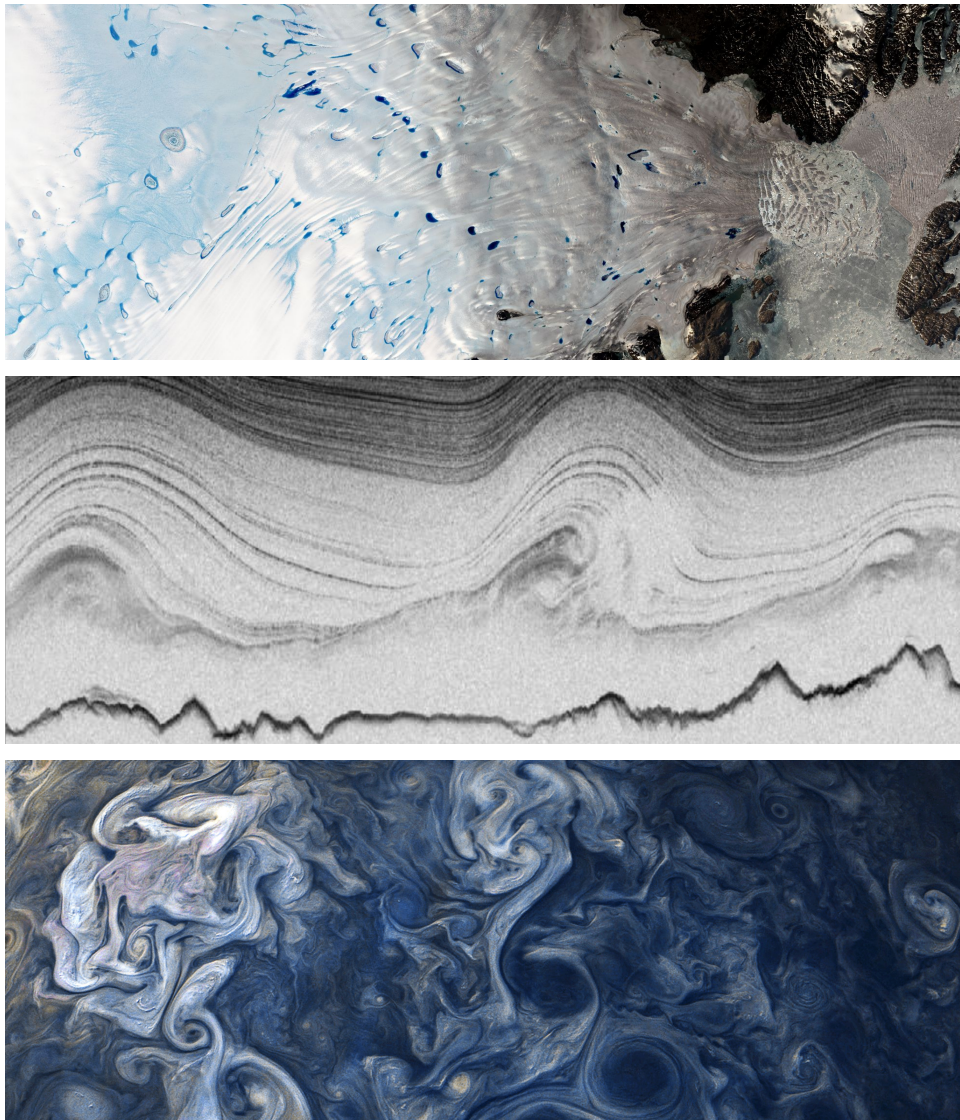


Figure 1.1: The nonlinear flows studied in this thesis:

*Top:* Marine-terminating glaciers of ice sheets subject to spatio-temporal variable forcings. The image shows the seasonal surface melting over the Zachariae outlet glacier in northeast Greenland which influences its discharge of ice into the ocean. The image is a composite of images taken between July 22–26, 2016, by NASA’s Landsat 8 satellite and processed by the author. The horizontal scale is approximately 80 km.

*Middle:* Disturbed internal layers deep within ice sheets. The image shows a 52 km long vertical transect over Greenland constructed from CReSIS’s ice-penetrating radar. The distinct horizontal curves are internal layers with different dielectric properties, suggesting increasingly disturbed layers with depth. The vertical scale is approximately 1 km, and the dark bottom curve is the bedrock, located at 2.5 km below the surface.

*Bottom:* The turbulent energy cascade. Color-enhanced image taken by NASA’s Juno spacecraft of the high clouds over Jupiter at latitude  $57^\circ$ , October 24, 2017. The image shows the turbulent motion of Jupiter’s atmosphere and the large range of scales of motion (eddy sizes). The horizontal scale is approximately 20 375 km.

Image credits: U.S. Geological Survey (top), NASA Operation IceBridge campaign 2011 (middle), and NASA/JPL-Caltech/Gerald Eichstädt/Seán Doran (bottom)

## 1.1 Ice sheet dynamics

The movement of glaciers and ice sheets generally conforms with the slow, viscosity-dominated nature of *creeping* flows. These flows display an insignificant effect of inertia and typically creep around obstacles, compared to turbulent fluids that spin off compact velocity structures such as vortices (Lautrup, 2005).

Dominated by internal friction, creeping flows are characterized by small Reynolds numbers,  $Re \ll 1$ , defined as  $Re = UL/\nu$  where  $U$  is the characteristic fluid velocity,  $L$  is the characteristic linear dimension, and  $\nu$  is the kinematic viscosity of the fluid. In this limit, the advective acceleration can be neglected in the momentum balance and the fluid description (Stokes flow) is therefore free of the nonlinear terms that tend to spontaneously break spatio-temporal flow symmetries in turbulent flows. In the case of glacier and ice sheet flows, however, the *constitutive equation* (flow law) — the relation between internal stresses and irreversible viscous momentum transfers caused by the relative motion of fluid particles — is itself nonlinear. Ice is an example of a shear-thinning fluid, meaning its effective viscosity decreases under shear straining. Fluids for which the effective viscosity depends on strain-rate or strain-rate history are collectively classified as *non-Newtonian fluids*, in contrast to constant-viscosity *Newtonian fluids*.

In the case of ice, nonlinearities allow for exotic stress-gradient phenomena to occur such as stress bridges and flow coupling (Kamb and Echelmeyer, 1986; Van Der Veen and Whillans, 1989), the latter allowing boundary conditions to exert far-reaching influence upstream (typically up to ten ice thicknesses), and allowing fast and slow moving regions to be dynamically connected.

Considering the full stress balance, such as the governing equation for ice flow prescribes, is, however, predominantly done only for process studies. For numerical projections, the iterative solution processes becomes too computationally expensive if the time-scales of interest are long. Depending on the research questions asked, several useful approximations to the governing equation (stress balance) have been developed (Hutter, 1983; Morland, 1987; MacAyeal, 1989; Pattyn, 2003), which can considerably ease the iterative processes of solving the boundary value problem w.r.t. the velocity and pressure fields.

Part I of this thesis considers, in broad terms, two different applications the governing equations for ice flow, assuming ice flow is to a good approximation a Stokes flow. In study #1, the terminus region of the northeast Greenland ice stream is considered (figure 1.1, top), which potentially has a large contribution to near-term sea level rise. The study investigates the controlling mechanisms of the observed seasonal speed-up by numerical modelling and from observational data, which might give some important insight into the future, longer-term behaviour with possible implications for other outlet systems around Greenland. In study #2, the transient deformation of internal layers within ice sheets is investigated using a transversely isotropic flow law. Justified by the physical properties measured from ice cores, the material symmetry group of deep layers cannot be assumed isotropic, and Glen's isotropic flow law is therefore arguably less applicable there.

Using a new two-dimensional vertical cross-section model, this study therefore explores how internal layer deformation is affected by accounting for transverse isotropy under idealized circumstances. This work has potential implications for the interpretation of ice core stratigraphies and chronologies, as well as further advancing the understanding of how internal disturbances are formed (defined as the buckling and folding of internal layers such as in figure 1.1) and how adjacent flow fields might be affected.

## 1.2 Turbulent cascade dynamics

Turbulent fluids can be characterized as composed of distinct, compact velocity structures with chaotic and self-advecting vorticity fields (Davidson, 2004). Unlike Stokes flows, inertia plays a significant role in turbulent flows. Consequently, the Reynolds numbers associated with fully developed turbulence are typically very large,  $Re \gg 1$ , and the advective acceleration can therefore not be neglected in the momentum balance.

Incompressible Newtonian fluids are the most studied, which have a simple linear constitutive equation and the Navier–Stokes equation as their corresponding governing equation. Unlike the governing equation for ice flow, where nonlinearities arise through the nonlinear constitutive equation, the rich spatio-temporal structure of turbulence is caused by the nonlinear advective acceleration and pressure gradient term.

For small viscosities (high Reynolds numbers), a large scale-separation develops between the large (integral) scales, where the flow is forced, and the small (Kolmogorov) viscous scale, where kinetic energy is dissipated into heat. In between the two scales, a range of self-similar scales of inertial flow develop in three-dimensional (3D) turbulence through which energy cascades intermittently from the largest to the smallest scale. Investigating the dynamics facilitating the cascade of energy is central to the study of turbulence and is the focus of studies #3 and #4 in part II of this thesis.

In literature, emphasis has historically been put on understanding the rich multi-fractal nature of velocity point-correlation and structure functions in the hope that important insights might be gained [see e.g. Batchelor (1953); Davidson (2004)]. Intriguingly, the Navier–Stokes equation has largely resisted analysis, and analytical results are rare and few. The nonlinear term is predominately to blame for this by causing the governing equations of statistical quantities not to close (Frisch, 1995; Landau and Lifshitz, 1959). As a result, a lot of effort has been put into creating closure schemes for a variety of different applications, each having their caveats (Davidson, 2004).

For both analytical and numerical analyses of the Navier–Stokes equation, representing the flow in spectral space in terms of plane waves has proven useful. In this representation, the nonlinear terms of the Navier–Stokes equation become a sum over three-wave (spectral) interactions, or *triad interactions*. It turns out

that inviscid quadratic invariants, such as energy, are conserved within each triad interaction, which makes the spectral representation particularly useful for studying the dynamics of the energy cascade. Furthermore, this representation has led to remarkable ties being found between 3D and 2D (two-dimensional) turbulence (Kraichnan, 1967, 1971).

Part II of this thesis presents work on the role of inviscid quadratic invariants in 3D turbulence by considering the helical decomposition of the spectral-space dynamics (Waleffe, 1992) using a simple energy cascade model (shell model). In study #3, the role played by helicity, a quadratic invariant in 3D, is investigated using the spectral-helical decomposition of the velocity field. In this decomposition, the number of triad interactions is increased by a factor of eight. Unfortunately, direct numerical simulations of the Navier–Stokes equation for high Reynolds number flows are still too computationally expensive to allow all eight types of interactions to be simultaneously coupled (as the Navier–Stokes equation prescribes). Motivated by this, study #3 introduces a new reduced wave-space model (shell model) capable of coupling the eight types of interactions in a computationally efficient way, thus allowing the role played by helicity and the eight individual triad interactions to be explored in a coupled configuration. In study #4, the role played by a new quadratic invariant, identified in study #3, is further investigated. This new quantity resembles enstrophy, a quadratic invariant in 2D, which is known to cause a reversed (or inverse) energy cascade from small to large scales in 2D. Being conserved only by a subset of the eight triad interactions, the new quantity is not globally conserved like energy and helicity (or enstrophy in 2D). This study therefore considers in isolation the interactions conserving the new quantity to determine their similarity to enstrophy-conserving interactions in 2D.

Understanding the connections between 2D and 3D turbulence, and how nonlinear interactions and boundary conditions may influence the direction of the energy cascade, has important implications for geophysical flows such as the atmosphere and oceans. Viewing such flows as being either confined by large aspect ratios, rotation, or fluid stratification, vertical motion in the atmosphere and oceans is in many places suppressed. The degree to which the energy cascade is reversed, and by what means, not only influences energy and momentum transports in climate, but also limits predictability due to back-propagation of (small-scale) errors in initial-value fields (Lorenz, 1969; Leith, 1971) potentially affecting large scale motion at later times.

### 1.3 Structure

Being mainly a collection of research articles, this thesis is a synopsis of three published research articles and one unpublished study.

The thesis is structured in two parts:

- Part I addresses the two studies in ice flow dynamics (one published research

article, one unpublished study).

- Part II addresses the two studies on the turbulent energy cascade (two published research articles).

Since both subjects are part of the wider theme of continuum mechanics, some elementary background on continuum mechanics is briefly introduced in chapter 2 before parts I and II. Within each part, additional subject-specific background is provided, followed by the individual studies and outlooks.

## 1.4 Notation

The notation used in this work varies between regular vector calculus notation and the more powerful index (tensor) notation, recognizing the trade-off between readability, notational compactness, and tradition in literature. In vector calculus notation, tensors of rank 1 (vectors) or larger are denoted with bold, e.g.  $\mathbf{A}$ , implying the tensor rank is implicit unless otherwise stated explicitly for readability, such as  ${}^{(4)}\mathbf{A}$  or  ${}^{(6)}\mathbf{A}$  for tensors of rank 4 and 6, respectively. In index notation, the ranks are naturally explicit, e.g.  $A_{ijkl}$ . Note only orthogonal coordinate systems are considered here, implying no need to distinguish between covariant and contravariant components. Furthermore, the Einstein summation notation for repeated indices is adopted unless otherwise stated, and the following compact notation for derivatives is generally used

$$\partial_i f = \frac{\partial f}{\partial x_i} \quad \text{and} \quad \partial_t f = \frac{\partial f}{\partial t}.$$

Stated explicitly as convenient examples, the following expressions are therefore equivalent:

$$\begin{aligned} \partial_i u_j &= \nabla \mathbf{u} \\ \partial_i u_i &= \nabla \cdot \mathbf{u} \\ \partial_{ij} u_k &= \partial_i \partial_j u_k \\ \partial_{jj} u_i &= \nabla^2 \mathbf{u} \\ A_{ik} B_{kj} &= \mathbf{A} \cdot \mathbf{B} \\ A_{ik} B_{kl} C_{lj} &= \mathbf{A} \cdot \mathbf{B} \cdot \mathbf{C} \\ A_{ii} &= \mathbf{A} : \mathbf{I} = \text{Tr} \mathbf{A} \\ A_{lk} B_{kl} &= \mathbf{A} : \mathbf{B} = \text{Tr}(\mathbf{A} \cdot \mathbf{B}) \\ A_{mk} B_{kl} C_{lm} &= \mathbf{A} : (\mathbf{B} \cdot \mathbf{C}) = \text{Tr}(\mathbf{A} \cdot \mathbf{B} \cdot \mathbf{C}). \end{aligned}$$

Finally, note that the exponent notation for repeated inner products, e.g.  $\mathbf{A} \cdot \mathbf{A} = \mathbf{A}^2$ , is used throughout.

## Chapter 2

# Continuous matter

Fluid dynamics concerns itself with the temporal evolution of a moving fluid. This description typically includes the evolution of field variables such as velocity  $\mathbf{u}(t, \mathbf{x})$ , pressure  $p(t, \mathbf{x})$ , density  $\rho(t, \mathbf{x})$ , and temperature  $T(t, \mathbf{x})$ , all of which are regarded as continuous due to the macroscopic nature of the phenomena studied. Because the equations governing the evolution of field variables are often complicated and coupled, simplifications are frequently considered such as fluid incompressibility and isothermality, thereby decoupling density and temperature from the problem. Furthermore, the dependencies on space ( $\mathbf{x}$ ) and time ( $t$ ) are generally assumed implicit and therefore suppressed, a tradition which is adopted here too.

This chapter introduces some basic background on the momentum balance, relevant for both parts I and II, the content and style of which follows Landau and Lifshitz (1959) and Naumenko and Altenbach (2007).

### 2.1 Incompressibility and the momentum balance

Mass conservation within some infinitesimal volume element,  $dV$ , implies any local change of mass must be caused by a net mass flux through the enclosing surface of the volume element, that is

$$\partial_t \int \rho dV = - \oint \rho u_i dS_i ,$$

where  $dS_i$  is an infinitesimal element of the enclosing surface. Applying the divergence theorem the surface integral becomes  $\int \partial_i(\rho u_i) dV$ , implying  $\partial_t \rho = -\partial_i(\rho u_i)$  by equating integrands. For incompressible fluids (constant density,  $\rho$ ), mass conservation thus translates into a divergence-free velocity field

$$\partial_i u_i = 0. \tag{2.1}$$

A similar approach may be adopted for the rate of change of momentum,  $\rho u_i$ . In this case, any local change of momentum in some volume element must be balanced

by a net momentum flux into the element and by body forces acting on the element, that is

$$\partial_t \int \rho u_i dV = -\oint \Pi_{ij} dS_j + \int \rho b_i dV,$$

where  $\Pi_{ij}$  is the momentum-flux density of the  $i$ th component of momentum in the  $j$ th direction, and  $b_i$  is the sum of all body forces per unit mass. Rewriting the surface integral using Green's theorem it becomes  $-\int \partial_j \Pi_{ij} dV$ , implying

$$\partial_t(\rho u_i) = -\partial_j \Pi_{ij} + \rho b_i.$$

Further decomposing  $\Pi_{ij}$  into advective components,  $(\rho u_i)u_j$  ( $i$ th momentum component in  $j$ th direction), and viscous momentum transfers by stresses on the enclosing surface,  $-\sigma_{ij}$ , gives  $\rho \partial_t u_i = -\rho u_j \partial_j u_i + \partial_j \sigma_{ij} + \rho b_i$  assuming incompressibility. Denoting the material derivative by  $D_t(\cdot) = \partial_t(\cdot) + u_j \partial_j(\cdot)$ , the momentum balance becomes

$$\rho D_t u_i = \partial_j \sigma_{ij} + \rho b_i. \quad (2.2)$$

Decomposing the stress tensor ( $\sigma_{ij}$ ) into its normal ( $-p\delta_{ij}$ ) and deviatoric ( $\tau_{ij}$ ) parts

$$\sigma_{ij} = -p\delta_{ij} + \tau_{ij},$$

where the pressure ( $p$ ) and the deviatoric-stress tensor ( $\tau_{ij}$ ) are defined as

$$p = -\sigma_{jj}/3 \quad \text{and} \quad \tau_{ij} = \begin{pmatrix} \sigma_{xx} + p & \sigma_{xy} & \sigma_{xz} \\ \sigma_{yx} & \sigma_{yy} + p & \sigma_{yz} \\ \sigma_{zx} & \sigma_{zy} & \sigma_{zz} + p \end{pmatrix},$$

leaves  $\tau_{ij}$  traceless such that it vanishes for any material at rest. Using the stress decomposition, the balance of momentum becomes

$$\rho D_t u_i = -\partial_i p + \partial_j \tau_{ij} + \rho b_i. \quad (2.3)$$

In order to apply the momentum balance to a particular material, a *constitutive relation* must be given, relating the material's kinematic response to an applied stress. That is, a stress-strain relationship,  $\tau_{ij}(\epsilon_{ij}, \dot{\epsilon}_{ij})$ , must be specified. Here, the *strain tensor*,  $\epsilon_{ij}$ , is defined in terms of the symmetric gradient of the displacement vector field,  $d_i$ , as

$$\epsilon_{ij} = \frac{1}{2} (\partial_j d_i + \partial_i d_j), \quad (2.4)$$

and the *strain-rate tensor* is defined similarly in terms of velocity gradients as

$$\dot{\epsilon}_{ij} = \frac{1}{2} (\partial_j u_i + \partial_i u_j), \quad (2.5)$$

since the velocity field is by definition the time derivative of the displacement field. Typically, materials with constitutive relations depending on the displacement field exhibit elastic (Hookean) behaviour, whereas material with constitutive relations depending on the strain-rate exhibit viscous fluid behaviour.

Note that the velocity gradient,  $\partial_j u_i$ , can more generally be decomposed into its symmetric part (2.5) and antisymmetric part, the latter defined as

$$\omega_{ij} = \frac{1}{2} (\partial_j u_i - \partial_i u_j), \quad (2.6)$$

such that  $\partial_j u_i = \dot{\epsilon}_{ij} + \omega_{ij}$ . Viscous constitutive relations, however, typically rely only on  $\dot{\epsilon}_{ij}$  since  $\omega_{ij}$  is related to the rotation rate of fluid elements and does not contribute to the deformational rate of change.

## 2.2 Constitutive relations

Constitutive relations are often derived either from first principles or from empirical studies. Generally, they reduce the material description to depend on relatively few free macroscopic parameters, e.g. the elastic moduli in homogeneous isotropic Hookean solids, or the isotropic viscosity in linear-viscous (Newtonian) isotropic fluids. In the latter case, the constitutive equation follows from noting that internal friction is caused by the relative motion of fluid particles, implying viscous stresses,  $\tau_{ij}$ , must depend on spatial derivatives of the velocity field. For small velocity gradients, dependence on first-order derivatives is generally assumed to suffice, in which case the constitutive equation becomes (Landau and Lifshitz, 1959)

$$\tau_{ij} = \eta \dot{\epsilon}_{ij}, \quad (2.7)$$

where  $\eta = \rho\nu$  is the dynamic viscosity.

Constitutive equations are frequently prescribed in their forward form,  $\dot{\epsilon}_{ij}(\tau_{ij})$ , giving the response of a material to an applied stress. In order to obtain a material's governing equation, the constitutive equation must first be posed in its so-called inverse form,  $\tau_{ij}(\dot{\epsilon}_{ij})$  [as in (2.7)], thus allowing it to be inserted into the stress-divergence term of the momentum balance (2.3). In the case of Newtonian fluids, this leads to the governing equation known as the Navier–Stokes equation (assuming incompressibility and neglecting  $b_i$ )

$$D_t u_i = -\rho^{-1} \partial_i p + \nu \partial_{jj} u_i. \quad (2.8)$$

In viscous fluids, viscosity acts as a momentum sink, which, unlike in purely elastic materials, implies energy is dissipated through a load cycle. Consequently, simple linear *viscoelastic* materials with mixed viscous and elastic properties can modelled by simple one-dimensional constitutive models combining springs and dashpots (viscous dampers) in series, parallel, or in more complicated configurations. As an example, consider the Kelvin–Voigt viscoelastic model where a Hookean

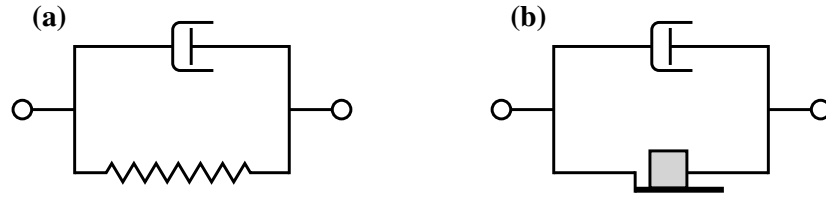


Figure 2.1: Simple one-dimensional material models. (a) Kelvin–Voigt viscoelastic material represented by a parallel connection between a purely viscous damper and a purely elastic spring. (b) Bingham viscoplastic material represented by a parallel connection between a purely viscous damper and frictional sliding block.

spring and a linear-viscous dashpot are connected parallel [figure 2.1.(a)]. For such a material, the straining of both components must be identical and equal the total strain,  $\epsilon = \epsilon_s = \epsilon_d$  (subscripts referring to spring and dashpot components, respectively), whereas the total stress must equal the sum of component-wise contributions,  $\sigma = \sigma_s + \sigma_d$ . Invoking the (one-dimensional) constitutive models for each component,  $\sigma_s = E\epsilon_s$  and  $\sigma_d = \eta\dot{\epsilon}_d$ , where  $E$  is the elastic modulus and  $\eta$  the viscosity, the constitutive relation becomes  $\sigma = E\epsilon + \eta\dot{\epsilon}$ .

In addition to viscoelastic materials, a class *viscoplastic* materials also exists. While viscoelastic materials experience little permanent deformation after a load cycle (both elastic and viscous strains recovering), viscoplastic materials experience irreversible deformation when subjected to stresses exceeding some characteristic yield stress,  $\sigma_{\text{yield}}$ . In other words, the slow time-dependent viscous deformation, or *creep*, is irreversible in such materials (Naumenko and Altenbach, 2007). In terms of mechanical components like springs and dashpots, plastic flows are analogous to sliding block components where sliding occurs once an applied stress exceeds the frictional resistance. A viscoplastic material can therefore be modelled in simple terms by e.g. a dashpot and sliding block element connected in parallel, also known as a Bingham material [figure 2.1.(b)]. Several microphysical mechanisms have been proposed to explain creeping flows (Courtney, 2005). In this work, however, only those related to the creep of polycrystalline ice are treated (chapter 3).

Purely viscous materials may also creep in a plastic fashion if governed by a nonlinear constitutive relation, such as the Norton–Hoff model

$$\begin{aligned}\dot{\epsilon} &= \eta^{-1}\sigma \\ \eta^{-1} &= A\sigma^{n-1},\end{aligned}$$

which effectively exhibits a yield stress for large flow exponents,  $n$ , where  $A$  is a material parameter. In this sense, the subject of *rheology* concerns itself with the constitutive relations of materials with nonlinear deformational behaviours, complicated directional dependencies (material symmetries), and mixed fluid–solid properties.

**Part I**

**Ice sheet dynamics**



## Chapter 3

# Creep of polycrystalline ice

The motion of ice under an applied stress conforms with the slow moving, highly viscous, and continuously remoulding nature of creep. Glen (1955) was the first to show experimentally that ice is not a simple linear-viscous (Newtonian) fluid, but rather a nonlinear-viscous (non-Newtonian) viscoplastic fluid, governed by a Norton–Hoff type constitutive relation

$$\begin{aligned}\dot{\epsilon} &= \eta^{-1} \tau \\ \eta^{-1} &= A \tau^{n-1},\end{aligned}\tag{3.1}$$

where  $\dot{\epsilon}$  is the strain-rate response to an applied deviatoric stress,  $\tau$ , and  $A$  is a material parameter. The degree of plasticity is captured by the flow exponent,  $n$ , which in the case of glaciers and ice sheets typically ranges from 2 to 3 (Cuffey and Paterson, 2010). The rheology of ice is therefore regarded as intermediary between a Newtonian fluid ( $n = 1$ ) and a perfectly plastic material (large  $n$ ).

The ice material in glaciers and ice sheets consists of an aggregate of ice crystals of the kind  $I_h$  (or simply *grains*) with varying sizes and orientations depending on the deformational history. The individual grains in multi-grained ice (*polycrystalline ice*), are structured as crystal lattices, composed of hexagonal molecular rings. The hexagonal rings [figure 3.1.(a)] arrange themselves in stacked planes

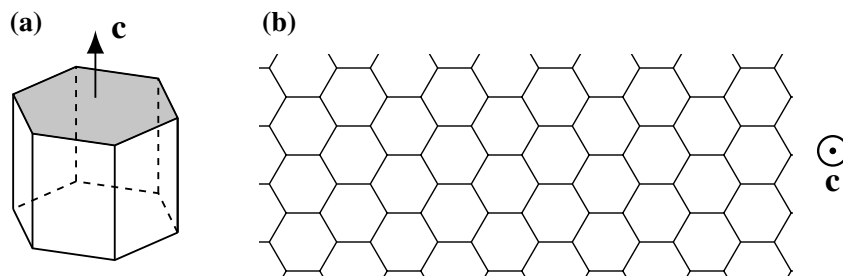


Figure 3.1: A single hexagonal molecular ring and its normal direction  $\mathbf{c}$  (panel a), and a top-down view (along the  $\mathbf{c}$ -axis) onto a basal plane constructed from hexagonal rings forming a hexagonal mesh (panel b).

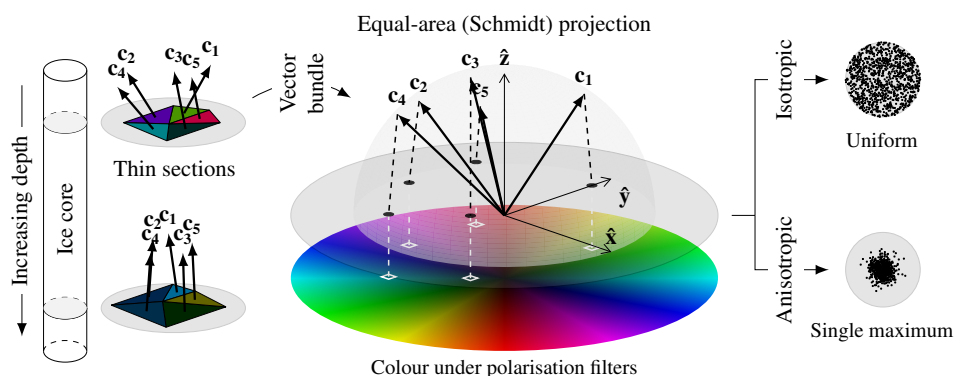


Figure 3.2: Schmidt diagrams (right-hand side) are derived from ice-core thin sections (left-hand side), defined as the equal-area projection of  $\mathbf{c}$ -axes from the thin sections (middle). The two idealized diagrams on the right-hand side show the difference between an isotropic fabric (top) and a single-maximum fabric with a vertical symmetry axis (bottom).

of rings [figure 3.1.(b)], or *basal planes*<sup>1</sup>, thereby allowing a basal-plane normal direction ( $\mathbf{c}$ -axis) to be defined per grain (crystal) as a natural measure of the microstructure orientation. In this regard, the *ice fabric*, short for  $\mathbf{c}$ -axis fabric, refers to the ensemble/distribution of crystal  $\mathbf{c}$ -axes from a sample of ice. Depending on the deformational history, the fabric may range from isotropic (no preferred  $\mathbf{c}$ -axes direction) to anisotropic with a *single-maximum* or *multiple-maxima* ( $\mathbf{c}$ -axes distributed nonuniformly by clustering around one or multiple preferred directions), or other exotic types such as band or girdle fabrics ( $\mathbf{c}$ -axes distributed along conical surfaces and planes) (Cuffey and Paterson, 2010).

The fabric may be quantified using so-called Schmidt diagrams, defined as the equal-area projection of  $\mathbf{c}$ -axes from a thin section sample of an ice core (figure 3.2). In figure 3.3, Schmidt diagrams are shown for the North Greenland ice core project (NGRIP) ice core (Svensson et al., 2003), exemplifying the development of a strong single maximum with depth, a common fabric type found in deep layers (Hooke, 1973; Gow and Williamson, 1976; Herron and Langway, 1982).

Under an applied stress, the deformation of single crystals strongly favour the slipping of basal planes relative to one another (basal plane shearing), whereas shearing along nonbasal planes can be up to four orders of magnitude harder (Duval et al., 1983). The basal-plane slipping, synonymous to *basal glide* or *easy glide*, is facilitated by the movement of dislocations, the principle mechanism of deformation (Cuffey and Paterson, 2010). For shearing along nonbasal planes, so-called *hard glide*, deformation is also facilitated by the movement of dislocations but along the prismatic or pyramidal planes (figure 3.4) or by dislocation climb normal to basal planes (Fukuda et al., 1987).

The bulk creep behaviour of polycrystalline ice is effectively controlled by rate-limiting mechanisms acting in conjunction with basal glide. For example, in

<sup>1</sup>Basal planes are in fact slightly uneven due to the hexagonal rings not being strictly flat.

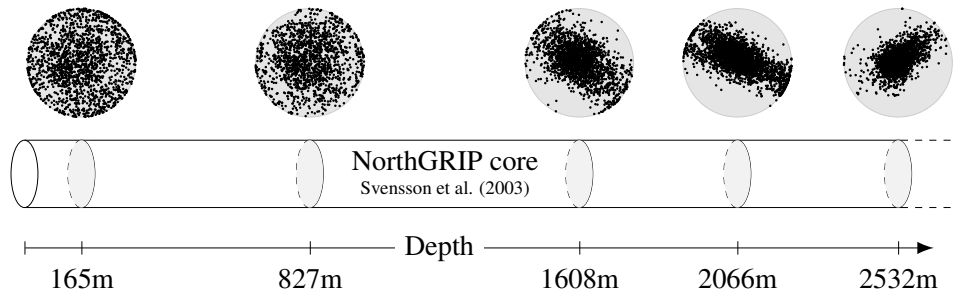


Figure 3.3: Distribution of  $c$ -axes (Schmidt diagrams) with depth for the North Greenland ice core project (NGRIP) ice core (Svensson et al., 2003), showing a strong single maximum developing towards the bottom. Replotted with permission from Anders Svensson.

fine grained ice, grain boundary sliding has been suggested to play a rate-limiting role (Goldsby and Kohlstedt, 2001), or, in the case of a polycrystalline aggregate with a multitude of grain orientations, grains unfavourably oriented for basal glide may be rate-limiting by dislocations being stressed to move in the hard directions (Fukuda et al., 1987; Duval and Castelnau, 1995), known as *dislocation creep*.

The creep behaviour associated with larger-scale motion, however, requires a continuum description involving macroscopic flow parameters such as the effective fluid viscosity. To determine such parameters, a micro–macro model is needed to connect the physical properties of the fabric microstructure to the effective macroscopic flow parameters. Alternatively, simplifying assumptions can be made about the fabric microstructure, such as idealizing the microstructure symmetry group, allowing the flow parameters to be determined from deformational tests without knowledge of the detailed micro state. The most celebrated flow law for ice is the *Nye–Glen isotropic flow law* (Glen, 1955; Nye, 1957) (or simply Glen’s law) which multi-axially extends (3.1) by assuming fabric isotropy, thereby reducing the deformational description (flow law) to depend on just one flow parameter, the

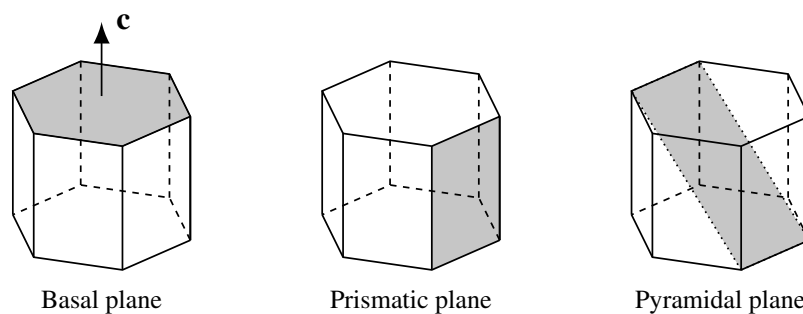


Figure 3.4: Crystallographic planes along which dislocation glide occurs, the principle mechanism by which ice deforms. Shearing along nonbasal planes can be up to four orders of magnitude harder than along basal planes (Duval et al., 1983).

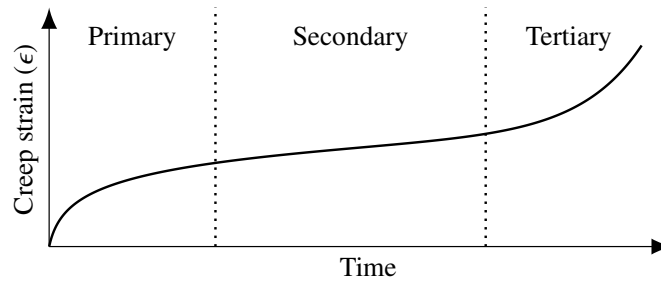


Figure 3.5: The three stages of creep: primary, secondary and tertiary. In the secondary stage, the creep strain-rate is approximately steady.

rate-factor (isotropic fluidity).

In the following background material, Glen's law is treated in detail, which provides a natural stepping stone for considering the more complicated transversely isotropic flow law in study #2. In addition, because Weertman's sliding law and the block-flow approximation of Glen's law are central background for study #1, the two subjects are briefly introduced in the following too.

### 3.1 Steady state creep

Creep deformation can be regarded as taking place in three stages (figure 3.5) (Cuffey and Paterson, 2010):

1. Primary (transient) creep is characterised by relatively high strain-rates which decrease with time due to internal stress redistribution and material hardening processes (e.g. strain, time, and kinematic hardening), subsequently transitioning into the second stage.
2. Secondary creep is characterised by an approximate balance between softening and hardening processes, and may be regarded as a steady state in which the strain-rate approaches a minimum value. In this stage, damage (softening) and recovery (hardening) processes are concurrent and no material strength is therefore lost.
3. Tertiary creep is characterised by progressive damage by microscopic void and pore growth, thereby weakening the material's strength until fracture finally occurs.

When modelling ice flow, as well as in many engineering applications, the proposed constitutive models often assume secondary creep for simplicity (Cuffey and Paterson, 2010; Naumenko and Altenbach, 2007). If strains are infinitesimally small, the strain-rate tensor,  $\dot{\epsilon}_{ij}$ , may be partitioned into contributions from elastic

and viscous creep, respectively, that is

$$\dot{\epsilon}_{ij} = \dot{\epsilon}_{ij}^{\text{elastic}} + \dot{\epsilon}_{ij}^{\text{creep}}.$$

In the case of ice flow, however, elastic deformation is typically disregarded in secondary creep (Cuffey and Paterson, 2010). From here on, only the inelastic creep component is therefore considered ( $\dot{\epsilon}_{ij} = \dot{\epsilon}_{ij}^{\text{creep}}$ ).

In this work, the steady-state creep theory by Odqvist (1974) is adopted, itself based on the original work by Richard von Mises's potential formulations. In short, one considers the variational problem  $\delta W(\boldsymbol{\sigma}) = \delta \boldsymbol{\sigma} : \dot{\boldsymbol{\epsilon}}$ , rooted in thermodynamic extremum principles and related to viscous energy dissipation (Ziegler, 1963; Naumenko and Altenbach, 2007), which gives rise to the *flow rule* (synonymous to *flow law* or *constitutive equation*)

$$\dot{\boldsymbol{\epsilon}} = \frac{\partial W(\boldsymbol{\sigma})}{\partial \boldsymbol{\sigma}}, \quad (3.2)$$

where  $W$  is known as the *creep potential*. Note that this formulation gives the *forward* flow law — the material's response to an applied stress — and not the inverse law,  $\boldsymbol{\tau}(\dot{\boldsymbol{\epsilon}})$ , needed for the stress-divergence term in the momentum balance.

From (3.2), constitutive equations are constrained by requiring frame indifference for relevant (orthogonal) symmetry transformations,  $\mathbf{Q}$ , which is enforced by requiring  $W(\boldsymbol{\sigma})$  be indifferent under the same transformations in the sense that

$$W(\mathbf{Q} \cdot \boldsymbol{\sigma} \cdot \mathbf{Q}^T) = W(\boldsymbol{\sigma}). \quad (3.3)$$

Choosing the relevant symmetry transformations should ideally be guided by the material and physical symmetry groups; that is microstructure symmetries such as crystalline symmetries, fiber arrangements, and behavioural symmetries identified from elastic- and creep-deformation experiments.

Due to the frame indifference imposed by (3.3), the creep potential can be reduced to depend only on the stress-tensor (orthogonal) invariants  $I_1(\boldsymbol{\sigma}), \dots, I_N(\boldsymbol{\sigma})$  associated with the relevant group of symmetry transformations, where  $N$  is the total number of invariants. For example, in the case of Glen's flow law for ice, three invariants exist under isotropy,  $\text{Tr } \boldsymbol{\sigma}$ ,  $\text{Tr } \boldsymbol{\sigma}^2$ , and  $\text{Tr } \boldsymbol{\sigma}^3$ .

The functional dependence of  $W$  on  $I_i(\boldsymbol{\sigma})$  is often, and for the present purpose, expressed in terms of a single *equivalent stress* or *effective stress*,  $\sigma_E(I_1(\boldsymbol{\sigma}), \dots, I_N(\boldsymbol{\sigma}))$ , such that

$$W(\boldsymbol{\sigma}) = W(\sigma_E(I_1(\boldsymbol{\sigma}), \dots, I_N(\boldsymbol{\sigma}))), \quad (3.4)$$

implying

$$\dot{\boldsymbol{\epsilon}} = \frac{\partial W(\sigma_E)}{\partial \sigma_E} \frac{\partial \sigma_E}{\partial \boldsymbol{\sigma}} = \epsilon_E \frac{\partial \sigma_E}{\partial \boldsymbol{\sigma}}, \quad \text{where } \epsilon_E = \frac{\partial W(\sigma_E)}{\partial \sigma_E}, \quad (3.5)$$

$\epsilon_E$  being the *equivalent strain-rate* or *effective strain-rate*. The functional dependence of  $\sigma_E$  on  $I_i(\boldsymbol{\sigma})$  is, in turn, a phenomenological model.

In the interest of generalizing the approach for deriving flow laws reflecting a given symmetry, the present work adopts the following expression for  $\sigma_E$  (Naumenko and Altenbach, 2007)

$$\begin{aligned} \sigma_E(I_1(\boldsymbol{\sigma}), \dots, I_N(\boldsymbol{\sigma})) &= \alpha \mathcal{I}_1(I_1(\boldsymbol{\sigma}), \dots, I_N(\boldsymbol{\sigma})) \\ &+ \beta \mathcal{I}_2(I_1(\boldsymbol{\sigma}), \dots, I_N(\boldsymbol{\sigma})) \\ &+ \gamma \mathcal{I}_3(I_1(\boldsymbol{\sigma}), \dots, I_N(\boldsymbol{\sigma})), \end{aligned} \quad (3.6)$$

where  $\mathcal{I}_1, \mathcal{I}_2$  and  $\mathcal{I}_3$  are each weighted sums (material parameters as weights) over products of the basic stress-tensor invariants,  $I_i(\boldsymbol{\sigma})$ , resulting in first, second and third order dependence on  $\boldsymbol{\sigma}$ , respectively. Models with  $\gamma = 0$  are referred to as classical creep models, whereas  $\gamma \neq 0$  are nonclassical due to their constitutive equations having *tensorially* nonlinear terms.

The functions  $\mathcal{I}_1, \mathcal{I}_2$  and  $\mathcal{I}_3$  can in general be prescribed by the help of material tensors  $\mathbf{A}$ ,  ${}^{(4)}\mathbf{B}$  and  ${}^{(6)}\mathbf{C}$  (rank 2, 4 and 6, respectively) (Naumenko and Altenbach, 2007)

$$\mathcal{I}_1 = \mathbf{A} : \boldsymbol{\sigma}, \quad \mathcal{I}_2^2 = \boldsymbol{\sigma} : {}^{(4)}\mathbf{B} : \boldsymbol{\sigma}, \quad \mathcal{I}_3^3 = \boldsymbol{\sigma} : (\boldsymbol{\sigma} : {}^{(6)}\mathbf{C} : \boldsymbol{\sigma}), \quad (3.7)$$

which too must be invariant under the same set of symmetry transformations,  $\mathbf{Q}$ , that is

$$\mathbf{A}' = \mathbf{Q} \cdot \mathbf{A} \cdot \mathbf{Q}^\top = \mathbf{A} \quad (3.8)$$

$${}^{(4)}\mathbf{B}' = \mathbf{Q} \cdot \mathbf{Q} \cdot {}^{(4)}\mathbf{B} \cdot \mathbf{Q}^\top \cdot \mathbf{Q}^\top = {}^{(4)}\mathbf{B} \quad (3.9)$$

$${}^{(6)}\mathbf{C}' = \mathbf{Q} \cdot \mathbf{Q} \cdot \mathbf{Q} \cdot {}^{(6)}\mathbf{C} \cdot \mathbf{Q}^\top \cdot \mathbf{Q}^\top \cdot \mathbf{Q}^\top = {}^{(6)}\mathbf{C}. \quad (3.10)$$

For example in the case of isotropy, the material tensors  $\mathbf{A}$ ,  ${}^{(4)}\mathbf{B}$  and  ${}^{(6)}\mathbf{C}$  must be functions of (products of) the identity matrix, the only rank 2 isotropic tensor.

In general terms using material tensors, the flow law can thus be written as

$$\dot{\boldsymbol{\epsilon}} = \epsilon_E \left( \alpha \frac{\partial \mathcal{I}_1}{\partial \boldsymbol{\sigma}} + \beta \frac{\partial \mathcal{I}_2}{\partial \boldsymbol{\sigma}} + \gamma \frac{\partial \mathcal{I}_3}{\partial \boldsymbol{\sigma}} \right) \quad (3.11)$$

$$= \epsilon_E \left( \alpha \mathbf{A} + \beta \frac{{}^{(4)}\mathbf{B} : \boldsymbol{\sigma}}{\mathcal{I}_2} + \gamma \frac{\boldsymbol{\sigma} : {}^{(6)}\mathbf{C} : \boldsymbol{\sigma}}{\mathcal{I}_3^2} \right), \quad (3.12)$$

where (3.6) and the chain rule have been used.

## 3.2 Glen's isotropic flow law

For an isotropic fabric, the material tensors  $\mathbf{A}$ ,  ${}^{(4)}\mathbf{B}$  and  ${}^{(6)}\mathbf{C}$  must be invariant under transformations  $\mathbf{Q} \in \mathcal{SO}(3)$  (full rotational symmetry). Consequently, the material tensors must be functions of elementary isotropic tensors, which for ranks

2, 4 and 6 imply they can be functions of (products of) only the rank 2 identity tensor,  $\delta_{ij}$ . More precisely, it can be shown that (Kearsley and Fong, 1975)

$$\begin{aligned}
A_{ij} &= a_1 \delta_{ij}, \\
B_{ijkm} &= b_1 \delta_{ij} \delta_{km} + b_2 \delta_{ik} \delta_{jm} + b_3 \delta_{im} \delta_{jk}, \\
C_{ijkmpq} &= \delta_{ij} (c_1 \delta_{km} \delta_{pq} + c_2 \delta_{kp} \delta_{mq} + c_3 \delta_{kq} \delta_{mp}) \\
&\quad + \delta_{ik} (c_4 \delta_{jm} \delta_{pq} + c_5 \delta_{jp} \delta_{mq} + c_6 \delta_{jq} \delta_{mp}) \\
&\quad + \delta_{im} (c_7 \delta_{jk} \delta_{pq} + c_8 \delta_{jp} \delta_{kq} + c_9 \delta_{jq} \delta_{kp}) \\
&\quad + \delta_{ip} (c_{10} \delta_{jk} \delta_{mq} + c_{11} \delta_{jm} \delta_{kq} + c_{12} \delta_{jq} \delta_{km}) \\
&\quad + \delta_{iq} (c_{13} \delta_{jk} \delta_{mp} + c_{14} \delta_{jm} \delta_{kp} + c_{15} \delta_{jp} \delta_{km}),
\end{aligned} \tag{3.13}$$

where  $a_i$ ,  $b_i$  and  $c_i$  are coefficients.

Noting that the basic invariants of rank 2 tensors are given by

$$I_1(\boldsymbol{\sigma}) = \text{Tr } \boldsymbol{\sigma}, \quad I_2(\boldsymbol{\sigma}) = \text{Tr } \boldsymbol{\sigma}^2, \quad I_3(\boldsymbol{\sigma}) = \text{Tr } \boldsymbol{\sigma}^3, \tag{3.14}$$

inserting (3.13) into (3.7), one finds

$$\begin{aligned}
\mathcal{I}_1 &= \mu_{1,1} I_1 \\
\mathcal{I}_2^2 &= \mu_{2,1} I_1^2 + \mu_{2,2} I_2 \\
\mathcal{I}_3^3 &= \mu_{3,1} I_1^3 + (\mu_{3,2} + \mu_{3,3}) I_1 I_2 + \mu_{3,4} I_3,
\end{aligned} \tag{3.15}$$

where the coefficients have been grouped together for convenience by

$$\begin{aligned}
\mu_{1,1} &= a_1, \\
\mu_{2,1} &= b_1, \quad \mu_{2,2} = b_2 + b_3, \\
\mu_{3,1} &= c_1, \quad \mu_{3,2} = c_4 + c_7, \quad \mu_{3,3} = c_2 + c_3 + c_{12} + c_{15}, \\
\mu_{3,4} &= c_5 + c_6 + c_8 + c_9 + c_{10} + c_{11} + c_{13} + c_{14}.
\end{aligned}$$

By similar calculations, contracting the material tensors according to (3.12), one finds

$$\begin{aligned}
{}^{(4)}\mathbf{B} : \boldsymbol{\sigma} &= \mu_{2,1} I_1 \mathbf{I} + \mu_{2,2} \boldsymbol{\sigma} \\
\boldsymbol{\sigma} : {}^{(6)}\mathbf{C} : \boldsymbol{\sigma} &= \mu_{3,1} I_1^2 \mathbf{I} + \mu_{3,2} I_2 \mathbf{I} + \mu_{3,3} I_1 \boldsymbol{\sigma} + \mu_{3,4} \boldsymbol{\sigma}^2.
\end{aligned} \tag{3.16}$$

From the above expressions, the constitutive equation can be constructed by inserting into (3.12). Two simplifying assumptions are, however, frequently adopted when considering the flow of ice masses: (i) polycrystalline ice is incompressible (no volumetric creep), and (ii) nonclassical (second order) terms are neglected ( $\gamma = 0$ ) because laboratory experiments find they have little influence (Jun et al., 1996). Such nonclassical effects include creep normal or parallel to shear planes (Poynting–Swift effect) (Naumenko and Altenbach, 2007). In addition, the creep potential has not yet been specified, preventing the effective strain-rate,  $\epsilon_E$ , from being calculated (3.5) and therefore also the effective viscosity. In the following subsections, these points are treated before finally arriving at Glen's flow law.

### Incompressibility

The density of ice in glaciers and ice sheets varies through the top-most  $\sim 100$  m of the ice column where snow gradually transforms to firn, and then subsequently to ice with a constant density of  $917 \text{ kg m}^{-3}$ . During this transformation, air passages between grains are sealed off (pore closeoff), and at greater depths bubbles become highly compressed until finally being absorbed into the crystal lattice (air-hydrate crystals, or clathrates). When modelling thick ice masses, ice can therefore be regarded as approximately incompressible.

Recalling that  $\boldsymbol{\sigma} = -p\mathbf{I} + \boldsymbol{\tau}$  and letting the stress-deviator invariants,  $I_i(\boldsymbol{\tau})$ , be defined similarly to (3.14), equations (3.15) and (3.16) can be written, respectively, as (neglecting nonclassical terms  $\gamma = 0$ )

$$\mathcal{I}_1 = -3\mu_{1,1}p$$

$$\mathcal{I}_2^2 = 3\mu_{2,2} \left( 3\frac{\mu_{2,1}}{\mu_{2,2}} + 1 \right) p^2 + \mu_{2,2}I_2(\boldsymbol{\tau})$$

and

$${}^{(4)}\mathbf{B} : \boldsymbol{\sigma} = -\mu_{2,2} \left( 3\frac{\mu_{2,1}}{\mu_{2,2}} + 1 \right) p\mathbf{I} + \mu_{2,2}\boldsymbol{\tau}.$$

Enforcing incompressibility requires eliminating pressure dependencies, which is fulfilled if the expressions in the parentheses vanish, implying

$$\mu_{1,1} = 0 \quad \text{and} \quad \frac{\mu_{2,1}}{\mu_{2,2}} = -\frac{1}{3}, \quad (3.17)$$

reducing the constitutive equation (3.12) to

$$\dot{\boldsymbol{\epsilon}} = \epsilon_E \beta \mu_{2,2}^{1/2} (I_2(\boldsymbol{\tau}))^{-1/2} \boldsymbol{\tau} \quad (3.18)$$

Note that the constraints (3.17) reduce  $\sigma_E$  to depend only on the deviatoric-stress invariants,  $I_i(\boldsymbol{\tau})$ . In order to conform with literature in the following, the effective deviatoric stress,  $\tau_E$ , is therefore referred to instead, which is equal to  $\sigma_E$  due to (3.17). In addition, invariants may unambiguously be assumed to be functions of the deviatoric stress, and in the following the suppressed notation  $I_i = I_i(\boldsymbol{\tau})$  is therefore adopted unless stated otherwise.

### Effective viscosity

In equation (3.18), the prefactor  $\eta^{-1} = \epsilon_E \beta \mu_{2,2}^{1/2} I_2^{-1/2}$  is the effective material fluidity (reciprocal viscosity). However, in order to be fully prescribed, the effective strain-rate,  $\epsilon_E = \partial W(\tau_E) / \partial \tau_E$ , must be calculated, which requires the potential to be specified. Nye (1957) proposed the effective stress and strain-rates follow

the observed power law found from shearing experiments of single (tensorial) components (3.1) (Glen, 1955), that is

$$\epsilon_E = A_0 \tau_E^n, \quad \text{or equivalently} \quad W(\tau_E) = \frac{A_0}{n+1} \tau_E^{n+1}, \quad (3.19)$$

also known as a Norton–Bailey potential, implying the fluidity is

$$\eta^{-1} = A_0 \left( \beta [\mu_{2,2} I_2]^{1/2} \right)^n \beta \mu_{2,2}^{1/2} I_2^{-1/2} = A I_2^{(n-1)/2}, \quad (3.20)$$

where the rate factor,  $A$ , is defined as the product  $A = A_0 \beta^{n+1} \mu_{2,2}^{(n+1)/2}$ .

The value of the exponent  $n$  typically ranges from 2 to 3, but most often  $n = 3$  is found to fit (Cuffey and Paterson, 2010). Lower values around  $n = 1.8$  have however also been suggested in situations where grain-boundary sliding is the rate-limiting mechanism, such as in fined-grained ice (Goldsby and Kohlstedt, 2001). Note that these values are neither linear viscous  $n = 1$  (Newtonian) nor plastic (large  $n$ ), and ice is therefore generally regarded as an intermediary, or *viscoplastic*.

### Glen's law

Combining (3.20) with (3.18), one arrives the *Nye–Glen isotropic flow law* (Glen, 1955; Nye, 1957), or simply *Glen's law*

$$\dot{\epsilon} = \eta^{-1} \tau \quad (3.21)$$

$$\eta^{-1} = A I_2^{(n-1)/2}, \quad (3.22)$$

which is tensorially isotropic but non-Newtonian due to the effective viscosity,  $\eta$ , depending on the second invariant,  $I_2(\tau)$ .

### Rate-factor $A$

The rate-factor,  $A$ , is a macroscopic flow parameter which in principle accounts for all the material properties influencing the fluidity (reciprocal viscosity). Soluble impurities can for example soften ice by introducing additional lattice defects assisting the movement of dislocations, thereby enhancing deformation by up to a factor of 10 (Jones and Glen, 1969). Particulate impurities, on the other hand, can lead to both enhanced and reduced flow rates by causing new dislocations that soften the ice (enhancing the flow rate), or by causing increased resistance to grain boundary sliding (reducing the flow rate) (Cuffey and Paterson, 2010).

The rate-factor also depends strongly on temperature, which may be accounted by a simple Arrhenius-type law (Weertman, 1983)

$$A = A_0 \exp(-Q/RT'), \quad (3.23)$$

where  $T'$  is the temperature adjusted for melting point depression [thereby indirectly accounting for the pressure dependence, which might be overpredicting the impact

of pressure on deformability (Greve et al., 2014)],  $R = 8.314 \text{ J mol}^{-1} \text{ K}^{-1}$  is the universal gas constant,  $Q$  is the creep activation energy obtained from laboratory experiments [around  $Q = 6 \times 10^4 \text{ J mol}^{-1}$  for temperatures below 263 K and  $Q = 1.15 \times 10^5 \text{ J mol}^{-1}$  above 263 K (Cuffey and Paterson, 2010)], and  $A_0$  is a material parameter. The rate-factor enhancement induced by the temperature changes can be quite large: the rate-factor increases by approximately factor of ten between  $-30^\circ\text{C}$  and  $-10^\circ\text{C}$ , and up to another factor of ten to  $0^\circ\text{C}$  (Cuffey and Paterson, 2010). Above  $-10^\circ\text{C}$ , however, the Arrhenius relationship is unable to correctly account for the softening, which has been attributed liquid water facilitating an increased grain boundary sliding (Barnes et al., 1971).

### 3.3 Inverse constitutive equation

When modelling ice flow, the constitutive equation must be posed in the inverse form,  $\tau(\dot{\epsilon})$ , for it to be inserted into the momentum balance (2.3). Unfortunately, a closed-form solution of the inverse problem does not always exist (Shames, 1997). In the case of the Glen's tensorially-linear law, it is however possible. Consider (3.21)–(3.22) combined and rearranged as

$$\tau = A^{-1} (I_2(\tau))^{(1-n)/2} \dot{\epsilon}. \quad (3.24)$$

From this expression, it is clear that the second invariant  $I_2(\tau)$  must be re-expressed in terms of  $\dot{\epsilon}$ . Calculating  $I_2(\tau)$  using (3.24), one immediately finds  $I_2(\tau) = \tau : \tau = A^{-2} (I_2(\tau))^{1-n} I_2(\dot{\epsilon})$ , where the strain-rate tensor invariants are defined similarly to (3.14). Solving for  $I_2(\tau)$  gives  $I_2(\tau) = A^{-2/n} (I_2(\dot{\epsilon}))^{1/n}$ , which if back substituted into (3.24) gives the inverted, closed-form of the Glen's law

$$\tau = \eta \dot{\epsilon} \quad (3.25)$$

$$\eta = A^{-1/n} (I_2(\dot{\epsilon}))^{(1-n)/2n}. \quad (3.26)$$

### 3.4 Block flow

In numerical glacier and ice-sheet models, solving the full momentum balance (full Stokes balance) for the velocity field in long transient problems is generally too computationally expensive. Consequently, approximations are typically applied to reduce the number of terms appearing in the balance equation, guided by the external geometrical or dynamical circumstances shaping the problem. The most popular approximation is the shallow ice approximation, applicable to large regions of ice sheets where horizontal strain-rates are small. By noting the aspect ratio of ice sheets is on the order of  $10^{-3}$  and scaling all variables to dimensionless forms, the shallow ice approximation is the outcome of keeping only terms with zeroth order dependence on the aspect ratio (Le Meur et al., 2004). What remains is a balance between gravity and the basal drag, and that only shear stresses act on

internal (horizontal) planes. The motion of ice is therefore caused solely by internal shear deformation along horizontal planes (vertical shearing).

In regions of fast flowing ice, however, the ice fluidity may be insufficient for internal deformation to alone account for the flow speed. Instead, the ice mass is assumed to approximately slide over the bed in a block-like fashion with negligible internal deformation. Considering the vertically-integrated stress balance, the flow is locally governed by a balance between the gravity-driven stress (driving stress) and basal drag, longitudinal stresses, lateral stresses, and bridging stresses (Van Der Veen and Whillans, 1989). Bridging effects are however small enough in practice to be neglected (Kamb and Echelmeyer, 1986), thereby reducing the vertically-integrated stress balance to

$$\begin{aligned}\rho g H \alpha &= (\tau_b)_x - \partial_x (2H\bar{\eta} [2\partial_x u_x + \partial_y u_y]) - \partial_y (H\bar{\eta} [\partial_y u_x + \partial_x u_y]) \\ \rho g H \alpha &= (\tau_b)_y - \partial_y (2H\bar{\eta} [2\partial_y u_y + \partial_x u_x]) - \partial_x (H\bar{\eta} [\partial_y u_x + \partial_x u_y]),\end{aligned}\tag{3.27}$$

where  $\alpha$  is the surface slope,  $\tau_b(\mathbf{u})$  is the basal drag,  $H$  is the ice thickness,  $u_x$  and  $u_y$  are the depth-averaged velocities, and  $\bar{\eta}$  is the depth-averaged effective viscosity such that  $\bar{\tau} = \bar{\eta}\dot{\epsilon}$ .

In the block-flow approximation (3.27), the basal slipperiness/drag is therefore parametrised by the drag relation  $\tau_b(\mathbf{u})$ , and the driving stress is balanced not only by basal drag, but additionally also by stresses transmitted longitudinally (compressional/extensional forces due to e.g. down- or upstream topographical bumps) and stresses transmitted laterally (such as side-wall drag due to rigid margins or viscous shear-margins surrounding fast flowing ice).

### 3.5 Drag over hard beds

The basal drag relation,  $\tau_b(\mathbf{u})$ , generally depends on local bed properties such as the bed type, deformability of the subglacial sedimentary substrate (till), and the basal water pressure. In literature, a distinction is made between soft deformable beds and hard undeformable beds. While the drag relation for soft beds is based on the rheology of till (incorporating granulometry, porosity, consolidation, dilatancy, hydraulic permeability, and more) (Cuffey and Paterson, 2010), hard beds are widely described using Weertman's sliding law (Weertman, 1957) which parametrizes the drag in the presence of undeformable obstacles by assuming *regelation* and *enhanced creep* occur concurrently.

If ice is at its pressure melting point, regelation accounts for the melting of ice on the upstream side of a bump and the subsequent transport and refreezing on the downstream side due to the pressure difference between the up- and downstream sides. Specifically, the higher pressure on the upstream side means the ice is colder there (Clausius–Clapeyron relation), causing heat to flow from the warmer downstream side to the upstream side (figure 3.6). This process is however ineffective for bumps larger than  $\sim 1$  m in length which greatly impede heat conduction (Cuffey

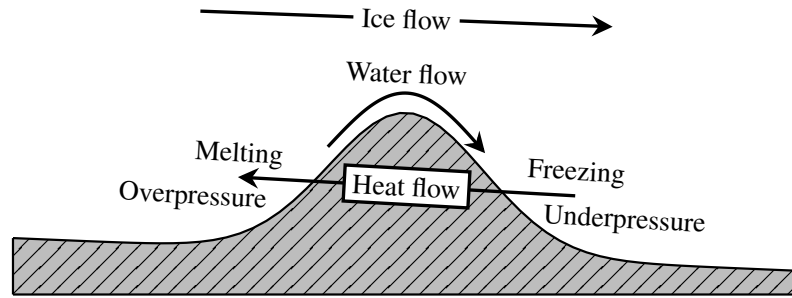


Figure 3.6: Basal sliding by regelation. The figure shows the flow directions of ice, heat, and water, corresponding to the description in the text.

and Paterson, 2010). Enhanced creep, on the other hand, is most effective for large bumps and is a viscous deformation process. The process works by bumps inducing an upstream region of increased stress, which in turn enhances deformation due to the stress dependence of the effective viscosity. Thus, the bigger the bumps, the larger the stress increase, which implies this mechanism is most effective for large bumps.

Weertman's sliding velocity is defined as the sum of the velocity due to regelation and enhanced creep by considering idealized cubic bumps. The two velocities are calculated from simple thermodynamical considerations and near-field estimates of longitudinal stress perturbations in the presence of bumps, respectively. Weertman argued that the basal sliding velocity is largely set by the resistance of intermediate sized bumps, for which none of the processes are effective. Calculating the size of such controlling obstacles allows the basal drag relationship to be reduced to just one term, namely

$$\tau_b(\mathbf{u}) = c|\mathbf{u}|^{1/m-1}\mathbf{u}, \quad (3.28)$$

where  $\mathbf{u}$  is the basal sliding velocity,  $c$  is a spatially variable drag-coefficient, and  $m$  is typically taken to be around 2 (Cuffey and Paterson, 2010).

# Chapter 4

## Study #1

### 4.1 Introduction

The fast-flowing northeast Greenland ice stream (NEGIS) is a remarkable and rare flow feature of ice sheets (figure 4.1). Extending in a wedge-like shape more than 600 km from the interior of the ice sheet to the coast, it potentially holds 1.1 m of sea level rise in its marine-based sector alone (Morlighem et al., 2014; Mouginot et al., 2015). Relatively recently, Zachariae, one of its three marine outlet glaciers, was reported to experience a significant inter-annual speed-up (Mouginot et al., 2015). This observation, combined with the newly available high spatio-temporally resolved surface imagery available from the European Space Agency (ESA) Sentinel 1A satellite, provided the motivation for this study.

The cloud-penetrating synthetic aperture radar (SAR) images taken by Sentinel 1A may be analysed for surface features appearing repeatedly in consecutive images, thereby allowing surface velocity maps to be derived every  $\sim 12$  to 20 days. This work was carried out by recognizing that important insights might be made into how marine-terminating outlets (such as Zachariae) could respond to future (longer time-scale) changes in forcings by studying how Zachariae, and its neighbouring outlet Nioghalvfjærdsfjorden, respond to seasonal-scale changes in forcings.

Study #1 addresses this question by combining climate data (observed and modelled) with numerical modelling in order to investigate the influence of four specific processes thought to affect the seasonal velocity response along the twin outlets. Figure 4.2 shows a schematic cross-sections along the flow of Zachariae and Nioghalvfjærdsfjorden together with the four processes considered: the influence of (1) subglacial lubrication due to surface meltwater penetrating to the bed, (2) subglacial sticky spots such as topographical bumps, (3) the  $\sim 76$  km long floating ice shelf at the termination of Nioghalvfjærdsfjorden possibly adding resistance to the flow, and (4) the seasonal ice mélange in front of Zachariae possibly adding a small resistance to the flow.

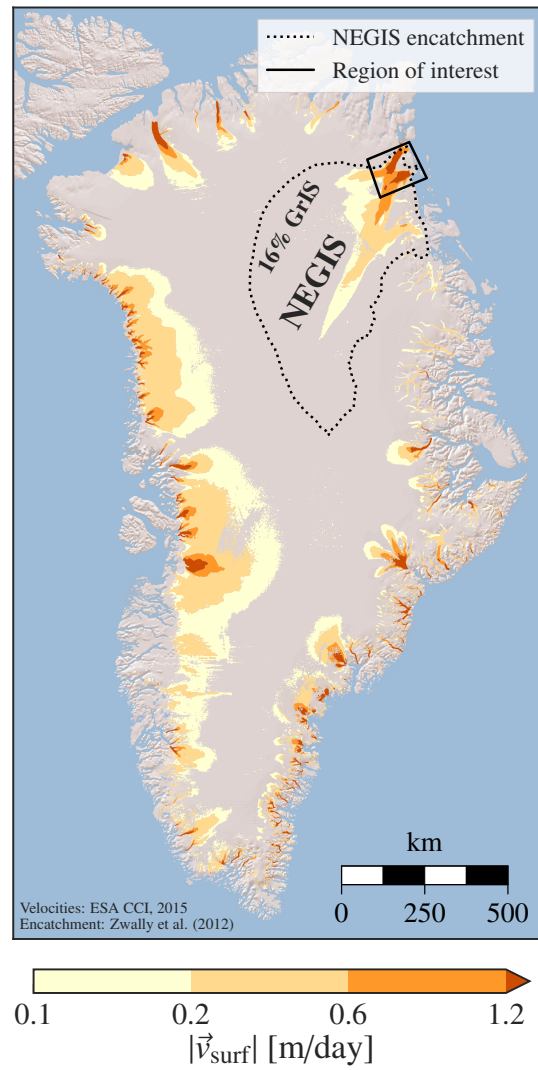


Figure 4.1: The NEGIS terminus region considered in this work (black bounding box) and the NEGIS encatchment area (dashed line). Coloured contours show the surface velocity wherever  $|v_{\text{surf}}| > 0.1 \text{ m d}^{-1}$ .

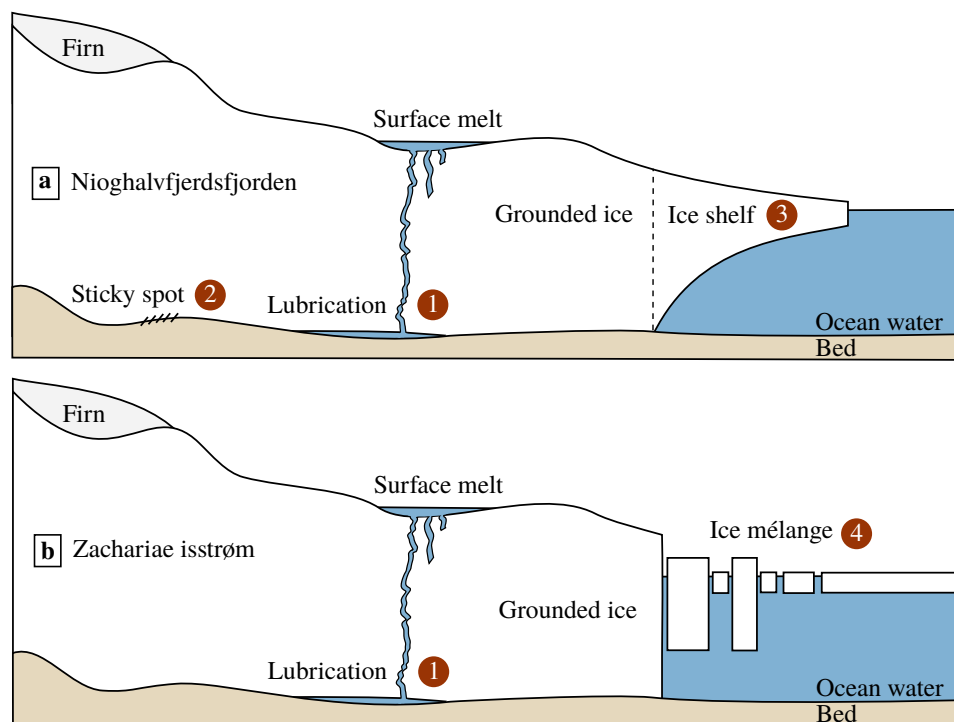


Figure 4.2: Schematic cross-section along flow of Nioghalvfjærdsfjorden (a) and Zachariae (b) depicting the four processes studied (red circles).

For visual reference, figure 4.3 shows the extent of seasonal surface melting during 22–26 July 2016 over the region of interest compared to spring (15–20 April 2016), processed from optical imagery taken by the Landsat 8 satellite, which, unlike SAR imagery, is not cloud penetrating.

Processes 1 and 4 were investigated by processing raw (level 0) SAR images from Sentinel 1A to estimate the onset of seasonal surface melting and the Zachariae ice mélange break-up. This involved processing raw image bands by applying instrument calibration and converting the instrument measure to the relevant physical quantity, the surface backscatter  $\sigma_0$  (normalized radar cross-section)

Processes 1, 2 and 3 were investigated using the numerical ice flow model  $\acute{U}a$  (Gudmundsson et al., 2012) and relies on Weertman’s basal sliding law for hard (undeformable) beds and the block-flow approximation of Glen’s law (introduced in sections 3.4 and 3.5 above).

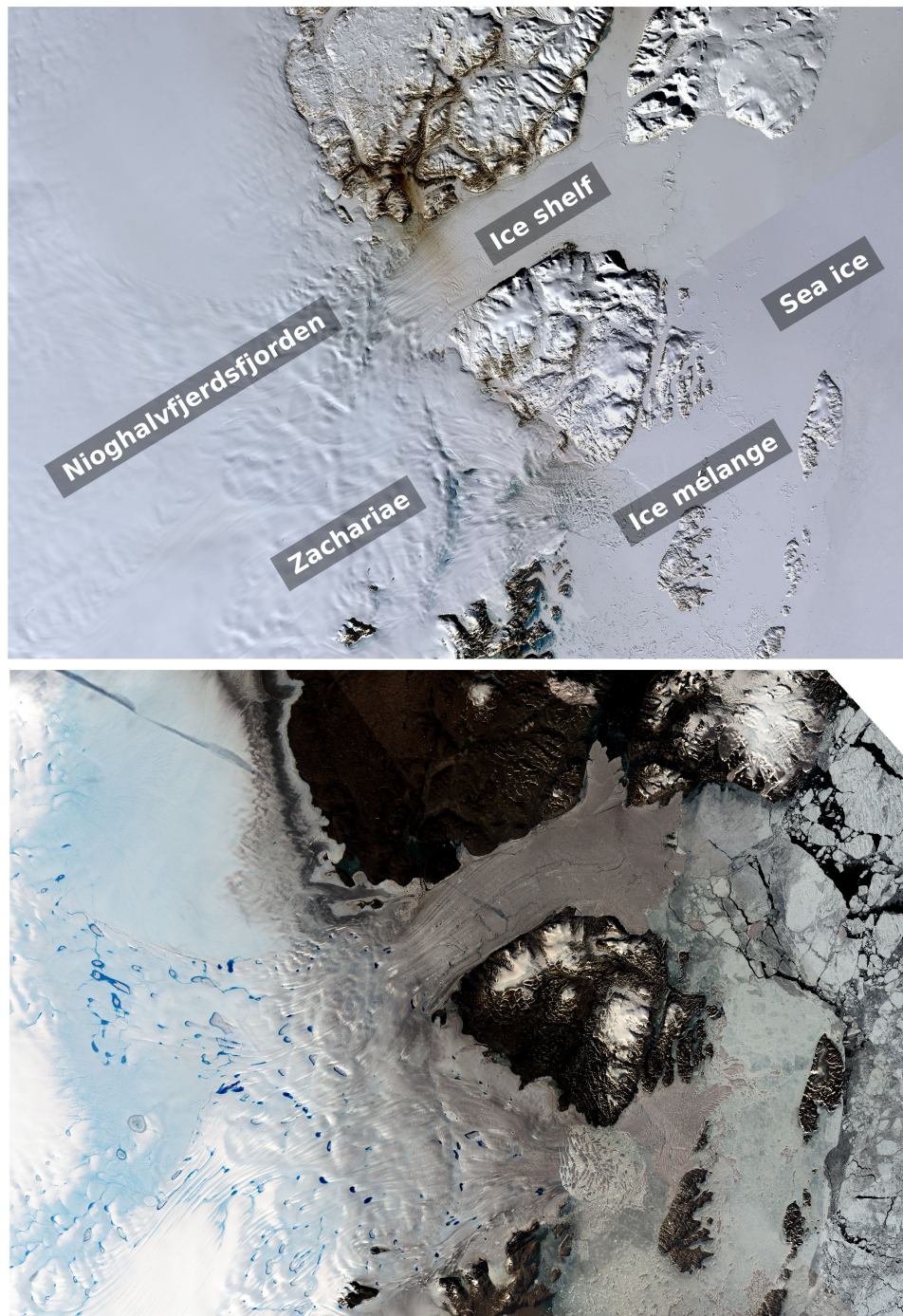


Figure 4.3: Optical Landsat 8 satellite images showing the seasonal surface melting in shades of blue (bottom, 22–26 July 2016) compared to spring (top, 15–20 April 2016) over the Nioghalvfjærdsfjorden and Zachariae outlet systems. Processed from raw imagery data available from the U.S. Geological Survey (USGS).

## **4.2 The paper**

(intentionally blank)





## RESEARCH LETTER

10.1002/2017GL074368

## Key Points:

- The 2016 seasonal velocity speedups of Zachariae and 79N are 14% and 11%, respectively, consistent with elsewhere on Greenland and are likely triggered by enhanced subglacial sliding due to surface melting
- The 79N speedup is unaffected by subglacial sticky spots and is incompatible with enhanced sliding along the sidewalls confining its floating tongue, whereas for Zachariae the ice mélange at its front might play an important role
- The 76 km long floating tongue of 79N provides, at most, only little resistance from its innermost part, and the remaining outer ~56–66 km could be lost without large consequences

## Supporting Information:

- Supporting Information S1

## Correspondence to:

N. M. Rathmann,  
rathmann@nbi.ku.dk

## Citation:

Rathmann, N. M., C. S. Hvidberg, A. M. Solgaard, A. Grinsted, G. H. Gudmundsson, P. L. Langen, K. P. Nielsen, and A. Kusk (2017), Highly temporally resolved response to seasonal surface melt of the Zachariae and 79N outlet glaciers in northeast Greenland, *Geophys. Res. Lett.*, *44*, doi:10.1002/2017GL074368.

Received 3 JUN 2017

Accepted 20 AUG 2017

Accepted article online 24 AUG 2017

## Highly temporally resolved response to seasonal surface melt of the Zachariae and 79N outlet glaciers in northeast Greenland

N. M. Rathmann<sup>1</sup> , C. S. Hvidberg<sup>1</sup>, A. M. Solgaard<sup>2</sup>, A. Grinsted<sup>1</sup>, G. H. Gudmundsson<sup>3</sup> , P. L. Langen<sup>4</sup> , K. P. Nielsen<sup>4</sup>, and A. Kusk<sup>5</sup>

<sup>1</sup>Center for Ice and Climate, Niels Bohr Institute, University of Copenhagen, Copenhagen, Denmark, <sup>2</sup>Geological Survey of Denmark and Greenland, Copenhagen, Denmark, <sup>3</sup>British Antarctic Survey, Cambridge, United Kingdom, <sup>4</sup>Danish Meteorological Institute, Copenhagen, Denmark, <sup>5</sup>National Space Institute, Technical University of Denmark (DTU), Lyngby, Denmark

**Abstract** The seasonal response to surface melting of the Northeast Greenland Ice Stream outlets, Zachariae and 79N, is investigated using new highly temporally resolved surface velocity maps for 2016 combined with numerical modeling. The seasonal speedup at 79N of 0.15 km/yr is suggested to be driven by a decrease in effective basal pressure induced by surface melting, whereas for Zachariae its 0.11 km/yr seasonal speedup correlates equally well with the breakup of its large ice mélange. We investigate the influence 76 km long floating tongue at 79N, finding it provides little resistance and that most of it could be lost without impacting the dynamics of the area. Furthermore, we show that reducing the slipperiness along the tongue-wall interfaces produces a velocity change spatially inconsistent with the observed seasonal speedup. Finally, we find that subglacial sticky spots such as bedrock bumps play a negligible role in the large-scale response to a seasonally enhanced basal slipperiness of the region.

**Plain Language Summary** The Northeast Greenland Ice Stream may potentially contribute significantly to near-term sea level rise and is one of the lesser studied Greenlandic systems, partly due to its remoteness. We present a new high temporally resolved velocity data set derived from Sentinel 1-A which allows capturing changes on a seasonal timescale, a feature which only the newest generation satellites now permit. We show how surface melting may be linked to the observed seasonal velocity changes, giving important insights into the possible future (range of) behavior and sensitivity of the ice stream outlets to atmospheric changes. In addition, we present a detailed study of possible moderating factors on the seasonal velocity response. In particular, we find that (i) the large ice mélange in front of the Zachariae outlet might be dampening the outlet's response, (ii) small-scale subglacial topographical bumps (sticky spots) exert very limited control on the flow, and (iii) the 76 km long floating tongue of the 79N outlet is largely a passive feature, suggesting that most of it (~80%) could be lost without effecting the outlet's contribution to near-term sea level rise. This has broad implications for assessing the future mass loss of ice sheets since it points to the importance of studying every major calving event individually.

### 1. Introduction

The Northeast Greenland Ice Stream (NEGIS) is a remarkable and rare dynamical flow feature of ice sheets. Being the only of its kind in Greenland, it extends more than 600 km into the interior of the ice sheet (Figure 1a, inset, colored contours) and terminates in three marine glaciers, 79N (NI), Zachariae (ZA), and Storstrømmen [Fahnestock *et al.*, 2001a; Joughin *et al.*, 2001]. The northernmost two, NI and ZA, drain approximately 198,380 km<sup>2</sup> (12%) of the ice sheet surface area (16% considering all three, dashed line in Figure 1, inset [Zwally *et al.*, 2012]), holding 1.1 m of sea level rise equivalent in their marine-based sector alone [Morlighem *et al.*, 2014; Mougnot *et al.*, 2015] (Figure 1b, blue contours).

Because of its unusual geometry and potentially large contribution to near-term sea level rise, NEGIS is being studied with increasing interest in order to quantify, and better understand, possible mass-flux drivers and responses to perturbations under the present and a warming climate. On one hand, numerical models used to quantify ice flow are increasingly attempting to resolve NEGIS as a coherent flow structure in large scale

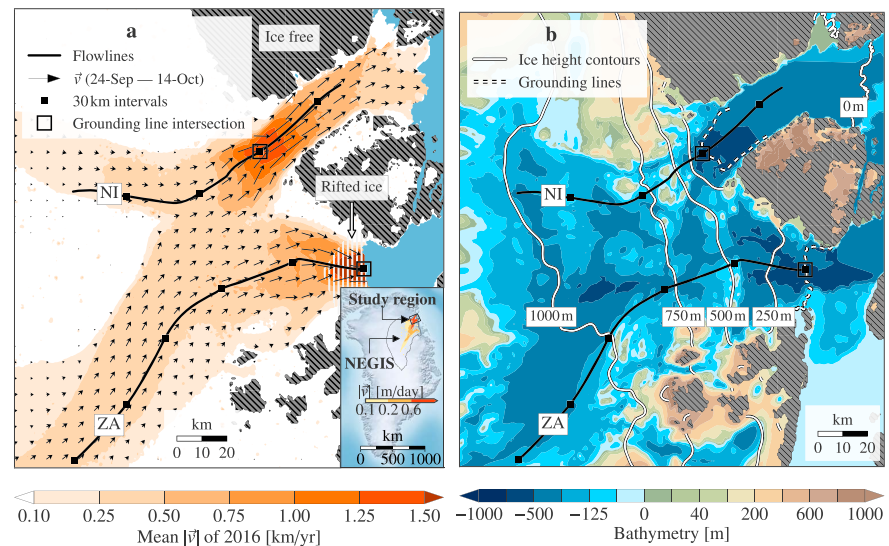


**Figure 1.** Ice surface velocities ( $\vec{v}$ ), flow lines, and bed/surface topography of Zachariae (ZA) and 79N (NI) outlet glaciers. (a) Mean  $\bar{v}$  of 2016 (colored contours),  $\vec{v}$  (wherever  $|\vec{v}| > 0.1$  km/yr) between 24 September and 14 October 2016 (arrows), and ZA and NI flow lines (black lines). The inset shows the northeast Greenland ice stream (NEGIS) drainage area [Zwally et al., 2012] (dashed black line) together with the NEGIS surface velocity wherever  $|\vec{v}| > 0.1$  m/d (colored contours). (b) Basal topography (colored contours) [Bamber et al., 2001; Morlighem et al., 2014], smoothed ice height contours (white lines) [Howat et al., 2014], and ESA CCI 2016 grounding lines (dashed white lines) [ENVEO, 2016a] and calving fronts [ENVEO, 2016b]. Gray hatched regions mark ice-free surfaces in both panels.

(ice sheet wide) modeling [Greve and Otsu, 2007; Seddik et al., 2012; Greve and Herzfeld, 2013; Schlegel et al., 2013; Ahlkrona et al., 2016], thereby allowing for insights into, e.g., the role played by basal friction and topography [Joughin et al., 2001; Greve and Otsu, 2007; Sergienko et al., 2014; Schlegel et al., 2015; Krabbendam, 2016], the stationarity of its position [Karlsson and Dahl-Jensen, 2015], and the influence of external forcings on downstream mass fluxes [Schlegel et al., 2015]. On the other hand, new observational data continues to shed light on otherwise unknown, or poorly understood, features of the flow, such as the geothermal hotspot suggested to initiate NEGIS by lubricating the bed [Fahnestock et al., 2001b; Layberry and Bamber, 2001; Bamber et al., 2013; Christianson et al., 2014; Keisling et al., 2014; Rogozhina et al., 2016], dynamically induced mass losses by a multitude of external forcings [Khan et al., 2014], the influence of sea ice and the warm regional ocean circulation around NI [Thomsen et al., 1997; Mayer et al., 2000; Reeh et al., 2000, 2001], the complicated ice rheology near the upstream bounding shear margins [Bell et al., 2014], and interannual surface velocities suggesting nontrivial, dissimilar behaviors of the two neighboring terminus glaciers, NI and ZA [Mouginot et al., 2015].

In this work, we further investigate the seasonal behavior of the ZA and NI outlets by considering new high-temporal resolution surface velocity maps available every  $\sim 12$ – $20$  days throughout 2016, combined with atmospheric, subsurface, and ice flow modeling. Our aim is to put the observed interannual speedup of ZA and NI into a seasonal context and to investigate to what extent seasonal and interannual drivers are similar, which may help to better understand future changes.

## 2. Method and Results

Our analysis focuses on the observed 2016 seasonal behavior along the flow lines of ZA and NI (Figure 1). The dimensions of the region investigated were chosen based on the interferometric wide swath width of European Space Agency (ESA)'s Sentinel-1, which roughly overlaps with the domain considered by Mouginot et al. [2015]. We use ESA Sentinel-1 synthetic aperture radar (SAR) data from tracks 074, 170, and 112 with a 12 day repeat (24 day repeat in one case) between images to derive ice velocities. Data from these three tracks were combined to construct 28 surface ice velocity maps for 2016 of the ZA and NI area with best possible spatial coverage. The operational interferometric post processing (IPP) chain [Dall et al., 2015], developed at the Technical University of Denmark (DTU) Space and upgraded with offset tracking for ESA's Climate

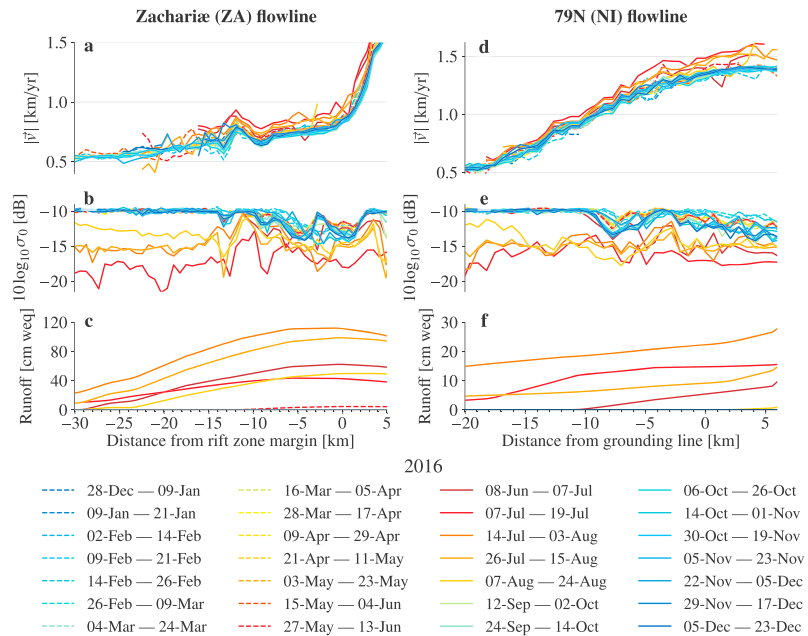


**Figure 2.** Flow line profiles along ZA and NI. (a and d) Ice surface speeds,  $|\vec{v}|$ . (b and e) Radar cross-section  $\sigma_0$  (surface backscatter) from Sentinel-1A synthetic aperture radar (SAR) images [Copernicus, 2016] (high/low values are dry/wet surface conditions). (c and f) Simulated accumulated runoff estimates (between the legend periods) using the subsurface model by [Langen et al., 2015, 2017].

Change Initiative (CCI) Greenland project, was employed to derive the surface movement using offset tracking [Strozzi et al., 2002] assuming surface parallel flow using the digital elevation model from the Greenland mapping project (GIMP DEM) by Howat et al. [2014, 2015]. The ice velocity data are freely available from www.promice.dk.

Figure 1a shows the 2016 mean surface velocity in colored contours based on the 28 velocity maps covering 2016, and Figure 1b shows the bounding geometry of the region based on basal topography by Bamber et al. [2001] and Morlighem et al. [2014], ice thicknesses from the GIMP DEM, and calving fronts and grounding lines by ENVEO [2016a, 2016b]. We note that the true ZA grounding line of 2016 is most likely located ~15 km upstream of the ESA grounding line, as suggested by the heavily rifted ice occurring on the remnant shelf after the recent collapse of its floating tongue (vertically white hatched area in Figure 1a, see the supporting information section S2).

These new highly temporally resolved surface velocity maps uniquely allow for detailed, remote process studies. The top panels in Figure 2 show the along-flow line velocity profiles of (a) ZA and (d) NI for selected, approximately evenly spaced, intervals of dates throughout 2016, ranging from winter (dashed blue) through summer (dashed/solid red) to winter (solid blue). At the ZA outlet, a seasonal speedup is initiated between 8 June and 7 July, reaching more than 15 km–30 km upstream from the rifted ice margin (supporting information section S2). After peaking with an increase of approximately 0.11 km/yr (14%) near the rifted ice margin, a return to the winter baseline occurs between 12 September to 2 October. For NI, the speedup, too, starts between 8 June to 7 July, peaks in 7–19 July with an increase of approximately 0.15 km/yr (11%) near the grounding line, and returns to its winter baseline between 7 and 24 August.

In regions of fast flowing ice, such as ice streams, the motion is generally attributed to a plug-like flow (constant velocity and strain rate throughout the thickness of the ice column) whereby the ice slides over the bed due to deformation of soft sedimentary substrate (till) or due to a low effective pressure in the subglacial drainage system, defined as the difference between the overburden and basal water pressure [Rose, 1979; Alley et al., 1986; Clarke, 1987; Macayeal et al., 1995; Luthi et al., 2002]. While the far upstream part of NEGIS likely experiences a lowered effective pressure (permitting enhanced sliding) due to large basal melt

rates [Fahnestock et al., 2001b; Christianson et al., 2014; Keisling et al., 2014], the basal state of the lower part is less known. It is, however, likely that the downstream basal environment is not water saturated in the sense that any additional water source could further enhance basal sliding. If so, it is plausible that the observed speedups are caused by seasonal surface melt penetrating through the ice and decreasing the effective pressure and/or lubricating the bed, as opposed to, e.g., ocean warming at the fronts suggested to trigger the observed decadal speedups [Mouginot et al., 2015]. This mechanism has previously been suggested as a driver of seasonal speedups at different outlet glaciers by subglacial channels being flooded at the onset of the melt season, thereby increasing the basal water pressure leading to distributed drainage through interconnected cavities (effectively creating a small film of water lifting the ice from its substrate) [Joughin et al., 2008a; Stearns et al., 2008; Schoof, 2010; Chandler et al., 2013; Moon et al., 2014]. Later in the melt season when larger subglacial conduits (channels) effectively dominate the water transport, the water pressure drops (effective pressure increases) and the enhanced sliding ceases. This behavior has led to the suggestion that melt water variability, rather than the mean flux or total amount, plays an important role in seasonally enhanced sliding [Bartholomaus et al., 2008; Cuffey and Paterson, 2010; Schoof, 2010].

To test this hypothesis at ZA and NI, surface backscatter (radar cross section,  $\sigma_0$ ) from Sentinel-1A synthetic aperture radar (SAR) images [Copernicus, 2016] was investigated for signs of melting synchronous with the velocity speedups. Since SAR backscattering over snow covers arises from subsurface volume scatterers of snow/ice structures, such backscattering is sensitive to the wetness of the surface layer, which has previously successfully been used to identify surface melting over Greenland on diurnal and seasonal timescales [Nghiem et al., 2001; Steffen et al., 2004]. Figures 2b and 2e show that the backscatter along the two flow lines indeed drops synchronously with the speedups (high/low values indicating dry/wet conditions), suggesting the melt water quickly penetrates the ice (e.g., through crevasses or by hydraulic fracturing [Fountain et al., 2005; van der Veen, 2007; Bartholomaus et al., 2008; Das et al., 2008]). Figure S1 in the supporting information further displays the spatial extent of the melting, indicating not only surface melting reaching far upstream but also a multitude of surface melt lakes, some as large as  $\approx 5$  km in diameter and rivers up to  $\approx 20$  km long, confirming the presence of large amounts of surface melt water. Note that the existence of large lakes could, potentially, delay the delivery of large volumes of water to the bed since filling and draining of lakes may be separated by several weeks.

To further quantify the amount of liquid water equivalent (weq) present, we invoke the firn (subsurface) model used in HIRHAM5 as documented by Langen et al., 2015 [HIRHAM5, 2017] but used in an operational setup forced with 6-hourly surface energy fluxes and precipitation from the Danish Meteorological Institute's weather forecast model, HIRLAM 7.3 K05 [Undén et al., 2002; Rontu et al., 2009; Kjellström et al., 2005]. The firn model allows the surface liquid water budget to be decomposed into components such as surface melt water runoff, retention in snow pack, refreezing, and more. The accumulated runoff along the two flow lines is shown in Figures 2c and 2f (accumulated over the time span indicated by the legends), suggesting poor retention in the firn and potentially large amounts of surface melt that could reach the bed.

The fact that similar velocity changes occur along ZA and NI with almost an order of magnitude more runoff along ZA compared to NI (on equal time intervals, Figures 2c and 2f) might suggest that melt water variability, and not the total amount, is driving the observed speedup. Claiming that melting is the driver alone, however, would be disregarding the possible seasonally dependant effects of the large ice mélange in front of ZA, the floating tongue of NI, and the differences in basal environment along ZA and NI which could, potentially, moderate their responses due to, e.g., sticky spots. If increased (upstream) basal lubrication is indeed causing the observed changes alone, one might expect the ice mélange, floating tongue, and potential sticky spots to exert only limited control over the velocity.

### 2.1. Role of the 79N Floating Tongue

To determine the influence of the 79N floating tongue, we further investigate if the tongue provides any resistance at the grounding line, and to what degree it might change during the seasonal speedup. Principally, such change could be caused either by a softening/warming of the fabric, thereby changing the internal stress configuration of the tongue, or by an enhanced sliding occurring along the tongue-wall interfaces. In the supporting information section S3, we show that derived strain rate maps indicate no seasonality, suggesting little internal stress redistribution over the season. Moreover, noting that the NI shear margins are relatively confined (Figure 3a), one might expect a weak coupling between the tongue and sidewalls. However, noting the upstream shear margin widths are similar, and that our estimates of slipperiness along the sidewalls

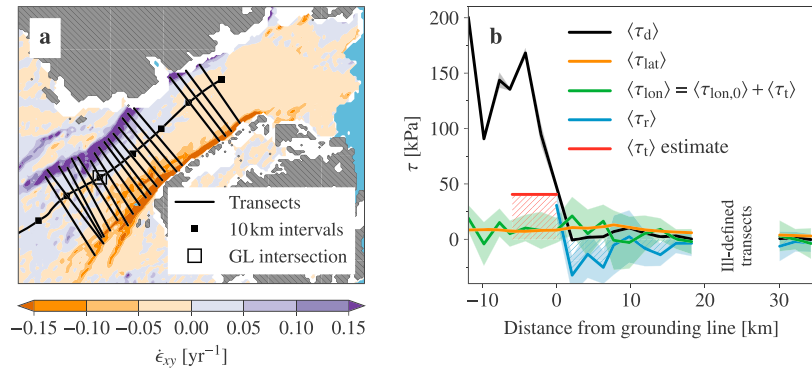


**Figure 3.** 79N stress budget derived from observations. (a) Strain rate field  $\dot{\epsilon}_{xy}$  of 24 September and 14 October (in the local basis of the ground line transect) used to delineate transects; (b) transect-averaged stress components, where full lines are 2016 annual means and shades cover  $\pm 1$  standard deviation.

are comparable to the subglacial values (supporting information section S4), we in the following give a more detailed account of the role played by the tongue.

We note, however, that floating tongues are unlikely to contribute to the stress budget of upstream grounded ice by actively providing resistance since (i) basal drag and lateral resistance from shear margins generally support grounded ice well, (ii) low-sloping equilibrium profiles are more likely to develop than tongues with frictionless bases holding back high-sloping grounded ice, and (iii) shear margins of sidewall-bounded tongues are likely weak (soft) because shearing tends to warm the ice, which, unlike for (unbounded) grounded ice shear margins, is not replaced with cold ice by cross-margin flow.

In section 2.1.1, we adopt the data-oriented approach by *Van Der Veen et al.* [2011] to show that even if the ice is assumed anchored to the sidewalls, the potential size (upper limit) of the resistive stress is indeed small compared to the total (driving) stress budget. Note that while this suggests the tongue is mostly a dynamically passive feature, it is not passive in the sense that removing the tongue would still produce a speedup because the sea water column alone can no longer balance the weight of the ice. Subsequently in section 2.1.2, we study the sensitivity of 79N to perturbations in basal slipperiness along the tongue-sidewall interfaces and over the remaining grounded ice using the numerical ice flow model  $\dot{U}$ a [*Gudmundsson et al.*, 2012], suggesting the seasonal speedup is likely related to upstream changes in basal slipperiness and not enhanced sidewall slipperiness.

### 2.1.1. Potential Resistance Provided by the 79N Tongue

In the *Van Der Veen et al.* [2011] approach, the sizes of the different stress components are estimated along the flow line by calculating their average values over transects locally perpendicular to the flow. These transects, which are picked at evenly spaced intervals (here  $\Delta x = 2$  km), are delineated by their intersection with the ice stream shear margins, defined as the parallel belts of maxima and minima in the strain rate field  $\dot{\epsilon}_{xy}$  (Figure 3a, orange/purple belts). Note that while transect orientations do not change much over the course of 2016, their widths (i.e., shear margin positions) do during the summer speedup, in part due to poorer spatial coverage, which is accommodated for in the following by calculating transect widths for each velocity map. Note also that  $x$  and  $y$  denote the local (transect-wise) along-flow and normal directions.

Assuming plug flow, a transect-wise stress balance on the grounded part of NI implies that the driving stress ( $\tau_d$ ) is balanced by flow-resisting stresses associated with lateral drag imposed by shear margins ( $\tau_{\text{lat}}$ ), along-flow longitudinal tension/compression ( $\tau_{\text{lon}}$ ), and basal drag ( $\tau_b$ ), that is

$$\tau_d = \tau_{\text{lat}} + \tau_{\text{lon}} + \tau_b \quad (\text{grounded part}). \quad (1)$$

The first three terms are defined as  $\tau_d = -\rho g \overline{H \partial h / \partial x}$ ,  $\tau_{\text{lat}} = 2B(H_N \dot{\epsilon}_{xy,N}^{1/n} - H_S \dot{\epsilon}_{xy,S}^{1/n})/W$ , and  $\tau_{\text{lon}} = -2B \partial (H \dot{\epsilon}_{xx}^{1/n}) / \partial x$ , where  $\overline{(\cdot)}$  denotes the transect average,  $\rho = 917 \text{ kg/m}^3$  the density of ice,  $g = 9.8 \text{ m/s}^2$  the gravitational acceleration,  $H$  the ice thickness,  $h$  the surface height,  $W$  the transect width, and  $n = 3$  is the Glen flow exponent. The flow parameter  $B$  was set to  $B = A^{-1/n} = 275 \text{ kPa/a}^3$  ( $A$  being the rate factor),

corresponding to an ice temperature of  $-5^{\circ}\text{C}$ , assuming the ice is warmer than the mean surface air temperature, which in 2016 was  $-13^{\circ}\text{C}$  between the NI grounding line and 20 km upstream (HIRLAM 7.3 K05 data). Finally, the subscripts in  $H_N$  and  $H_S$  denote point evaluations on the northern (N) and southern (S) shear margins respectively (similarly for  $\dot{\epsilon}_{xy,N}$  and  $\dot{\epsilon}_{xy,S}$ ).

Note that the quantity of interest here, the tongue's (resistive) contribution to the longitudinal stress field, hereafter referred to as  $\tau_r$ , is not directly obtainable from the observed strain rates,  $\dot{\epsilon}_{xx}$ , since these reflect the influence of the net longitudinal stress,  $\tau_{\text{lon}} = \tau_{\text{lon},0} + \tau_r$ , where  $\tau_{\text{lon},0}$  is the component associated with the local ice geometry.

For the floating tongue, however, there is no basal drag, and the stress balance becomes

$$\tau_d = \tau_{\text{lat}} + \tau_{\text{lon}} + \tau_r \quad (\text{floating part}), \quad (2)$$

where  $\tau_d = -1/2\rho g(1 - \rho/\rho_w)\partial H^2/\partial x$ ,  $\rho_w = 1027 \text{ kg/m}^3$  being the density of sea water, and  $\tau_r = \tau_d - \tau_{\text{lat}} - \tau_{\text{lon}}$  is the stress residual/imbalance, which is  $\tau_r = 0$  along the buttressed part of the tongue and  $\tau_r < 0$  along the part potentially contributing to resisting the upstream flow.

Figure 3b shows the 2016-averaged components (full lines)  $\langle \tau_d \rangle$ ,  $\langle \tau_{\text{lat}} \rangle$ ,  $\langle \tau_{\text{lon}} \rangle$ , and the residual  $\langle \tau_r \rangle$ , together with their standard deviation (filled colors). The figure indicates that (i) the residual,  $\langle \tau_r \rangle$ , is negative, suggesting the tongue may provide some resistance, but (ii) that resistance is predominately provided by the first 10–20 km of the tongue, after which  $\langle \tau_r \rangle \approx 0$ .

In order to estimate the size of  $\tau_r$ , we note that the integrated stress residual (hatched blue in Figure 3b) must be balanced at the grounding line by the integral of  $\tau_r$  from the grounding line and one coupling length upstream (hatched red in Figure 3b), here chosen as 10 grounding line ice thicknesses ( $10H_{\text{gl}} = 6.0 \text{ km}$ ), that is

$$\int_{0\text{km}}^{15\text{km}} \langle \tau_r \rangle dx = \int_{-10H_{\text{gl}}}^{0\text{km}} \langle \tau_r \rangle dx \approx 10H_{\text{gl}} \langle \tau_r \rangle. \quad (3)$$

Note that previous reports on coupling lengths suggest values between 7 and 15 ice thicknesses [Howat *et al.*, 2005, 2008; Kamb and Echelmeyer, 1986]. Assuming  $\langle \tau_r \rangle$  to be evenly distributed over the coupling length, rightmost integral in equation (3) may be approximated accordingly, thus allowing for a low order estimation of  $\langle \tau_r \rangle$  (red line in Figure 3b). In this case, the average ratio of (tongue) resistive stress to driving stress over the coupling length is  $\langle \tau_r \rangle / \langle \tau_d \rangle^* = 34\%$ , where  $\langle \tau_d \rangle^* = (10H_{\text{gl}})^{-1} \int_{-10H_{\text{gl}}}^{0\text{km}} \langle \tau_d \rangle dx$ . Note the above are upper estimates in the sense that the tongue might not be fully anchored to its sidewalls.

### 2.1.2. 79N Sensitivity to Tongue Length and Basal Slipperiness

In addition to estimating the potential resistive stress using the above data-oriented method, we also numerically consider the velocity response along 79N to changes in basal slipperiness and tongue length by using the finite-element ice flow model  $\dot{U}$ a [Gudmundsson *et al.*, 2012] based on the shallow shelf approximation.

In section S4 in the supporting information, we use  $\dot{U}$ a for two separate sets of perturbation experiments whereby the basal slipperiness and tongue length are covaried: in the first set the slipperiness along the tongue-sidewall interfaces is uniformly perturbed relative to the slipperiness inverted from winter time velocities, whereas in the second set the slipperiness under the remaining (upstream) grounded ice is uniformly perturbed. Considering both sets of perturbations thus allows us to test the hypothesis that seasonal changes are caused by an upstream increase in basal slipperiness (melt-induced enhanced sliding) rather than e.g., downstream enhanced sliding along the sidewalls of the tongue.

The results suggest that once the tongue is less than 15 km long, the grounding line velocity becomes very sensitive to any further decrease in tongue length, which is in agreement with the observational based analysis in section 2.1.1, suggesting the innermost part might provide resistance. Note, however, that some speedup is to be expected even without a tongue providing resistance because of the large thickness changes that occur over the innermost part—cutting off the tongue there produces a force imbalance since the weight of the removed tongue is replaced by the weight of a smaller column of sea water.

Considering the flow line response to uniform slipperiness perturbations over the grounded ice, the model suggests that a  $\sim 20\%$  increase in upstream slipperiness is enough to reproduce both the amplitude and spatial extent of the seasonal velocity change. Moreover, we find that enhanced sliding along the tongue-sidewall margins alone gives rise to velocity changes only locally over the tongue. Thus, it seems unlikely the tongue

plays a role in the seasonal speedup in the sense that increased sliding along the tongue-sidewall interface cannot account for the full spatial extent of the observed seasonality. Instead, the speedup magnitude and spatial extent seems consistent with a ~20% increase in upstream basal slipperiness.

### 2.2. Role of the Zachariae Ice Mélange

In the supporting information, we further investigate the influence and timing of the Zachariae ice mélange breakup. By defining the mélange as being mobilized/broken-up by the loss of surface feature correlation between consecutive SAR images, indicating fast moving ice escaping the feature tracking window and/or surface features being degraded due to melting, we find that the break up coincides with the onset of surface melting upstream of the rifted zone, approximately 8 June. Note that because of the large height differences of around 250 m–500 m between the rifted front and the upstream part, this needed not be so. The two events coinciding does, unfortunately, not allow us to discern whether the ice mélange is in fact strong enough to trigger upstream changes upon disintegration, or if surface melting is responsible. Nonetheless, Zachariae is potentially an important case for further understanding the relative roles played by ice mélanges and surface melting/basal lubrication in seasonal changes, one where mélange modeling and multi-year seasonal velocity datasets may prove useful.

### 2.3. Role of Potential Subglacial Sticky Spots

Localized patches of basal friction, or “sticky spots,” have previously been suggested to play an important role in the dynamics of ice streams [Kamb, 1991; Alley, 1993; Stokes *et al.*, 2007]. Generally caused by bedrock bumps, till-free areas, or subglacial meltwater frozen to the bed, sticky spots may help to stabilize ice streams [Kamb, 1991; Stokes *et al.*, 2007]. Because bedrock bumps are regarded as likely sources of sticky spots [Alley, 1993] and are possibly influential under active ice streams [Stokes *et al.*, 2007], we further investigate in supporting information section S4.2 their potential role in moderating the seasonal velocity changes observed along ZA and NI.

Noting that the area along ZA with the greatest seasonal speedup is deeper, and likely weaker, than further upstream close to a couple of bedrock bumps, one might suspect the large number of bedrock bumps along NI to be especially influential. To determine their influence, we perform two sets of slipperiness perturbation experiments using  $\dot{U}_a$  whereby (i) the slipperiness is varied for all grounded ice except over small-scale bedrock bumps (defined as bumps being taller than sea level) and (ii) the slipperiness is varied for all grounded ice in addition to bedrock bumps being flattened (artificially set to sea level height). We find that while the influence of bedrock bumps on the velocity field is small in magnitude and spatially local for both NI and ZA (not shown for latter), the details of the subglacial environment potentially exert a greater control on the seasonal velocity response compared to e.g., changes in slipperiness along the tongue-sidewall interfaces.

## 3. Discussion and Conclusions

Glaciers that discharge into the ocean are potentially large contributors to the uncertainty of sea level rise predictions of the near future. In particular, glaciers with floating tongues add to this uncertainty by their tongues possibly acting as a downstream plug holding back the flow of ice. This underlines the need for understanding the processes leading to the breaking up of floating tongues—be it by mechanical failure due to changes in the stress configuration, subsurface hot water plumes destabilizing the tongue, related to calving by surface melting filling up crevasses, or the ice mélange breaking up because of wind stresses. While there has been some debate over the driving mechanism behind the sudden doubling in ice discharge of Jakobshavn Isbræ coincident with the collapse of its floating tongue in 1998 [Truffer and Echelmeyer, 2003; Joughin *et al.*, 2008b; Holland *et al.*, 2008; Van Der Veen *et al.*, 2011], it stands, together with the recent large calving event at the Larsen C ice shelf, as important examples of the need to understand the processes governing the stability of floating tongues/shelves and whether they provide any resistance.

In this work, we found that the 76 km long floating tongue of 79N might provide some (small) resistance from the innermost 15 km, suggesting a greater speedup may follow a potential collapse than otherwise expected if it were just buttressed (albeit the resistance is small). This, we argue, emphasizes the need to consider the consequences of calving events on an individual basis. In the light of the results presented here, it seems important to understand the structural integrity of the 79N tongue to, e.g., the reported increasing surrounding mean ocean temperature over the last decade [Mouginot *et al.*, 2015]. In this context, we propose

that high temporally resolved velocity data sets might provide unique opportunities to understand the strength and durability of floating tongues (and their upstream systems) when exposed to changes in external forcings over long time scales by investigating their response to forcings on a seasonal time scale, such as attempted here.

In summary we presented a highly temporally resolved velocity data set derived from Sentinel-1A SAR imagery allowing for insights into the seasonal behavior and drivers of the Zachariae (ZA) and 79N (NI) outlet glaciers in northeast Greenland. We showed that extensive surface melt is present over ZA and NI, both area wise and in terms of water equivalent, by combining SAR images with a numerical firn (subsurface) model to quantify the seasonal runoff. In particular, we suggest that the observed speedups during the summer of 2016 of approximately 0.15 km/yr along NI is driven by surface melt water penetrating the ice and lubricating the bed (decreasing the effective basal pressure), whereas the 0.11 km/yr speedup along ZA correlates equally well with both the onset of surface melting and the breakup of its large ice mélange, making it less clear whether the ice mélange is in fact strong enough to induce the observed seasonal changes upon break up.

By decomposing the near-terminus stress budget of NI, we find the potential resistance provided by the floating tongue is at most on the order of 34% of the near-terminus stress budget (assuming the tongue is actually anchored to the wall) and is constant across season, suggesting it is unlikely that the tongue moderates the seasonal response much. By covarying the basal slipperiness and tongue length using the numerical ice flow model  $\dot{U}_a$ , we furthermore found (i) that the outermost ~56–66 km of the tongue can be removed without making NI unstable, (ii) that only an upstream increase in basal slipperiness of the grounded ice can induce a change in the velocity field spatially consistent with the observed seasonal speedup (as opposed to, e.g., enhanced sliding along the tongue-sidewall interfaces), and (iii) that subglacial sticky spots, such as small-scale bedrock bumps, seem only to induce velocity changes small in magnitude and spatially local for both NI and ZA, thus probably not providing large-scale moderation of the observed seasonal response.

#### Acknowledgments

We wish to express our sincere thanks to two anonymous reviewers for valuable comments that helped greatly improve this manuscript. The research leading to these results has received funding from the European Research Council under the European Community's Seventh Framework Programme (FP7/2007-2013)/ERC grant agreement 610055 as part of the ice2ice project and from the Villum Investigator Project IceFlow. Ice velocity maps were produced from ESA Sentinel-1 remote sensing data as part the Programme for Monitoring of the Greenland Ice Sheet (PROMICE) and the ESA Greenland Ice Sheet Climate Change Initiative and were provided by the Geological Survey of Denmark and Greenland (GEUS) (freely available at [www.promice.dk](http://www.promice.dk)). Finally, we wish to acknowledge the important contribution made during the ice2ice bootcamp 2017 to section 2.1.1 by Faezeh M. Nick, Iben Koldtoft, Benjamin Keisling, Sijje Smith-Johnsen, and Andreas Plach.

#### References

- Ahlkrona, J., P. Lötstedt, N. Kirchner, and T. Zwinger (2016), Dynamically coupling the non-linear Stokes equations with the shallow ice approximation in glaciology: Description and first applications of the ISCAL method, *J. Comput. Phys.*, *308*, 1–19.
- Alley, R. B. (1993), In search of ice-stream sticky spots, *J. Glaciol.*, *39*(133), 447–454.
- Alley, R. B., D. D. Blankenship, C. R. Bentley, and S. Rooney (1986), Deformation of till beneath ice stream B, West Antarctica, *Nature*, *322*(6074), 57–59.
- Bamber, J. L., R. L. Layberry, and S. Gogineni (2001), A new ice thickness and bed data set for the Greenland ice sheet: 1. Measurement, data reduction, and errors, *J. Geophys. Res.*, *106*(D24), 33,773–33,780, doi:10.1029/2001JD900054.
- Bamber, J. L., M. J. Siegert, J. A. Griggs, S. J. Marshall, and G. Spada (2013), Paleofluvial mega-canyon beneath the central Greenland ice sheet, *Science*, *341*(6149), 997–999.
- Bartholomäus, T. C., R. S. Anderson, and S. P. Anderson (2008), Response of glacier basal motion to transient water storage, *Nat. Geosci.*, *1*(1), 33–37.
- Bell, R., K. Tinto, I. Das, M. Wolovick, W. Chu, T. Creyts, N. Frearson, A. Abdi, and J. Paden (2014), Deformation, warming and softening of Greenland's ice by refreezing meltwater, *Nat. Geosci.*, *7*, 497–502.
- Chandler, D. et al. (2013), Evolution of the subglacial drainage system beneath the Greenland ice sheet revealed by tracers, *Nat. Geosci.*, *6*(3), 195–198.
- Christianson, K., L. E. Peters, R. B. Alley, S. Anandakrishnan, R. W. Jacobel, K. L. Riverman, A. Muto, and B. A. Keisling (2014), Dilatant till facilitates ice-stream flow in northeast Greenland, *Earth Planet. Sci. Lett.*, *401*, 57–69.
- Clarke, G. K. (1987), Fast glacier flow: Ice streams, surging, and tidewater glaciers, *J. Geophys. Res.*, *92*(B9), 8835–8841.
- Copernicus (2016), Copernicus sentinel data [2016]. [Available at <https://scihub.copernicus.eu/>]
- Cuffey, K. M., and W. S. B. Paterson (2010), *The Physics of Glaciers*, Acad. Press, New York.
- Dall, J., A. Kusk, U. Nielsen, and J. P. Merryman Boncori (2015), Ice velocity mapping using topsar data and offset tracking, in *Proceedings of 9th International Workshop Fringe 2015*, vol. 731, edited by L. Ouwehand, p. 14, ESA-SP, Frascati, Italy.
- Das, S. B., I. Joughin, M. D. Behn, I. M. Howat, M. A. King, D. Lizarralde, and M. P. Bhatia (2008), Fracture propagation to the base of the Greenland ice sheet during supraglacial lake drainage, *Science*, *320*(5877), 778–781.
- ENVEO (2016a), ENVEO/ESA Greenland Icesheet CCI, grounding lines from SAR interferometry. [Available at <http://cryoportale.enveo.at/>]
- ENVEO (2016b), ENVEO/ESA Greenland Icesheet CCI, calving frontline locations. [Available at <http://cryoportale.enveo.at/>]
- Fahnestock, M., I. Joughin, T. Scambos, R. Kwok, W. Krabill, and S. Gogineni (2001a), Ice-stream-related patterns of ice flow in the interior of northeast Greenland, *J. Geophys. Res.*, *106*(D24), 34,035–34,045, doi:10.1029/2001JD900194.
- Fahnestock, M., W. Abdalati, I. Joughin, J. Brozena, and P. Gogineni (2001b), High geothermal heat flow, basal melt, and the origin of rapid ice flow in central Greenland, *Science*, *294*(5550), 2338–2342.
- Fountain, A. G., R. W. Jacobel, R. Schlichting, and P. Jansson (2005), Fractures as the main pathways of water flow in temperate glaciers, *Nature*, *433*(7026), 618–621.
- Greve, R., and U. C. Herzfeld (2013), Resolution of ice streams and outlet glaciers in large-scale simulations of the Greenland Ice Sheet, *Ann. Glaciol.*, *54*(63), 209–220.
- Greve, R., and S. Otsu (2007), The effect of the north-east ice stream on the Greenland Ice Sheet in changing climates, *Cryosphere Discuss.*, *1*(1), 41–76.
- Gudmundsson, G. H., J. Krug, G. Durand, L. Favier, and O. Gagliardini (2012), The stability of grounding lines on retrograde slopes, *Cryosphere*, *6*(6), 1497–1505, doi:10.5194/tc-6-1497-2012.

- Holland, D. M., R. H. Thomas, B. De Young, M. H. Ribergaard, and B. Lyberth (2008), Acceleration of Jakobshavn Isbrae triggered by warm subsurface ocean waters, *Nat. Geosci.*, *1*(10), 659.
- Howat, I. M., I. Joughin, S. Tulaczyk, and S. Gogineni (2005), Rapid retreat and acceleration of Helheim Glacier, east Greenland, *Geophys. Res. Lett.*, *32*, L22502, doi:10.1029/2005GL024737.
- Howat, I. M., I. Joughin, M. Fahnestock, B. E. Smith, and T. A. Scambos (2008), Synchronous retreat and acceleration of southeast Greenland outlet glaciers 2000–06: Ice dynamics and coupling to climate, *J. Glaciol.*, *54*(187), 646–660.
- Howat, I. M., A. Negrete, and B. E. Smith (2014), The Greenland Ice Mapping Project (GIMP) land classification and surface elevation data sets, *Cryosphere*, *8*(4), 1509–1518, doi:10.5194/tc-8-1509-2014.
- Howat, I. M., A. Negrete, and B. E. Smith (2015), Measures Greenland Ice Mapping Project (GIMP) digital elevation model, version 1, *Cryosphere*, *8*, 1509–1518, doi:10.5067/NV34YUJLXLP9W.
- Joughin, I., M. Fahnestock, D. MacAyeal, J. L. Bamber, and P. Gogineni (2001), Observation and analysis of ice flow in the largest Greenland ice stream, *J. Geophys. Res.*, *106*(D24), 34,021–34,034, doi:10.1029/2001JD900087.
- Joughin, I., S. B. Das, M. A. King, B. E. Smith, I. M. Howat, and T. Moon (2008a), Seasonal speedup along the western flank of the Greenland Ice Sheet, *Science*, *320*(5877), 781–783.
- Joughin, I., I. M. Howat, M. Fahnestock, B. Smith, W. Krabill, R. B. Alley, H. Stern, and M. Truffer (2008b), Continued evolution of Jakobshavn Isbrae following its rapid speedup, *J. Geophys. Res.*, *113*, F04006, doi:10.1029/2008JF001023.
- Kamb, B. (1991), Rheological nonlinearity and flow instability in the deforming bed mechanism of ice stream motion, *J. Geophys. Res.*, *96*(B10), 16,585–16,595.
- Kamb, B., and K. A. Echelmeyer (1986), Stress-gradient coupling in glacier flow: IV. Effects of the “*T*” term, *J. Glaciol.*, *32*(112), 342–349.
- Karlssohn, N., and D. Dahl-Jensen (2015), Response of the large-scale subglacial drainage system of northeast Greenland to surface elevation changes, *Cryosphere*, *9*(4), 1465–1479.
- Keisling, B. A., K. Christianson, R. B. Alley, L. E. Peters, J. E. Christian, S. Anandakrishnan, K. L. Riverman, A. Muto, and R. W. Jacobel (2014), Basal conditions and ice dynamics inferred from radar-derived internal stratigraphy of the northeast Greenland ice stream, *Ann. Glaciol.*, *55*(67), 127–137.
- Khan, S. A. et al. (2014), Sustained mass loss of the northeast Greenland ice sheet triggered by regional warming, *Nat. Clim. Change*, *4*(4), 292–299.
- Kjellström, E. et al. (2005), A 140-year simulation of European climate with the new version of the Rossby Centre regional atmospheric climate model (RCA3), in *SMHI Reports Meteorology and Climatology No. 108*, 54 pp., SMHI, SE-60176, Norrköping, Sweden.
- Krabbendam, M. (2016), Sliding of temperate basal ice on a rough, hard bed: creep mechanisms, pressure melting, and implications for ice streaming, *Cryosphere*, *10*(5), 1915–1932.
- Langen, P. et al. (2015), Quantifying energy and mass fluxes controlling Godthåbsfjord freshwater input in a 5-km simulation (1991–2012), *J. Clim.*, *28*(9), 3694–3713.
- Langen, P. L., R. S. Fausto, B. Vandecrux, R. H. Mottram, and J. E. Box (2017), Liquid water flow and retention on the Greenland ice sheet in the regional climate model HIRHAM5: Local and large-scale impacts, *Front. Earth. Sci.*, *4*, 110.
- Layberry, R., and J. Bamber (2001), A new ice thickness and bed data set for the Greenland ice sheet: 2. Relationship between dynamics and basal topography, *J. Geophys. Res.*, *106*(D24), 33,781–33,788.
- Luthi, M., M. Funk, A. Iken, S. Gogineni, and M. Truffer (2002), Mechanisms of fast flow in Jakobshavn Isbrae, West Greenland: Part III. Measurements of ice deformation, temperature and cross-borehole conductivity in boreholes to the bedrock, *J. Glaciol.*, *48*(162), 369–385.
- MacAyeal, D. R., R. A. Bindschadler, and T. A. Scambos (1995), Basal friction of ice stream E, West Antarctica, *J. Glaciol.*, *41*(138), 247–262.
- Mayer, C., N. Reeh, F. Jung-Rothenhäusler, P. Huybrechts, and H. Oerter (2000), The subglacial cavity and implied dynamics under Nioghalvfjærdsfjorden Glacier, NE-Greenland, *Geophys. Res. Lett.*, *27*(15), 2289–2292.
- Moon, T., I. Joughin, B. Smith, M. R. Broeke, W. J. Berg, B. Noël, and M. Usher (2014), Distinct patterns of seasonal Greenland glacier velocity, *Geophys. Res. Lett.*, *41*(20), 7209–7216, doi:10.1002/2014GL061836.
- Morlighem, M., E. Rignot, J. Mouginot, H. Seroussi, and E. Larour (2014), Deeply incised submarine glacial valleys beneath the Greenland ice sheet, *Nat. Geosci.*, *7*(6), 418–422, doi:10.1038/ngeo2167.
- Mouginot, J., E. Rignot, B. Scheuchl, I. Fenty, A. Khazendar, M. Morlighem, A. Buzzi, and J. Paden (2015), Fast retreat of Zachariae Isstrøm, northeast Greenland, *Science*, *350*(6266), 1357–1361.
- Nghiem, S., K. Steffen, R. Kwok, and W.-Y. Tsai (2001), Detection of snowmelt regions on the Greenland ice sheet using diurnal backscatter change, *J. Glaciol.*, *47*(159), 539–547.
- Reeh, N., C. Mayer, O. B. Olesen, E. L. Christensen, and H. H. Thomsen (2000), Tidal movement of Nioghalvfjærdsfjorden glacier, northeast Greenland: Observations and modelling, *Ann. Glaciol.*, *31*(1), 111–117.
- Reeh, N., H. H. Thomsen, A. K. Higgins, and A. Weidick (2001), Sea ice and the stability of north and northeast Greenland floating glaciers, *Ann. Glaciol.*, *33*(1), 474–480.
- Rogozhina, I. et al. (2016), Melting at the base of the Greenland ice sheet explained by Iceland hotspot history, *Nat. Geosci.*, *9*, 366–369, doi:10.1038/ngeo2689.
- Rontu, L., F. Obleitner, S. Gollvik, C. Zingerle, and S. Tijn (2009), HIRLAM experiments on surface energy balance across Vatnajökull, Iceland, *Meteorol. Atmos. Phys.*, *103*(1), 67–77.
- Rose, K. (1979), Characteristics of ice flow in Marie Byrd Land, Antarctica, *J. Glaciol.*, *24*(90), 63–75.
- Schlegel, N., E. Larour, H. Seroussi, M. Morlighem, and J. Box (2013), Decadal-scale sensitivity of northeast Greenland ice flow to errors in surface mass balance using ISSM, *J. Geophys. Res. Earth Surf.*, *118*, 667–680, doi:10.1002/jgrf.20062.
- Schlegel, N.-J., E. Larour, H. Seroussi, M. Morlighem, and J. Box (2015), Ice discharge uncertainties in northeast Greenland from boundary conditions and climate forcing of an ice flow model, *J. Geophys. Res. Earth Surf.*, *120*, 29–54, doi:10.1002/2014JF003359.
- Schoof, C. (2010), Ice-sheet acceleration driven by melt supply variability, *Nature*, *468*(7325), 803–806.
- Seddik, H., R. Greve, T. Zwinger, F. Gillet-Chaulet, and O. Gagliardini (2012), Simulations of the Greenland ice sheet 100 years into the future with the full Stokes model Elmer/Ice, *J. Glaciol.*, *58*(209), 427–440.
- Sergienko, O., T. T. Creyts, and R. Hindmarsh (2014), Similarity of organized patterns in driving and basal stresses of Antarctic and Greenland ice sheets beneath extensive areas of basal sliding, *Geophys. Res. Lett.*, *41*, 3925–3932, doi:10.7916/D85X28CW.
- Stearns, L. A., B. E. Smith, and G. S. Hamilton (2008), Increased flow speed on a large East Antarctic outlet glacier caused by subglacial floods, *Nat. Geosci.*, *1*(12), 827–831.
- Steffen, K., S. Nghiem, R. Huff, and G. Neumann (2004), The melt anomaly of 2002 on the Greenland ice sheet from active and passive microwave satellite observations, *Geophys. Res. Lett.*, *31*, L20402, doi:10.1029/2004GL020444.

- Stokes, C. R., C. D. Clark, O. B. Lian, and S. Tulaczyk (2007), Ice stream sticky spots: A review of their identification and influence beneath contemporary and palaeo-ice streams, *Earth Sci. Rev.*, *81*(3), 217–249.
- Strozzi, T., A. Luckman, T. Murray, U. Wegmuller, and C. L. Werner (2002), Glacier motion estimation using SAR offset-tracking procedures, *IEEE Trans. Geosci. Remote Sens.*, *40*(11), 2384–2391.
- Thomsen, H. H., N. Reeh, O. B. Olesen, C. E. Bøggild, W. Starzer, A. Weidick, and A. K. Higgins (1997), The Nioghalvfjærdsfjorden glacier project, North-East Greenland: A study of ice sheet response to climatic change, *Geol. Surv. Den. Greenl.*, *176*, 95–103.
- Truffer, M., and K. A. Echelmeyer (2003), Of isbrae and ice streams, *Ann. Glaciol.*, *36*(1), 66–72.
- Undén, P., L. Rontu, H. Järvinen, P. Lynch, and J. Calvo (2002), The HIRLAM-5 scientific documentation. HIRLAM-5 project, c/o per undén SMHI, s-601 76 Norrköping, Sweden. [Available at <http://hirlam.org>.]
- van der Veen, C. J. (2007), Fracture propagation as means of rapidly transferring surface meltwater to the base of glaciers, *Geophys. Res. Lett.*, *34*, L01501, doi:10.1029/2006GL028385.
- Van Der Veen, C. J., J. Plummer, and L. Stearns (2011), Controls on the recent speed-up of Jakobshavn Isbræ, West Greenland, *J. Glaciol.*, *57*(204), 770–782.
- Zwally, H. J., M. B. Giovinetto, M. A. Beckley, and J. L. Saba (2012), Antarctic and Greenland drainage systems: GSFC Cryospheric Sciences Laboratory. [Available at [http://icesat4.gsfc.nasa.gov/cryo\\_data/ant\\_grn\\_drainage\\_systems.php](http://icesat4.gsfc.nasa.gov/cryo_data/ant_grn_drainage_systems.php).]

**Supporting Information for  
“Highly temporally resolved response to seasonal surface melt of the Zachariae  
and 79N outlet glaciers in northeast Greenland”**

**N. M. Rathmann**<sup>1\*</sup>, **C. S. Hvidberg**<sup>1</sup>, **A. M. Solgaard**<sup>2</sup>, **A. Grinsted**<sup>1</sup>, **G. H. Gudmundsson**<sup>3</sup>,  
**P. L. Langen**<sup>4</sup>, **K. P. Nielsen**<sup>4</sup>, **A. Kusk**<sup>5</sup>

<sup>1</sup>Center for ice and climate (CIC), Niels Bohr Institute, University of Copenhagen, Denmark

<sup>2</sup>The Geological Survey of Denmark and Greenland (GEUS), Copenhagen, Denmark

<sup>3</sup>British Antarctic Survey (BAS), Cambridge, United Kingdom

<sup>4</sup>Danish Meteorological Institute (DMI), Copenhagen, Denmark

<sup>5</sup>National Space Institute, Technical University of Denmark (DTU), Lyngby, Denmark

**Contents**

1. Supplementary sections S1–S4
2. Supplementary figures S1–S7

---

\*Juliane Maries Vej 30, 2100, Copenhagen, Denmark

Corresponding author: N. M. Rathmann, [rathmann@nbi.ku.dk](mailto:rathmann@nbi.ku.dk)

## S1 Backscatter and surface melt maps

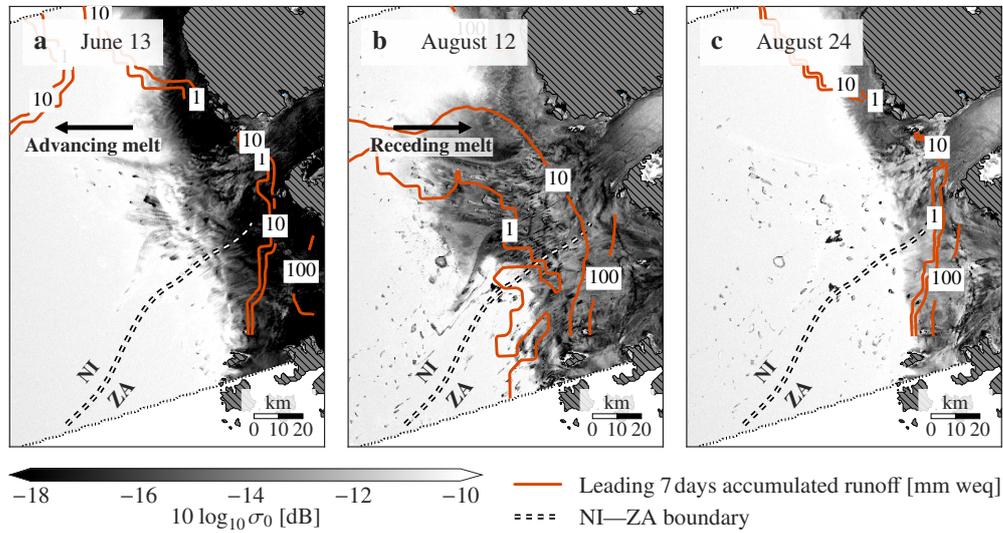


Figure S1: **Summer surface melt estimates.** Advancing and receding seasonal surface melt over ZA and NI as shown by Sentinel 1A SAR images (grayscale) including kilometre-large surface melt lakes forming (black/gray spots). Black/gray coloured areas coincide with low backscatter, indicating wet surface conditions, whereas white areas indicates dry surface conditions. Overlaid are runoff estimates of the 7 days leading the panel timestamps using the subsurface (firn) model of [Langen *et al.*, 2015, 2017] forced with 6-hourly surface energy fluxes and precipitation from the DMI weather forecast model HIRLAM 7.3 K05 (orange lines).

## S2 The timing and influence of the Zachariæ ice mélange break up

In the main text, we investigate the relative influences of seasonal surface melting (possibly lubricating the bed) and the break-up/mobilization of the ice mélange on the observed 2016 seasonal velocity speed-up along Zachariæ. In this section, we present the analysis of the timing of the break-up of the ice mélange, suggesting it coincides with the onset of surface melting.

By studying weekly/sub-weekly Sentinel 1A SAR images from tracks 074 and 140, we find the outer-most part of Zachariæ (ZA) is heavily rifted down-stream of the dashed line(s) in figure S2, which is a seemingly a stable margin throughout 2016. This margin was in part determined by (i) visually investigating where rifting occurs, (ii) by the large change in the velocity gradient along the flowline(s), and (iii) by the location of the large, spatially coherent, high-backscattering patch near the mélange (visible in panels a and d of figure S2), the latter likely being sub-surface ice exposed due to rifting (having a higher backscatter than surrounding ice). Note that this patch is approximately unchanged across the seasonal speed-up, suggesting the rifting may be a stationary feature after the recent collapse of the floating tongue, or, at least, very slowly progressing.

In order to determine the timing of the collapse/mobilization of the ice mélange, we suggest the loss of correlation (over time) between surface features is a useful measure, implying a sudden reduced spatial coverage of surface velocities over the mélange is to be expected upon break-up. Throughout January until June, the velocity pattern surrounding the mélange is unchanged (figure S2a, red/orange contour lines), after which the velocity coverage diminishes from around June 08 (figure S2b), indicating fast moving ice escaping the feature tracking window and/or surface features being degraded due to melting. During August (figure S2c), the mélange reaches its minimum extent with high-speed ice drifting occurring (no velocities could be extracted from feature tracking due to the fast flow), followed by re-consolidation of the mélange in early September (figure S2d), determined by the return of the velocity structure over the mélange. We note the timing of both the break-up and re-consolidation overlap with the onset and ending of the melt season, making it less obvious which of these mechanisms might be controlling the up-stream changes, whereas the down-stream, near-terminus speed-ups are likely controlled by mélange dynamics.

In figure S3, the seasonal velocity profiles are shown along the main ZA flowline and two additional auxiliary "upper" and "lower" flowlines (FL) adjacent to the main (solid white lines in figure S2). Because of the degraded, patchy velocity maps near terminus (our region of interest) during the summer melt season, we include these two additional auxiliary flowlines to better determine the spatial extent of the velocity changes. We note that all three flowlines indicate  $\sim 0.11$  km/yr ( $\sim 14\%$ ) increases 15 km up-stream from the rifted margin, while the upper flowline, having a better up-stream coverage, suggests the speed-up may extend as far back as 30 km from the rifted margin.

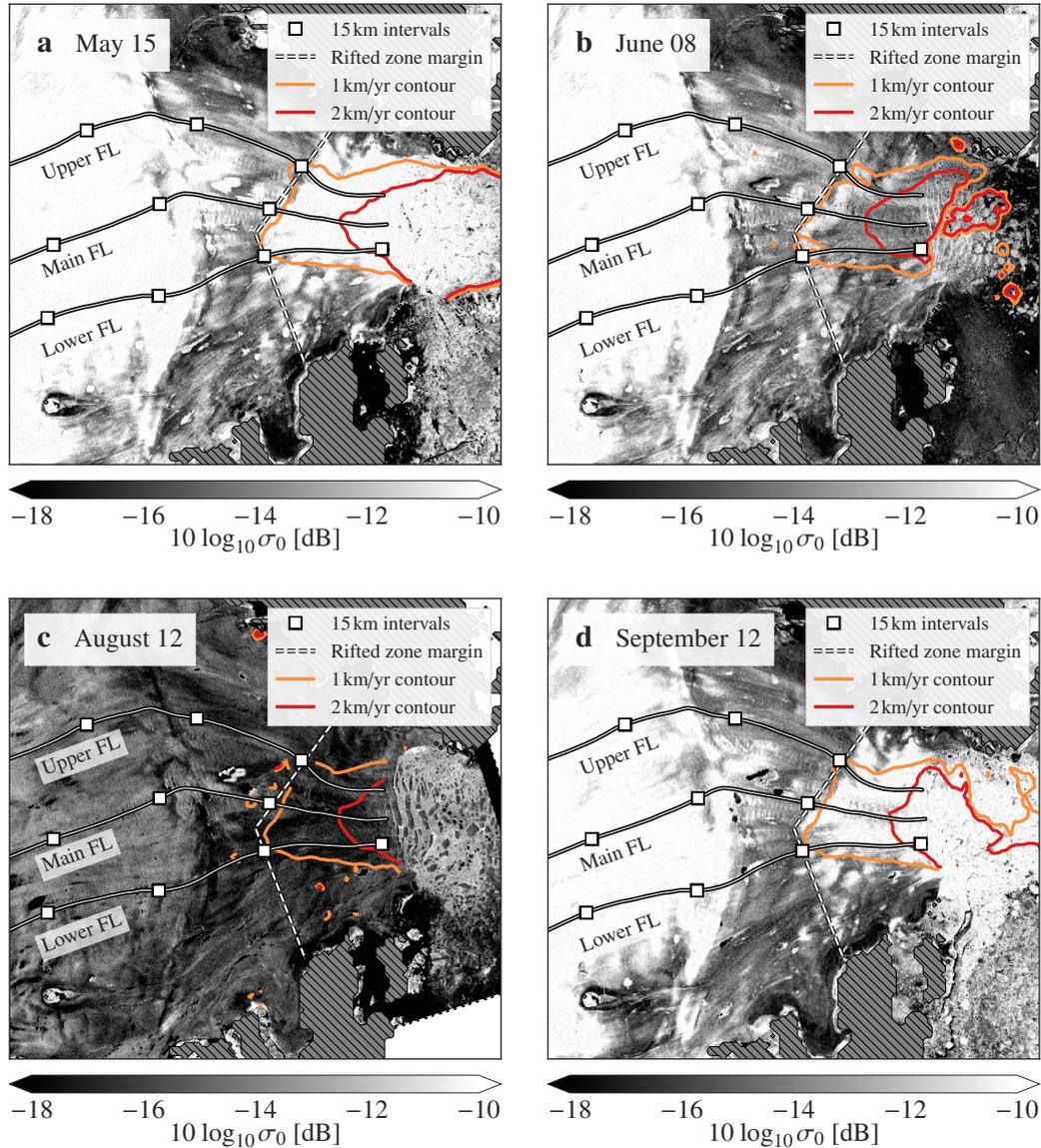
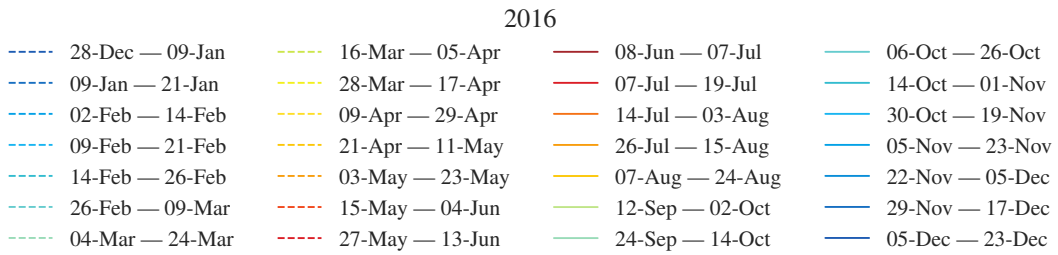
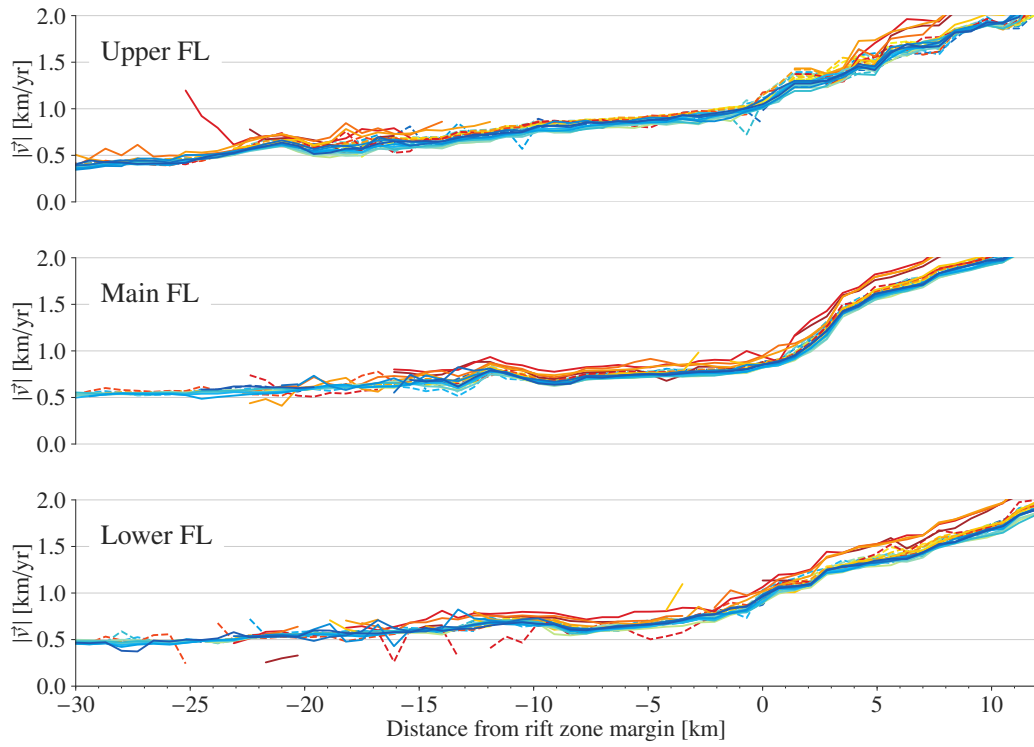


Figure S2: **Seasonality of Zachariae ice mélange and rifted ice zone.** Sentinel-1A SAR images (surface backscatter in grayscale) over Zachariae across the 2016 summer melt season showing the ice mélange being mobilized and breaking up around June 08 (b), followed by re-consolidation in early September (d). Overlaid is the main flowline (FL), considered in the main text, plus two additional upper and lower flowlines (solid white lines) considered in figure S3. The coloured contours are the 1 km/yr (orange) and 2 km/yr (red) velocity contours, used to estimate the timing of the ice mélange mobilizing. The dashed line indicates the approximate margin downstream of which the ice is heavily rifted, which is most pronounced within the 1 km/yr contour (orange line).



**Figure S3: Velocity profiles along Zachariae.** Velocity profiles along the Zachariae flowlines shown in figure S2. The main flowline is identical to that in the main text, whereas the auxiliary upper and lower flowlines (FL) show the adjacent flow. The spotty/noisy summer profiles are due to surface melting degrading the correlation between surface structures used in the offset tracking.

### S3 79N strain-rates across season

Figure S4 shows in detail the 79N strain-rates near and over the floating tongue. In addition to the transverse winter strain-rates shown in figure 3a of the main text, figure S4a also shows the corresponding longitudinal winter strain-rates. Furthermore, the differences between summer and winter strain-rates are shown in panels b and d for  $\dot{\epsilon}_{xx}$  and  $\dot{\epsilon}_{xy}$ , respectively, suggesting little stress redistribution over the tongue during the period of speed-up. Note the summer strain-rate maps were generated using a composition of summer maps between May-15 2016 — Aug-15 2016 to improve the spatial coverage.

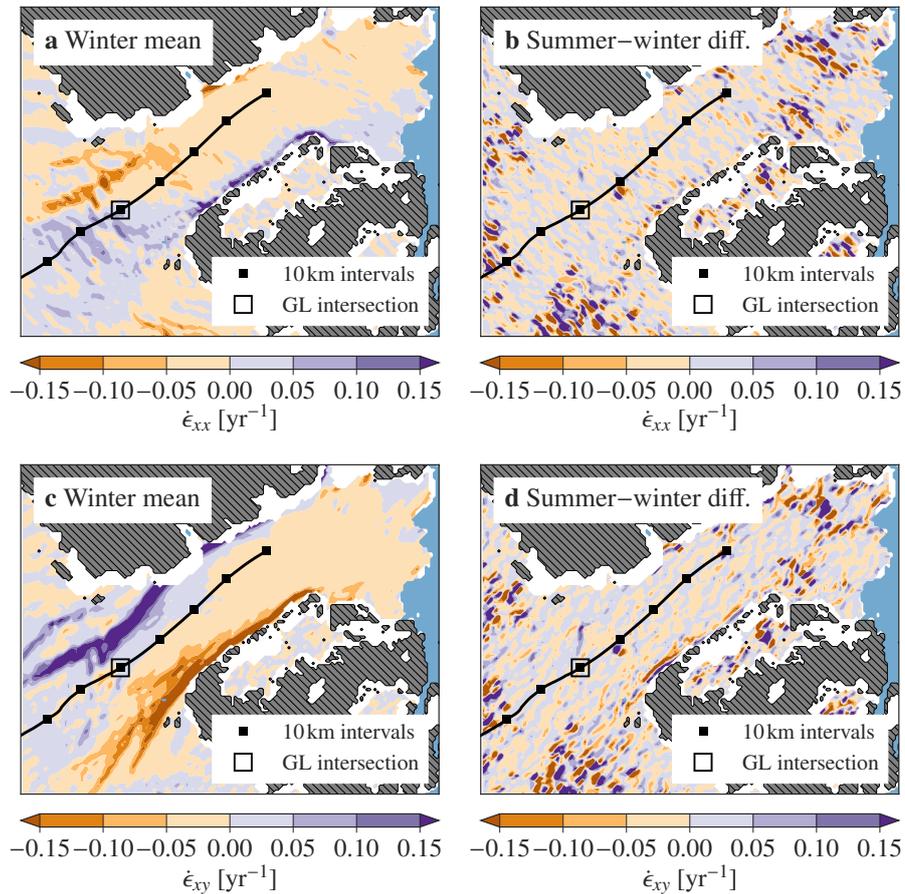


Figure S4: **79N strain-rates.** Strain-rates along flow ( $\dot{\epsilon}_{xx}$ , top panels) and transverse to the flow ( $\dot{\epsilon}_{xy}$ , bottom panels) calculated using the average observed winter/spring velocities during Jan-01 2016 — May-15 2016 (left-hand panels), and the difference between summer melt season (May-15 2016 — Aug-15 2016) and the winter/spring season (right-hand panels).

## S4 Úa perturbation experiments

In order to accurately represent the current stress configuration of the NEGIS outlets, we estimate the unknown basal slipperiness coefficient,  $C$ , using  $\dot{U}_a$  [Gudmundsson *et al.*, 2012], which is related to the basal drag by Wertman’s sliding law,  $\tau_b = C^{-1/m} |\dot{v}|^{1/m-1} \dot{v}$ , with an exponent of  $m = 2$ . Setting up  $\dot{U}_a$  on the domain shown in main text figure 1 with element sizes of approximately  $0.4 \text{ km}^2$  and flow parameters as in main text section 2.1.1, the basal slipperiness was determined for each velocity map using the built-in, inverse estimation of basal drag. Unfortunately, during the melt season the velocity maps contain large patches of missing data due to bad correlation between surface features, giving less confidence in the inverted basal slipperiness maps due to large errors in modelled surface velocities (not shown). Because of this, we propose the effect of seasonally enhanced slipperiness may be expressed, to low order, by uniformly scaling the slipperiness map of one of the winter/spring inversions with good coverage. For this purpose, we choose the 09-Apr–29-Apr map, hereafter referred to as the  $C_0$  slipperiness map (figure S5e). Figures S5a,b,c show the corresponding modelled velocities using  $\dot{U}_a$  (a) compared to observations (b) and the model error (c), indicating an overall reasonable fit. Note that refining the mesh further did not improve the model error (not shown).

In the slipperiness perturbation experiments considered here, the ice-covered, non-floating computational domain was partitioned into three (finite) element subsets:

1. grounded ice elements up-stream of the grounding line ( $\Omega$  set),
2. a subset of grounded ice elements which may, potentially, be sticky spots, defined as small-scale bedrock bumps taller than sea level ( $\Omega_s$  set),
3. elements along the tongue–wall interfaces ( $\Gamma$  set).

Figure S5d shows the model mesh and the element types. Using this model setup, we performed four types of slipperiness perturbation experiments with the aim of understanding the hypothesized seasonally enhanced sliding along 79N.

### S4.1 Perturbing $\Omega$ and $\Gamma$ slipperinesses

Figure S6 shows the model response to uniform slipperiness perturbations (scaling  $C_0$  by  $-20\%$ ,  $-15\%$ ,  $\dots$ ,  $50\%$ ) of the  $\Omega$  and  $\Gamma$  element sets, respectively, as a function of the 79N tongue length  $L/L_0 = 0.0, 0.1, \dots, 1.0$  ( $L_0 = 76 \text{ km}$  being the present day length) in forward diagnostic solutions (solving only the momentum equations).

Figures S6a,c show the velocity response at the reference point shown in figure S5e, indicating a relatively strong sensitivity to changes in basal slipperiness for the grounded part compared to along the tongue–wall interfaces. Moreover, it is seen that once  $L/L_0 \lesssim 0.2$  (i.e.  $L \lesssim 15 \text{ km}$ ) the grounding-line velocity becomes very sensitive to the length of the tongue.

Figures S6b,d furthermore show the full 79N flowline response to selected slipperiness perturbations compared to observations, indicating: (i) slipperiness changes along the tongue–sidewall interfaces produce only a velocity response locally on the tongue (figure S6d), whereas changes over the grounded part leads to changes along the full flowline (figure S6b), and (ii) a  $\sim 20\%$  increase in slipperiness over the grounded part,  $\Omega$ , gives rise to a flowline velocity response comparable in magnitude and spatial extent to the observed seasonal change (figure S6b).

### S4.2 Perturbing $\Omega \setminus \Omega_s$ slipperinesses and the bedrock topography

In order to estimate the influence of the potential sticky spots below 79N on the seasonal speed-up, two additional perturbation experiments were performed. In the first experiment, the slipperiness was uniformly scaled for the  $\Omega \setminus \Omega_s$  element set (all grounded elements except the sticky spots), which may be interpreted as a more realistic seasonal slipperiness perturbation since the slipperiness of high-laying sticky spots might be less effected by an

increase in the subglacial water content. In the second experiment, all small-scale bumps in bedrock topography taller than sea level were flattened by re-setting their height to zero (sea level), followed by the slipperiness field being scaled for all grounded elements ( $\Omega$  set).

Figures S7a,b show the flowline responses in the two experiments, respectively. From figure S7a we note that when perturbing the slipperiness of only non-sticky grounded elements ( $\Omega \setminus \Omega_s$ ), the velocity response is almost indistinguishable from when perturbing all grounded elements ( $\Omega$ , figure S6b). Similarly, when flattening the small-scale bumps constituting the potential sticky spots the flowline response (figure S7b) is almost identical to that without a flattening (figure S6b).

Taking both results together, this suggests that small-scale topographical details such as bedrock bumps do not exert large-scale control over the magnitude of the seasonal speed-up. In fact, on closer inspection of figures S7a,b, the difference in flowline responses, compared to when perturbing all grounded elements (figure S6b), is mostly locally around the sticky spots ( $\sim 30$  km from the grounding line). We note, however, that while the influence of bedrock bumps on the velocity field is small in magnitude and spatially local for both NI and ZA (not shown for latter), the details of the subglacial environment potentially exert a greater control on the seasonal velocity response compared to, e.g., changes in slipperiness along the tongue–sidewall interfaces (figure S6d).

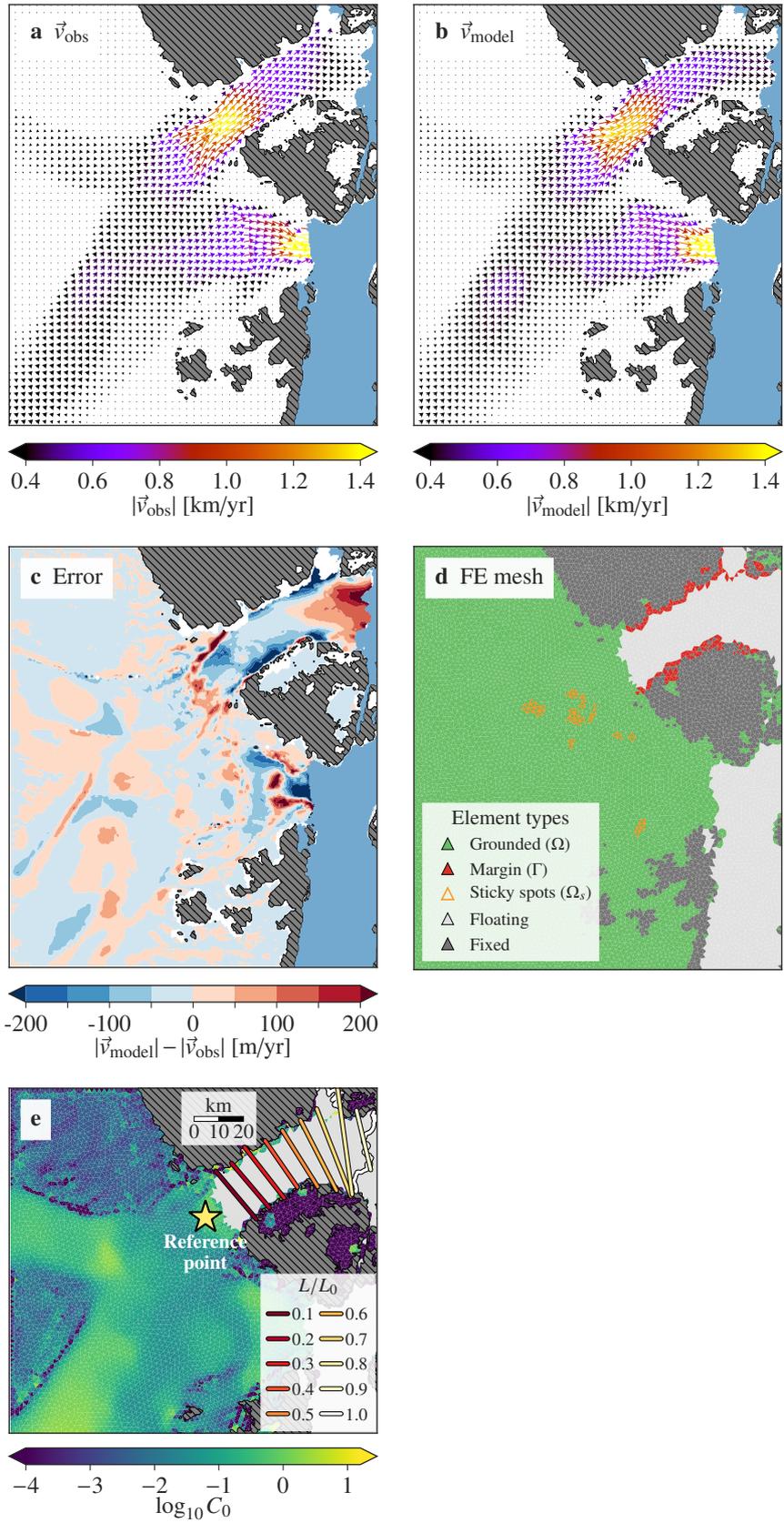


Figure S5: Úa performance and mesh. Observed (a) and modelled (b) surface velocities for 09-Apr–29-Apr. (c) Model error. (d) Finite element (FE) mesh with element types labelled in color. (e) inverted basal slipperiness for 09-Apr–29-Apr and perturbed tongue lengths ( $L/L_0$ ).

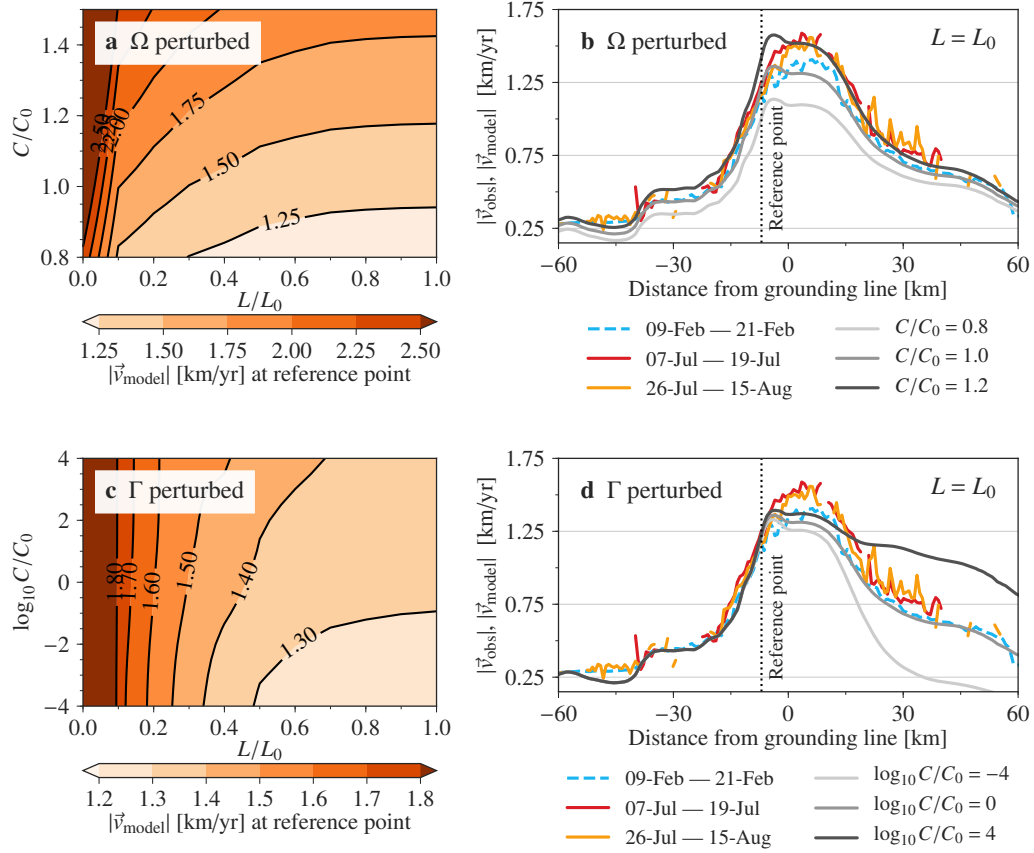


Figure S6: **Slipperiness perturbation experiments using  $\bar{U}_a$** . Modelled velocity responses to uniform slipperiness perturbations of the  $\Omega$  elements (grounded ice, panels a and b) and the  $\Gamma$  elements (tongue–sidewall interfaces of 79N, panels c and d) (see figure S5d for details on the element masks). Panels a and c show the model response at the reference point (see figure S5e) as a function of the floating tongue length,  $L$ , whereas panels b and d show the full 79N flowline response for selected perturbations using the present tongue length ( $L=L_0$ ).

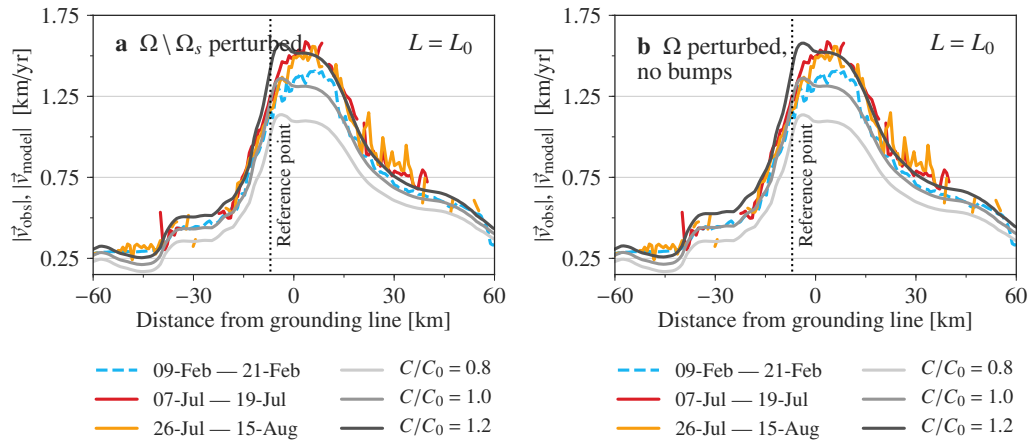


Figure S7: **Sticky spots perturbation experiments using Úa.** Modelled velocity responses to uniform slipperiness perturbations (scaling) of (a) non-sticky grounded ice ( $\Omega \setminus \Omega_s$  elements), and (b) grounded ice ( $\Omega$  elements) after having flattened small-scale bedrock topography taller than sea level (potential sticky spots). In both experiments the present tongue length is used ( $L = L_0$ ).

## References

- Gudmundsson, G. H., J. Krug, G. Durand, L. Favier, and O. Gagliardini (2012), The stability of grounding lines on retrograde slopes, *The Cryosphere*, 6(6), 1497–1505, doi: 10.5194/tc-6-1497-2012.
- Langen, P., R. Mottram, J. Christensen, F. Boberg, C. Rodehacke, M. Stendel, D. van As, A. Ahlstrøm, J. Mortensen, S. Rysgaard, et al. (2015), Quantifying energy and mass fluxes controlling godthåbsfjord freshwater input in a 5-km simulation (1991–2012)\*,+, *Journal of Climate*, 28(9), 3694–3713.
- Langen, P. L., R. S. Fausto, B. Vandecrux, R. H. Mottram, and J. E. Box (2017), Liquid water flow and retention on the greenland ice sheet in the regional climate model HIRHAM5: local and large-scale impacts, *Frontiers in Earth Science*, 4, 110.

### 4.3 Outlook

The subglacial environment of ice sheets is by and large inaccessible with only little direct evidence existing on the state of the ice–bed interface. While radio-echo sounding surveys such as Christianson et al. (2014) over NEGIS can be instrumental in deducing the thermal state of the bed by e.g. inferring basal melting from the dipping of isochrones, or by bed reflections being consistent with certain types of ice–bed interfaces and not others, such inferences are all indirect. Deep ice core drilling projects, on the other hand, provide a unique opportunity to study the bed by direct access through the empty bore hole, thereby providing valuable in-situ measurements of the ice–bed interface. Unfortunately, such measurements are too few to extrapolate basal properties to the spatio–temporal scales needed to constrain boundaries of ice-sheet models for more accurate future projections.

An alternative approach is to infer the basal state by inverting for the free parameters in the basal drag relation, constrained against observed surface velocities, such as done in the present study. This line of approach has proven fruitful for understanding the magnitude of basal resistance as well as revealing the range of possible spatial structure (Sergienko et al., 2014; Shapero et al., 2016).

With the newest generation of satellites, it might be possible to further extend the scope of what can be learned from inverse modelling. Considering high temporally resolved velocity maps as here, it might be possible to invert for the basal state on time scales not previously possible. Having estimates of how the basal state changes during a melt season could, for example, have important implications for validating hydrological (water routing) models, as well as informing where future surveys on water routing processes should be conducted.

Inverting for the basal resistance is, however, an under-determined problem in the sense that multiple solutions might have the same cost-function value. It is therefore not completely clear what methodology would allow the inversion of basal resistance (for consecutive velocity maps) to reflect the actual physical subglacial change over time, and not some unphysical change due to over-fitting of velocity artefacts. One method that might work would be to represent the unknown basal-resistance map as a linear combination of smoothly varying basis functions, such that the coefficients of the basis function are the unknowns inverted for (a sort of regularization). If the chosen basis functions allow only coarse spatial structure to be resolved (coarse needing to be defined), it is possible that the inversion would allow the actual physical subglacial change to be extracted (difference between consecutive inverted maps of basal resistance).

Other intriguing prospects of highly spatio-temporally resolved surface imagery and velocity maps includes the ability to systematically compare the timing and response to seasonal surface melting across a multitude of outlet glaciers in e.g. Greenland. This might allow quantifying the types and ranges of responses, and could help predict which outlet systems might be particularly sensitive to future changes in atmospheric heat content and thus contribute to near-term sea level rise.

# Chapter 5

## Study #2

### 5.1 Introduction

In the deep layers of ice sheets, the **c**-axis fabric of polycrystalline ice is typically not isotropic but displays a range of rotational symmetries. A fabric commonly found at large depths is the single-maximum fabric (figure 3.3), which exhibits a single preferred **c**-axis direction (Hooke, 1973; Gow and Williamson, 1976; Herron and Langway, 1982; Svensson et al., 2003). Caused by recrystallization processes and crystal deformation processes (Cuffey and Paterson, 2010, chap. 3.3), single-maximum fabrics have an approximate material rotational symmetry around their preferred direction — they are *transversely isotropic*. Consequently, the material microstructural symmetry element should be reflected by the corresponding rheology too (section 3.1). Most theoretical and modelling analyses of ice flow, however, ignore this fact and assume fabric isotropy. While assuming fabric isotropy *is* an excellent approximation, often demonstrated by the success of ice flow models in reproducing observed surface flow fields<sup>1</sup>, Glen's isotropic flow law can, in this respect, typically be justified only for the top-most, undeveloped fabric of glaciers and ice sheets.

Although no general creep relation exists taking fabric anisotropy into account (Cuffey and Paterson, 2010, p. 78), a large collection of literature has led to significant advances. Lile (1978) first considered the effect of preferred-orientation fabrics by investigating how intragranular strain-rates of single crystals were influenced by stress redistribution, accomplished by introducing an enhancement factor depending on a geometrical tensor. Later, more elaborate work by Azuma (1994, 1995); Azuma and Goto-Azuma (1996); Thorsteinsson (2001) and others extended the idea of a geometrical tensor to describe the bulk aggregate orientation in order to enhance deformation by basal glide in polycrystalline ice [relating microscopic (single-crystal) stresses to macroscopic (polycrystal) stresses]. Moreover, work has been done to extend this method to idealized crystallographic symmetries and

---

<sup>1</sup>The rate-factor,  $A$ , is frequently multiplied by an enhancement factor,  $E$ , to achieve a better fit, which conveniently allows to account for unknown material softening and hardening effects.

evolving anisotropy (Lliboutry, 1993; Castelnau and Duval, 1994; Van der Veen and Whillans, 1994), and to so-called viscoplastic self-consistent models allowing crystal slip not only along basal planes, but along prismatic and pyramidal planes too (figure 3.4) (Castelnau et al., 1996; Meyssonier and Philip, 1996).

Supposing that certain idealized microstructural symmetries exist, plastic potential theory (section 3.1) allows developing more general anisotropic flow-laws relying on free macroscopic parameters—that is, effective, macroscopic directional viscosities along principal (symmetry) directions—which depend (in an unspecified way) on local grain orientation distributions. Johnson (1977) considered such an approach for modelling directionally solidified metallic alloys as transversely isotropic, and several glaciological studies have embraced the use of plastic potential theory in proposing orthotropic and transversely isotropic constitutive equations (Meyssonier and Philip, 1996; Gödert and Hutter, 1998; Svendsen and Hutter, 1996; Lliboutry, 1993; Staroszczyk and Gagliardini, 1999; Gillet-Chaulet et al., 2005).

This approach, however, relies not only on specifying additional models for the free macroscopic flow parameters, which must depend on the local microstructural distributions of grain orientation, size, etc., but also requires accurately representing such microstructural distributions including their co-evolution with flow.

From a practical point of view, the above mentioned discrete-grain resolving models have the drawback of needing to track and evolve individual grains with time. Typically hundreds of grains are needed to adequately describe the fabric at a given point (Staroszczyk and Gagliardini, 1999), which can become impractical for large computational domains needed for larger scale flow problems. To overcome this problem, continuous representations of *c*-axis orientations have been proposed using orientation distribution functions (ODFs) (Lliboutry, 1993; Meyssonier and Philip, 1996; Svendsen and Hutter, 1996), inspired by material sciences (Bunge, 2013).

Independently of choice of microstructural representation, introducing models for the free macroscopic flow parameters (in terms of the microscopic aggregate by e.g. homogenization procedures) adds an additional layer of model complexity to the evolution of ice masses. This work makes the case that much is still to be learned by studying idealized transversely isotropic flows (from plastic potential theory) with prescribed macroscopic flow parameters; that is, without the added layer of realism provided by modelling the evolution of microstructural grain distributions and the corresponding effect on macroscopic flow parameters, thus decoupling the problem of a co-evolving fabric and ice flow.

Specifically, this work attempts to investigate the relation between deep internal layer disturbances — such as the folding/buckling observed from ice-penetrating radar transects (figure 1.1, middle) — and the dynamics introduced by a macroscopic transversely isotropic rheology. Understanding the mechanisms behind internal layer disturbances has implications for the interpretation of ice core stratigraphies and chronologies, as well as understanding how disturbances might influence adjacent flow, such as near the shear-margins of the northeast Greenland ice stream (NEGIS)

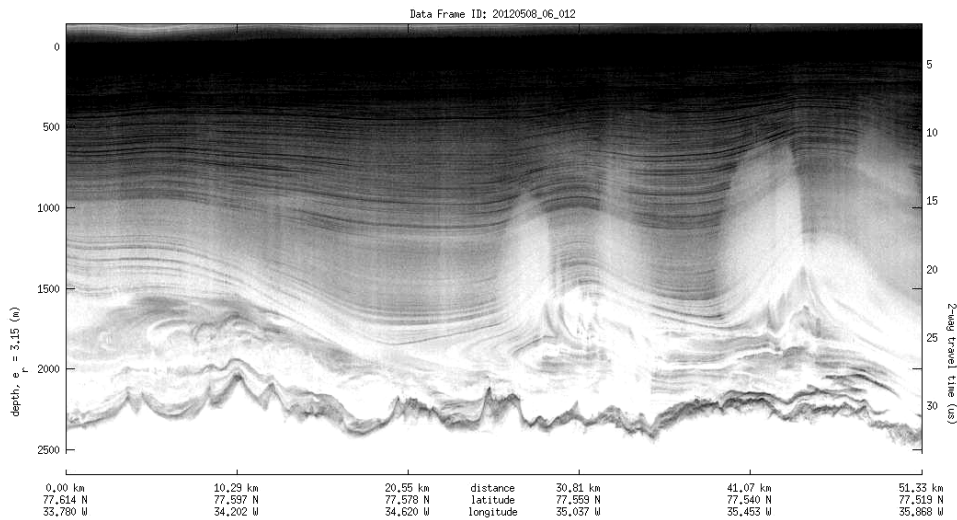


Figure 5.1: Disturbed flow captured in the near-bed layers from an ice-penetrating radar transect over Greenland. The distinct horizontal curves are internal layers with different dielectric properties. The transect is approximately 210 km to 230 km north of the East Greenland Ice Core Project (EGRIP) camp. Image credit: CReSIS’s ice-penetrating radar, NASA Operation IceBridge campaign 2012.

where large disturbances may occur (figure 5.1).

In the following sections the forward and inverse flow law for a transversely isotropic symmetry is introduced, constructed by requiring tensorial linearity (classical von Mises type law) with a Norton–Bailey potential (3.19) thus ensuring conformity with Glen’s isotropic law. Subsequently, a new two-dimensional, finite-element anisotropic Lagrangian numerical ice-flow model is introduced, developed by the author. This model is used to investigate the effect of discrete, strong single-maximum layers on transient internal layer deformation (morphology) under idealized circumstances. Specifically, it is shown that the transient buckling and folding of internal layers, such as observed from ice-penetrating radar transects (figure 5.1), might be explained by vertical shear (change in horizontal velocity with depth) being opposed in slightly nonvertical single-maximum fabrics if nonbasal (hard) glide is suppressed.

## 5.2 Transversely isotropic creep

A transversely isotropic flow law can too be constructed from the material tensors  $\mathbf{A}$ ,  ${}^{(4)}\mathbf{B}$  and  ${}^{(6)}\mathbf{C}$ , in which case the material tensors are built from products of the two elementary transversely isotropic tensors: the identity,  $\mathbf{I}$ , and the fabric (rotational) symmetry axis,  $\mathbf{m}$ , the latter defined as the normalized  $\mathbf{c}$ -axis vector sum of a given

local bundle

$$\mathbf{m} = \sum_i \mathbf{c}_i / \left\| \sum_i \mathbf{c}_i \right\|. \quad (5.1)$$

In this sense, the transversely isotropic flow law is local due to its dependency on the local symmetry axis direction, hereafter interchangeably referred to as the single-maximum direction<sup>2</sup>. This work, however, adopts a similar approach to that of Johnson (1977) by instead constructing  $\mathcal{I}_1, \mathcal{I}_2$  and  $\mathcal{I}_3$  directly from the five transversely isotropic basic invariants<sup>3</sup> (Johnson, 1977; Naumenko and Altenbach, 2007)

$$\begin{aligned} I_1(\boldsymbol{\sigma}) &= \text{Tr } \boldsymbol{\sigma}, & I_2(\boldsymbol{\sigma}) &= \text{Tr } \boldsymbol{\sigma}^2, & I_3(\boldsymbol{\sigma}) &= \text{Tr } \boldsymbol{\sigma}^3, \\ I_4(\boldsymbol{\sigma}) &= \text{Tr}(\boldsymbol{\sigma} \cdot \mathbf{M}), & I_5(\boldsymbol{\sigma}) &= \text{Tr}(\boldsymbol{\sigma}^2 \cdot \mathbf{M}), \end{aligned} \quad (5.2)$$

where  $\mathbf{M}$  is given by the outer (dyadic) product

$$\mathbf{M} = \mathbf{m} \otimes \mathbf{m}. \quad (5.3)$$

The possible combinations resulting in first, second and third order dependence on  $\boldsymbol{\sigma}$  are, respectively,

$$\begin{aligned} \mathcal{I}_1 &= \mu_{1,1} I_1 + \mu_{1,2} I_4 \\ \mathcal{I}_2^2 &= \mu_{2,1} I_1^2 + \mu_{2,2} I_1 I_4 + \mu_{2,3} I_4^2 + \mu_{2,4} I_2 + \mu_{2,5} I_5 \\ \mathcal{I}_3^3 &= \mu_{3,1} I_1^3 + \mu_{3,2} I_1 I_2 + \mu_{3,3} I_3 + \mu_{3,4} I_4^3 + \mu_{3,5} I_4 I_5 \\ &\quad + \mu_{3,6} I_1^2 I_4 + \mu_{3,7} I_1 I_4^2 + \mu_{3,8} I_2 I_4 + \mu_{3,9} I_1 I_5, \end{aligned}$$

where  $\mu_{i,j}$  are material parameters. Note that  $I_1, I_2$  and  $I_3$  are shared with Glen's isotropic law (3.14) while  $I_4$  and  $I_5$  are new, and that  $\mu_{2,4}$  is related to the isotropic rate-factor,  $A$ , analogous to  $\mu_{2,2}$  in the above isotropic case (3.20).

Disregarding nonclassical, second-order effects ( $\gamma = 0$ ) and setting  $\alpha = 0$  following von Mises' work on the plasticity of crystals (Mises, 1928), thus ensuring conformity with Glen's law in the isotropic limit, the flow law (3.11) becomes

$$\dot{\boldsymbol{\epsilon}} = \epsilon_E \beta \frac{\partial \mathcal{I}_2}{\partial \boldsymbol{\sigma}} = \epsilon_E \beta \frac{1}{2} \mathcal{I}_2^{-1} \frac{\partial \mathcal{I}_2^2}{\partial \boldsymbol{\sigma}}, \quad (5.4)$$

where the chain rule was used to conveniently re-express the derivative. By substituting  $\boldsymbol{\sigma} = -p\mathbf{I} + \boldsymbol{\tau}$  into  $\mathcal{I}_2$  and  $\partial \mathcal{I}_2^2 / \partial \boldsymbol{\sigma}$ , and relabelling  $\mu_i \equiv \mu_{2,i}$  for notational

<sup>2</sup>Other rotationally symmetric fabrics such as girdle fabrics are also transversely isotropic and are equally well explained by a transversely isotropic flow law. This work, however, is motivated by observations and measurements based on single-maximum fabrics and therefore focuses its treatment on this special case of transverse isotropy. Throughout, little distinction is therefore made between transversely isotropic fabrics and single-maximum fabrics.

<sup>3</sup> $I_1, \dots, I_5$  are invariant under coordinate transformations  $\mathbf{Q}$  that preserve the symmetry-axis orientation ( $\mathbf{m}$ ) for any rotation ( $\phi$ ) about it (subset of full 3D rotation group), defined as

$$\mathbf{Q}(\phi, \mathbf{m}) = \mathbf{M} + (\mathbf{I} - \mathbf{M}) \cos \phi + \mathbf{m} \times \mathbf{I} \sin \phi \in \mathcal{SO}(3).$$

brevity since only  $\mathcal{I}_2$  contributions are considered, one finds

$$\mathcal{I}_2^2 = \mu_4 p (g_{\text{II}} p - g_{\text{I}} I_4) + \mu_3 I_4^2 + \mu_4 I_2 + \mu_5 I_5 \quad (5.5)$$

$$\frac{\partial \mathcal{I}_2^2}{\partial \boldsymbol{\sigma}} = -\mu_4 p (g_{\text{III}} \mathbf{I} + g_{\text{I}} \mathbf{M}) + \mu_2 I_4 \mathbf{I} + 2\mu_3 I_4 \mathbf{M} + 2\mu_4 \boldsymbol{\tau} + \mu_5 \{\boldsymbol{\tau}, \mathbf{M}\}, \quad (5.6)$$

where  $I_i = I_i(\boldsymbol{\tau})$  is implied [defined similarly to (5.2)],  $\{\boldsymbol{\tau}, \mathbf{M}\}$  is the anticommutator between  $\boldsymbol{\tau}$  and  $\mathbf{M}$

$$\{\boldsymbol{\tau}, \mathbf{M}\} = \mathbf{M} \cdot \boldsymbol{\tau} + \boldsymbol{\tau} \cdot \mathbf{M}, \quad (5.7)$$

and material parameters have been grouped together for convenience as

$$\begin{aligned} g_{\text{I}} &= 3 \frac{\mu_2}{\mu_4} + 2 \frac{\mu_3}{\mu_4} + 2 \frac{\mu_5}{\mu_4}, & g_{\text{II}} &= 9 \frac{\mu_1}{\mu_4} + 3 \frac{\mu_2}{\mu_4} + \frac{\mu_3}{\mu_4} + 3 + \frac{\mu_5}{\mu_4}, \\ g_{\text{III}} &= 6 \frac{\mu_1}{\mu_4} + \frac{\mu_2}{\mu_4} + 2. \end{aligned} \quad (5.8)$$

Note the invariant derivatives occurring when calculating (5.6) are given by

$$\begin{aligned} \partial_{\boldsymbol{\sigma}} I_1(\boldsymbol{\sigma}) &= \mathbf{I}, & \partial_{\boldsymbol{\sigma}} I_1(\boldsymbol{\sigma})^2 &= 2I_1(\boldsymbol{\sigma}) \mathbf{I}, & \partial_{\boldsymbol{\sigma}} I_2(\boldsymbol{\sigma}) &= 2\boldsymbol{\sigma}, \\ \partial_{\boldsymbol{\sigma}} I_4(\boldsymbol{\sigma}) &= \mathbf{M}, & \partial_{\boldsymbol{\sigma}} I_4(\boldsymbol{\sigma})^2 &= 2I_4(\boldsymbol{\sigma}) \mathbf{M}, & \partial_{\boldsymbol{\sigma}} I_5(\boldsymbol{\sigma}) &= \{\boldsymbol{\sigma}, \mathbf{M}\}, \end{aligned}$$

which is most easily shown in index notation.

Incompressibility requires no dependence on the pressure in (5.5)–(5.6), implying  $g_{\text{I}}$ ,  $g_{\text{II}}$  and  $g_{\text{III}}$  must vanish. Solving the three equations  $g_{\text{I}}$ ,  $g_{\text{II}}$ ,  $g_{\text{III}} = 0$  with five unknowns, the parameters are related by

$$\frac{\mu_2}{\mu_4} = -6 \frac{\mu_1}{\mu_4} - 2 \quad \text{and} \quad 9 \frac{\mu_1}{\mu_4} = \frac{\mu_5}{\mu_4} + \frac{\mu_3}{\mu_4} - 3. \quad (5.9)$$

Because this system is under-determined, the transversely isotropic constitutive equation has  $5 - 3 = 2$  additional flow parameters compared to isotropy. The two additional flow parameters, being defined relative to the isotropic (Glen) parameter  $\mu_4$  in (5.9), play the role of enhancement factors and are hereafter referred to by

$$E' = \frac{\mu_3}{\mu_4} \quad \text{and} \quad E'' = \frac{\mu_5}{\mu_4}. \quad (5.10)$$

In the two-dimensional case treated below, it is shown that a special combination of  $E'$  and  $E''$  may be interpreted as the basal-plane (easy) and nonbasal-plane (hard) glide enhancement factors.

Applying the incompressibility constraints (5.9) to (5.5)–(5.6), the two terms reduce to

$$\mathcal{I}_2^2 = \mu_4 (I_2 + E' I_4^2 + E'' I_5) \quad (5.11)$$

$$\frac{\partial \mathcal{I}_2^2}{\partial \boldsymbol{\sigma}} = 2\mu_4 \left( \boldsymbol{\tau} + E' I_4 \mathbf{M} + \frac{E''}{2} \{\boldsymbol{\tau}, \mathbf{M}\} - \frac{E' + E''}{3} I_4 \mathbf{I} \right). \quad (5.12)$$

From here, assuming a Norton–Bailey potential such that  $\epsilon_E = A_0 \tau_E^n = A_0 \beta^n \mathcal{I}_2^n$ , and defining the rate-factor as  $A = A_0 \beta^{n+1} \mu_4^{(n+1)/2}$ , the constitutive equation (5.4) becomes

$$\dot{\epsilon} = \eta^{-1} \left( \boldsymbol{\tau} + E' I_4 \mathbf{M} + \frac{E''}{2} \{\boldsymbol{\tau}, \mathbf{M}\} - \frac{E' + E''}{3} I_4 \mathbf{I} \right) \quad (5.13)$$

$$\eta^{-1} = A (I_2 + E' I_4^2 + E'' I_5)^{(n-1)/2}, \quad (5.14)$$

which is uniquely defined by the three macroscopic flow parameters  $A$ ,  $E'$  and  $E''$ , and reduces to Glen's flow law (3.21)–(3.22) for  $E', E'' = 0$ .

### 5.2.1 Inverse two-dimensional constitutive equation

Posing the transversely isotropic constitutive equation in an inverse, closed form,  $\boldsymbol{\tau}(\dot{\epsilon})$ , is algebraically more challenging than for Glen's law. While in Glen's law the problem amounts to solving one equation with one unknown, in the present case three equations with three unknowns must be solved in order to re-express  $I_i(\boldsymbol{\tau})$  in terms of  $I_i(\dot{\epsilon})$ .

First, the stress deviator,  $\boldsymbol{\tau}$ , must however be isolated in (5.13). By rearranging terms, it follows that

$$\boldsymbol{\tau} + \frac{E''}{2} \{\boldsymbol{\tau}, \mathbf{M}\} = \eta(\boldsymbol{\tau}) \dot{\epsilon} - E' I_4(\boldsymbol{\tau}) \mathbf{M} + \frac{E' + E''}{d} I_4(\boldsymbol{\tau}) \mathbf{I}_d, \quad (5.15)$$

which is a anti-commutator matrix equation (Sylvester equation). Here  $d$  is the dimensionality of the problem, and  $\mathbf{I}_d$  is the  $d \times d$  identity matrix. Note that  $d = 3$  was considered without loss of generality in the above section 5.2. Solving Sylvester's equation in a symbolic manner is not straight forward and requires vectorizing each term by the stacking columns according to

$$\text{vec}(X_{ij}) = [X_{11}, \dots, X_{m1}, X_{12}, \dots, X_{m2}, \dots, X_{1n}, \dots, X_{mn}]^T.$$

Vectorizing (5.15) can then be shown to give

$$\mathbf{P}_{d^2} \text{vec}(\boldsymbol{\tau}) = \eta(\boldsymbol{\tau}) \text{vec}(\dot{\epsilon}) - E' I_4(\boldsymbol{\tau}) \text{vec}(\mathbf{M}) + \frac{E' + E''}{d} I_4(\boldsymbol{\tau}) \text{vec}(\mathbf{I}_d), \quad (5.16)$$

where  $\mathbf{P}_{d^2}$  is a  $d^2 \times d^2$  matrix defined as

$$\mathbf{P}_{d^2} = \mathbf{I}_{d^2} + \frac{E''}{2} (\mathbf{M} \otimes \mathbf{I}_d + \mathbf{I}_d \otimes \mathbf{M}), \quad (5.17)$$

and " $\otimes$ " is the Kronecker product (generalized outer product).

Applying  $\mathbf{P}_{d^2}^{-1}$  to both sides of (5.16) and subsequently reverting the vectorization, gives

$$\begin{aligned} \boldsymbol{\tau} = \eta(\boldsymbol{\tau}) & \left( \dot{\boldsymbol{\epsilon}} + \frac{E''}{E'' + 2} \left( \frac{E''}{E'' + 1} I_4(\dot{\boldsymbol{\epsilon}}) \mathbf{M} - \{\dot{\boldsymbol{\epsilon}}, \mathbf{M}\} \right) \right) \\ & - \frac{E''}{E'' + 1} \left( \frac{E'}{E''} + \frac{E' + E''}{d} \right) I_4(\boldsymbol{\tau}) \mathbf{M} + \frac{E' + E''}{d} I_4(\boldsymbol{\tau}) \mathbf{I}, \end{aligned} \quad (5.18)$$

which follows from noting that

$$\begin{aligned} \mathbf{P}_{d^2}^{-1} \text{vec}(\mathbf{M}) &= \frac{1}{E'' + 1} \text{vec}(\mathbf{M}), \\ \mathbf{P}_{d^2}^{-1} \text{vec}(\mathbf{I}) &= \text{vec}(\mathbf{I}) - \frac{E''}{E'' + 1} \text{vec}(\mathbf{M}), \\ \mathbf{P}_{d^2}^{-1} \text{vec}(\dot{\boldsymbol{\epsilon}}) &= \text{vec}(\dot{\boldsymbol{\epsilon}}) - \frac{E''}{E'' + 2} \left( \text{vec}(\{\dot{\boldsymbol{\epsilon}}, \mathbf{M}\}) + \frac{E''}{E'' + 1} I_4(\dot{\boldsymbol{\epsilon}}) \text{vec}(\mathbf{M}) \right). \end{aligned}$$

Expression (5.18) is, however, not in a closed form due to the invariants  $I_i(\boldsymbol{\tau})$  on the right-hand side depending on  $\boldsymbol{\tau}$  [note that  $\eta(\boldsymbol{\tau})$  too depends on  $I_i(\boldsymbol{\tau})$ , as defined in (5.14)]. In order to fully invert (5.18), it is thus necessary to reexpress the unknowns,  $I_i(\boldsymbol{\tau})$ , in terms of  $I_i(\dot{\boldsymbol{\epsilon}})$ , which may be achieved by calculating  $I_2(\boldsymbol{\tau}) = \text{tr}(\boldsymbol{\tau}^2)$ ,  $I_4(\boldsymbol{\tau}) = \text{tr}(\boldsymbol{\tau} \cdot \mathbf{M})$ , and  $I_5(\boldsymbol{\tau}) = \text{tr}(\boldsymbol{\tau}^2 \cdot \mathbf{M})$  using (5.18) and subsequently solving for  $I_2(\boldsymbol{\tau})$ ,  $I_4(\boldsymbol{\tau})$ , and  $I_5(\boldsymbol{\tau})$  (not shown).

In the present work, the two-dimensional relation ( $d = 2$ ) is desired for implementing in an idealized vertical-cross-section ice-flow model. Solving for the invariants with  $d = 2$  and adopting the following change of free flow parameters:

$$E_{\parallel} = 1 + E' + E'' \quad \text{and} \quad E_{\perp} = 1 + E''/2, \quad (5.19)$$

the inverse two-dimensional flow law is uncovered

$$\boldsymbol{\tau} = \eta \left( E_{\parallel}^{-1/n} \dot{\boldsymbol{\epsilon}} + \left[ E_{\perp}^{-1/n} - E_{\parallel}^{-1/n} \right] I_4 \mathbf{R} \right) \quad (5.20)$$

$$\eta = A^{-1/n} \left( E_{\parallel}^{-1/n} I_2 + 2 \left[ E_{\perp}^{-1/n} - E_{\parallel}^{-1/n} \right] I_4^2 \right)^{(1-n)/2n}, \quad (5.21)$$

where  $E_{\parallel}$  and  $E_{\perp}$  are anisotropic enhancement factors (elaborated on below), and  $\mathbf{R}(\theta) \in \mathcal{O}(2)$  is the orthogonal transformation

$$\mathbf{R}(\theta) = 2\mathbf{M} - \mathbf{I} = \begin{pmatrix} -\cos 2\theta & \sin 2\theta \\ \sin 2\theta & \cos 2\theta \end{pmatrix}, \quad (5.22)$$

which gives the reflection of a point about a line passing through the origin and extended outward at an angle  $\theta$  from the y-axis. The angle  $\theta$  here represents the symmetry-axis orientation such that

$$\mathbf{m} = (\sin \theta, \cos \theta), \quad (5.23)$$

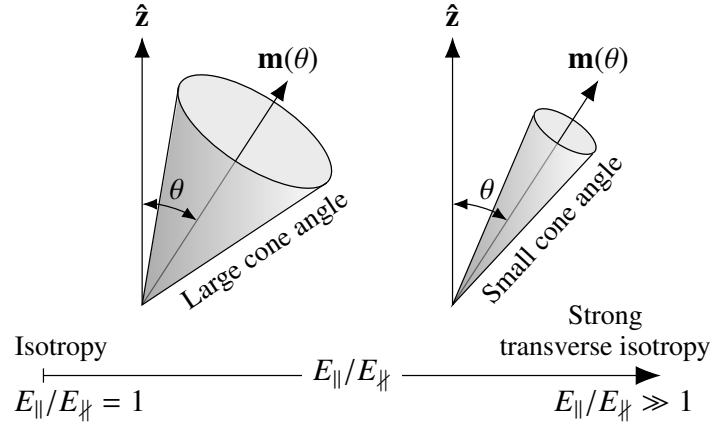


Figure 5.2: Qualitative relation between the anisotropic enhancement-factor ratio,  $E_{\parallel}/E_{\perp}$ , and the local  $\mathbf{c}$ -axis spread, the latter defined in terms of the cone-angle around the fabric symmetry-axis direction,  $\mathbf{m}(\theta)$ . The transversely isotropic flow-law reduces to Glen–Nye’s isotropic law for  $E_{\parallel}/E_{\perp} = 1$ , while the limit  $E_{\parallel}/E_{\perp} \gg 1$  corresponds to a strongly developed preferred-direction fabric (strong transverse isotropy).

and allows the fourth invariant,  $I_4$ , to be written compactly as

$$I_4(\theta) = \dot{\epsilon}_{yy} \cos 2\theta + \dot{\epsilon}_{xy} \sin 2\theta. \quad (5.24)$$

Thus, as one might expect, the rotational symmetry around  $\mathbf{m}$  in three dimensions ( $d = 3$ ) reduces to a reflection symmetry across  $\mathbf{m}$  in two dimensions ( $d = 2$ ), as represented by the reflection transformation,  $\mathbf{R}(\theta)$ .

### 5.2.2 Phenomenology of two-dimensional flow law

The two-dimensional flow law (5.20)–(5.21) collapses to Glen’s isotropic law in the special case  $E_{\parallel} = E_{\perp}$ , in which case the two enhancement factors reduce to the regular isotropic enhancement factor amending Glen’s law. The relative magnitude,  $E_{\parallel}/E_{\perp}$ , must therefore contain information about  $\mathbf{c}$ -axis *spread* around the preferred direction, with larger ratios corresponding to smaller spread (figure 5.2).

It is, meanwhile, not immediately clear how the anisotropic departure from Glen’s law manifests itself functionally. The effect of the anisotropic term may be understood by considering fabrics with the uniform orientations  $\theta = \{0^\circ, 45^\circ, 90^\circ\}$ , in which case (5.20)–(5.21) become

$$\boldsymbol{\tau} = \eta \times \begin{cases} \begin{pmatrix} E_{\perp}^{-1/n} \dot{\epsilon}_{xx} & E_{\parallel}^{-1/n} \dot{\epsilon}_{xy} \\ E_{\parallel}^{-1/n} \dot{\epsilon}_{xy} & E_{\perp}^{-1/n} \dot{\epsilon}_{yy} \end{pmatrix} & \text{for } \theta = \{0^\circ, 90^\circ\} \\ \begin{pmatrix} E_{\parallel}^{-1/n} \dot{\epsilon}_{xx} & E_{\perp}^{-1/n} \dot{\epsilon}_{xy} \\ E_{\perp}^{-1/n} \dot{\epsilon}_{xy} & E_{\parallel}^{-1/n} \dot{\epsilon}_{yy} \end{pmatrix} & \text{for } \theta = 45^\circ. \end{cases} \quad (5.25)$$

Thus, for a fabric with a vertical symmetry-axis ( $\theta = 0^\circ$ ), the shear component ( $\dot{\epsilon}_{xy}$ ) is enhanced by a factor of  $E_{\parallel}$  (to some power of  $n$ ), that is

$E_{\parallel}$  is the basal-plane (easy) glide enhancement factor,

while for a fabric axis tilting at  $\theta = 45^\circ$  the shear component ( $\dot{\epsilon}_{xy}$ ) is enhanced by a factor of  $E_{\nparallel}$  (to some power of  $n$ ), that is

$E_{\nparallel}$  is the nonbasal-plane (hard) glide enhancement factor.

The fact that  $E_{\nparallel}$  is the nonbasal, hard glide enhancement is justified by deformation experiments on single-maximum fabrics from the Dye 3 ice core where the resistance along shear planes tilting away from the fabric axis was investigated (Shoji and Langway Jr, 1985; Shoji and Langway, 1988). Specifically, it was found that shear planes oriented at  $45^\circ$  from the fabric axis were the hardest (harder than for an isotropic fabric), while shearing parallel to basal planes was the softest angle (softer than for an isotropic fabric), implying  $E_{\parallel} > 1 > E_{\nparallel}$ .

The presented form of the transversely isotropic flow law (5.20)–(5.21) is therefore particularly useful because the two new flow parameters,  $E_{\parallel}$  and  $E_{\nparallel}$ , may be interpreted in terms of deformation experiments. For small-spread single-maximum fabrics, the ratio between soft and stiff orientations has been reported to be as large as  $E_{\parallel}/E_{\nparallel} \sim 10^2$  to  $10^4$  (Shoji and Langway Jr, 1985; Shoji and Langway, 1988; Duval et al., 1983).

In addition to enhancing the shear component ( $\dot{\epsilon}_{xy}$ ), the transversely isotropic flow-law also enhances the normal components ( $\dot{\epsilon}_{xx}, \dot{\epsilon}_{yy}$ ) too, as evident from the nonzero diagonals of (5.25); that is, for nonvertical fabric axes, the basal and nonbasal glide enhancements influence the longitudinal ( $\tau_{xx}$ ) and vertical ( $\tau_{yy}$ ) normal components too.

Finally, note that when components in (5.25) transform as  $\tau_{ij} = E^{-1/n} \dot{\epsilon}_{ij}$ , the components are effectively reduced in the momentum balance for  $E^{-1/n} < 1$  (or vice-versa), implying the strain-rate solution must be enhanced relative to  $E = 1$  to overcome the suppressing factor of  $E^{-1/n}$  (or vice-versa). Thus, because of the negative enhancement exponent,  $-1/n$ , the shear component  $\dot{\epsilon}_{xy}$  solving the balance is effectively reduced as  $\theta \rightarrow 45^\circ$  if  $E_{\nparallel} < 1$ , but enhanced as  $\theta \rightarrow 0^\circ$  if  $E_{\parallel} > 1$ .

### Bounds on $E_{\parallel}$ and $E_{\nparallel}$

The anisotropic enhancement factors,  $E_{\parallel}$  and  $E_{\nparallel}$ , are thermodynamically constrained by requiring that viscous energy dissipation decreases the mechanical energy. Calculating the rate of change of energy using the momentum balance (2.2), it follows that (Landau and Lifshitz, 1959)

$$\frac{\partial}{\partial t} \int \frac{1}{2} \rho u^2 dV = - \oint (\rho C \mathbf{u} - \mathbf{u} \cdot \boldsymbol{\tau}) \cdot d\mathbf{S} - \frac{1}{2} \int \boldsymbol{\tau} : \dot{\boldsymbol{\epsilon}} dV,$$

where  $C = u^2/2 + \rho^{-1}p$  is the Bernoulli function. Extending the integral domain to include the entire fluid domain, the first integral on the right-hand side vanishes. Consequently, the enhancement factors are bound by  $\tau : \dot{\epsilon} > 0$ . Using (5.20)–(5.21), one finds (noting  $\dot{\epsilon} : \mathbf{R} = 2I_4$ )

$$\tau : \dot{\epsilon} = A^{-1/n} \left( E_{\parallel}^{-1/n} I_2 + 2 \left[ E_{\parallel\parallel}^{-1/n} - E_{\parallel}^{-1/n} \right] I_4^2 \right)^{(1+n)/2n}.$$

Since  $I_2$  and  $I_4^2$  are strictly positive, it follows that

$$E_{\parallel} \geq E_{\parallel\parallel} > 0, \quad (5.26)$$

which conforms with deformational experiments (Shoji and Langway Jr, 1985; Shoji and Langway, 1988).

### 5.3 The model

In order to investigate the influence of fabric anisotropy on transient internal layer deformation, the author developed a new two-dimensional, finite-element ice flow model for solving the momentum balance (2.3) with the transversely isotropic rheology (5.20)–(5.21). A new model is justified by the need to accurately displace material elements and their physical properties ( $A$ ,  $E_{\parallel}$ ,  $E_{\parallel\parallel}$ ,  $\theta$ ) with time, since the solution to the momentum balance depends on the exact material configuration. This is typically not the case in existing (isotropic) ice flow models, such as vertically integrated models, which address different questions. Boundaries between internal layers must therefore be represented as Lagrangian interfaces, and nonuniform material properties must too be displaced in a Lagrangian fashion — e.g.  $\theta$  which might change due to local processes and flow. Note that for isotropic layers with uniform rate-factors, only the bounding interfaces between layers need to be accurately displaced with time.

Due to the Lagrangian nature of the problem, the model is implemented as a finite-element numerical model, thereby allowing (i) interfaces between layers to be naturally defined along cell (element) edges, and (ii) physical properties to be defined on a conservative, per-cell basis. The model is written in Python and relies on FEniCS (Alnæs et al., 2015) to solve the stress balance given the external ice geometry and internal material configuration. FEniCS is an open-source computing platform for solving partial differential equations, itself relying on a collection of components equally deserving credit (Logg and Wells, 2010; Kirby and Logg, 2006; Alnæs et al., 2014; Kirby, 2004; Alnæs et al., 2009). Furthermore, the model relies on the software Gmsh for generating finite-element meshes subject to constraints such as the vertex density along internal interfaces or external boundaries. The cross-component communication, time-stepping, and fabric evolution (including the nontrivial task of correctly dissecting complicated folded layers across external mesh boundaries) is not handled by third-party software.

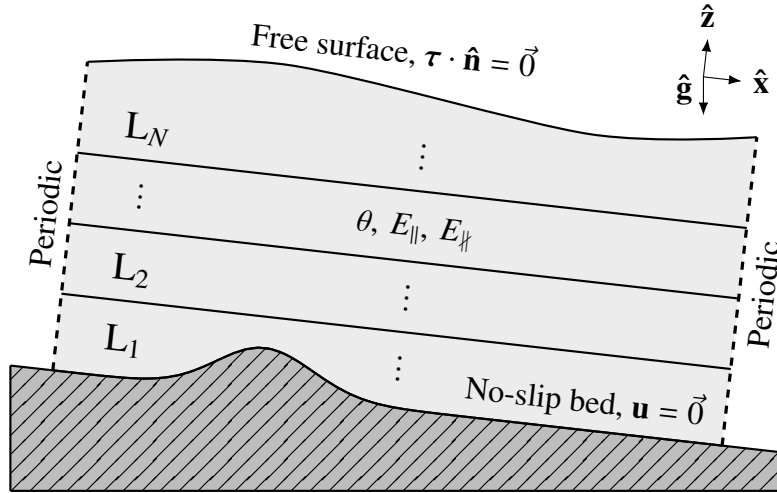


Figure 5.3: Schematical representation of the two-dimensional, Lagrangian-layered ice flow model. The model consists of  $n$  layers ( $L_1, \dots, L_n$ ), each layer having distinct, constant flow parameters  $A, E_{\parallel}, E_{\perp}$ , whereas the single-maximum direction,  $\theta$ , is spatio-temporally variable. The surface is traction-free, while the bed constitutes a no-slip interface, sloping at a constant angle with a small Gaussian bump superimposed. The left- and right-hand boundaries are assumed periodic for simplicity.

It is not a priori clear how the morphology of internal layers changes with single-maximum strength. Therefore, the present work seeks to investigate the evolution of internal layers in simplest possible terms by removing other influences that might have a significant affect. Since Stokes flows are boundary-value problems, the model considers idealized periodic left–right boundaries (figure 5.3). Furthermore, the surface is assumed traction-free (natural boundary condition), and the whole ice slab rests with a no-slip Dirichlet boundary condition on a constant-slope bed, perturbed by a small superimposed Gaussian bump to break the time-translational symmetry (figure 5.3).

The model adopts the popular triangular Taylor–Hood (mixed) finite element (Hood and Taylor, 1974) which fulfils the *inf-sup* condition for the Stokes flow problem (saddle-point problem), critical for stability and convergence (Arnold et al., 1984). Taylor–Hood elements generally consist of Lagrange elements of order  $k$  for pressure and  $k + 1$  for velocity. In the model, first- and second-order Lagrange elements ( $CG_1$  and  $CG_2$  elements) are used for pressure and velocity, respectively, while physical properties are represented on a per-cell basis using the zeroth-order discontinuous Lagrange element,  $DG_0$  (figure 5.4).

Lagrangian numerical models (unrelated to Lagrange finite elements) are unconditionally stable, implying the time-step size is in principle unrestricted. The accuracy of a transient simulation does, however, depend on the step size, which is found to be characteristically on the order of 1/1000 of a year in order to achieve convergence for flows with internal interface speeds on the order of kilometres

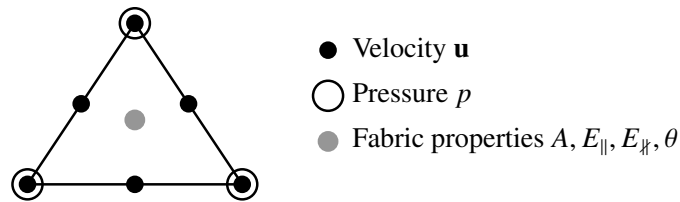


Figure 5.4: Taylor–Hood element used in the model. The element consists of triangular Lagrange elements of order 2 for velocity ( $\mathbb{CG}_2$ ) and of order 1 for pressure ( $\mathbb{CG}_1$ ). In addition, physical properties are regarded cell based and are represented using discontinuous Lagrange elements of order 0 ( $\mathbb{DG}_0$ ). The figure shows the corresponding placement of the degrees of freedom (circles).

per year. Time integration is carried out using the Euler method, and internal interfaces are updated by displacing them according to the velocity field solution. This allows an updated mesh to be generated using Gmsh by explicitly specifying the new interface positions, which are constructed under the constraint of an approximately equidistant vertex spacing along the new internal interfaces (transfinite meshing). Therefore, the accuracy of a transient simulation also depends on the chosen vertex spacing since large spacings (large cells) will tend to smooth out kinks/excursions along the interface due to transfinite meshing not necessarily including the spline-defining vertices (figure 5.5).

The fabric orientation,  $\theta$ , must evolve at the end of each time step by co-rotating with the *effective* material rotation-rate, which generally depends on both the local velocity curl and strain-rate tensor (Aravas, 1994; Gödert and Hutter, 1998; Svendsen and Hutter, 1996). As an initial step, however, this work considers fabric

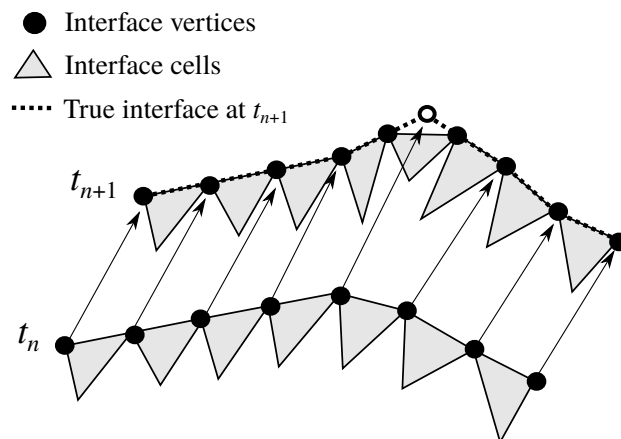


Figure 5.5: Lagrangian displacement of an internal interface, demonstrating the potential error when regridding an interface at a later time step ( $t_{n+1}$ ) by requiring approximately equidistant vertex spacing (transfinite meshing).

evolution as a function of the local velocity curl only (solid co-rotation with flow) as a prototype for how an evolving fabric might influence flow. That is

$$D_t \theta = \alpha f(\omega) \quad (5.27)$$

where  $\alpha$  is some constant between 0 and 1. Note that in this work, fabric processes such as re-crystallization etc. are neglected for simplicity.

After evolving the orientation field, it is subsequently regrided onto the mid-points of the updated mesh (DG<sub>0</sub> nodes) using a high-order cubic interpolation on a per layer basis, thus ensuring information does not unphysically cross internal layers when interpolating.

The transient problem is thus an active scalar problem in the sense that the momentum balance solution (velocity and pressure) depends on the fabric orientation,  $\theta$ , which in turn may dynamically evolve according to the local velocity structure by (5.27).

### 5.3.1 Weak formulation

The finite element method, unlike many other numerical schemes, approximates the solution to a partial differential equation (PDE) and not the equation itself. In short, the computational domain is partitioned into elements (cells) in which the solution is approximated by a linear combination of basis functions. The basis coefficients are solved for by assembling coefficient equations for each element, yielding a large system of algebraic equations. Constructing the coefficient equations requires posing the Stokes flow PDE in its *weak* or *variational form*, in contrast to the *strong form*

$$-\nabla \cdot \boldsymbol{\tau} + \nabla p = \rho \mathbf{g} \quad (5.28)$$

$$\nabla \cdot \mathbf{u} = 0. \quad (5.29)$$

While accounting for the finite element variational formulation in detail is out of scope for the present work, this section is devoted to deriving the weak form of (5.28)–(5.29) and its discretization, but leaves out the details on the coefficient equations etc.

Starting with the momentum balance (5.28) by forming the inner product with a *test function*  $\mathbf{v}$ , followed by integrating over the domain  $\Omega$  (an open subset of  $\mathbb{R}^d$  where  $d = \dim \mathbf{u}$ ), one finds

$$-\int_{\Omega} (\nabla \cdot \boldsymbol{\tau}) \cdot \mathbf{v} \, d\mathbf{x} + \int_{\Omega} (\nabla p) \cdot \mathbf{v} \, d\mathbf{x} = \int_{\Omega} \rho \mathbf{g} \cdot \mathbf{v} \, d\mathbf{x}, \quad (5.30)$$

where  $(\mathbf{u}, p) \in H_0^1(\Omega)^d \times L^2(\Omega)$  and  $\mathbf{v} \in H_0^1(\Omega)^d$ ; that is to say that  $\mathbf{u}$ ,  $\mathbf{v}$ ,  $\nabla \mathbf{u}$ ,  $\nabla \mathbf{v}$  and  $p$  are square integrable and  $p$  is defined up to a constant (Bercovier and Pironneau, 1979). The first term in (5.30) may be rewritten using the product rule

and integrating by parts, giving

$$\begin{aligned} - \int_{\Omega} (\nabla \cdot \boldsymbol{\tau}) \cdot \mathbf{v} \, d\mathbf{x} &= \int_{\Omega} [\boldsymbol{\tau} : \nabla \mathbf{v} - \nabla \cdot (\boldsymbol{\tau} \cdot \mathbf{v})] \, d\mathbf{x} \\ &= \int_{\Omega} \boldsymbol{\tau} : \nabla \mathbf{v} \, d\mathbf{x} - \int_{\partial\Omega} \mathbf{n} \cdot (\boldsymbol{\tau} \cdot \mathbf{v}) \, dS, \end{aligned} \quad (5.31)$$

where  $\partial\Omega$  is the boundary of  $\Omega$ . Similarly, the second term may be rewritten as

$$\begin{aligned} \int_{\Omega} (\nabla p) \cdot \mathbf{v} \, d\mathbf{x} &= \int_{\Omega} [\nabla \cdot (p\mathbf{v}) - p\nabla \cdot \mathbf{v}] \, d\mathbf{x} \\ &= \int_{\partial\Omega} \mathbf{n} \cdot (p\mathbf{v}) \, dS - \int_{\Omega} p\nabla \cdot \mathbf{v} \, d\mathbf{x}. \end{aligned} \quad (5.32)$$

Inserting (5.31) and (5.32) into (5.30), noting that  $\mathbf{n} \cdot (p\mathbf{v}) - \mathbf{n} \cdot (\boldsymbol{\tau} \cdot \mathbf{v}) = \mathbf{n} \cdot ([p\mathbf{I} - \boldsymbol{\tau}] \cdot \mathbf{v}) = \mathbf{n} \cdot (-\boldsymbol{\sigma} \cdot \mathbf{v}) = -\mathbf{n} \cdot \boldsymbol{\sigma} \cdot \mathbf{v}$ , and exploiting the symmetry of  $\boldsymbol{\tau}$  to rewrite  $\boldsymbol{\tau} : \nabla \mathbf{v} = 1/2(\tau_{ij} + \tau_{ji})\partial_j v_i = 1/2(\tau_{ij}\partial_j v_i + \tau_{ij}\partial_i v_j) = \boldsymbol{\tau} : (\nabla \mathbf{v} + \{\nabla \mathbf{v}\}^T)/2$ , gives

$$\begin{aligned} \int_{\Omega} \left[ \boldsymbol{\tau} : (\nabla \mathbf{v} + \{\nabla \mathbf{v}\}^T)/2 - p\nabla \cdot \mathbf{v} \right] \, d\mathbf{x} \\ - \int_{\partial\Omega} \mathbf{n} \cdot \boldsymbol{\sigma} \cdot \mathbf{v} \, dS = \int_{\Omega} \rho \mathbf{g} \cdot \mathbf{v} \, d\mathbf{x}. \end{aligned} \quad (5.33)$$

Secondly, multiplying the incompressibility (5.29) with the pressure test function,  $q \in L^2(\Omega)$  and integrating over  $\Omega$ , gives

$$\int_{\Omega} q \nabla \cdot \mathbf{u} \, d\mathbf{x} = 0. \quad (5.34)$$

Adding the two expressions (5.33) and (5.34), one finally finds

$$\begin{aligned} \int_{\Omega} \left[ \boldsymbol{\tau} : (\nabla \mathbf{v} + \{\nabla \mathbf{v}\}^T)/2 + q \nabla \cdot \mathbf{u} - p\nabla \cdot \mathbf{v} \right] \, d\mathbf{x} \\ - \int_{\partial\Omega} \mathbf{n} \cdot \boldsymbol{\sigma} \cdot \mathbf{v} \, dS = \int_{\Omega} \rho \mathbf{g} \cdot \mathbf{v} \, d\mathbf{x}, \end{aligned} \quad (5.35)$$

which is the sought after weak form. Equation (5.35) is a mixed variational form, that is a form where both  $\mathbf{u}$  and  $p$  are simultaneously approximated.

The weak form (5.35) is still a continuous problem in terms of infinite dimensional vector spaces. In order to be discretized by finite elements, the problem needs to be restated in terms of the finite dimensional spaces  $\mathbf{V}_h$  of  $H_0^1(\Omega)^d$  and  $\mathbf{Q}_h$  of  $L^2(\Omega)$ . Approximating the solution  $(\mathbf{u}, p)$  by  $(\mathbf{u}_h, p_h) \in \mathbf{V}_h \times \mathbf{Q}_h$  with basis functions  $(\phi_i, \psi_i)$  respectively [and likewise for  $(\mathbf{v}, q)$ , i.e. a Galerkin method], such that

$$\mathbf{u}_h = c_i^{(\mathbf{u})} \phi_i \quad \text{and} \quad p_h = c_i^{(p)} \psi_i,$$

allows the equations for the coefficients ( $c_i^{(u)}, c_i^{(p)}$ ) to be written as a linear system.

A convenient property of the variational approach is that test functions vanish along the parts of the boundary where the solution is known (Langtangen and Mardal, 2016). In the case of an ice flow model, the external boundary may be divided into the four parts  $\partial\Omega = \Gamma_{\text{surface}} \cup \Gamma_{\text{bed}} \cup \Gamma_{\text{left}} \cup \Gamma_{\text{right}}$ . If a no-slip condition is assumed at the glacier bed,  $\Gamma_{\text{bed}}$ , the boundary term  $\int_{\partial\Omega} \mathbf{n} \cdot \boldsymbol{\sigma} \cdot \mathbf{v} \, dS$  consequently vanishes there. Similarly, ice flow models generally assume a traction-free surface ( $\mathbf{n} \cdot \boldsymbol{\sigma} = 0$ ), implying the boundary term too vanishes at the surface,  $\Gamma_{\text{surface}}$ . Finally, in the case of periodic left/right boundaries (as in the above model), the boundary terms trivially vanish too.

## 5.4 Model setup and experiments

The aim of this study is to evaluate, in simplest possible terms, the implications of enhanced basal glide ( $E_{\parallel} > 1$ ) and suppressed nonbasal glide ( $E_{\parallel} < 1$ ) on the transient deformation of internal layers. The model is therefore configured with just three discrete layers: a single anisotropic layer sandwiched between two isotropic (Glen) layers. In addition, control simulations are also presented in which all three layers are isotropic but with a rate-factor contrast (enhancement) in the middle layer.

Although ice is a nonlinear viscous fluid with a typical flow exponent of around  $n = 3$ , the nonlinear solver has not yet been fully implemented in the model for transient simulations. In the following, all simulations are therefore conducted with  $n = 1$  (linear viscous), which can, in a sense, be considered as a low-order estimate of how nonlinear viscous ice might behave. A significant difference between the linear-viscous and the nonlinear-viscous isotropic flow law is the narrowing of the effective vertical-shear zone with increasing  $n$  because ice shear softens: the larger  $n$ , the more confined towards the bottom the shear zone is, and the larger a fraction of the (upper) ice column moves in a rigid fashion without shearing. Simulating layer deformation with  $n = 3$  might therefore exhibit stronger disturbances (due to the larger shear), but also limit the disturbances to occur only in the lower, near-bed layers.

The surface and all internal interfaces are initially assumed flat (undisturbed), and the middle layer is 100 m thick and positioned at 150 m from the bed. The bed is chosen to slope with an inclination of  $10^\circ$ , and the modelled ice slab has a uniform isotropic rate-factor of  $A = 1 \times 10^{-13} \text{ Pa}^{-1} \text{ s}^{-1}$ . The value of  $A$  was chosen such that the surface velocity approximately matches that of the corresponding nonlinear solution with  $n = 3$  with  $A = 1 \times 10^{-25} \text{ Pa}^{-3} \text{ s}^{-1}$  (corresponding to ice at approximately  $-20^\circ\text{C}$ ). The time-step is taken to be  $\Delta t = 0.004 \text{ yr}$ , the gravitational acceleration is  $g = 9.82 \text{ m s}^{-2}$ , and the density of ice is  $\rho = 917 \text{ kg m}^{-3}$ .

While the transversely isotropic flow law fully prescribes the tensorial structure of the strain-rate enhancements as a function of the single-maximum orientation,  $\theta$ , the magnitudes of the enhancement factors must contain information about  $\mathbf{c}$ -axis

#	$\alpha$	$\theta$	$E_{\parallel}$	$E_{\parallel}/E_{\nparallel}$	L2 is effectively...
1	—	—	1	1	a trace layer (indifferent from L1 and L3)
2	—	—	10	1	isotropically softened
3	—	—	0.01	1	isotropically hardened
4	0	$0^{\circ}$	10	10	vertical-shear softened
5	0	$45^{\circ}$	1	100	vertical-shear hardened
6	0.1	$\theta(t)$	1	100	nonbasal-shear hardened + evolving fabric

Table 5.1: Numerical experiments performed: experiments #1–#3 are the isotropic control experiments, whereas experiments #4–#6 are the anisotropic experiments. From left to right, the columns are respectively: the material rotation-rate fraction ( $\alpha$ ), the fabric orientation  $\theta$ , the easy (basal glide) enhancement ( $E_{\parallel}$ ),  $E_{\parallel}$  relative to the hard (nonbasal glide) enhancement ( $E_{\nparallel}$ ), and a description of how the parameter choice mechanically affects the middle layer (L2).

*spread* around the single-maximum direction. Specifically, they must vary from their largest/smallest values in the case of a strong single-maximum (small spread) and become  $E_{\parallel} = E_{\nparallel} = 1$  in the limit of isotropy (figure 5.2). The exact dependence, however, requires a micro–macro model to be accounted for. Striving to keep the problem simple, this study instead considers a constant, time-independent strong single-maximum fabric in the middle layer, layer 2 (L2). Guided by deformational tests suggesting  $E_{\parallel}/E_{\nparallel} \sim 10^2$  to  $10^4$  and  $E_{\parallel} \sim 10$  for strong single-maximum fabrics (Shoji and Langway Jr, 1985; Shoji and Langway, 1988; Duval et al., 1983), the values  $E_{\parallel}/E_{\nparallel} = 100$  and  $E_{\parallel} = 10$  were used in the following experiments.

Six different numerical experiments were conducted in total (table 5.1). Across all experiments, the top (L3) and bottom (L1) layers were kept isotropic. The configuration of the middle layer (L2) differs, however, between experiments. In the control experiments #1–#3, L2 is assumed isotropic too but with rate-factor enhancements of 1, 10 and 0.1, respectively — i.e. L2 is isotropically unenhanced, softened, and hardened compared to the surrounding layers, respectively.

In order to determine the separate effects of basal and nonbasal glide, anisotropic experiments #4–#5 systematically consider one glide type enhanced/suppressed while the other is unbiased (compared to isotropy) in the fabric configurations maximally biased towards each glide type, namely the time-independent (static), uniform fabric fields  $\theta = 0^{\circ}$  and  $\theta = 45^{\circ}$  for easy and hard glide, respectively. That is:

#4: L2 is vertical-shear softened (enhanced) uniformly: the fabric is statically maximally biased towards vertical shear by basal glide ( $\theta = 0^{\circ}$ ) with basal glide enhanced, while nonbasal glide is unbiased compared to isotropy ( $E_{\nparallel} = 1$ ),

#5: L2 is vertical-shear hardened (suppressed) uniformly: the fabric is statically

maximally biased towards vertical shear by nonbasal glide ( $\theta = 45^\circ$ ) with nonbasal glide suppressed, while basal glide is unbiased compared to isotropy ( $E_{\parallel} = 1$ ),

The corresponding enhancement factors are listed in table 5.1.

For all experiments but #6, the fabric axes do not evolve with time. In experiment #6 — which is otherwise identical to experiment #5 — the fabric field is allowed to evolve kinematically starting from  $\theta = 0^\circ$  according to the local rotation rate ( $\omega_{xy}$ ) by

$$D_t \theta = 0.1 \omega_{xy},$$

i.e.  $\alpha = 0.1$ ,  $f(\omega) = \omega_{xy}$  in (5.27). Experiment #6 thus seeks to investigate how the layer morphology with evolving (nonuniform) fabric axes might be different from that of uniform static-fabric layers. Note that experiment #6 considers the case where hard glide is suppressed in L2 while easy glide is unbiased compared to isotropy (as in experiment #5), and not oppositely (as in experiment #4), because disturbed flow is found for experiment #5.

Since no dynamic recrystallization etc. is accounted for in experiment #6,  $\theta$  will continue to increase with time due to shearing, eventually approaching  $\theta \sim 90^\circ$  and larger. Such large deviations from vertical is seldom found in ice core thin sections, and, consequently, is unlikely to be a fabric state generally realized over larger scales. The value  $\alpha = 0.1$  was therefore chosen to effectively slow down the time-scale of fabric rotation in the absence of recrystallization, thereby allowing the simulated disturbances to evolve before the fabric orientation deviates considerably from vertical.

## 5.5 Results

The left-hand panels of figures 5.6–5.9 show the L2 interface positions (black lines) at four different points in time for experiments #1, #3, #5, and #6, respectively (panels (a) showing the solution at  $t = 0$ ). Here, the downslope direction is from left to right. Note that the four times are not identical in each figure, which were chosen per experiment to illustrate the range of simulated behaviour. The yellow–red coloured contours show the corresponding strain-rate magnitudes in terms of  $I_2(\dot{\epsilon})$ , whereas the blue contours depict the regions where the vertical velocity is negative. The right-hand panels show the horizontal velocity component on the periodic boundary (dashed line in left-hand panels) compared to the initial velocity profile (full versus dotted lines).

Figure 5.6 (experiment #1) shows the unenhanced, isotropic deformation of L2 (trace layer experiment). Starting from a flat, undisturbed layer geometry [figure 5.6.(a)], this configuration leads to undulations on the upper and lower L2 interfaces that propagate throughout the simulation. The same was found for the isotropically

softened experiment (#2) and the enhanced vertical-shear experiment (#4) (not shown for brevity), but with much larger interfacial propagation speeds. In all three cases (#1,#2 and #4), the layer evolution is stable in the sense that no disturbances develop.

Figure 5.7 (experiment #3), on the other hand, shows that an isotropically hardened layer with negligible internal shear-deformation can generate some slight buckling behaviour, caused by a transverse wave being mediated.

Figure 5.8 (experiment #5) shows the simulated effect of L2 being vertical-shear hardened, in which case severe buckling develops [figure 5.8.(c,d)]. Note that in this experiment, vertical shearing is hardened relative to longitudinal and transverse deformation, unlike the isotropically hardened experiment #3 (figure 5.7). For reference, the black arrows show the (static) fabric axes orientations along the L2 interface cells.

Figure 5.8 (experiment #6) shows the simulated effect of suppressing nonbasal plane shear in L2 — similarly to experiment #5 — but with a kinematically evolving (nonstatic) fabric. For reference, the black arrows show the instantaneous fabric axes orientations along the L2 interface cells. In this experiment, severe buckling also develops, although the vertical extents are slightly smaller compared to experiment #5, and layer folding is found to occur relatively fast [figure 5.8.(d)].

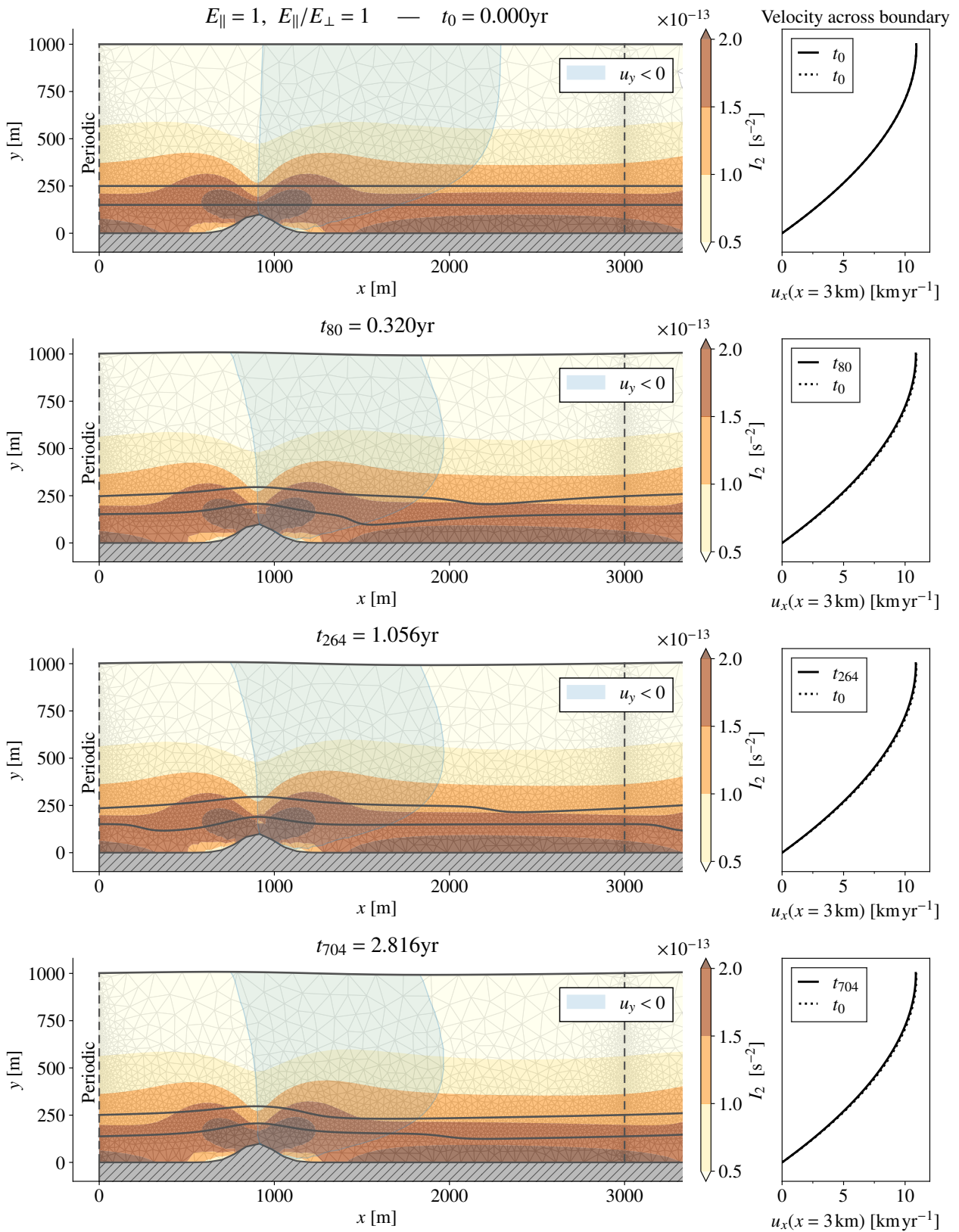


Figure 5.6: **Experiment #1.** Left-hand panels: L2 interface position (black full lines) at four points in time (a)–(d) (top–bottom) and the corresponding strain-rate magnitude in terms of  $I_2(\dot{\epsilon})$  in yellow–red contours. Right-hand panels: Instantaneous vertical profile of  $u_x$  (full line) at the periodic boundary ( $x = 3$  km) compared to at the initial profile at  $t = 0$  (dotted line).

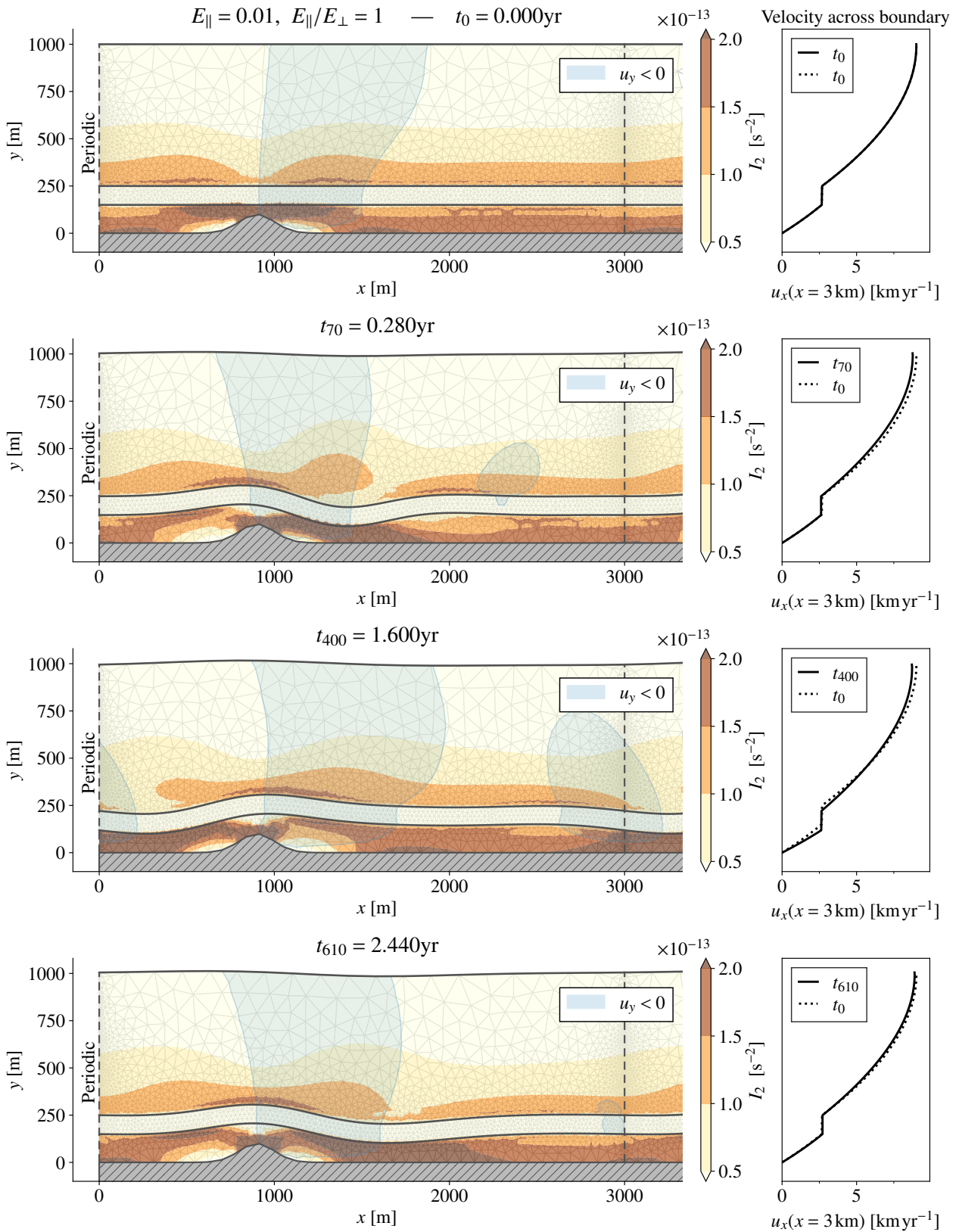


Figure 5.7: **Experiment #3.** Left-hand panels: L2 interface position (black full lines) at four points in time (a)–(d) (top–bottom) and the corresponding strain-rate magnitude in terms of  $I_2(\dot{\epsilon})$  in yellow–red contours. Right-hand panels: Instantaneous vertical profile of  $u_x$  (full line) at the periodic boundary ( $x = 3\text{ km}$ ) compared to at the initial profile at  $t = 0$  (dotted line).

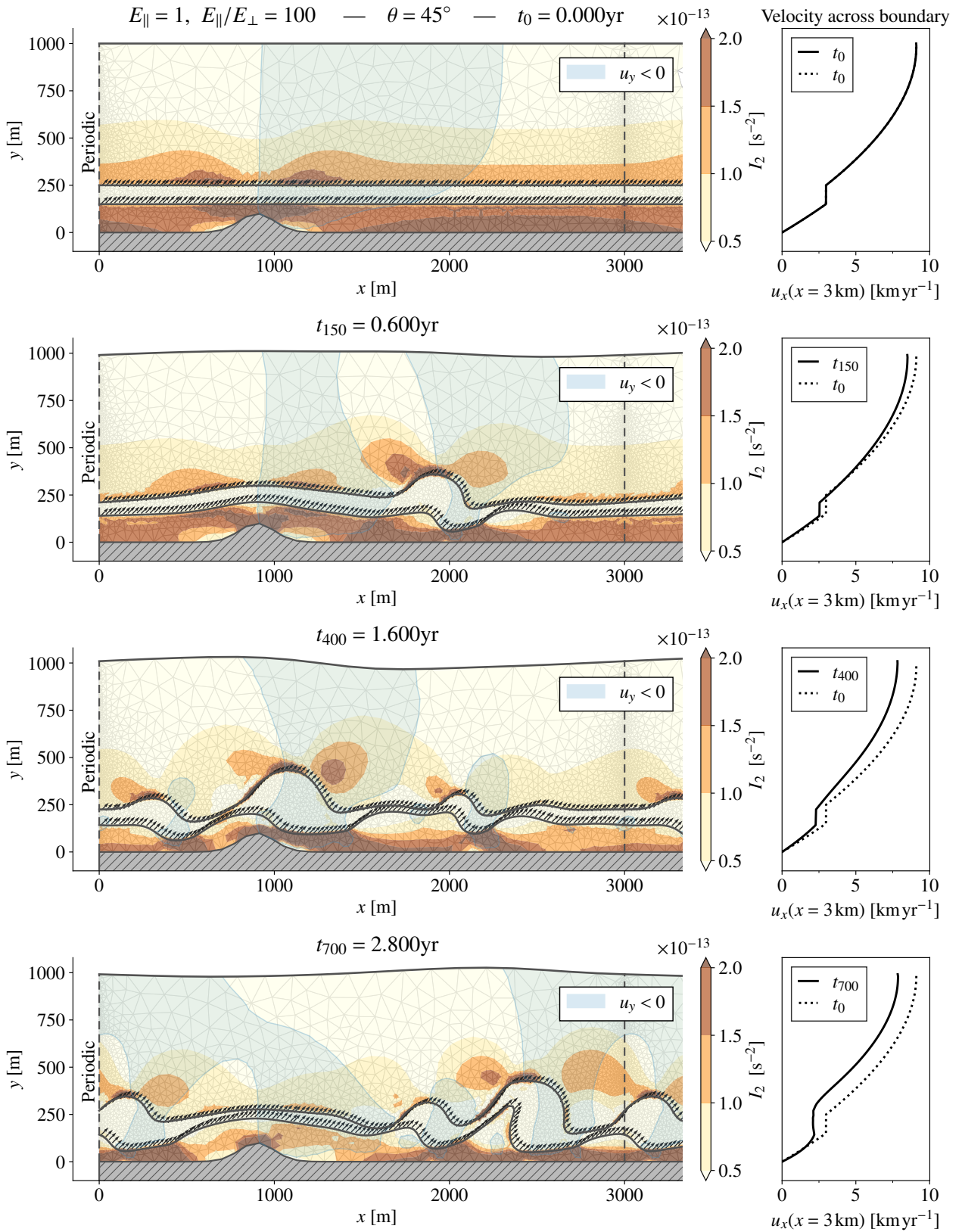


Figure 5.8: **Experiment #5.** Left-hand panels: L2 interface position (black full lines) at four points in time (a)–(d) (top–bottom) and the corresponding strain-rate magnitude in terms of  $I_2(\dot{\epsilon})$  in yellow–red contours. Right-hand panels: Instantaneous vertical profile of  $u_x$  (full line) at the periodic boundary ( $x = 3$  km) compared to at the initial profile at  $t = 0$  (dotted line). For reference, the black arrows in the left-hand panels show the instantaneous fabric axes orientations associated with the cells along the L2 interfaces.

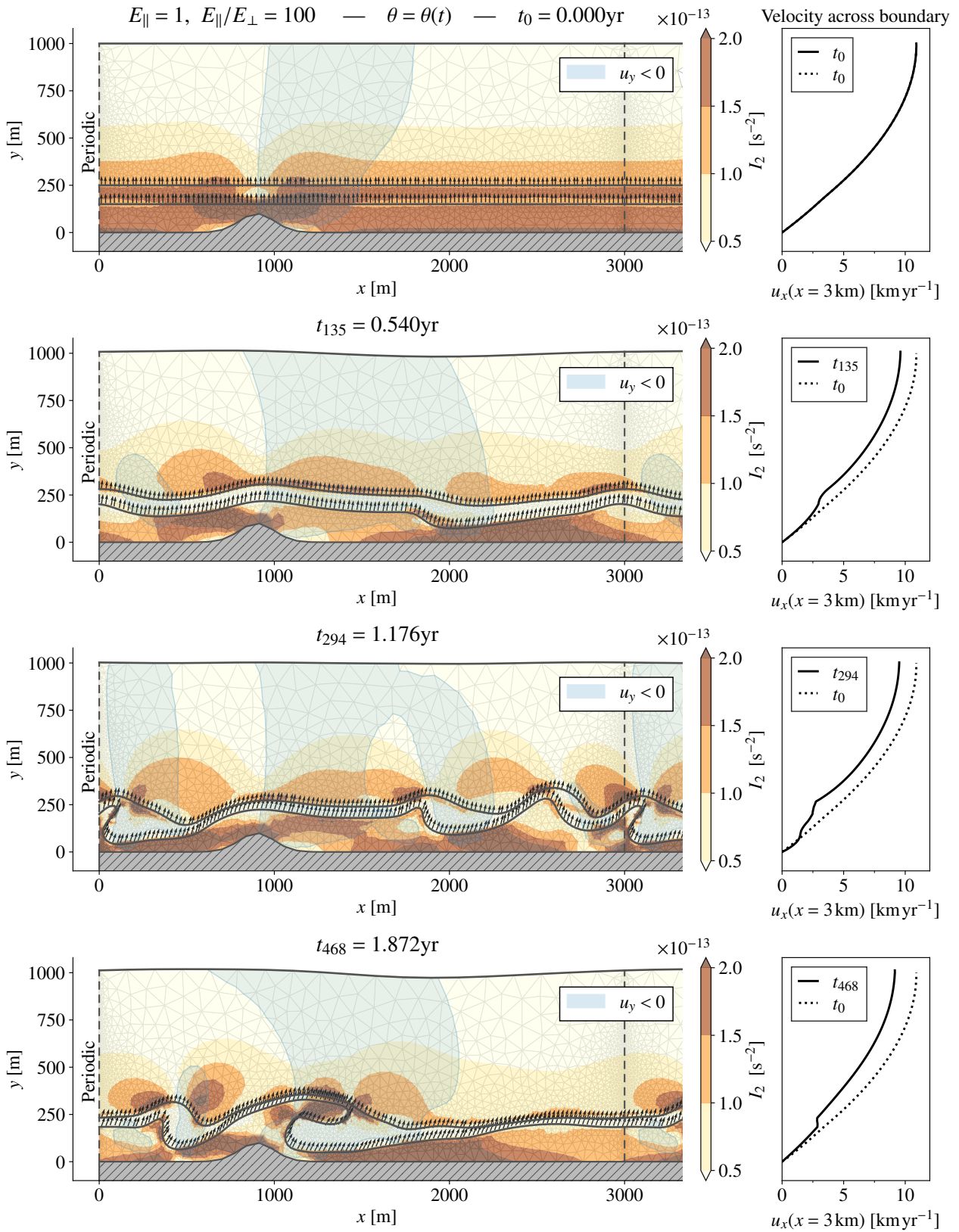


Figure 5.9: **Experiment #6.** *Left-hand panels:* L2 interface position (black full lines) at four points in time (a)–(d) (top–bottom) and the corresponding strain-rate magnitude in terms of  $I_2(\dot{\epsilon})$  in yellow–red contours. *Right-hand panels:* Instantaneous vertical profile of  $u_x$  (full line) at the periodic boundary ( $x = 3\text{ km}$ ) compared to at the initial profile at  $t = 0$  (dotted line). For reference, the black arrows in the left-hand panels show the instantaneous fabric axes orientations associated with the cells along the L2 interfaces.

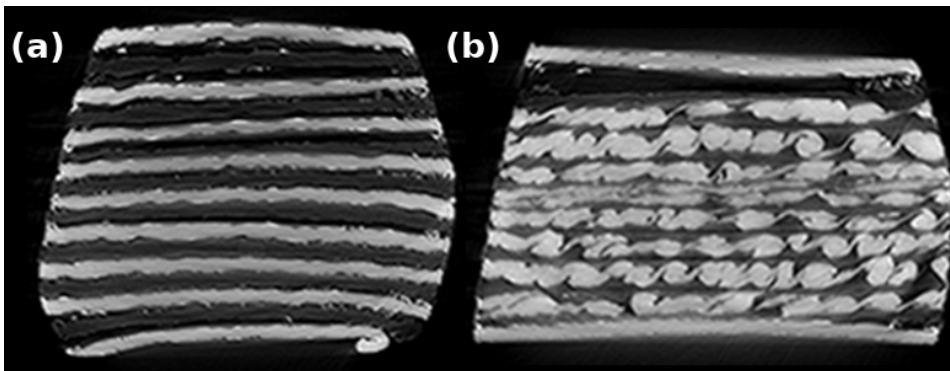


Figure 5.10: Morphological evolution of multilayered Al/Cu compound (brighter phases are Cu) consisting of stacked disks which are sheared with a 1 RPM rotation-rate parallel to the layers. The left-hand panel (a) shows the initial layer configuration, and the right-hand panel (b) shows the configuration at some later time. The images are acquired by 3D X-ray synchrotron tomography, and the horizontal scale of each panel is approximately 500  $\mu\text{m}$ . The panels are reprinted with permission by Mohsen Pouryazdan Panah under the Creative Commons Attribution 4.0 International License (<http://creativecommons.org/licenses/by/4.0>) and correspond to panels *f* and *h* of figure 2 in Pouryazdan et al. (2017).

## 5.6 Discussion and outlook

In the idealized simulations presented here, disturbances (significant buckling and folding) are found to occur only in layers opposing hard glide, sandwiched between relatively soft layers. This can be interpreted as the soft, bounding layers provide a differential drag on the upper and lower interfaces of a shear-hardened layer which then buckles if unwilling to shear. The buckling may subsequently evolve into fold if (i) the upper, concave part of a buckle finds itself in a faster flow regime, in which case the fold is trivially induced by the velocity-shear structure, or (ii) if the fabric evolves in some nonuniform way rendering the buckling unstable. The fact that disturbances evolve in mechanically hard layers was also recently found to be the case in deformation experiments and numerical simulations of multilayered metallic compounds (Pouryazdan et al., 2017). Specifically, they considered multilayered samples of Al/Cu and Ag/Cu, finding that mechanically stronger layers, embedded in thicker layers of weaker material, developed quasi-regular folds in both deformational experiments (figure 5.10) and in numerical simulations by modelling the material as a nonlinear fluid. Comparing the present simulated disturbances to their work, or, for that matter, to geological phenomena such as the folding of kilometre-thick rock layers (Fossen, 2010), the similarity is quite remarkable given the large differences in material type and spatial scale (millimetres vs. kilometre).

Vertical-shear profiles derived from the Dye 3 borehole tilt reveal that deep ice from the last glaciation (ice-age) is about 2.5 times softer for vertical shearing com-

pared to Holocene ice (present interglacial) (Dahl-Jensen and Gundestrup, 1987), and that ice-age ice generally has smaller crystals, larger dust/impurity concentrations, and a stronger single-maximum fabric. While dust and other impurities can in principle enhance deformation rates, the concentrations found in ice-age ice are generally too small to affect deformability<sup>4</sup> (Cuffey and Paterson, 2010). If crystal sizes are to play an important role in the development of internal disturbances, the numerical simulations above suggest that size distribution changes with depth might not alone be enough: If crystal sizes vary in an otherwise isotropic fabric, such an effect could be captured macroscopically by an isotropic enhancement factor. Isotropic enhancements are meanwhile found not impact the development of disturbances according to control simulations #2 and #3. If the fabric is anisotropic, however, there is no reason to believe that  $E_{\parallel}$  and  $E_{\perp}$  should have identical dependencies on crystal sizes. In this sense, crystal sizes might be relevant for explaining disturbed flow only insofar the fabric is anisotropic, in which case the enhancement ratio  $E_{\parallel}/E_{\perp}$  might be affected.

The present simulations are rather idealized in an attempt to probe the morphology of single-maximum layers. A natural next step would be to increase the realism by considering a nonlinear rheology with e.g.  $n = 3$ . Independently of  $n$ , however, it is not a priori clear whether the transition to disturbed flow is a gradual function of  $E_{\parallel}/E_{\perp}$ . It would therefore be interesting to study the deformational behaviour for different  $n$  across a range of enhancement factor ratios, and to compare with measured ice core fabrics together with radargrams adjacent to the coring sites (revealing whether the flow is disturbed or not). Moreover, experiment #6 suggests that large deviations from vertical fabric axes might not be necessary to cause disturbed flows, which could also be compared against ice core fabrics and radargrams.

Improving upon the model realism, it is not clear how the transient behaviour would be affected by initializing the model with a vertical layering based on observations. One could imagine, for example, that smoothly changing enhancement factors with depth in a many-layered configuration might lessen the susceptibility to buckling and folding because of reduced drag differences occurring between upper and lower interfaces. On the other hand, the present fabric evolution is crude and does not account for recrystallization processes. Given the difference between experiments #4, #5 and #6, a realistic account of fabric evolution might have a significant impact on the susceptibility of layers to buckle and fold.

The present work has demonstrated the usefulness of a Lagrangian layered ice-flow model in probing the morphology of internal layer disturbances, even for very idealized ice geometries. Specifically, the simulations presented here suggest that studying fabrics which suppress hard glide might provide important insight into the development of internal layer disturbances. Moreover, this work indicates

---

<sup>4</sup>Impurities may affect size distributions of crystals by (i) inhibiting growth by impeding grain-boundary migration, and (ii) increasing the dislocation density which induces the development of new grains by nucleation (Cuffey and Paterson, 2010).

that a lot might still be learned from studying how internal deformation depends on bulk, anisotropic macroscopic flow parameters, without the need to increase the realism of the fabric microstructure description using e.g. micro–macro models. For future work, one could therefore consider a more realistic internal layering as a natural next step, which may later be improved using micro–macro models once the large-scale dependence of ice flow on the macroscopic flow parameters is sufficiently understood for realistic geometries.



## **Part II**

# **Turbulent cascade dynamics**



## Chapter 6

# Hydrodynamical turbulence

Fully developed three-dimensional (3D) hydrodynamical turbulence is generally characterized by a nonlinear transfer of energy from the large forcing scale of motion (integral scale) to the small dissipative Kolmogorov scale,  $\eta$ . In the large Reynolds number (Re) limit,  $\eta \rightarrow 0$ , the forcing and dissipative scales are separated by a self-similar inertial subrange spanning many orders of magnitude. Within this subrange of inertial flow, far from both forcing and dissipation scales, energy *casades* from large scales to small scales due to inertial interactions. This cascade process may be understood in terms of the Richardson cascade picture (figure 6.1): large vortical flow structures, or *eddies*, break up into smaller ones, passing on their energy, which in turn break up into smaller ones, and so on until the characteristic eddy sizes reach the dissipation scale where viscous drag acts as an energy sink by transforming mechanical (kinetic) energy into heat. In a statistical steady state, the average *energy injection rate* (pumping),  $\varepsilon$ , therefore matches the average dissipation rate. Understanding the mechanisms behind this cascade of energy is central to the study of turbulence.

In two-dimensional (2D) turbulence, however, the energy cascade is *reversed*, synonymous to an *inverse* cascade, implying energy cascades upscale to ever larger scales until some large-scale drag effectively removes energy (figure 6.1). By considering the rate of change of energy in the Navier–Stokes equation (NSE), the reversal in 2D may be explained by the existence of *enstrophy*, another quadratic invariant besides energy, which effectively blocks the forward cascade of energy (Kraichnan, 1967, 1971). As a consequence, and partly because the NSE has notoriously resisted analytical analysis, quadratic invariants play a fundamental role in the understanding of turbulent cascade dynamics, which are central to studies #3 and #4 of this thesis.

Due to the cross-scale nature of turbulent fluid interactions, much literature focuses on the dynamics of turbulence in spectral space instead of real space. This has the advantage of providing a natural scale separation in terms of wavenumbers, albeit not perfect. Turbulent velocity fields consist of collections of compact vortical structures (eddies), self-advecting in a chaotic manner, which is different from a col-

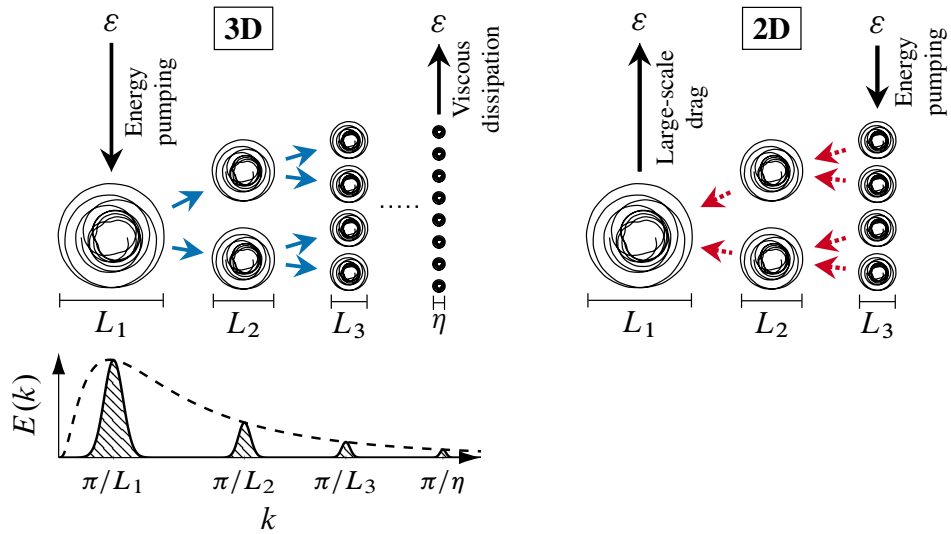


Figure 6.1: The Richardson energy cascade picture of turbulence. In three-dimensional (3D) turbulence (left figure), energy cascades from the large forcing scale of motion to the small energy dissipation scale (Kolmogorov scale,  $\eta$ ), while in two-dimensional (2D) turbulence (Kraichnan picture, right panel), energy cascades reversely to larger scales where large-scale drag effectively acts as an energy sink. The cascade picture involves eddies breaking up in 3D, or merging in 2D, within the inertial subrange, defined as the range of scales far from the forcing and dissipation scales in which only inertial interactions are present. The lower left axis shows schematically the spectral energy density of eddies as a function of their characteristic size,  $L$ , suggesting the spectral decomposition provides a useful (approximate) separation of scales of motion.

lections of waves (Davidson, 2004). However, by considering the energy density of a single eddy as schematically shown in figure 6.1 (lower left axis), the distribution is relatively narrowly defined around the inverse characteristic eddy size (Davidson, 2004). In this sense, considering spectral turbulence dynamics instead of real-space dynamics therefore proves a reasonable, but not perfect, separation of scales useful for studying the cross-scale dynamics of turbulent cascades.

In the following sections, background essential to studies #3 and #4 is briefly introduced, specifically the existence of quadratic quantities, triad dynamics, the spectral-helical decomposition, and shell models of turbulence.

## 6.1 Real-space invariants

Motivated by the Richardson energy cascade picture, consider the rate of change of kinetic energy,  $E = 1/2 \int u_i u_i \, dx$ , by calculating  $D_t E$  using the NSE (2.8) plus some external forcing,  $f_i$ . If the domain is periodic or has closed boundaries, all divergence terms vanish when applying the divergence theorem, and the rate of

change (the *energy equation*) becomes

$$D_t E = -\nu Z + F_E, \quad (6.1)$$

where the energy pumping is defined as  $F_E = \int u_i f_i \, d\mathbf{x}$ , enstrophy is defined as  $Z = \int \omega_i \omega_i \, d\mathbf{x}$  (vorticity squared), and  $\omega_i(\mathbf{x}) = (\nabla \times \mathbf{u}(\mathbf{x}))_i = \epsilon_{ijk} \partial_j u_k(\mathbf{x})$  is the vorticity ( $\epsilon_{ijk}$  being the Levi-Civita symbol). Thus, in a steady state, the energy pumping must be balanced by the viscosity,  $\nu$ , times enstrophy. With increasing Reynolds number (decreasing  $\nu$ ), enstrophy must therefore grow in order to balance the forcing, which is achieved by extending the inertial range, thereby allowing smaller-scale velocity gradients to be resolved.

By applying the curl to the NSE, one obtains the vorticity equation from which the rate of change of  $Z$  can in turn be derived by multiplying with  $\omega_i$  on both sides of the vorticity equation and integrating over the fluid domain, giving (the *enstrophy equation*)

$$D_t Z/2 = \int \omega_i \omega_j S_{ij} \, d\mathbf{x} - \nu \int |\epsilon_{ijk} \partial_j \omega_k|^2 \, d\mathbf{x} + F_Z. \quad (6.2)$$

The strain-rate tensor (2.5) is here denoted  $S_{ij}$ , and the enstrophy pumping is defined as  $F_Z = \int \omega_i \epsilon_{ijk} \partial_j f_k \, d\mathbf{x}$ . From (6.2), it follows that enstrophy may change in the inviscid ( $\nu = 0$ ), force-free limit by the vortex stretching/bending term,  $\int \omega_i \omega_j S_{ij} \, d\mathbf{x}$ , due to straining of the velocity field. In 2D turbulence, however, the stretching and bending term can be shown to be absent. Consequently, enstrophy is also inviscidly conserved (like energy) and can only grow by increased pumping (forcing). Enstrophy can therefore not grow with increasing Reynolds number (decreasing  $\nu$ ) for the steady state of (6.1) to be fulfilled. Instead, energy cascades reversely to larger scales, while enstrophy cascades down scale (figure 6.2) (Kraichnan, 1967, 1971).

Finally, a third hydrodynamical inviscid invariant, helicity, also exists, which was only relatively recently identified (Brissaud et al., 1973; André and Lesieur, 1977). Helicity is defined as the inner product between velocity and vorticity,  $H = \int u_i \omega_i \, d\mathbf{x}$ , and is related to the flow *chirality* (handedness). Applying the NSE and vorticity equation to the definition of  $H$ , the rate of change of helicity is given by (assuming periodic or closed boundaries)

$$D_t H/2 = -\nu \int (\partial_j u_i)(\partial_j \omega_i) \, d\mathbf{x} + F_H, \quad (6.3)$$

where the helicity pumping is defined as  $F_H = 1/2 \int (\omega_i f_i + \omega_i \epsilon_{ijk} \partial_j f_k) \, d\mathbf{x}$ . Note that helicity has two important properties relevant in the following: (i) unlike energy and enstrophy, helicity is not sign-definite, and (ii) helicity is identically zero in 2D since vorticity is always perpendicular to the plane of flow.

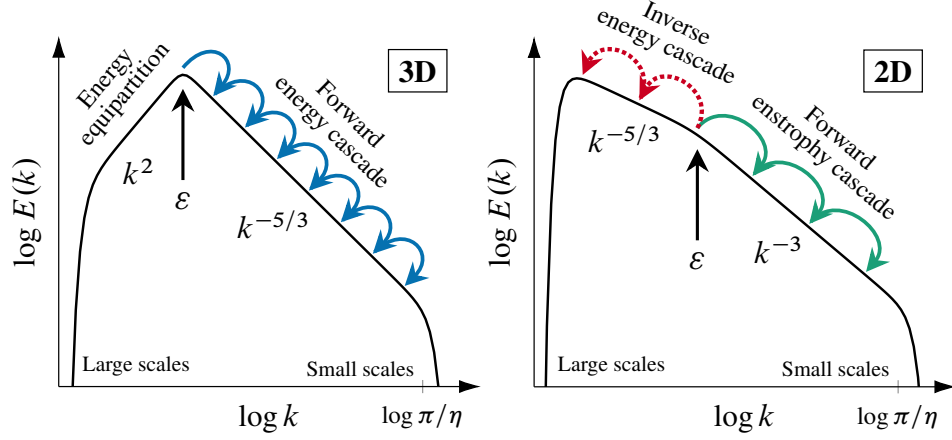


Figure 6.2: Ideal time-averaged energy spectra,  $E(k)$ , in 3D (left) and 2D (right), showing the average energy and enstrophy cascade directions relative to the energy pumping (forcing) scale (black arrow). Note that small  $k$  correspond to large spatial scales and vice-versa. The scaling exponents follow from a Kolmogorov "K41" (Kolmogorov, 1941a,b) dimensional analysis for both the energy ( $k^{-5/3}$ ) (Rose and Sulem, 1978; Frisch, 1995) and enstrophy ( $k^{-3}$ ) (Kraichnan, 1967; Batchelor, 1969) inertial ranges.

## 6.2 Spectral-space dynamics

The dynamics of turbulence in spectral space are obtained by applying the velocity field Fourier transform pair

$$u_i(\mathbf{k}) = (2\pi)^{-3} \int u_i(\mathbf{x}) e^{-i\mathbf{k}\cdot\mathbf{x}} d\mathbf{x} \quad \text{and} \quad u_i(\mathbf{x}) = \int u_i(\mathbf{k}) e^{i\mathbf{k}\cdot\mathbf{x}} d\mathbf{k} \quad (6.4)$$

to the NSE and the incompressibility constraint. Note that factors of  $i$  are here the imaginary unit, not to be confused with component indices (subscripts) of the velocity field, e.g.  $u_i(\mathbf{k})$ .

In spectral space, incompressibility,  $\partial_i u_i(\mathbf{x}) = 0$ , translates into  $\int e^{-i\mathbf{k}\cdot\mathbf{x}} \partial_i \int u_i(\mathbf{k}') e^{i\mathbf{k}'\cdot\mathbf{x}} d\mathbf{k}' d\mathbf{x} = 0$ , implying

$$k_i u_i(\mathbf{k}) = 0, \quad (6.5)$$

where the identity  $\delta(\mathbf{k} - \mathbf{k}') = (2\pi)^{-3} \int \exp(i(\mathbf{k} - \mathbf{k}') \cdot \mathbf{x}) d\mathbf{x}$  was used. That is, the velocity components are orthogonal to their wave vectors.

For the NSE, the spectral-space version becomes (normalizing units such that  $\rho = 1$ ) (Kraichnan and Montgomery, 1980; Ditlevsen, 2010)

$$(\partial_t + \nu k^2) u_i(\mathbf{k}) = i \iint_{\mathbf{k}+\mathbf{k}'+\mathbf{k}''=0} \left( \delta_{il} - \frac{k_i k_l}{k^2} \right) k_j'' u_j^*(\mathbf{k}') u_l^*(\mathbf{k}'') d\mathbf{k}' d\mathbf{k}'' + f_i(\mathbf{k}), \quad (6.6)$$

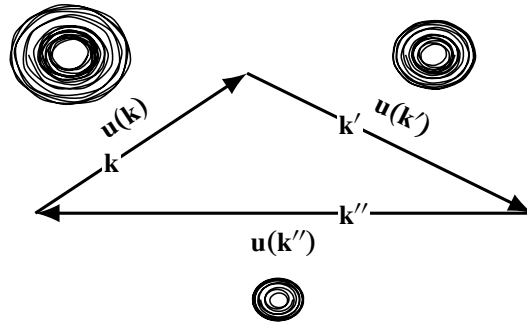


Figure 6.3: A triad of waves  $\{\mathbf{k}, \mathbf{k}', \mathbf{k}''\}$  and the spectral velocity components  $\{u_i(\mathbf{k}), u_j(\mathbf{k}'), u_l(\mathbf{k}'')\}$  involved in the corresponding triad interaction. For reference, vortices are drawn adjacent to each leg, schematically illustrating the (approximate) inverse relationship between wavenumber and characteristic eddy size.

using Parseval's identity  $u_i(-\mathbf{k}) = u_i^*(\mathbf{k})$ , and where  $p(\mathbf{k})$  has conveniently been written in terms of  $u_i(\mathbf{k})$  by taking the divergence of the NSE [giving  $\partial_{ii} p(\mathbf{x}) = -\partial_i(u_j(\mathbf{x})\partial_j u_i(\mathbf{x}))$ ] and Fourier transforming the result.

From (6.6), the evolution of a given spectral velocity component,  $u_i(\mathbf{k})$ , is governed by the sum over all three-wave interactions, or *triad interactions*, between velocity components  $\{u_i(\mathbf{k}), u_j(\mathbf{k}'), u_l(\mathbf{k}'')\}$  given that their wave vectors fulfil  $\mathbf{k} + \mathbf{k}' + \mathbf{k}'' = 0$  (triangles in spectral space, figure 6.3). Studying turbulent cascade dynamics in spectral space therefore amounts to studying the behaviour of triad interactions, such as how triad interactions of different (triangular) geometries contribute to the energy and helicity cascades (or enstrophy cascade in 2D). While the forward energy cascade in 3D is dominated by local<sup>1</sup> triad interactions (Batchelor, 1953), the 2D inverse energy cascade is dominated by nonlocal<sup>2</sup> interactions

<sup>1</sup>Wavenumbers of approximately similar size, i.e. approximately equilateral triangles.

<sup>2</sup>The smallest wavenumber being less than one-fifth the middle wavenumber.

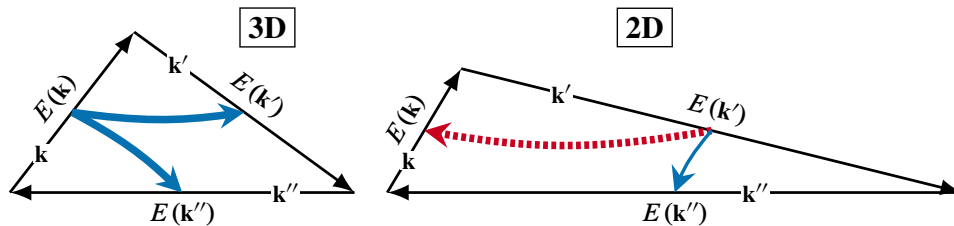


Figure 6.4: Mean energy transfers between triad components (legs) in 3D (left) and 2D (right). In 3D, local interactions are predominantly responsible for the (forward) energy cascade (Batchelor, 1953), whereas in 2D, nonlocal interactions are predominantly responsible for the (reverse) energy cascade (Kraichnan, 1971). The component-wise energies are defined as  $E(\mathbf{k}) = u_i(\mathbf{k})u_i^*(\mathbf{k})/2$ . Solid blue (dashed red) arrows denote mean forward (reverse) energy transfers, while thick (thin) arrows represent dominant (subordinate) transfers.

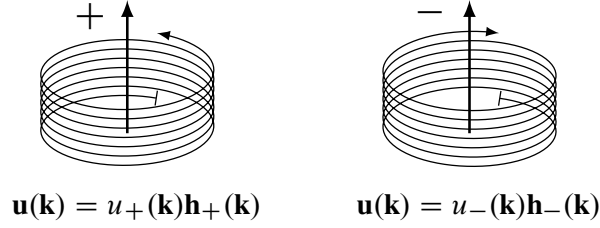


Figure 6.5: Positive (left) and negative (right) helical flows, defined as flows parallel or antiparallel to the local curl.

(Kraichnan, 1971) and is bidirectional (Fjørtoft, 1953; Batchelor, 1953; Kraichnan, 1967; Kraichnan and Montgomery, 1980) — implying energy is transferred from the middle wave mode into both the larger mode (dominant transfer) and smaller mode (subordinate transfer) (Kraichnan, 1967; Kraichnan and Montgomery, 1980) (figure 6.4).

### 6.3 Spectral–helical decomposition

In literature, the spectral-helical decomposition has proven particularly fruitful for understanding the role played by helicity and its relation to enstrophy in 2D. The helical decomposition exploits spectral incompressibility,  $\mathbf{k} \cdot \mathbf{u}(\mathbf{k})$ , by decomposing  $\mathbf{u}(\mathbf{k})$  onto two orthogonal basis modes,  $\mathbf{h}_+(\mathbf{k})$  and  $\mathbf{h}_-(\mathbf{k})$ , that is

$$\mathbf{u}(\mathbf{k}) = u_+(\mathbf{k})\mathbf{h}_+(\mathbf{k}) + u_-(\mathbf{k})\mathbf{h}_-(\mathbf{k}), \quad (6.7)$$

which are simultaneously also eigen modes of the (spectral) curl operator,  $i\mathbf{k} \times (\cdot)$ .

In real space, helicity is defined as  $H = \int \mathbf{u}(\mathbf{x}) \cdot \nabla \times \mathbf{u}(\mathbf{x}) \, d\mathbf{x}$ , and a flow is characterized as maximally positive (negative) helical if  $\mathbf{u}(\mathbf{k})$  is parallel (antiparallel) to  $\nabla \times \mathbf{u}(\mathbf{k})$  (figure 6.5). In this sense, decomposing  $\mathbf{u}(\mathbf{k})$  onto curl eigen modes is particularly advantageous since any maximally positive or negative helical flow is given entirely in terms of one basis mode, e.g.  $\mathbf{u}(\mathbf{k}) = u_+(\mathbf{k})\mathbf{h}_+(\mathbf{k})$  or  $\mathbf{u}(\mathbf{k}) = u_-(\mathbf{k})\mathbf{h}_-(\mathbf{k})$  (figure 6.5).

Waleffe (1992) showed that  $\mathbf{h}_s(\mathbf{k}) = i s \hat{\mathbf{i}}(\mathbf{k}) + \hat{\mathbf{j}}(\mathbf{k})$  is exactly such a curl eigen basis if  $\hat{\mathbf{i}}(\mathbf{k}) = \mathbf{k} \times \mathbf{r} / |\mathbf{k} \times \mathbf{r}|$  and  $\hat{\mathbf{j}}(\mathbf{k}) = -\hat{\mathbf{k}}(\mathbf{k}) \times \hat{\mathbf{i}}(\mathbf{k})$ , where  $\mathbf{r}$  is an arbitrary vector and  $s = \pm$  is a sign coefficient, in which case the eigen-value is  $sk$  [i.e.  $i\mathbf{k} \times \mathbf{h}_s(\mathbf{k}) = sk\mathbf{h}_s(\mathbf{k})$ ]. In addition to  $\mathbf{k} \cdot \mathbf{h}_s(\mathbf{k}) = 0$  by definition, the basis has other useful properties such as  $\mathbf{h}_s^*(\mathbf{k}) = \mathbf{h}_s(-\mathbf{k}) = \mathbf{h}_{-s}(\mathbf{k})$  and  $\mathbf{h}_s(\mathbf{k}) \cdot \mathbf{h}_t^*(\mathbf{k}) = 2\delta_{st}$ , which ensures the reality of  $\mathbf{u}(\mathbf{x})$  and leads to the particularly simple expressions for the spectral densities of energy, helicity and enstrophy, respectively

$$\begin{aligned} E(\mathbf{k}) &= \mathbf{u}(\mathbf{k}) \cdot \mathbf{u}^*(\mathbf{k})/2 = (|u_+(\mathbf{k})|^2 + |u_-(\mathbf{k})|^2)/2 \\ H(\mathbf{k}) &= \mathbf{u}(\mathbf{k}) \cdot \boldsymbol{\omega}^*(\mathbf{k}) = k(|u_+(\mathbf{k})|^2 - |u_-(\mathbf{k})|^2) \\ Z(\mathbf{k}) &= \boldsymbol{\omega}(\mathbf{k}) \cdot \boldsymbol{\omega}^*(\mathbf{k}) = k^2|u_+(\mathbf{k})|^2 + |u_-(\mathbf{k})|^2. \end{aligned}$$

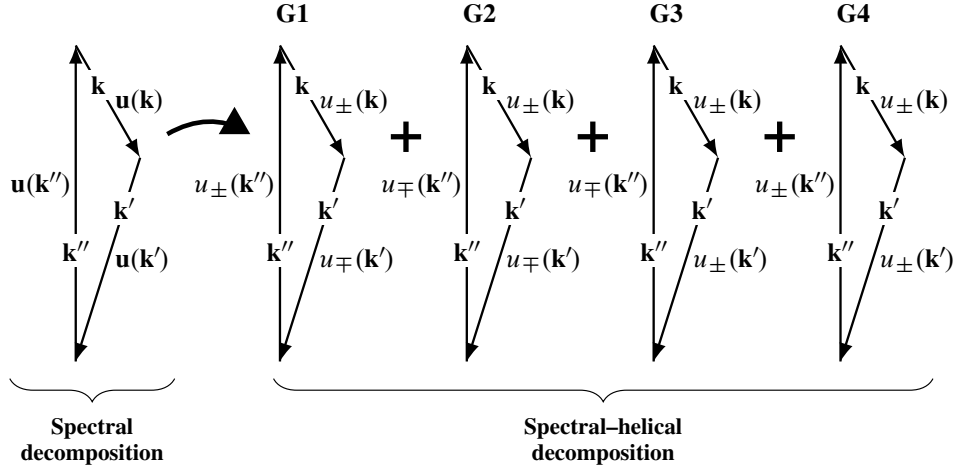


Figure 6.6: The eight helical triad interactions reduce to four groups (G1–G4) when sorting against shared coupling coefficients.

That is, the spectral densities are given entirely in terms of the positive and negative helical energy densities,  $|u_+(\mathbf{k})|^2$  and  $|u_-(\mathbf{k})|^2$ .

In the helical basis, the two helical velocity components,  $u_+(\mathbf{k})$  and  $u_-(\mathbf{k})$  ( $s = \pm$ ), are related to the regular spectral components by  $u_s(\mathbf{k}) = 1/2 \mathbf{h}_s^*(\mathbf{k}) \cdot \mathbf{u}(\mathbf{k})$  using the above basis identities. The *spectral-helical NSE* directly follows by calculating

$$\partial_t u_s(\mathbf{k}) = 1/2 \mathbf{h}_s^*(\mathbf{k}) \cdot \partial_t \mathbf{u}(\mathbf{k}), \quad (6.8)$$

where  $\partial_t \mathbf{u}(\mathbf{k}) = \int \partial_t \mathbf{u}(\mathbf{x}) e^{-i\mathbf{k} \cdot \mathbf{x}} d\mathbf{x}$ . Instead of inserting the real-space NSE given by (2.8), an alternative symmetric form is particularly convenient: invoking the vector calculus identity  $(\mathbf{u}(\mathbf{x}) \cdot \nabla) \mathbf{u}(\mathbf{x}) = \nabla u^2(\mathbf{x})/2 - \mathbf{u}(\mathbf{x}) \times (\nabla \times \mathbf{u}(\mathbf{x}))$  and symmetrizing  $\boldsymbol{\omega}(\mathbf{x}) \times \mathbf{u}(\mathbf{x}) = \frac{1}{2} (\boldsymbol{\omega}(\mathbf{x}) \times \mathbf{u}(\mathbf{x}) - \mathbf{u}(\mathbf{x}) \times \boldsymbol{\omega}(\mathbf{x}))$ , the real-space NSE may be written as

$$(\partial_t + \nu \nabla^2) \mathbf{u}(\mathbf{x}) = -\nabla C(\mathbf{x}) - \frac{1}{2} (\boldsymbol{\omega}(\mathbf{x}) \times \mathbf{u}(\mathbf{x}) - \mathbf{u}(\mathbf{x}) \times \boldsymbol{\omega}(\mathbf{x})), \quad (6.9)$$

where  $C(\mathbf{x}) = \rho^{-1} p(\mathbf{x}) + u^2(\mathbf{x})/2$  is the Bernoulli function, and vorticity is by definition  $\boldsymbol{\omega}(\mathbf{x}) = \nabla \times \mathbf{u}(\mathbf{x})$ .

Fourier transforming (6.9) and inserting the result into (6.8), the helically decomposed NSE (spectral-helical NSE) is uncovered (Waleffe, 1992)

$$(\partial_t + \nu k^2) u_s(\mathbf{k}) = -1/4 \iint_{\mathbf{k}+\mathbf{k}'+\mathbf{k}''=0} \sum_{s',s''} (s'k' - s''k'') g u_{s'}^*(\mathbf{k}') u_{s''}^*(\mathbf{k}'') d\mathbf{k}' d\mathbf{k}'', \quad (6.10)$$

where

$$g = \mathbf{h}_{s'}^*(\mathbf{k}') \times \mathbf{h}_{s''}^*(\mathbf{k}'') \cdot \mathbf{h}_s^*(\mathbf{k}) \quad (6.11)$$

is a factor that depends on both triad shape and orientation (see section below on coupling weights), and  $(s'k' - s''k'')$   $g$  is the effective triad coupling weight.

Importantly, the spectral-helical NSE (6.10) differs from the ordinary spectral NSE (6.6) in that each triad interactions is split into  $2^3 = 8$  triad sub-interactions between helical velocity components, as indicated by the inner sum over helical signs  $\{s, s', s''\}$  in (6.10). By sorting against shared coupling coefficients, four *groups* of sub-interactions emerge (figure 6.6):

$$\{s, s', s''\} = \pm\{+, -, +\}, \pm\{+, -, -\}, \pm\{+, +, -\}, \pm\{+, +, +\},$$

hereafter referred to as G1–G4, respectively. The spectral-helical NSE (6.10) thus has the cross-helical triad dynamics explicitly resolved, which is the starting point in studies #3 and #4.

### G1–G4 triad behaviours

Isolating terms involving only a single triad of waves,  $\{\mathbf{k}, \mathbf{k}', \mathbf{k}''\}$ , in the discrete form of the spectral–helical NSE (6.10), one finds (using the cyclic property of  $g$ )

$$\begin{aligned} \dot{u}_s &= (s'k' - s''k'') g u_{s'}^* u_{s''}^* \\ \dot{u}_{s'} &= (s''k'' - sk) g u_{s''}^* u_s^* , \\ \dot{u}_{s''} &= (sk - s'k') g u_s^* u_{s'}^* \end{aligned} \quad (6.12)$$

where the compact notation for time derivatives,  $\dot{u}_s = d_t u_s(\mathbf{k})$ ,  $\dot{u}_{s'} = d_t u_{s'}(\mathbf{k}')$  and  $\dot{u}_{s''} = d_t u_{s''}(\mathbf{k}'')$ , is adopted. Note that the cyclic symmetry of (6.12) implies  $k \leq k' \leq k''$  can be assumed without loss of generality. Multiplying by  $u_s^*$ ,  $u_{s'}^*$  and  $u_{s''}^*$  in the three equations (6.12), respectively, it follows that each triad interaction conserves energy, and similarly helicity by multiplication of  $sk u_s^*$ ,  $s'k' u_{s'}^*$  and  $s''k'' u_{s''}^*$ , respectively. While the energy fluxes between the three triad legs (velocity components) are fixed and determined by the coefficients  $(s'k' - s''k'')$ ,  $(s''k'' - sk)$ , and  $(sk - s'k')$  in (6.12), the average energy-flux *direction* (to/from a leg) depends on the sign of the average triple-correlator  $\langle u_s^* u_{s'}^* u_{s''}^* \rangle + \text{c.c.}$  which is unknown.

Waleffe (1992) suggested that the leg-to-leg transfers in G1–G4 triads may be determined by a linear stability analysis of the steady solutions

$$\{u_s, u_{s'}, u_{s''}\} = \{U_0, 0, 0\}, \{0, U_0, 0\}, \{0, 0, U_0\},$$

using (6.12), where  $U_0$  is some initial value. That is, adding infinitesimal perturbations to the two energyless modes of each steady state, the linear stability of the velocity components may be assessed. In the case of  $\{u_s, u_{s'}, u_{s''}\} = \{U_0, 0, 0\}$ , for

example, the componentwise time-derivatives become

$$\begin{aligned} & \begin{cases} \dot{u}_s = 0, \\ \dot{u}_{s'} = (s''k'' - sk)gu_{s''}^*U_0^* \\ \dot{u}_{s''} = (sk - s'k')gU_0^*u_{s'}^* \end{cases} \\ \implies & \begin{cases} \ddot{u}_{s'} = (s''k'' - sk)(sk - s'k')|g||U_0|u_{s'} \\ \ddot{u}_{s''} = (s''k'' - sk)(sk - s'k')|g||U_0|u_{s''} \end{cases} . \end{aligned}$$

The second-order derivatives thus imply exponential growth whenever the coefficient  $(s''k'' - sk)(sk - s'k')$  is greater than zero. Similarly, the two other states predict exponential growth for legs  $\{u_s, u_{s''}\}$  and  $\{u_s, u_{s'}\}$  whenever  $(sk - s'k')(s'k' - s''k'') > 0$  and  $(s'k' - s''k'')(s''k'' - sk) > 0$ , respectively. Based on this observation, Waleffe (1992) suggested that energy, on average, flows out of the most unstable mode and into the other two, which coincides with the mode having the largest absolute coefficient value in (6.12). From a detailed analysis, it follows that the smallest leg (largest scale) is unstable in G1 and G3 interactions, thus contributing exclusively to a forward energy cascade (denoted F-class interactions), while in G2 and G4 interactions the middle leg is unstable, thus partly contributing to a reverse energy cascade (denoted R-class interactions). For G2 interactions, however, Waleffe (1992) showed that the dominant transfer might change from being forward (middle leg to largest leg) to reverse (middle leg to smallest leg) depending on triad geometry.

The predictions from a linear stability analysis are summarized in figure 6.7, showing the G1–G4 triad behaviours (leg-to-leg transfers) and the corresponding spectra based on scaling arguments.

The linear stability analysis and the role played by helicity is the focus in study #3 where a simple energy cascade model (shell model) is introduced. The model is used to test numerically whether the linear stability predictions carry over when G1–G4 triads are coupled as the NSE prescribes. In study #4, a novel explanation for the split forward/reverse cascade of G2 triads (figure 6.7 lower plots) is proposed in terms of a new quadratic invariant in analogy to enstrophy in 2D, and the behaviour near the transition geometries  $k'/k = 3.6$  is investigated numerically.

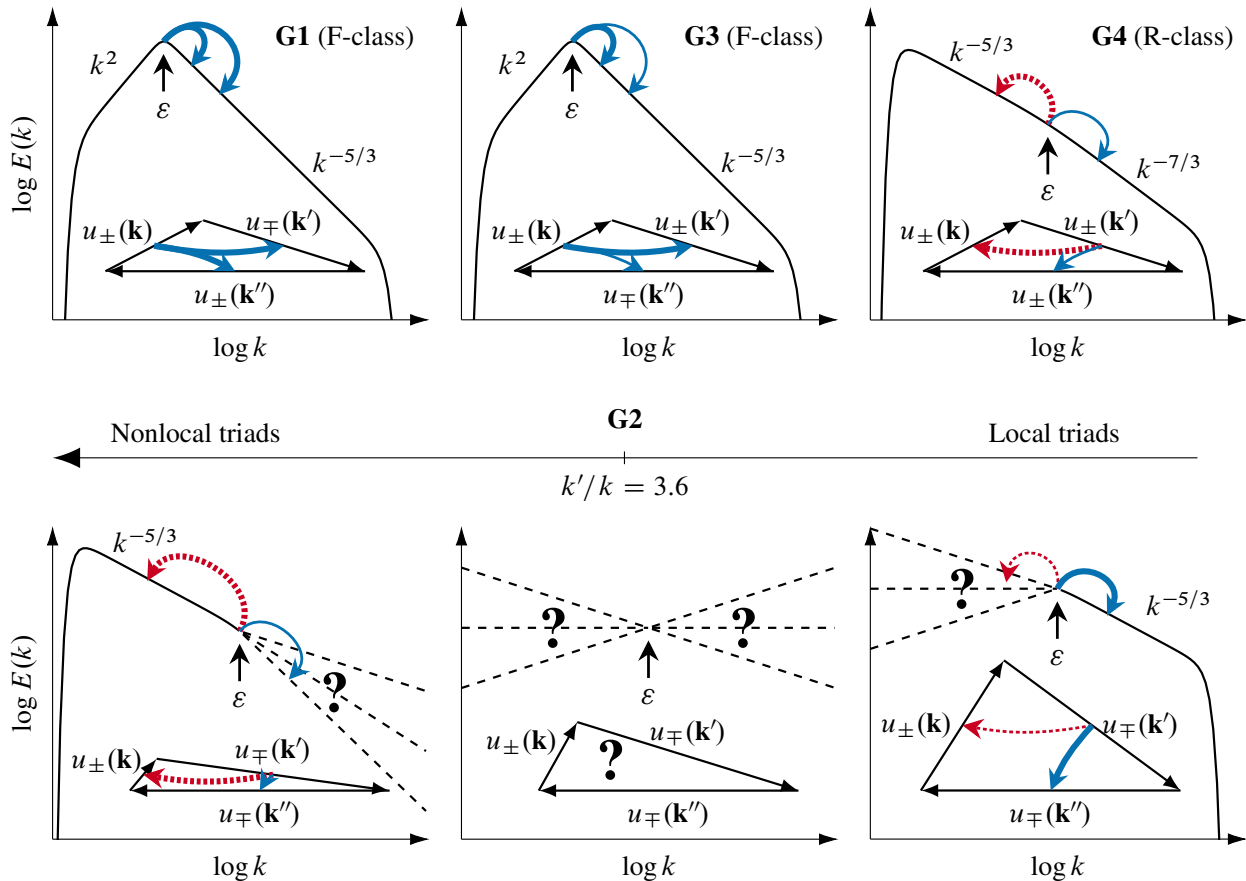


Figure 6.7: Behaviour of G1–G4 triads (leg-to-leg transfers) based on a linear stability analysis (Waleffe, 1992). G1 and G3 triads (F-class) contribute to a forward energy cascade (transfers from smallest to larger legs), and G2 and G4 triads (R-class) have a partly reversed energy cascade (transfers from middle to larger and smaller legs). G2 triads additionally exhibit a cascade reversal around geometries with a middle-to-smallest leg ratio of  $k'/k = 3.6$ , shifting the dominant energy transfer direction from forward (in local triads) to reverse (in nonlocal triads) Waleffe (1992). The scaling exponent  $-7/3$  below the forcing scale in G4 corresponds to a forward cascade of helicity (Brissaud et al., 1973). In study #3, the behaviours of G1–G4 are studied numerically in both isolation and coupled together (as the NSE prescribes), and are compared to the linear stability predictions shown in this figure. In study #4, a physical mechanism responsible for the G2 reversal is proposed, and the behaviour near the transition geometries is investigated numerically (question marks in figure).

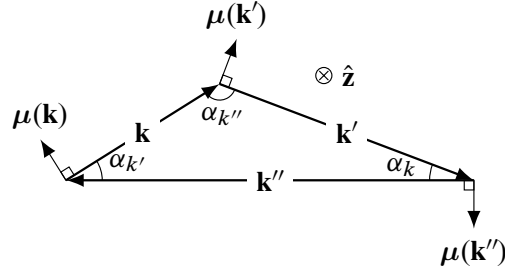


Figure 6.8: The rotated spectral-helical bases of each triad leg,  $\mu$  and  $\hat{z}$ , such that  $\hat{z}$  is shared among all legs and all  $\mu$  components lie on the triad plane.

### G1–G4 coupling weights

The geometry term  $g$  defined in (6.11) may be written in a particularly convenient form, which is central to the derivation of G1–G4 coupling weights in study #3 in the case of a shell model. Rotating the basis pair of each triad leg into frames sharing a component normal to the triad plane, denoted  $\hat{z}$ , the bases may be written as  $\mathbf{h}_s(\mathbf{k}) = is\hat{\mathbf{i}}(\mathbf{k}) + \hat{\mathbf{j}}(\mathbf{k}) = e^{is\phi_k}(\hat{z} + is\mu(\mathbf{k}))$  and similarly for  $\mathbf{h}_{s'}(\mathbf{k}')$  and  $\mathbf{h}_{s''}(\mathbf{k}'')$  by interchanging  $\{\mathbf{k}, s, \phi_k\} \rightarrow \{\mathbf{k}', s', \phi_{k'}\}, \{\mathbf{k}'', s'', \phi_{k''}\}$ , respectively. The shared component,  $\hat{z}$ , is, by definition of being normal to the triad plane, constrained by  $\hat{z} = \mathbf{k} \times \mathbf{k}' / |\mathbf{k} \times \mathbf{k}'| = \mathbf{k}' \times \mathbf{k}'' / |\mathbf{k}' \times \mathbf{k}''| = \mathbf{k}'' \times \mathbf{k} / |\mathbf{k}'' \times \mathbf{k}|$ , whereas the in-plane components are by orthogonality  $\mu(\mathbf{k}) = \hat{\mathbf{k}} \times \hat{z}$ ,  $\mu(\mathbf{k}') = \hat{\mathbf{k}}' \times \hat{z}$ , and  $\mu(\mathbf{k}'') = \hat{\mathbf{k}}'' \times \hat{z}$ . The resulting bases are shown in figure 6.8.

Using these rotated bases, the geometry term may instead be written as

$$\mathbf{h}_{s'}^*(\mathbf{k}') \times \mathbf{h}_{s''}^*(\mathbf{k}'') \cdot \mathbf{h}_s^*(\mathbf{k}) = -e^{-i(s\phi_k + s'\phi_{k'} + s''\phi_{k''})} \times \frac{Q(k, k', k'')}{2kk'k''} ss's''(sk + s'k' + s''k''), \quad (6.13)$$

where  $Q(k, k', k'') = (2k^2k'^2 + 2k'^2k''^2 + 2k''^2k^2 - k^4 - k'^4 - k''^4)^{1/2}$ , and the trigonometric identity  $\sin(\alpha_k)/k = \sin(\alpha_{k'})/k' = \sin(\alpha_{k''})/k'' = Q(k, k', k'') / (2kk'k'')$  has been used (Waleffe, 1992). Writing the geometry term this way thus allows to distinguish between contributions from a triad's shape versus orientation (the exponential).

## 6.4 Shell models

Direct numerical simulations of the NSE are still, by and large, computationally unfeasible even for short inertial subranges because: (i) of the large number of degrees of freedom required to establish inertial subranges, and (ii) because of the small time step needed to account for the dynamical stiffness of the NSE. As a consequence, a lot of effort has been put into developing reduced wave-space models of turbulence allowing long inertial subranges to be resolved in a computationally cost-effective manner.

Shell models are a class of such models in which only wave vectors with exponentially distributed magnitudes are considered. They may be regarded as structureless cascade models where the dimensionality of wave-space is reduced to one dimension and where the nonlinear triad interaction terms are carefully constructed to conserve all NSE invariants. Shell models have received a lot of attention in literature because of certain statistical quantities being remarkably similar to those found for the NSE. This includes their multi-scaling velocity correlations with nontrivial scaling exponents almost indistinguishable from the NSE case (Jensen et al., 1991), as well as their possession of an inertial law fixing the scaling of third-order structure functions in a similar fashion to the much celebrated four-fifths law (Ditlevsen, 2000).

The purpose of this section is to briefly introduce shell models since they play a central role in the experimental parts of studies #3 and #4. For more comprehensive review, the reader is referred to e.g. Biferale (2003); Ditlevsen (2010).

In general terms, shell models can be written in a form similar to the regular<sup>3</sup> spectral NSE (6.6) (no summation over repeated indices implied)

$$(d_t + \nu k_n^2)u(k_n) = i k_n \sum_{m,l} I_{n;m,l} u^*(k_m) u^*(k_l) + f_n, \quad (6.14)$$

where  $u(k_n)$  is the spectral velocity component of the  $n$ th shell (shell velocity), and  $I_{n;m,l}$  are interaction coefficients constrained to preserve energy, helicity (or enstrophy), and phase-space volume, similarly to the NSE. The discretely resolved wavenumbers are given by the geometric series

$$k_n = k_0 \lambda^n, \quad (6.15)$$

where  $k_0$  is the wavenumber of the largest scale,  $\lambda$  is the shell (wavenumber) spacing, and  $n = 0, 1, \dots, N$  where  $N$  corresponds to the largest resolved shell number (smallest scale). The forcing term  $f_n$  is typically applied to a single shell only and may be constructed to allow full control over the average inputs of energy, helicity (or enstrophy). Finally,  $\nu k_n^2 u(k_n)$  is a dissipation term similar to the corresponding term in the NSE.

The exact functional form of  $I_{n;m,l}$  is what distinguishes the shell models (Biferale, 2003; Frisch, 1995; Ditlevsen, 2010). For the purpose of this introduction, consider the simple, widely studied nearest-neighbour limit of triad interactions where the middle and largest triad legs are, respectively,  $\lambda$  and  $\lambda^2$  times bigger than the smallest leg, inspired by the Richardson cascade picture of local interactions being dominant. In this limit, the interaction model is giving by (Ditlevsen, 2000)

$$I_{n;m,l} = \delta_{n+1,m} \delta_{-(n+2),l} - \frac{\epsilon}{\lambda} \delta_{n-1,m} \delta_{-(n+1),l} + \frac{1-\epsilon}{\lambda^2} \delta_{-(n-1),m} \delta_{-(n-2),l},$$

<sup>3</sup>Studies #3 and #4 consider a helically decomposed version the shell model introduced here, which is structurally similar.

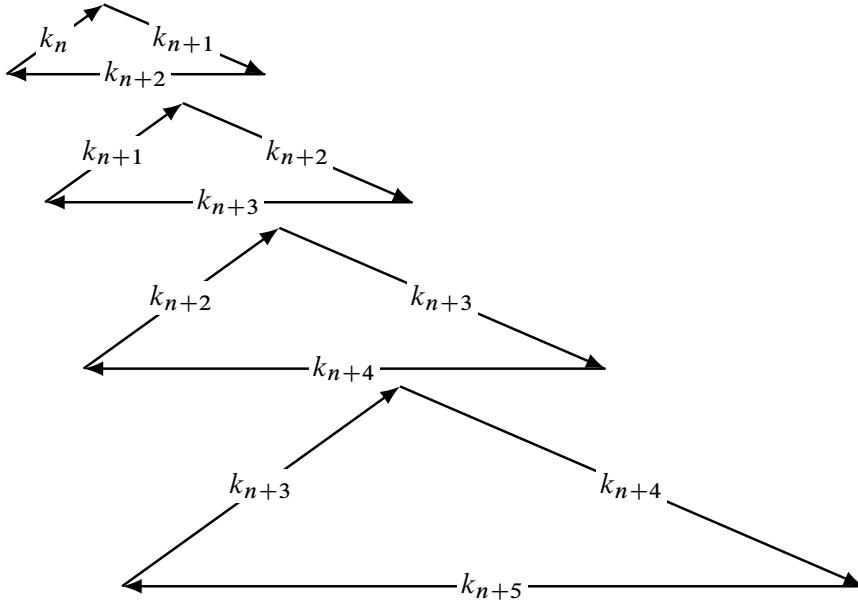


Figure 6.9: Example of four consecutively resolved triad geometries in the nearest-neighbour limit of triad interactions (middle and largest triad leg being  $\lambda$  and  $\lambda^2$  times bigger than the smallest leg, respectively) with  $\lambda = 1.4$ . All triads have identical shapes but are scaled versions of each other (scaled by  $\lambda$ ) and therefore share two legs with the previous/next triad.

where  $\delta_{i,j}$  is the Kronecker delta,  $\epsilon$  is a model parameter, and negative wavenumber indices are defined such that  $u(k_{-n}) \equiv u(-k_n) = u^*(k_n)$ . Inserting  $I_{n;m,l}$  into (6.14), the shell model takes the form

$$(d_t + \nu k_n^2)u(k_n) = ik_n \left( u^*(k_{n+1})u(k_{n+2}) - \frac{\epsilon}{\lambda} u^*(k_{n-1})u(k_{n+1}) + \frac{1-\epsilon}{\lambda^2} u(k_{n-2})u(k_{n-1}) \right) + f_n.$$

The closing of triads in the NSE dictates that the shell spacing,  $\lambda$ , must be bounded by the triangle inequality, which in the nearest-neighbour limit amounts to  $k_n + \lambda k_n \geq \lambda^2 k_n \implies 1 + \lambda \geq \lambda^2$ , implying  $1 < \lambda \leq g$ , where  $g$  is the golden ratio. Furthermore, because  $k_n$  (6.15) is a geometric series, the resolved triad shapes are identical for a given shell spacing  $\lambda$  and model  $I_{n;m,l}$  (unless models are mixed), and are thus scaled versions (multiples of  $\lambda$ ) of each other (exemplified in figure 6.9 for the nearest-neighbour limit).

In study #3, this nearest-neighbour limit is considered in the case of a helically decomposed shell model (coupling G1–G4), while study #4 explores the nonlocal, acute triad limit  $m, l \gg n$  relevant for the cascade reversal associated with G2 interactions (figure 6.7).



# Chapter 7

## Study #3

### 7.1 Introduction

In literature, a linear stability analysis is frequently relied on to explain the behaviour of individual helical triads (G1–G4) — that is, how energy is transferred between triad components — based on the linear stability of the terms in (6.10) corresponding to a single triad (6.12). In fully developed turbulence, however, it is not clear to what extent linear stability is relevant. Such an analysis, which considers single-triad states that are unlikely to be realized in physical flows, is very different from the full NSE which simultaneously resolves all possible triad interactions. In this regard, it is plausible that the behaviour of coupled triad configurations (G1–G4) cannot generally be explained by studying the stability of steady solutions of single triad systems.

Direct numerical simulations of the NSE (6.10) therefore seem unavoidable if wanting to understand the influence of G1–G4 interactions in coupled configurations and to what extent linear stability is relevant. Unfortunately, such simulations are still relatively computationally expensive. As an alternative, important insights might instead be made by gradually increasing the realism of reduced wave-space models of the NSE such as shell models; that is by increasing the number of resolved triad interactions in a systematic way. The present study adopts this methodology by introducing a new nonlocal, helically decomposed shell model, derived from the NSE and related to the helically decomposed Sabra shell model (De Pietro et al., 2015). One important difference compared to other shell models is, however, that the model comes with G1–G4 coupling weights directly related the NSE (no rationale exists otherwise for choosing coupling weights). Using this model, the coupled versus uncoupled G1–G4 behaviours are investigated, and how the energy cascade is partitioned into separate components carried by G1–G4 interactions.

## **7.2 The paper**

(intentionally blank)

## Role of helicity in triad interactions in three-dimensional turbulence investigated by a new shell model

Nicholas M. Rathmann\* and Peter D. Ditlevsen†

*Niels Bohr Institute, University of Copenhagen, 1017 Copenhagen K, Denmark*

(Received 7 February 2016; revised manuscript received 26 June 2016; published 27 September 2016)

Fully developed homogeneous isotropic turbulence in two dimensions is fundamentally different from that in three dimensions. In two dimensions, the simultaneous inviscid conservation of both kinetic energy and enstrophy within the inertial range of scales leads to a forward cascade of enstrophy and a reverse cascade of energy. In three dimensions, helicity, the integral of the scalar product of velocity and vorticity, is also an inviscid flow invariant along with the energy. Unlike the enstrophy, however, the helicity does not block the forward cascade of energy to small scales. Energy and helicity are conserved not only globally but also within each nonlinear triadic interaction between three plane waves in the spectral form of the Navier-Stokes equation (NSE). By decomposing each plane wave into two helical modes of opposite helicities, each triadic interaction is split into a set of eight helical triadic interactions between helical modes [F. Waleffe, *Phys. Fluids A* **4**, 350 (1992)]. Recently it was found that a subset of these helical interactions, which render both signs of helicity separately conserved (enstrophy-like), leads to an inverse cascade of (part of) the energy [L. Biferale *et al.*, *Phys. Rev. Lett.* **108**, 164501 (2012)]. Motivated by this finding we introduce a new shell model, obtained from the NSE expressed in the helical basis, allowing the eight helical interactions to be coupled as in the NSE and their relative contributions evaluated as a function of both the net helicity input and triad geometry. By numerically integrating the new model, we find that the intermittency of the energy cascade decreases with the net helicity input. Studying the partitioning of the energy cascade between the eight helical interactions, we find that the decrease in intermittency is related to a shift in the dominating helical interactions when helically forced, two of which exhibit a larger cascade intermittency than the other six interactions. Among the relatively local triad geometries considered here, the partitioning of the energy and helicity cascades between the eight helical interactions shows no sign of change with triad geometry.

DOI: [10.1103/PhysRevE.94.033115](https://doi.org/10.1103/PhysRevE.94.033115)

### I. INTRODUCTION

The role played by helicity in the cascade processes of fully developed three-dimensional (3D) turbulence is elusive. Helicity, the integral of the scalar product of vorticity and velocity, is an inviscid invariant thought to be more or less passively advected through the energy cascade from the large integral scale to the small viscous (dissipating) Kolmogorov scale of the flow. This stands in contrast to two-dimensional (2D) turbulence, where the enstrophy, the integral of the vorticity squared, is a second positive inviscid invariant besides energy. The ratio of the dissipation of enstrophy to the dissipation of energy scales with the Kolmogorov scale  $\eta$  as  $\eta^{-2}$ , thus for  $\eta \rightarrow 0$  the forward cascade of enstrophy prevents a forward cascade of energy, which instead is transported to larger scales. Following Waleffe [1] we refer to this as a reverse cascade, synonymous to an inverse or upscale cascade.

A similar scaling argument for 3D turbulence leads to the ratio of dissipation of helicity to dissipation of energy scaling as  $\eta^{-1}$ . Thus for a constant dissipation of helicity the dissipation of energy vanishes when  $\eta \rightarrow 0$ . Unlike the 2D case, however, this does not prevent a forward cascade of energy because helicity is not sign specific, implying that the separate dissipation of positive and negative helicity structures can grow as  $\eta^{-1}$ , while the net dissipation of both energy and helicity balance their respective inputs at the forcing scale. In recent work by Biferale *et al.* [2] it was proposed that

if only interactions between same-signed helicity modes are considered, a phenomenon corresponding to the reverse energy cascade in 2D turbulence could be present in the 3D case, with sign-fixed helicity playing the role of enstrophy.

In the spectral representation of the Navier-Stokes equation (NSE), nonlinear interactions are represented by exchanges of energy and helicity between three plane waves under the constraint that their wave vectors (momenta) sum to 0, thereby forming triangles (triads). In the interest of investigating the role played by helicity in an incompressible flow, it is useful to further decompose the spectral velocity components  $\mathbf{u}(\mathbf{k})$  in terms of helical modes. Under the helical decomposition spectral velocity components  $\mathbf{u}(\mathbf{k})$  are decomposed onto a plane perpendicular to  $\mathbf{k}$  using the incompressibility  $\mathbf{k} \cdot \mathbf{u}(\mathbf{k}) = 0$  such that  $\mathbf{u}(\mathbf{k}) = u_+(\mathbf{k})\mathbf{h}_+(\mathbf{k}) + u_-(\mathbf{k})\mathbf{h}_-(\mathbf{k})$ . The basis vectors  $\mathbf{h}_\pm(\mathbf{k})$  are eigenvectors of the curl operator, i.e.,  $i\mathbf{k} \times \mathbf{h}_\pm(\mathbf{k}) = \pm k\mathbf{h}_\pm(\mathbf{k})$ , leading to the energy and helicity being given by

$$E = \sum_{\mathbf{k}} (|u_+(\mathbf{k})|^2 + |u_-(\mathbf{k})|^2), \quad (1)$$

$$H = \sum_{\mathbf{k}} k(|u_+(\mathbf{k})|^2 - |u_-(\mathbf{k})|^2) \quad (2)$$

and the spectral form of the NSE being given by [1]

$$(\partial_t + \nu k^2)u_s(\mathbf{k}) = -1/4 \sum_{\mathbf{k}+\mathbf{k}'+\mathbf{k}''=0} \sum_{s',s''} (s'k' - s''k'') \mathbf{h}_{s'}^*(\mathbf{k}') \times \mathbf{h}_{s''}^*(\mathbf{k}'') \cdot \mathbf{h}_s(\mathbf{k}) u_{s'}^*(\mathbf{k}') u_{s''}^*(\mathbf{k}''), \quad (3)$$

where  $\{s, s', s''\} = \pm 1$  are helical signs. The inner sum indicates that each triadic interaction is split into a set of  $2^3 = 8$

\*rathmann@nbi.ku.dk

†pditlev@nbi.ku.dk

distinct helical triadic interactions, or *subinteractions*, among the helical modes. The interaction coefficient

$$(s'k' - s''k'')\mathbf{h}_{s'}^*(\mathbf{k}') \times \mathbf{h}_{s''}^*(\mathbf{k}'') \cdot \mathbf{h}_s^*(\mathbf{k}) \quad (4)$$

will, for a given triad of waves  $\mathbf{k} + \mathbf{k}' + \mathbf{k}'' = 0$ , give the relative weights of the different subinteractions. By sorting the subinteractions, four pairs with similar interaction coefficients arise [1],  $\{s, s', s''\} = \pm\{+, -, +\}$ ,  $\pm\{+, -, -\}$ ,  $\pm\{+, +, -\}$ ,  $\pm\{+, +, +\}$ , hereafter referred to as the four types of subinteractions instead of the eight distinct.

By isolating terms in (3) involving only the three wave vectors  $\{\mathbf{k}, \mathbf{k}', \mathbf{k}''\}$  (a single triad), one finds

$$\begin{aligned} \partial_t u_s(\mathbf{k}) &= (s'k' - s''k'') g u_{s'}^*(\mathbf{k}') u_{s''}^*(\mathbf{k}''), \\ \partial_t u_{s'}(\mathbf{k}') &= (s''k'' - sk) g u_{s''}^*(\mathbf{k}'') u_s^*(\mathbf{k}), \\ \partial_t u_{s''}(\mathbf{k}'') &= (sk - s'k') g u_s^*(\mathbf{k}) u_{s'}^*(\mathbf{k}'), \end{aligned} \quad (5)$$

where  $g = -1/4 \mathbf{h}_s^*(\mathbf{k}) \times \mathbf{h}_{s'}^*(\mathbf{k}') \cdot \mathbf{h}_{s''}^*(\mathbf{k}'')$ . Multiplying by  $u_s^*(\mathbf{k})$ ,  $u_{s'}^*(\mathbf{k}')$ , and  $u_{s''}^*(\mathbf{k}'')$ , respectively, in the three equations, (5), it immediately follows that energy is conserved within each triad since  $\partial_t (|u_s(\mathbf{k})|^2 + |u_{s'}(\mathbf{k}')|^2 + |u_{s''}(\mathbf{k}'')|^2) = 0$ , and similarly for the helicity since  $\partial_t (sk|u_s(\mathbf{k})|^2 + s'k'|u_{s'}(\mathbf{k}')|^2 + s''k''|u_{s''}(\mathbf{k}'')|^2) = 0$ . Nonlinear fluxes of energy and helicity thus result as the sum of exchanges of these quantities between the three triad legs. Furthermore, by considering the generalized energy- and helicity-like quantities

$$E^{(\alpha)} = \sum_{\mathbf{k}} k^\alpha (|u_+(\mathbf{k})|^2 + |u_-(\mathbf{k})|^2), \quad (6)$$

$$H^{(\beta)} = \sum_{\mathbf{k}} k^\beta (|u_+(\mathbf{k})|^2 - |u_-(\mathbf{k})|^2), \quad (7)$$

it is straightforward to show that such quantities are similarly conserved within each triad if the exponents  $\alpha$  and  $\beta$  fulfill

$$\begin{aligned} (s'k'/k - s''k''/k) + (k'/k)^\alpha (s''k''/k - s) \\ + (k''/k)^\alpha (s - s'k'/k) = 0 \end{aligned} \quad (8)$$

and

$$\begin{aligned} s(s'k'/k - s''k''/k) + s'(k'/k)^\beta (s''k''/k - s) \\ + s''(k''/k)^\beta (s - s'k'/k) = 0, \end{aligned} \quad (9)$$

respectively. The quantities  $E^{(\alpha)}$  and  $H^{(\beta)}$ , hereafter referred to as the *pseudoenergy* and *pseudohelicity*, clearly depend on both the specific triad shape by  $\{k, k', k''\}$  and the subinteraction by  $\{s, s', s''\}$ , whereas the proper energy ( $\alpha = 0$ ) and helicity ( $\beta = 1$ ) are globally conserved across all triadic interactions, as they should be.

Given the triad dynamics governed by (5), the linear stability of the fixed points  $\{u_s(\mathbf{k}), u_{s'}(\mathbf{k}'), u_{s''}(\mathbf{k}'')\} = \{U_0, 0, 0\}, \{0, U_0, 0\}, \{0, 0, U_0\}$  may easily be calculated. Waleffe [1] proposed that the average energy transfer directions between triad legs might be determined by the stability of these fixed points such that energy flows out of the unstable mode (leg) and into the other two. By this rationale, the above four subinteractions may be divided into two classes (each class consisting of two subinteractions): one class in which energy flows from the smallest wave mode (large scales) into the two larger wave modes (smaller scales), termed the ‘‘forward’’ class, and one class in which the energy flows out of the middle

mode and into the largest and smallest modes, termed the ‘‘reverse’’ class. Here the subinteractions between same-signed helical modes corresponding to the 2D turbulence case are of the reverse class. Note that the largest wave mode (smallest scale) is never an unstable mode.

In fully developed 3D turbulence it is not clear to what extent linear stability analysis is relevant or, more importantly, to what extent mixing of the four subinteractions is essential for the overall behavior of the flow. Even if the flow by some strong symmetry constraints could be prepared in a maximally helical state (of only one helical sign), linear instability would make energy flow into modes of opposite sign, obeying the helicity conservation by creating equal amounts of helicity of both signs in the process. In this work we thus seek to investigate numerically the relative importance of the four subinteractions in a coupled context—in particular, quantifying their relative contributions to the energy and helicity cascades and the energy cascade intermittency as a function of the net helicity input and triad shape. Motivated by this we introduce a new helical shell model inspired by (3) allowing the four subinteractions to be coupled as in the NSE.

Helically decomposed shell models derived from the regular GOY [3] and Sabra [4,5] shell models have already been studied [6–10]. Applying the helical decomposition to these regular models four possible helical shell models may be constructed, each one corresponding to one of the four subinteractions. So far, however, only uncoupled configurations of these four separate helical shell models have been considered [6–10].

Our new model is advantageous over previous helical shell models because:

(1) It is structurally closer to the helically decomposed NSE, (3), by being obtained directly from it.

(2) It contains the coupling strengths equivalent to (4) for the four types of subinteractions (which are naturally derived from the NSE), unlike previous models, for which there currently exists no rationale for coupling the subinteractions.

Similarly to previous helical shell models our new model also consists of four separate models, each one corresponding to one of the four subinteractions among helical modes. In the following we therefore refer to these as the four *submodels* of the new shell model.

In summary the purpose of this work is (a) to introduce the new model (Sec. II), (b) to numerically investigate the roles played by the four submodels (subinteractions) in a coupled configuration as a function of the triad geometry and helicity input (Sec. III), and (c) to compare the new uncoupled submodels with previous studies of (uncoupled) helical shell models, in particular, the helical Sabra model, which is structurally closest to the new model (Sec. IV).

## II. THE NEW SHELL MODEL

The new model (source freely available at <https://github.com/nicholasmr/rdshellmodel>) is obtained from the helically decomposed NSE, (3), in Appendix A by defining complex velocity components  $u_n^s \equiv u_s(k_n)$  ( $s = \pm$ ) on an exponentially thinned set of wave-vector magnitudes  $k_n = k_0 \lambda^n$  for  $n = 0, 1, \dots, N$ . Within this discretized wave space triadic interactions are permitted only between waves fulfilling the triangle

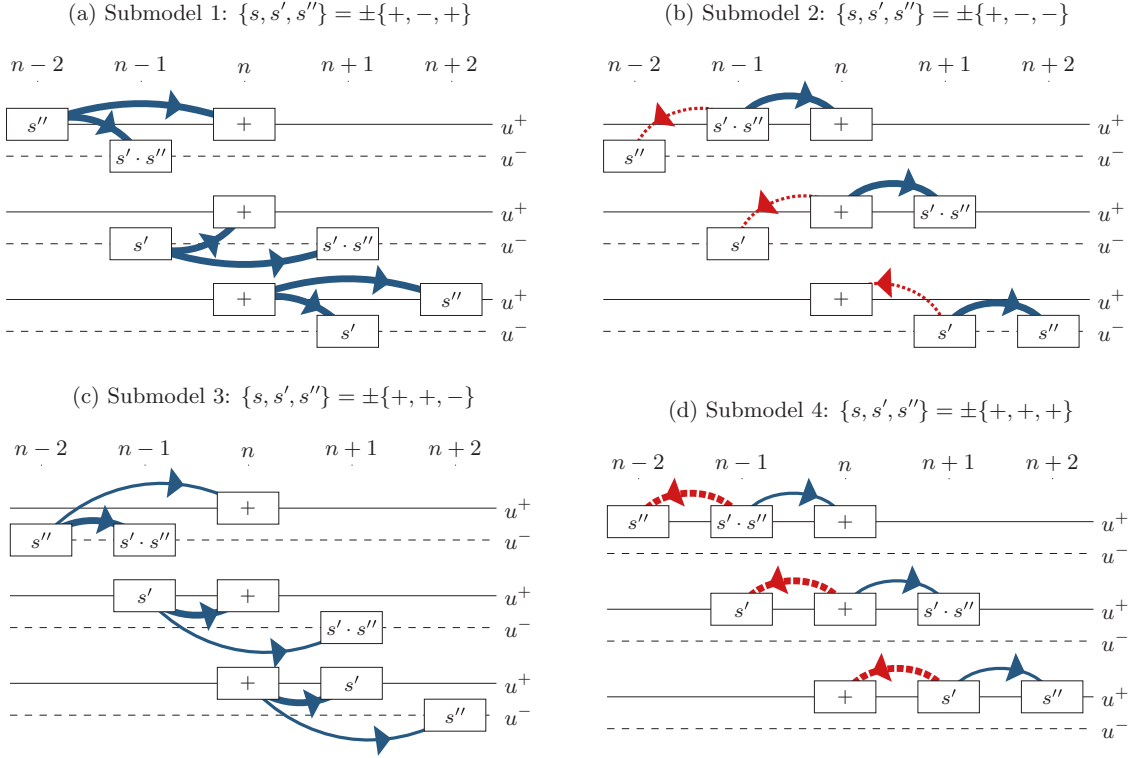


FIG. 1. Schematic of the three nonlinear helical interactions of each submodel coupling to  $u_n^+$ . All interactions are sign flipped for complementary interactions coupling to  $u_n^-$  (not shown). Arrows indicate the average energy transfer direction within each triadic interaction resulting from a linear stability analysis [1,10]: solid blue (dashed red) arrows denote forward (reverse) energy transfers, while thick (thin) arrows represent dominant (subordinate) transfers.

inequality  $k_n + k_{n+p} \geq k_{n+q}$  (the shell model equivalent of the NSE constraint  $\mathbf{k} + \mathbf{k}' + \mathbf{k}'' = 0$ ) and  $0 < p < q$  [a model constraint ensuring that waves do not self-interact (unilateral triangles) such that Liouville's theorem is fulfilled as for the inviscid part of the NSE].

In the limit of nearest-neighbor interactions the new model is

$$(d_t + D_n)u_n^s = sk_n \sum_{s',s''} g^{s',s''} \left( u_{n+1}^{s',s'',*} u_{n+2}^{s',s''} - \frac{\epsilon^{s',s''}}{\lambda} u_{n-1}^{s',s'',*} u_{n+1}^{s',s''} + \frac{\xi^{s',s''}}{\lambda^2} u_{n-2}^{s',s''} u_{n-1}^{s',s''} \right) + f_n^s, \quad (10)$$

where  $\lambda$ ,  $k_0$ , and  $N$  are free model parameters and  $u_n^{s,*}$  is the complex conjugate of  $u_n^s$ . The helical signs of the interacting modes depend on the specific submodel, here written compactly by introducing effective signs built on products of  $s$ ,  $s'$ , and  $s''$ , e.g.,  $s \cdot s'$ . Forcing and viscous dissipation at the  $n$ th shell (scale  $k_n$ ) of helical sign  $s$  are  $f_n^s$  and  $(\nu k_n^2 + \nu_L k_n^{-4})u_n^s \equiv D_n u_n^s$ , respectively,  $\nu_L k_n^{-4} u_n^s$  being a large-scale drag added to remove any potential buildup of energy at large scales. The small- and large-scale viscosities  $\nu$  and  $\nu_L$  are free parameters, whereas the large-scale drag exponent ( $-4$ ) was chosen such that the large-scale dissipation is confined to the first few shells for the longest possible inertial range. The specific values of  $\nu_L$  and the large-scale

drag exponent were found not to influence the model behavior (not shown). The summation over  $\{s', s''\}$  is the weighted sum over the four submodels. The four possible pairs  $\{s', s''\} = \{-, +\}, \{-, -\}, \{+, -\}, \{+, +\}$  hereafter denote submodels 1–4, respectively, in accordance with previous literature. Thus, three helical triadic interactions are resolved per shell per submodel (Fig. 1).

The submodel weights  $g^{s',s''}$  and modal interaction coefficients  $\epsilon^{s',s''}$  and  $\xi^{s',s''}$  are given by (derived in Appendix A)

$$g^{s',s''}(\lambda) = -s's''(1 + s'\lambda - s''\lambda^2)(s'\lambda - s''\lambda^2), \quad (11)$$

$$\epsilon^{s',s''}(\lambda) = \frac{1 - s''\lambda^2}{\lambda - s's''\lambda^2}, \quad (12)$$

$$\xi^{s',s''}(\lambda) = -s''(1 - s'\epsilon^{s',s''}). \quad (13)$$

The interaction coefficients  $g^{s',s''}$ ,  $\epsilon^{s',s''}$ , and  $\xi^{s',s''}$  depend on the shell model spacing parameter  $\lambda$  which indicates the geometry of the resolved triads: for  $\lambda \rightarrow 1$  triangles become equilateral (leg lengths  $\{1, 1, 1\}$  relative to the smallest leg), while for  $\lambda \rightarrow (1 + \sqrt{5})/2 = \varphi$  (golden ratio) they collapse to a line (leg lengths  $\{1, \varphi, \varphi^2\}$  relative to the smallest leg). Note that unless triads are closed ( $\lambda \leq \varphi$ ), as the NSE requires, the interaction coefficients are not well defined (Appendix B).

Waleffe [1] hypothesized two classes of helical triadic interactions based on the average energy transfer directions

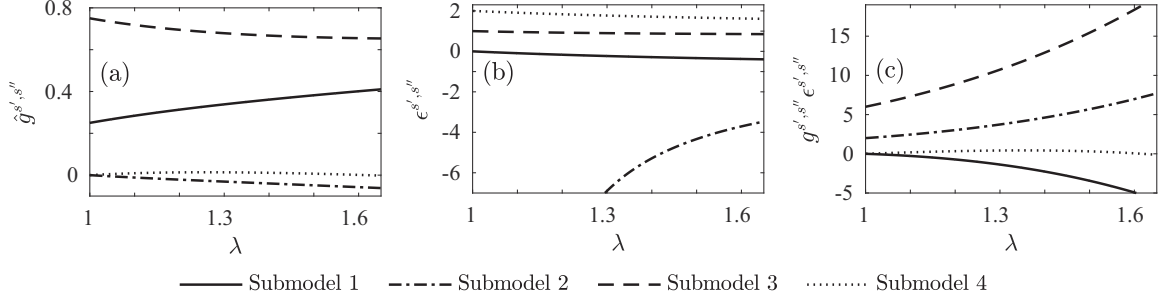


FIG. 2. Submodel (a) coupling strength  $g^{s',s''}$ , (b) interaction coefficient  $\epsilon^{s',s''}$ , and (c) their product as a function of  $\lambda$ .

using linear stability: (i) a class of forward interactions (F class) consisting of triads with opposite helical signs of the two largest wave modes and (ii) a class of reverse interactions (R class) consisting of triads with equal helical signs of the two largest wave modes. Thus, two of the four subinteractions belong to the F class, while the remaining two belong to the R class. The R-class interactions for which all three signs are not equal, however, were suggested by Waleffe [1], based on the above instability assumption and a scaling assumption, to become F class for local triadic interactions, defined as the ratio of the smallest to the middle wave number being higher than 0.278. Considering closed-triad nearest-neighbor interactions in the shell model thus renders these interactions purely F class since the ratio is bounded by  $1/\lambda \geq 1/\varphi = 0.618$ .

Because the product of helical signs between the two largest modes in all nonlinear terms of (10) is  $s' \cdot s''$ , each submodel consists only of interactions of one class. Like the helically decomposed GOY and Sabra models the new model therefore also consists of two submodels of the F class [ $s' \cdot s'' = -1$ ; Figs. 1(a) and 1(c)] and two of the R class [ $s' \cdot s'' = +1$ ; Figs. 1(b) and 1(d)], of which submodel 2 ( $\{s', s''\} = \{-, -\}$ ) contains the dual F- and R-class nature described above.

The interaction coefficients  $g^{s',s''}$  and  $\epsilon^{s',s''}$  are both plotted as functions of  $\lambda$  in Fig. 2. Figure 2(a) shows the normalized submodel weights  $\hat{g}^{s',s''} = g^{s',s''} / \sum_{s',s''} g^{s',s''}$ . Since two of the submodels belong to the F class their associated weights ( $g^{+,-}$  and  $g^{-,+}$ ) are expected to be the largest because 3D turbulence exhibits an average forward-dominated energy cascade. This is indeed found to be the case. The modal interaction coefficients  $\epsilon^{s',s''}$  plotted in Fig. 2(b) indicate that both  $s' \cdot s'' = -1$  (F-class) submodels have  $|\epsilon^{s',s''}| < 1$ , whereas both  $s' \cdot s'' = +1$  (R-class) submodels have  $|\epsilon^{s',s''}| > 1$ . This is appealing because the structure of the new model, (10), and functional forms of  $\epsilon^{s',s''}$ , (12), resemble, but are not identical to, the helically decomposed GOY and Sabra counterparts. In the GOY and Sabra models it is well known that the limit  $\epsilon^{s',s''} = 1$  marks the transition between 2D behavior of the energy cascade ( $1 < \epsilon^{s',s''} < 2$ ) and 3D behavior ( $\epsilon^{s',s''} < 1$ ). The values of  $\epsilon^{s',s''}$  thus seem to support the expected F- and R-class behavior based on the  $s' \cdot s''$  product.

#### Invariants and fluxes

Similarly to other shell models the nonlinear terms in (10) conserve both the energy  $E = \sum_{n=0}^N (|u_n^+|^2 + |u_n^-|^2)$  and the helicity  $H = \sum_{n=0}^N k_n (|u_n^+|^2 - |u_n^-|^2)$ . Additionally,

in the limit of nearest-neighbor interactions each submodel conserves one pseudoenergy quantity  $E^{(\alpha)} = \sum_{n=0}^N k_n^\alpha (|u_n^+|^2 + |u_n^-|^2)$  and one pseudohelicity quantity  $H^{(\beta)} = \sum_{n=0}^N k_n^\beta (|u_n^+|^2 - |u_n^-|^2)$ , where the exponents  $\alpha$  and  $\beta$  are, respectively, constrained by

$$1 - s' \lambda^\alpha \epsilon^{s',s''} + s'' (\lambda^\alpha)^2 \xi^{s',s''} = 0, \quad (14)$$

$$1 - \lambda^\beta \epsilon^{s',s''} + (\lambda^\beta)^2 \xi^{s',s''} = 0, \quad (15)$$

which are constraints similar to (8) and (9) of the NSE (see Appendix C). These pseudoinvariants are therefore specific to each submodel ( $\{s', s''\}$  pair) and the resolved triad shape by  $\lambda$ .

The existence of globally conserved (across all triad interactions) pseudoinvariants within each submodel can potentially influence the behavior of that submodel. However, because pseudoinvariants are not shared among submodels (or triad shapes), only the energy and helicity are globally conserved when mixing submodels (or triad shapes), similarly to the NSE (Appendix C).

Nonlinear spectral fluxes of energy and helicity through the  $n$ th shell are given as the transfers from all wave numbers less than  $k_n$  to wave numbers larger than  $k_n$ , that is,  $\Pi_n^E = d_t \sum_{m=0}^n (|u_m^+|^2 + |u_m^-|^2)$  and  $\Pi_n^H = d_t \sum_{m=0}^n k_m (|u_m^+|^2 - |u_m^-|^2)$ . Following the calculations through the yields for a single submodel (see Appendix D)

$$\Pi_n^E = \Delta_{n+1}^{-,s',s''} + (1 - s' \epsilon^{s',s''}) \Delta_n^{-,s',s''}, \quad (16)$$

$$\Pi_n^H = k_n (\Delta_{n+1}^{+,s',s''} + (\lambda^{-1} - \epsilon^{s',s''}) \Delta_n^{+,s',s''}), \quad (17)$$

where the correlators are defined as

$$\Delta_n^{\pm,s',s''} = 2k_{n-1} \text{Re} [u_{n-1}^{+,*} u_n^{s',*} u_{n+1}^{s''} \pm u_{n-1}^{-,*} u_n^{-s',*} u_{n+1}^{-s''}]. \quad (18)$$

For the coupled model the corresponding expressions are merely the weighted sums of (16) and (17) using weights  $g^{s',s''}$ .

### III. NUMERICAL RESULTS: 1. THE COUPLED MODEL

The coupling strengths, (11) [Fig. 2(a)], suggest that the influence of F-class interactions (submodels 1 and 3) should dominate over that of R-class interactions (submodels 2 and 4) in a coupled configuration. However, due to the strong nonlinearities present in (10) the relative influence of the four submodels might not be so simple and might possibly depend on the triad shape and net helicity input. In this work we are therefore interested in quantifying the relative

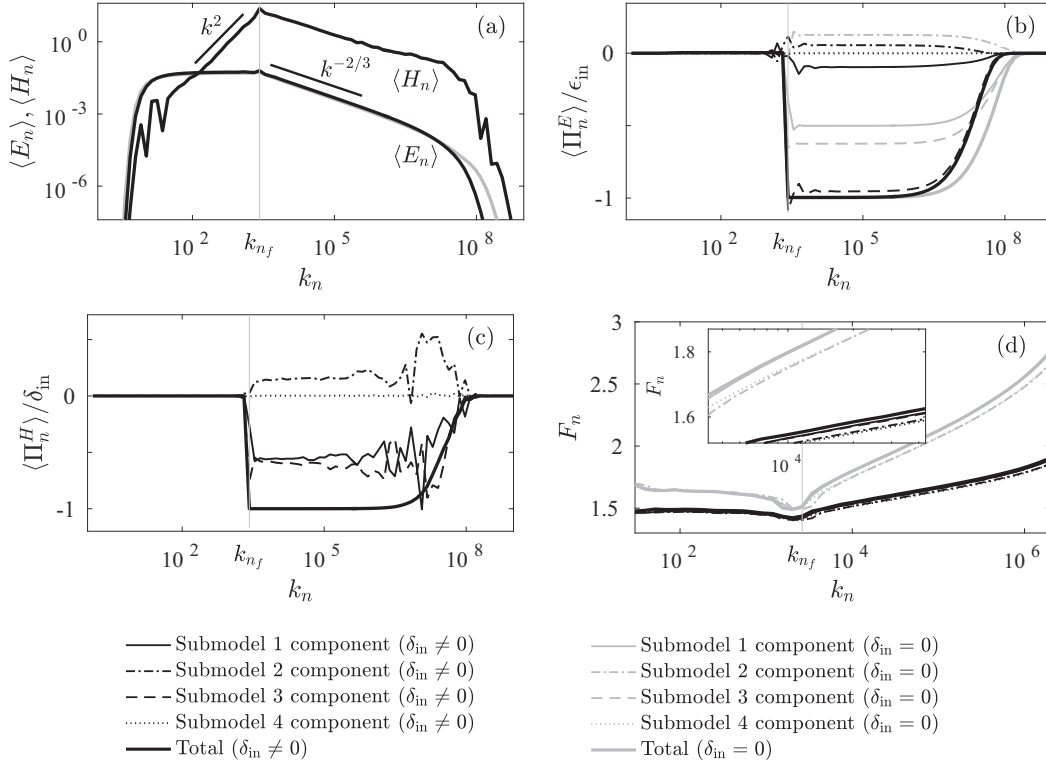


FIG. 3. Simulated coupled model (a) energy and helicity spectra and (b, c) energy and helicity fluxes. Also shown are (b, c) the individual submodel contributions of the energy and helicity cascades and (d) the energy cascade intermittency. Black lines denote the helically forced scenario ( $\delta_{in} \neq 0$ ), whereas gray lines denote the nonhelically forced scenario ( $\delta_{in} = 0$ ).

contributions from the four individual submodels to the energy and helicity cascades and the energy cascade intermittency as a function of the helicity input and triad shape. To do so we considered multiple triad shapes ( $\lambda$  values) along with two forcing scenarios: (i) a maximally helical forcing (of only one sign) and (ii) nonhelical forcing (of both signs). Since numerical results were found not to depend on the triad shape  $\lambda$  (discussed below), here, for the sake of brevity, we present the results of just one configuration— $\lambda = 1.3$ ,  $k_0 = 1$ ,  $N = 81$ ,  $\nu = 10^{-11}$ , and  $\nu_L = 10^3$ —implying the coupling strengths  $\{\hat{g}^{-,+}, \hat{g}^{-,-}, \hat{g}^{+,-}, \hat{g}^{+,+}\} = \{0.34, -0.03, 0.68, 0.01\}$  and  $\epsilon^{s',s''}$  values  $\{\epsilon^{-,+}, \epsilon^{-,-}, \epsilon^{+,-}, \epsilon^{+,+}\} = \{-0.23, -6.89, 0.89, 1.76\}$ . The value  $\lambda = 1.3$  was chosen for conformity with a future planned study considering coupled non-nearest-neighbor interactions ( $\lambda = 1.3$  allows a total of seven triad geometries; see Appendixes A and B for details). The values chosen for  $k_0$  and  $N$  were found not to influence the model behavior (not shown). The number of shells  $N$  determines the highest resolved wave number and is limited by hardware capabilities (integration time) due to the stiffness of the system. Because the large- and small-scale viscosities  $\nu$  and  $\nu_L$  affect only the length of the inertial ranges, and not their dynamics (not shown), their values were chosen such that dissipation occurs at the ends of the resolved wave space for the longest possible inertial ranges. A fourth-order Runge-Kutta integration scheme was applied in all simulations using  $dt = 5 \times 10^{-8}$  together with the forcing  $f_{n_f}^{\pm} = (1+i)/u_{n_f}^{\pm,*}$  applied to shell  $n_f = 30$ , supplying a constant input of energy  $\epsilon_{in}$  (not to be confused with the

interaction coefficient  $\epsilon^{s',s''}$ ) and helicity  $\delta_{in}$ . The choice of forcing scale was found not to influence the results (not shown). Two forcing scenarios were employed: one in which only the positive 30th helical shell is forced such that  $\epsilon_{in} = 2$ , hereafter referred to as the  $\delta_{in} \neq 0$  (helical) simulations (where  $\delta_{in} = k_{30}\epsilon_{in}$ ); and one in which both 30th helical shells are forced such that  $\epsilon_{in} = 4$ , hereafter referred to as the  $\delta_{in} = 0$  (nonhelical) simulations. All realizations are  $10^{11}$  time steps long and were initialized using the velocity profile  $u_n^{\pm} \sim k_n^{-1/3}$ . A spin-up of  $10^{10}$  time steps was performed to eliminate transients from the statistics, which was determined by the plateauing of the total energy content and the shell 1 and 20 energy content.

Figure 3(a) shows the coupled model simulated energy and helicity spectra for both the helically ( $\delta_{in} \neq 0$ ) and the nonhelically ( $\delta_{in} = 0$ ) forced case. Under both forcing scenarios the energy spectrum scales K41-like as  $\langle E_n \rangle \sim k_n^{-2/3}$  for wave numbers  $k_n > k_{n_f}$ , associated with a forward energy cascade [Fig. 3(b)]. For wave numbers  $k_n < k_{n_f}$  (large scales) the energy is found to equilibrate. The seemingly small positive  $\langle E_n \rangle$  scaling for  $k_n < k_{n_f}$  is due to an insufficiently short spectral range connecting the forcing scale with the large-scale sink, which is evident from equivalent simulations using a smaller forcing scale (not shown). The helicity spectrum is found to scale linearly with the energy spectrum for  $k_n > k_{n_f}$  [Fig. 3(a)], i.e.,  $\langle E_n \rangle \sim \langle H_n \rangle \sim k_n^{-2/3}$ , associated with a forward helicity cascade [Fig. 3(c)]. This behavior

matches expectations for the dual forward energy and helicity cascades envisaged by Brissaud *et al.* [11]. For the large scales  $k_n < k_{n_f}$  the helicity spectrum matches its equilibrium spectrum  $\langle H_n \rangle \sim k_n^2$  based on the equipartitioning of the energy and helicity (same method as presented in Sec. IV below; not shown).

Figures 3(b) and 3(c) additionally show how the total  $\langle \Pi_n^E \rangle$  and  $\langle \Pi_n^H \rangle$  fluxes are partitioned among the four submodels, calculated by (16) and (17) multiplied by the weights  $g^{s,s''}$ . Figure 3(b) shows the forward energy cascade in nonhelical turbulence (gray lines) is predominantly carried by submodel 1 and 3 interactions, whereas submodels 2 and 4 both contribute with relatively small up-scale cascades, the former being more than an order of magnitude larger than the latter. In helical turbulence, however, the forward energy cascade is carried almost entirely by submodel 3 interactions (black lines), whereas the forward helicity cascade is dominated equally by submodel 1 and 3 interactions while submodel 2 contributes a small reverse component [Fig. 3(c)]. In the interest of determining how this partitioning might depend on the triad geometry multiple  $\lambda$  values were additionally considered. The values tested were  $\lambda = \{1.1, 1.2, 1.3, 1.4, 1.5, 1.6\}$  together with  $N = \{223, 116, 81, 63, 52, 45\}$  and  $n_f = \{83, 44, 30, 24, 20, 17\}$ , respectively, thus ensuring that  $k_N$  and  $k_{n_f}$  are approximately unchanged. All interaction coefficients were updated according to (11)–(13) to reflect the different  $\lambda$  values. Across all  $\lambda$  values no change in cascade partitioning was found (not shown), albeit only relatively local triads (similar leg sizes) are possible in the nearest-neighbor interaction limit considered here.

In order to understand how the change in dominant helical interactions with the net helicity input influences the energy cascade intermittency we quantify the intermittency, similarly to De Pietro *et al.* [10], by the shell-energy flatness

$$F_n = S_4(k_n)/(S_2(k_n))^2, \quad (19)$$

where the structure functions  $S_q(k_n)$  are defined in terms of  $\Pi_n^E$  by

$$S_q(k_n) = \langle (k_n^{-1} |\Pi_n^E|)^{q/3} \rangle. \quad (20)$$

Figure 3(d) shows the flatness  $F_n$  calculated using the total energy flux as well as using the individual submodel contributions to  $\Pi_n^E$ . Interestingly, the energy cascade in helical turbulence is found to be less intermittent than that in nonhelical turbulence. The zoom-in in Fig. 3(d) shows that the flatnesses calculated using the individual submodel contributions to  $\Pi_n^E$  are largest for submodels 1 and 3 under both forcing scenarios.

As an explanation for the change in intermittency one might hypothesize that the different submodels each possess different degrees of cascade intermittency, such as found by De Pietro *et al.* [10], but this is masked in coupled configurations as Fig. 3(d) suggests. If so, one would anticipate the flatness of submodel 1 to be greatest among the four submodels in stand-alone uncoupled simulations. In the follow section we investigate this hypothesis and compare the uncoupled submodels with those in previous studies considering other helical shell models.

#### IV. NUMERICAL RESULTS: 2. THE UNCOUPLED SUBMODELS

The uncoupled submodels were integrated individually using the same configuration as listed in Sec. III. However, due to the submodel-dependent scaling of inertial ranges, the viscosity  $\nu$  was chosen separately for each submodel configuration to ensure that dissipation occurs at the end of the resolved wave space for the longest possible inertial ranges. The large-scale viscosity was meanwhile kept fixed at  $\nu_L = 10^3$ . For each of the four submodels the same two forcing scenarios were applied as in the coupled configuration.

Figures 4(a) and 4(c) show the submodel 1–4 energy fluxes and spectra, respectively, of the nonhelically forced simulations ( $\delta_{in} = 0$ ). The helically forced simulations ( $\delta_{in} \neq 0$ ) display similar results but are not shown in Fig. 4, for clarity. The results show that submodels 1–3 all exhibit the expected K41 scaling  $\langle E_n \rangle \sim k_n^{-2/3}$  associated with a forward energy cascade for wave numbers  $k_n > k_{n_f}$ . For wave numbers  $k_n < k_{n_f}$  (large scales) the three submodels have distinctly different spectra. Submodel 4, however, is different from submodels 1–3 in the entire spectrum. This submodel is found to transfer energy upscale but does not exhibit any scaling of the energy spectrum for  $k_n < k_{n_f}$ . The scaling for wave numbers  $k_n > k_{n_f}$  is approximately  $\langle E_n \rangle \sim k_n^{-4/3}$ , corresponding to a forward cascade of (positive) helicity.

Figures 4(b) and 4(d) show the helicity fluxes and spectra, respectively, of the helically forced simulations ( $\delta_{in} \neq 0$ ). The results show that submodels 2 and 3 both exhibit helicity spectra scaling K41-like as  $\langle H_n \rangle \sim k_n^{-2/3}$  for  $k_n > k_{n_f}$ , which are accompanied by forward cascades of helicity. Submodels 1 and 4 also exhibit downscale cascades of helicity but with spectra scaling as  $\langle H_n \rangle \sim k_n \langle E_n \rangle$ .

In order to explain the dissimilar submodel behaviors found for  $k_n < k_{n_f}$ , in the following we differentiate between the parts of the simulated energy spectra in which flow invariants equipartition among shells from those parts in which invariants cascade [12]. Using the equipartition theorem, a conservative system with quadratic invariants, in this case  $E$ ,  $E^{(\alpha)}$ ,  $H$ , and  $H^{(\beta)}$ , will on average distribute the conserved quantities equally between the degrees of freedom in the system [13]. In the present case the submodel partition function therefore takes the form  $Z = \int \exp[-\sum_n ((A + A^{(\alpha)}k_n^\alpha + Bk_n + B^{(\beta)}k_n^\beta)|u_n^+|^2 + (A + A^{(\alpha)}k_n^\alpha - Bk_n - B^{(\beta)}k_n^\beta)|u_n^-|^2)] \Pi_i du_i^+ du_i^-$ , where  $A$ ,  $A^{(\alpha)}$ ,  $B$ , and  $B^{(\beta)}$  are the inverse  $E$ ,  $E^{(\alpha)}$ ,  $H$ , and  $H^{(\beta)}$  temperatures, respectively. Using the partition function the equilibrated energy and helicity spectra are easily calculated, giving

$$\begin{aligned} \langle E(k_n) \rangle &= \frac{A + A^{(\alpha)}k_n^\alpha}{(A + A^{(\alpha)}k_n^\alpha)^2 - (Bk_n + B^{(\beta)}k_n^\beta)^2} \\ &\approx \frac{1}{A + A^{(\alpha)}k_n^\alpha}, \end{aligned} \quad (21)$$

$$\begin{aligned} \langle H(k_n) \rangle &= \frac{k_n(Bk_n + B^{(\beta)}k_n^\beta)}{(A + A^{(\alpha)}k_n^\alpha)^2 - (Bk_n + B^{(\beta)}k_n^\beta)^2} \\ &\approx \frac{k_n(Bk_n + B^{(\beta)}k_n^\beta)}{(A + A^{(\alpha)}k_n^\alpha)^2}, \end{aligned} \quad (22)$$

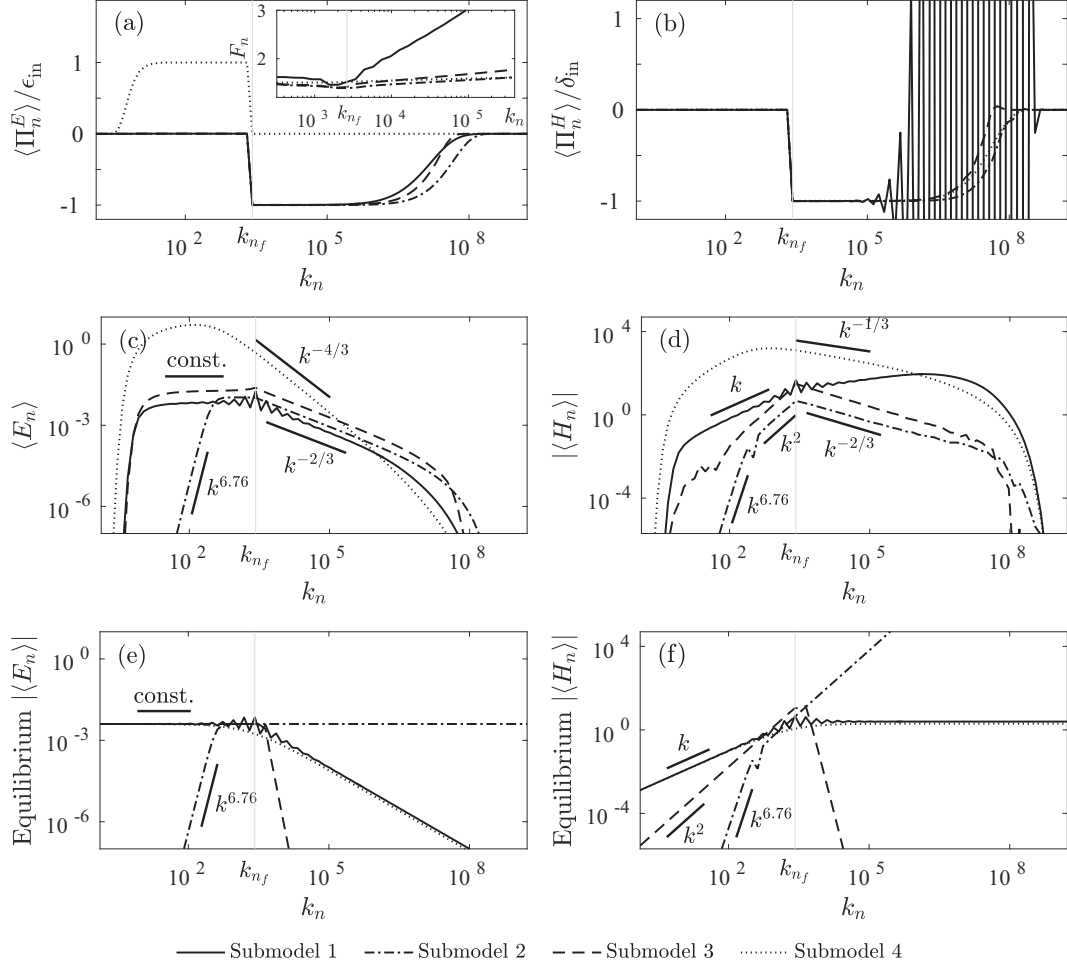


FIG. 4. Simulated uncoupled submodel (a, b) energy and helicity fluxes and (c, d) energy and helicity spectra. (a) The corresponding calculated flatnesses using (19). (e, f) Equilibrium spectra predicted by (21) and (22).

where  $(A + A^{(\alpha)}k_n^\alpha)^2 \gg (Bk_n + B^{(\beta)}k_n^\beta)^2$  has been used for the approximate forms by noting that the energy spectra of the helical ( $\delta_{in} \neq 0$ ) and nonhelical ( $\delta_{in} = 0$ ) simulations are similar (not shown). The inverse temperatures may be constrained by equating the average dissipation of the four invariants to their average inputs  $\epsilon_{in}$ ,  $\delta_{in} = k_{n_f} \epsilon_{in}$ ,  $\epsilon_{in}^{(\alpha)} = k_{n_f}^\alpha \epsilon_{in}$ , and  $\delta_{in}^{(\beta)} = k_{n_f}^\beta \epsilon_{in}$ , where  $n_f$  is the forcing shell. Of course, the actual dissipation is the integrated effect over a large range of scales. However, in order to obtain useful expressions for the temperatures we approximate these as one effective (Kolmogorov) scale per quantity, hereafter denoted  $k_E, k_{E^{(\alpha)}}, k_H$  and  $k_{H^{(\beta)}}$ . Equating input to dissipation then gives the approximate

expressions

$$\epsilon_{in} \approx D(k_E) \langle E(k_E) \rangle, \quad (23)$$

$$\delta_{in} \approx D(k_H) \langle H(k_H) \rangle, \quad (24)$$

$$\epsilon_{in}^{(\alpha)} \approx D(k_{E^{(\alpha)}}) k_{E^{(\alpha)}}^\alpha \langle E(k_{E^{(\alpha)}}) \rangle, \quad (25)$$

$$\delta_{in}^{(\beta)} \approx D(k_{H^{(\beta)}}) k_{H^{(\beta)}}^{\beta-1} \langle H(k_{H^{(\beta)}}) \rangle, \quad (26)$$

where  $D(k_n) = \nu k_n^2 + \nu_L k_n^{-4}$ ,  $\langle E^{(\alpha)}(k_n) \rangle = k_n^\alpha \langle E(k_n) \rangle$ , and  $\langle H^{(\beta)}(k_n) \rangle = k_n^{\beta-1} \langle H(k_n) \rangle$ . Combining the above expressions all temperatures are related to  $A$  by

$$\frac{A^{(\alpha)}}{A} = \frac{D(k_E) k_{E^{(\alpha)}}^{-\alpha} - D(k_{E^{(\alpha)}}) k_{n_f}^{-\alpha}}{D(k_{E^{(\alpha)}}) k_{n_f}^{-\alpha} k_{E^{(\alpha)}}^\alpha - D(k_E)}, \quad (27)$$

$$\frac{B^{(\beta)}}{B} = \frac{(1 + k_{H^{(\beta)}}^\alpha \frac{A^{(\alpha)}}{A}) D(k_H) k_{n_f}^{\beta-1} k_H^2 - (1 + k_H^\alpha \frac{A^{(\alpha)}}{A}) D(k_{H^{(\beta)}}) k_{H^{(\beta)}}^{\beta+1}}{(1 + k_H^\alpha \frac{A^{(\alpha)}}{A}) D(k_{H^{(\beta)}}) k_{H^{(\beta)}}^{2\beta} - (1 + k_{H^{(\beta)}}^\alpha \frac{A^{(\alpha)}}{A}) D(k_H) k_{n_f}^{\beta-1} k_H^{\beta+1}}, \quad (28)$$

$$\frac{B}{A} = \frac{D(k_E) k_{n_f} (1 + k_H^\alpha \frac{A^{(\alpha)}}{A})^2}{D(k_H) k_H (1 + k_E^\alpha \frac{A^{(\alpha)}}{A}) (k_H + k_H^\beta \frac{B^{(\beta)}}{B})}. \quad (29)$$

TABLE I. Approximate dissipation scales used in (27)–(29) for best fits of (21) and (22) with the simulated energy and helicity spectra in Figs. 4(c) and 4(d).

Submodel	$k_E$	$k_{E^{(\alpha)}}$	$k_H$	$k_{H^{(\beta)}}$
1	$4.2 \times 10^3$	$2.5 \times 10^3$	$2.5 \times 10^3$	$4.2 \times 10^3$
2	$1.0 \times 10^4$	$5.0 \times 10^2$	$4.5 \times 10^3$	$4.1 \times 10^2$
3	$4.2 \times 10^3$	$3.0 \times 10^3$	$5.5 \times 10^3$	$4.0 \times 10^3$
4	$5.0 \times 10^1$	$6.5 \times 10^4$	$6.5 \times 10^4$	$5.0 \times 10^1$

Inserting (27)–(29) into (21) and (22), Figs. 4(e) and 4(f) show the submodel equilibrium spectra with  $A = 1 \times 10^3$  [for offsets comparable to Figs. 4(c) and 4(d)] and  $n_f = 30$  (as in simulations) using the dissipation scales listed in Table I obtained from best fits to the simulated spectra in Figs. 4(c) and 4(d) and corresponding pseudoinvariant spectra (not shown).

Comparing the simulated spectra  $\langle E_n \rangle$  and  $\langle H_n \rangle$  of submodels 1–3 with the equilibrium spectra, one finds that they agree well, suggesting equipartitioning of the energy ( $E_n$ ) and pseudoenergy ( $k_n^\alpha E_n$ ) for  $k_n < k_{n_f}$ . As in the coupled model case the weak positive scaling of  $\langle E_n \rangle$  simulated by submodels 1 and 3 is due to an insufficiently short spectral range connecting the forcing scale with the large-scale sink, which is evident from equivalent simulations using a smaller forcing scale (not shown). The simulated  $\langle H_n \rangle$  spectra of submodels 1–3 also match the expected equilibrium spectra in Fig. 4(f) for  $k_n < k_{n_f}$ , which remarkably even captures the small dip exhibited by submodel 2.

Before moving on to submodel 4 let us consider the scaling behavior for wave numbers  $k_n > k_{n_f}$  of submodels 1–3. In this spectral range energy fluxes are constant, which is fulfilled if the correlators scale as  $\Delta_n^{-s',s''} \sim \text{const.}$ , implying velocity components scaling as  $u_n^\pm \sim k_n^{-1/3}$ . One would thus expect  $\langle E_n \rangle \sim k_n^{-2/3}$ , which is indeed found to be the case. The energy and helicity fluxes indicate dual downscale (forward) cascades of both quantities in submodels 1–3 [Figs. 4(a) and 4(b)]. Brissaud *et al.* [11] envisaged that such dual downscale cascades would manifest themselves by the helicity spectrum scaling linearly with the energy spectrum, i.e.,  $\langle E_n \rangle \sim \langle H_n \rangle \sim k_n^{-2/3}$ , which is here indeed found to be the case [Fig. 4(d)], similarly to the coupled model [Fig. 3(a)].

The energy and helicity spectra of submodel 4 do not resemble their equilibrium spectra, suggesting that equipartitioning of flow invariants is not responsible for the shapes of the spectra. Following the above K41 scaling argument one might expect the energy spectrum to scale as  $\sim k_n^{-2/3}$  for  $k_n < k_{n_f}$  due to the energy cascade and as  $\sim k_n^{-4/3}$  for  $k_n > k_{n_f}$  due to the helicity cascade (by a similar argument), but this is clearly not the case for  $k_n < k_{n_f}$ . The failure of the K41 argument may be understood from the specific ratios  $\langle \Pi_n^E \rangle / \langle \Pi_n^H \rangle$  in the two inertial ranges of the flow which allow the correlators to be scale dependent while simultaneously supporting constant energy and helicity fluxes. In submodel 4 helical modes of opposite signs do not interact, thus if there is no pumping of a specific sign of helicity, all modes of that sign will decay. In this case the correlators reduce to  $\Delta_n^{+,+,+} = \Delta_n^{-,+,+} = 2k_{n-1} \text{Re}[u_{n-1}^{+,*} u_n^{+,*} u_{n+1}^+] \equiv \Delta_n^*$ . Calculating the ratio  $\langle \Pi_n^E \rangle / \langle \Pi_n^H \rangle$  by inserting  $\Delta_n^*$  into (16) and

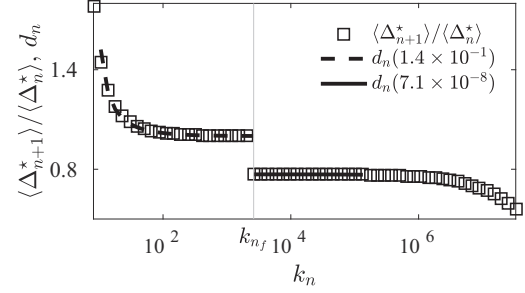


FIG. 5. Simulated submodel 4 correlator ratios (squares) and predicted ratios based on (30) (solid and dashed lines).

(17), one finds the exact relation

$$\frac{\langle \Delta_{n+1}^* \rangle}{\langle \Delta_n^* \rangle} = \frac{\epsilon^{+,+} - k_n \langle \Pi_n^E \rangle / \langle \Pi_n^H \rangle - 1}{1 - k_n \langle \Pi_n^E \rangle / \langle \Pi_n^H \rangle} \equiv d_n(\langle \Pi_n^E \rangle / \langle \Pi_n^H \rangle), \quad (30)$$

which may be scale sensitive depending on  $\langle \Pi_n^E \rangle / \langle \Pi_n^H \rangle$ . The simulated ratios are found to be  $\langle \Pi_n^E \rangle / \langle \Pi_n^H \rangle = 1.4 \times 10^{-1}$  in the inertial range  $k_n < k_{n_f}$  (shell 10–28 average) and  $\langle \Pi_n^E \rangle / \langle \Pi_n^H \rangle = 7.1 \times 10^{-8}$  in the inertial range  $k_n > k_{n_f}$  (shell 32–45 average). Using these ratios Fig. 5 shows the simulated  $\langle \Delta_{n+1}^* \rangle / \langle \Delta_n^* \rangle$  values compared to the anticipated  $d_n$  forms, plotted only in their valid ranges where fluxes are constant. The correlators clearly exhibit scale dependence for  $k_n < k_{n_f}$  following  $d_n$ , thus suggesting that the K41 argument leading to  $\langle E_n \rangle \sim k_n^{-2/3}$  is not necessarily valid.

The new shell model introduced here is obtained from the helical decomposition of the NSE. It is remarkable that the three helical interactions per shell of each submodel are similar to those of the helically decomposed GOY and Sabra submodels apart from the interaction coefficients [6–10]. Benzi *et al.* [7] implemented the four helical submodels in a GOY model. Interestingly, the (absolute) values of  $\epsilon^{s',s''}$  indicate that the new model, similarly to the GOY model, consists of two submodels (1 and 4) with canonical 2D and 3D  $\epsilon^{s',s''}$  configurations and one new 3D type (Sec. II). The last submodel (submodel 2) was found by Benzi *et al.* [7] to show signs of a reverse energy cascade, a property not shared by the new model in its nearest-neighbor limit (multiple free parameter combinations were tested as specified below; not shown).

Recent work by De Pietro *et al.* [10] also numerically investigated the Sabra model equivalent of submodel 2, finding the energy spectrum scaling as  $\langle E_n \rangle \sim k_n^{-0.28}$  for wave numbers  $k_n < k_{n_f}$ , as opposed to the energy/pseudoenergy equipartitioning found here. In order to test the possible influence of the choice of free parameters on the scaling properties of the new submodel 2 multiple parameter combinations were considered:  $\lambda = \{1.3, 1.4, 1.5\}$ ,  $k_0 = \{0.5, 1.4\}$ ,  $N = \{81, 63, 52\}$ ,  $n_f = \{30, 40, 50\}$ , and  $v_L = \{10^1, 10^2, 10^3\}$  (with different large-scale drag exponents:  $-2, -4$ ). All these configurations, which each properly closes triads as required by the NSE ( $\lambda \leq \varphi$ ), were found to behave similarly to the above results (not shown). If, on the other hand, the shell spacing  $\lambda$  exceeds the golden ratio  $\varphi$  (open triads), we find scaling behavior matching that found by De Pietro

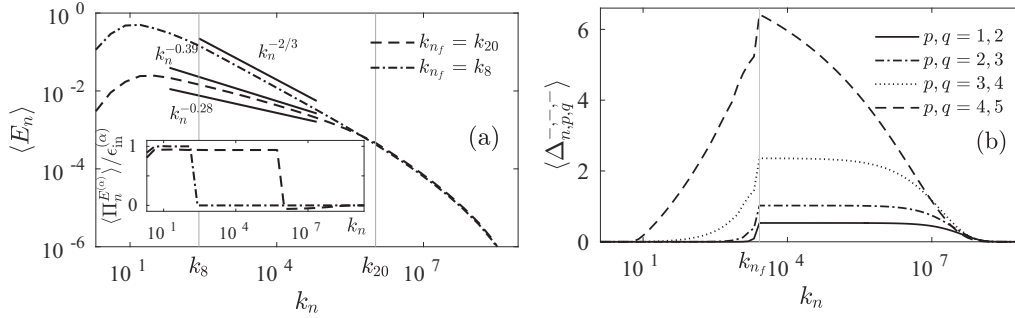


FIG. 6. (a) Simulated energy spectra of submodel 2 when configured as by De Pietro *et al.* [10] ( $\lambda = 2$  with  $k_{n_f} = k_8$  or  $k_{n_f} = k_{20}$ ) and (b) simulated energy correlators of submodel 2 ranging from nearest-neighbor  $\{p, q\} = \{1, 2\}$  (local) interactions to non-nearest-neighbor (nonlocal) interactions. Panel (a) additionally shows the existence of a reverse pseudoenergy cascade (normalized by the mean pseudoenergy input  $\epsilon_{in}^{(\alpha)} = k_{n_f}^\alpha \epsilon_{in}$ ).

*et al.* [10]. Figure 6(a) shows the simulated energy spectrum of submodel 2 configured approximately as by De Pietro *et al.* [10], with  $\lambda = 2$ ,  $N = 31$ ,  $\nu_L = 1$ , and  $\nu = 10^{-12}$ , forced either at shell  $n_f = 8$  or at shell  $n_f = 20$  using a helical forcing (a nonhelical forcing produces similar results; not shown). Here, however, we suggest that the scaling  $\langle E_n \rangle \sim k_n^{2\alpha/3} = k_n^{-0.39}$  for  $k_n < k_{n_f}$  arising from the reverse cascade of pseudoenergy [Fig. 6(a)] is a better fit compared to  $\langle E_n \rangle \sim k_n^{-0.28}$  based on a suggested zero-mode solution [10]. Note that the pseudo-invariants are shared between the two models since the interaction coefficients are related by  $\epsilon_{(Sabra)}^{s',s''} = s' \epsilon^{s',s''}$  and  $\xi_{(Sabra)}^{s',s''} = -s'' \xi^{s',s''}$ , leading to the same conservation constraint, (14), for the Sabra model.

Similarly to De Pietro *et al.* [10] we also find the flatnesses among the uncoupled submodels to be largest in submodel 1 for  $k_n > k_{n_f}$ , although they did not consider submodel 3.

Finally, De Pietro *et al.* [10] found that the direction of the energy cascade in a Sabra-type submodel 2 depends on triad shape as suggested by Waleffe [1]. By extending the interaction scope to interactions between shells  $\{n, n + p, n + q\}$  for  $0 < p < q$  ( $\{p, q\} = \{1, 2\}$  being the nearest-neighbor limit considered above), nonlocal triads (smallest-to-middle wave-number ratio  $< 0.278$ ) may be constructed, allowing the predicted F- to R-class transition to be investigated. Doing so, they explained the cascade transition by noting the time-averaged energy correlators of submodel 2,  $\langle \Delta_{n,p,q}^{-,s',s''} \rangle = \langle \Delta_{n,p,q}^{-,-,-} \rangle$ , are asymptotically constant (independent of  $n$ ) within inertial ranges. If so, the time-averaged non-nearest-neighbor equivalent of (16) (see Appendix D) becomes  $\langle \Pi_n^E \rangle = ((q - 1) + (q - p - 1)\epsilon_{p,q}^{-,-}) \langle \Delta_{n,p,q}^{-,-,-} \rangle \equiv F_{p,q} \langle \Delta_{n,p,q}^{-,-,-} \rangle$ , and the sign of  $F_{p,q}$  determines the cascade direction as a function of the triad shape (determined by  $\{\lambda, p, q\}$ ) since the sign of  $\langle \Delta_{n,p,q}^{-,-,-} \rangle$  may be determined from a linear stability analysis and is shape independent. However, because of the dissimilar correlator definitions between the Sabra model and the new model, the energy correlators of the new model might behave differently. In order to test this three additional simulations were carried out for the non-nearest-neighbor interactions  $\{p, q\} = \{2, 3\}, \{3, 4\}, \{4, 5\}$  (implying  $\epsilon_{p,q}^{-,-} = \{-6.31, -5.85, -5.50\}$ , respectively) using configurations otherwise similar to the submodel 2 setup described in Sec. IV (details on the non-nearest-neighbor interaction models is presented in Ap-

pendixes A–D). The simulated correlators are shown in Fig. 6(b) and are found to exhibit scale dependence with decreased interaction locality (large  $p, q$ ), suggesting that some other explanation is needed for the reversal of the energy cascade in the nonlocal triad limit (not shown). This will be the focus of a subsequent study considering in detail the role played by pseudo-invariants, which will be published elsewhere.

Gilbert *et al.* [14] showed that a regular Sabra model in the 2D configuration  $\epsilon^{+,+} > 1$ , corresponding to submodel 4 here, exhibits different  $\langle E_n \rangle$  scaling regimes depending on the value of  $\epsilon^{+,+}$ . Their work suggests that whenever  $\epsilon^{+,+}/\lambda < 1 + \lambda^{-2/3}$  the reverse energy flux regime should be accompanied by a proper K41 scaling energy spectrum, whereas above this critical value a quasiequilibrium energy spectrum should develop. Inserting  $\epsilon^{+,+}$  from (12) one would thus always expect a K41 scaling to occur. However, present simulations can hardly be said to scale as  $\langle E_n \rangle \sim k_n^{-2/3}$  or to be in quasiequilibrium for  $k_n < k_{n_f}$ . In order to further compare submodel 4 with their work, additional simulations were therefore conducted using  $\lambda = \{1.1, 1.2, 1.3, 1.4, 1.5, 1.6, 2.0\}$  with  $N = \{146, 76, 53, 41, 37, 34, 22\}$ , respectively (ensuring  $k_N$  are approximately the same). In all cases energy spectra were found to behave as in Fig. 4(c) (not shown), suggesting that the work by Gilbert *et al.* [14] does not carry over to submodel 4 of the new model.

## V. SUMMARY

The role of helicity in 3D turbulence was numerically investigated in the context of a new shell model obtained as a special case of the helically decomposed Navier-Stokes equation (NSE) [1]. Unlike previous shell models, the new model can couple the four naturally occurring subsets of helical triadic interactions (subinteractions) similarly to the NSE, thereby allowing their individual roles to be investigated in a coupled context. By considering forcing scenarios with and without an input of helicity we find that the (forward) energy cascade in helical turbulence is less intermittent than that in nonhelical turbulence for local triadic interactions. The energy cascade in helical turbulence was found to be carried almost entirely by subinteractions of the third type,

whereas in nonhelical turbulence the cascade is partitioned roughly equally between subinteraction 1 and subinteraction 3. This large influence exerted by subinteractions 1 and 3 matches expectations based on real 3D turbulence, in which these subinteractions are thought to exclusively contribute to a forward energy cascade [1]. Additionally, by varying the resolved triad shape we find no change in simulated behavior or cascade partitioning, albeit only relatively local triads (similar leg sizes) are possible in the nearest-neighbor interaction limit considered here.

In order to understand the decreased intermittency arising from a net helicity input the four individual subinteractions (submodels) were simulated separately (uncoupled) in the limit of local triadic interactions, which share several similarities with the four existing helically decomposed Sabra shell models. These simulations showed that the cascade intermittency of submodel 1 far exceeds the other three, thus explaining the decreased intermittency in helical turbulence where subinteraction type 1 is suppressed when coupled with the other three.

In accordance with expectations three of the four submodels (submodels 1–3) contribute with dual downscale (forward) cascades of energy and helicity, whereas the last submodel (submodel 4), which renders both signs of helicity separately inviscidly conserved (enstrophy-like), transfers energy upscale and helicity downscale.

In the coupled model and the three dual-cascading submodels (submodels 1–3) flow invariants were found to equipartition in the range of scales  $k_n < k_{n_f}$  ( $k_{n_f}$  being the forcing scale), which was explained using the equipartition theorem with multiple conserved quadratic quantities. The remaining submodel 4, however, exhibits a reverse energy cascade for  $k_n < k_{n_f}$  but has a very small weight in comparison to the other submodels in the full set of triadic interactions of the helically decomposed dynamics. By investigating the scaling behavior of the triple correlations used in energy and helicity flux calculations of submodel 4, it was found these cannot

necessarily be assumed to be scale independent within inertial ranges. If so, as was found to be the case numerically, this prevents the traditional shell model K41-style argument from being used, otherwise leading to an anticipated  $\langle E(k_n) \rangle \sim k_n^{-2/3}$  scaling energy spectrum within energy cascade regimes.

## APPENDIX A: THE NEW SHELL MODEL

In order to obtain the new model from the helically decomposed Navier-Stokes equation (NSE), (3), it is necessary to impose two constraints: (i) spectral velocity components are assumed to be independent of direction in  $\mathbf{k}$  space,  $u_s(\mathbf{k}) = u_s(k\hat{\mathbf{k}}) = u_s(k)$ , and (ii) reducing  $\mathbf{k}$  space to include only components which are increasingly spaced in magnitude according to the geometrical progression  $k_n = k_0\lambda^n$  for  $n = 0, 1, \dots, N$ . Within this wave set, only cross-scale triadic interactions are considered, i.e., triads in which all three wave components have different magnitudes, which is inspired by the structure of the GOY and Sabra shell models. Since only cross-magnitude interactions are considered, it is useful to split the triadic sum in the NSE, (3), into three separate sums, hereafter referred to as the three triad *groups*, for which  $\mathbf{k}$  is the smallest ( $k < k' < k''$ ), middle ( $k' < k < k''$ ), and largest ( $k' < k'' < k$ ) wave number. Note that double-primed vectors are chosen to be larger than single-primed ones, which leads to no loss of generality due to symmetry when interchanging the dummy waves  $\mathbf{k}' \leftrightarrow \mathbf{k}''$  (and  $s' \leftrightarrow s''$ ). Additionally, the vectorial condition  $\mathbf{k} + \mathbf{k}' + \mathbf{k}'' = 0$  on each triadic sum can be rewritten by expressing the largest mode as the sum of the two smaller and absorbing the resulting negative signs into the terms of the sums using reality  $\mathbf{u}(-\mathbf{k}) = \mathbf{u}^*(\mathbf{k})$  and the basis property  $\mathbf{h}_s(-\mathbf{k}) = \mathbf{h}_{-s}(\mathbf{k})$  [1]. The vectorial condition on each triadic sum thus becomes  $\mathbf{k} + \mathbf{k}' = \mathbf{k}''$ ,  $\mathbf{k} + \mathbf{k}'' = \mathbf{k}'$ , and  $\mathbf{k} = \mathbf{k}' + \mathbf{k}''$  for groups 1, 2, and 3, respectively, and the NSE, (3), then takes the form

$$\begin{aligned}
 (\partial_t + \nu k^2)u_s(\mathbf{k}) = & -\frac{1}{4} \sum_{s', s''} \left[ \sum_{\substack{\mathbf{k} + \mathbf{k}' = \mathbf{k}'' \\ k < k' < k''}} (s'k' - s''k'') \mathbf{h}_{s'}^*(\mathbf{k}') \times \mathbf{h}_{-s''}^*(\mathbf{k}'') \cdot \mathbf{h}_s^*(\mathbf{k}) u_{s'}^*(\mathbf{k}') u_{s''}(\mathbf{k}'') \right. \\
 & - \sum_{\substack{\mathbf{k} + \mathbf{k}' = \mathbf{k}'' \\ k' < k < k''}} (s'k' - s''k'') \mathbf{h}_s^*(\mathbf{k}) \times \mathbf{h}_{-s''}^*(\mathbf{k}'') \cdot \mathbf{h}_{s'}^*(\mathbf{k}') u_{s'}^*(\mathbf{k}') u_{s''}(\mathbf{k}'') \\
 & \left. + \sum_{\substack{\mathbf{k} = \mathbf{k}' + \mathbf{k}'' \\ k' < k'' < k}} (s'k' - s''k'') \mathbf{h}_{-s''}^*(\mathbf{k}'') \times \mathbf{h}_s^*(\mathbf{k}) \cdot \mathbf{h}_{s'}^*(\mathbf{k}') u_{s'}(\mathbf{k}') u_{s''}(\mathbf{k}'') \right] \quad (\text{A1})
 \end{aligned}$$

where the antisymmetric property of  $\mathbf{h}_{s'}^*(\mathbf{k}') \times \mathbf{h}_{s''}^*(\mathbf{k}'') \cdot \mathbf{h}_s^*(\mathbf{k})$  has been used to rearrange the order of basis components in a way which shall be useful later.

In the interest of dropping the direction dependencies  $\hat{\mathbf{k}}$ ,  $\hat{\mathbf{k}}'$ , and  $\hat{\mathbf{k}}''$ , consider further splitting the three triadic sums in (A1) into sums over triad shapes and triad orientations,

respectively,

$$\sum_{\substack{\mathbf{k}+\mathbf{k}'=\mathbf{k}'' \\ k < k' < k''}} = \sum_{\substack{k', k'' \\ k+k' \geq k'' \\ k < k' < k''}} \sum_{\substack{\hat{\mathbf{k}}, \hat{\mathbf{k}}'' \\ k\hat{\mathbf{k}}+k'\hat{\mathbf{k}}'=k''\hat{\mathbf{k}}''}} , \quad (\text{A2})$$

$$\sum_{\substack{\mathbf{k}+\mathbf{k}'=\mathbf{k}'' \\ k' < k < k''}} = \sum_{\substack{k', k'' \\ k+k' \geq k'' \\ k' < k < k''}} \sum_{\substack{\hat{\mathbf{k}}, \hat{\mathbf{k}}'' \\ k\hat{\mathbf{k}}+k'\hat{\mathbf{k}}'=k''\hat{\mathbf{k}}''}} , \quad (\text{A3})$$

$$\sum_{\substack{\mathbf{k}=\mathbf{k}'+\mathbf{k}'' \\ k' < k'' < k}} = \sum_{\substack{k', k'' \\ k'+k'' \geq k \\ k' < k'' < k}} \sum_{\substack{\hat{\mathbf{k}}, \hat{\mathbf{k}}'' \\ k\hat{\mathbf{k}}=k'\hat{\mathbf{k}}'+k''\hat{\mathbf{k}}''}} . \quad (\text{A4})$$

From here, reducing the  $\mathbf{k}$  space to include only components with magnitudes given by  $k_n = k_0 \lambda^n$  allows the three sums

over triad shapes to be rejoined: Depending on  $\lambda$ , the triangle inequality constrains the possible choices of  $n$  in  $k_n$  which can be combined to construct triads. Consider therefore the range of integers  $p$  and  $q$  sorted by  $0 < p < q$  which fulfill the triangle inequality  $k_n + k_{n+p} \geq k_{n+q}$ , thereby allowing any triad geometry to be constructed when  $\lambda \rightarrow 1$  for large or small enough values of  $\{p, q\}$ . From this reduction it immediately follows that  $\{k', k''\} = \{k_{n+p}, k_{n+q}\}$  for the first group, thus turning the sum over  $\{k', k''\}$  into a sum over  $\{p, q\}$ . The corresponding  $\{k', k''\}$  sums of groups 2 and 3 may be written in terms of the same  $\{p, q\}$  sum as group 1 by noting that the constraints imposed by (A3) and (A4) are, respectively, fulfilled if  $\{k', k''\} = \{k_{n-p}, k_{n+q-p}\}$  and  $\{k', k''\} = \{k_{n-q}, k_{n+p-q}\}$ , which produces triad shapes similar to group 1. Substituting in the above, one finds

$$\begin{aligned} (\partial_t + \nu k_n^2) u_s(k_n \hat{\mathbf{k}}) = & -\frac{1}{4} k_n \sum_{\substack{p, q \\ 0 < p < q \\ k_n + k_{n+p} \geq k_{n+q}}} \sum_{s', s''} \left[ \sum_{\substack{\hat{\mathbf{k}}, \hat{\mathbf{k}}'' \\ k_n \hat{\mathbf{k}} + k_{n+p} \hat{\mathbf{k}}' = k_{n+q} \hat{\mathbf{k}}''}} (s' \lambda^p - s'' \lambda^q) \mathbf{h}_s^*(k_{n+p} \hat{\mathbf{k}}') \times \mathbf{h}_{-s''}^*(k_{n+q} \hat{\mathbf{k}}'') \cdot \mathbf{h}_s^*(k_n \hat{\mathbf{k}}) u_{s'}^*(k_{n+p} \hat{\mathbf{k}}') u_{s''}^*(k_{n+q} \hat{\mathbf{k}}'') \right. \\ & - \sum_{\substack{\hat{\mathbf{k}}, \hat{\mathbf{k}}'' \\ k_n \hat{\mathbf{k}} + k_{n-p} \hat{\mathbf{k}}' = k_{n+q-p} \hat{\mathbf{k}}''}} \frac{s' - s'' \lambda^q}{\lambda^p} \mathbf{h}_s^*(k_n \hat{\mathbf{k}}) \times \mathbf{h}_{-s''}^*(k_{n+q-p} \hat{\mathbf{k}}'') \cdot \mathbf{h}_s^*(k_{n-p} \hat{\mathbf{k}}') u_{s'}^*(k_{n-p} \hat{\mathbf{k}}') u_{s''}^*(k_{n+q-p} \hat{\mathbf{k}}'') \\ & \left. + \sum_{\substack{\hat{\mathbf{k}}, \hat{\mathbf{k}}'' \\ k_n \hat{\mathbf{k}} = k_{n-q} \hat{\mathbf{k}}' + k_{n+p-q} \hat{\mathbf{k}}''}} \frac{s' - s'' \lambda^p}{\lambda^q} \mathbf{h}_{-s''}^*(k_{n+p-q} \hat{\mathbf{k}}'') \times \mathbf{h}_s^*(k_n \hat{\mathbf{k}}) \cdot \mathbf{h}_{-s'}^*(k_{n-q} \hat{\mathbf{k}}') u_{s'}^*(k_{n-q} \hat{\mathbf{k}}') u_{s''}^*(k_{n+p-q} \hat{\mathbf{k}}'') \right]. \quad (\text{A5}) \end{aligned}$$

Dropping now the direction dependencies  $\hat{\mathbf{k}}$ ,  $\hat{\mathbf{k}}'$ , and  $\hat{\mathbf{k}}''$ , the compact shell model notation  $u_n^{s,*} = u_s^*(k_n)$  is adopted. Moreover, because only one mode per magnitude is resolved, the inner sums over  $\{\hat{\mathbf{k}}, \hat{\mathbf{k}}'\}$  (triad orientation) are also dropped. Having assumed direction independence, the rotational term (complex exponential) in the geometry term is assumed to be discardable, allowing it to be written more compactly as

$$\begin{aligned} & \mathbf{h}_s^*(\mathbf{k}') \times \mathbf{h}_{s''}^*(\mathbf{k}'') \cdot \mathbf{h}_s^*(\mathbf{k}) \\ &= -\frac{Q(k, k', k'')}{2kk'k''} s s' s'' (s k + s' k' + s'' k'') \\ &\equiv \Lambda_{s', s'', s}(k', k'', k) = \Lambda_{s', s'', s}(\lambda^p, \lambda^q, 1) \equiv \Lambda_{s', s'', s}^{p, q}, \quad (\text{A6}) \end{aligned}$$

where (i) the group 1 associations  $\{k', k''\} = \{k_{n+p}, k_{n+q}\}$  are used in the  $\Lambda_{s', s'', s}^{p, q}$  definition (groups 2 and 3 could equally have been used), (ii) the scale-independent property  $\Lambda_{s', s'', s}(k_{n+p}, k_{n+q}, k_n) = \Lambda_{s', s'', s}(\lambda^p, \lambda^q, 1)$  has been used (i.e., only relative leg sizes matter), and (iii)  $Q(k, k', k'') = (2k^2 k'^2 + 2k'^2 k''^2 + 2k''^2 k^2 - k^4 - k'^4 - k''^4)^{1/2}$  (see Waleffe [1] for details). With this compacted notation Eq. (A5) may then be

written as

$$\begin{aligned} & (d_t + \nu k_n^2) u_n^s \\ &= -\frac{1}{4} k_n \sum_{\substack{p, q \\ 0 < p < q \\ k_n + k_{n+p} \geq k_{n+q}}} \sum_{s', s''} \left[ (s' \lambda^p - s'' \lambda^q) \Lambda_{s', -s'', s}^{p, q} u_{n+p}^{s',*} u_{n+q}^{s''*} \right. \\ & \quad - \frac{s' - s'' \lambda^q}{\lambda^p} \Lambda_{s, -s'', s'}^{p, q} u_{n-p}^{s',*} u_{n+q-p}^{s''*} \\ & \quad \left. + \frac{s' - s'' \lambda^p}{\lambda^q} \Lambda_{-s'', s, -s'}^{p, q} u_{n-q}^{s',*} u_{n+p-q}^{s''*} \right] \quad (\text{A7}) \end{aligned}$$

by using the scale-independent property of  $\Lambda_{s', s'', s}^{p, q}$ , allowing all wave magnitudes in the geometry terms of groups 2 and 3 in (A5) to be multiplied through by  $\lambda^p$  and  $\lambda^q$ , respectively.

This expression is in fact a weighted sum of four helical shell models in disguise. To realize this, one needs to expand the sum over helical signs. Doing so, one finds three terms per  $\{s', s''\}$  contribution involving

- (i)  $\Lambda_{+, -, +}^{p, q}$ ,  $\Lambda_{+, -, +}^{p, q}$ ,  $\Lambda_{-, +, -}^{p, q}$  for  $\{s', s''\} = \{+, +\}$ ,
- (ii)  $\Lambda_{+, +, +}^{p, q}$ ,  $\Lambda_{+, +, +}^{p, q}$ ,  $\Lambda_{+, +, -}^{p, q}$  for  $\{s', s''\} = \{+, -\}$ ,
- (iii)  $\Lambda_{-, -, +}^{p, q}$ ,  $\Lambda_{-, -, +}^{p, q}$ ,  $\Lambda_{-, +, +}^{p, q}$  for  $\{s', s''\} = \{-, +\}$ ,
- (iv)  $\Lambda_{-, +, +}^{p, q}$ ,  $\Lambda_{+, +, -}^{p, q}$ ,  $\Lambda_{+, +, +}^{p, q}$  for  $\{s', s''\} = \{-, -\}$ .

Collecting terms sharing  $\Lambda$  using the reflection property  $\Lambda_{-s',-s'',-s}^{p,q} = \Lambda_{s',s'',s}^{p,q}$  and defining  $G_{p,q}(\lambda) = 1/8 Q(1, \lambda^p, \lambda^q)/(\lambda^p \lambda^q)$ , the new shell model is uncovered,

$$(d_l + D_n)u_n^s = sk_n \sum_{\substack{p,q \\ 0 < p < q \\ k_n + k_{n+p} \geq k_{n+q}}} G_{p,q} \sum_{s',s''} g_{p,q}^{s',s''} \left( u_{n+p}^{s-s',*} u_{n+q}^{s-s'',*} - \frac{\epsilon_{p,q}^{s',s''}}{\lambda^p} u_{n-p}^{s-s',*} u_{n+q-p}^{s-s'',*} + \frac{\xi_{p,q}^{s',s''}}{\lambda^q} u_{n-q}^{s-s''} u_{n+p-q}^{s-s'} \right), \quad (\text{A8})$$

where  $\lambda$  and  $k_0$  are free parameters and  $D_n \equiv \nu k_n^2$ . The helical signs of the interacting modes depend on the specific  $\{s', s''\}$  set, here written compactly by introducing effective signs built on products of  $s$ ,  $s'$ , and  $s''$ , e.g.,  $s \cdot s'$ . The triad shape weight  $G_{p,q}$ , submodel weight  $g_{p,q}^{s',s''}$ , and modal interaction coefficients  $\epsilon_{p,q}^{s',s''}$  and  $\xi_{p,q}^{s',s''}$  are given by

$$G_{p,q}(\lambda) = 1/8 (2\lambda^{-2q} + 2\lambda^{-2p} + 2 - \lambda^{-2(p+q)} - \lambda^{2(p-q)} - \lambda^{2(q-p)})^{1/2}, \quad (\text{A9})$$

$$g_{p,q}^{s',s''}(\lambda) = -s's''(1 + s'\lambda^p - s''\lambda^q)(s'\lambda^p - s''\lambda^q), \quad (\text{A10})$$

$$\epsilon_{p,q}^{s',s''}(\lambda) = \frac{1 - s''\lambda^q}{\lambda^p - s's''\lambda^q}, \quad (\text{A11})$$

$$\xi_{p,q}^{s',s''}(\lambda) = -s''(1 - s'\epsilon_{p,q}^{s',s''}). \quad (\text{A12})$$

#### APPENDIX B: INTERACTION WEIGHTS

The functional forms of the three interaction coefficients  $g_{p,q}^{s',s''}$ ,  $\epsilon_{p,q}^{s',s''}$ , and  $\xi_{p,q}^{s',s''}$  in their local limit are addressed in Sec. II. Figure 7 shows plots of the remaining triad shape weight  $G_{p,q}$ , ranging from the limit of local interactions ( $\{p, q\} = \{1, 2\}$ ) to nonlocal ( $q = p + 1$ ,  $p \gg 1$ ) [Fig. 7(a)] and reduced nonlocal ( $q = p + i$ , where  $1 \leq i \leq 3$ ) interactions [Fig. 7(b)]. Three important results are noticed here. First, the K41 assumption of local interactions being dominant is supported by  $G_{p,q}$ . Second,  $G_{p,q}$  is proportional to the area of the triangle formed by  $\{k, k', k''\}$ , thereby automatically ensuring that the triangle inequality is fulfilled by  $G_{p,q} = 0$  if  $k_n + k_{n+p} < k_{n+q}$ . Consequently, interactions are well defined only for

$1 \leq \lambda \leq \varphi$ , where  $\varphi$  is the golden ratio. Third, reducing the nonlocalness of interactions by tending towards coupling three different scales weighs less compared to interactions involving two comparable scales [ $p \sim q$  in Fig. 7(b)].

#### APPENDIX C: INVARIANTS

In the helical basis the energy and helicity take the simple form  $E = \sum_{n=0}^N (|u_n^+|^2 + |u_n^-|^2)$  and  $H = \sum_{n=0}^N k_n (|u_n^+|^2 - |u_n^-|^2)$ , where  $n = 0$  and  $n = N$  are the first and last shells [1]. Here, however, we consider generalized quadratic invariants as introduced in Sec. I. Consider therefore the generalized energy-like and helicity-like quantities

$$E^{(\alpha)} = \sum_{n=0}^N k_n^\alpha (|u_n^+|^2 + |u_n^-|^2), \quad (\text{C1})$$

$$H^{(\beta)} = \sum_{n=0}^N k_n^\beta (|u_n^+|^2 - |u_n^-|^2), \quad (\text{C2})$$

where  $\alpha$  and  $\beta$  are some yet to be determined exponents. In this notation energy is given by  $\alpha = 0$  and helicity by  $\beta = 1$ .

It turns out that each of the four submodels, here defined as the four contributions from  $\sum_{s',s''}$  in (A8) (Sec. II), inviscidly conserve the energy and helicity separately for every triad shape ( $\{p, q, \lambda\}$  set). Taking the time derivative of (C1) using (A8) and telescoping sums by assuming a finite wave set (i.e.,  $u_n^s = 0$  for  $n < 0$  and  $n > N$ ), one finds the nonlinear (N.L.) rate of change of  $E^{(\alpha)}$  is given by the long but straightforward

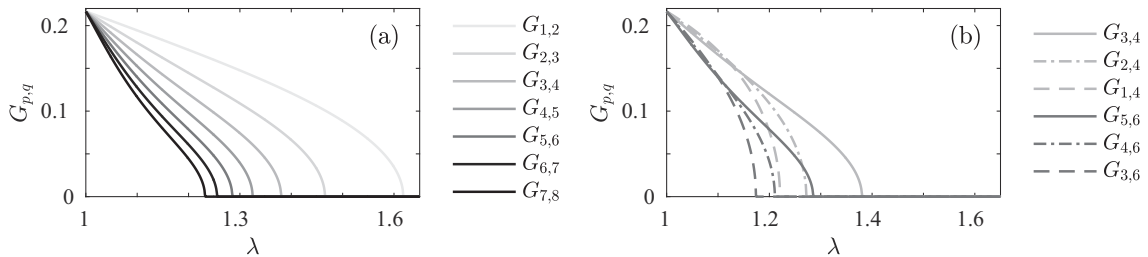


FIG. 7. Triad interaction weight  $G_{p,q}$  as a function of the triad geometry for (a) local ( $\{p, q\} = \{1, 2\}$ ) to nonlocal ( $q = p + 1$ ,  $p \gg 1$ ) triads and (b) reduced nonlocal ( $q = p + i$  where  $1 \leq i \leq 3$ ) triads.

calculation

$$\begin{aligned}
 d_t|_{\text{N.L.}} E^{(\alpha)} &= \sum_{n=0}^N k_n^\alpha (u_n^{+,*} d_t u_n^+ + u_n^{-,*} d_t u_n^-) + \text{c.c.} \\
 &= \sum_{\substack{p,q \\ 0 < p < q \\ k_n + k_{n+p} \geq k_{n+q}}} G_{p,q} \sum_{s',s''} g_{p,q}^{s',s''} \sum_{n=q}^N k_{n-q}^{\alpha+1} [(u_{n-q}^{+,*} u_{n-q+p}^{s',s''} u_n^{s''} - u_{n-q}^{-,*} u_{n-q+p}^{-s',s''} u_n^{-s''}) \\
 &\quad - (\lambda^\alpha)^p \epsilon_{p,q}^{s',s''} (u_{n-q}^{s',*} u_{n-q+p}^{+,*} u_n^{s''} - u_{n-q}^{-s',*} u_{n-q+p}^{-,*} u_n^{-s''}) + (\lambda^\alpha)^q \xi_{p,q}^{s',s''} (u_{n-q}^{s'',*} u_{n-q+p}^{s',*} u_n^+ - u_{n-q}^{-s'',*} u_{n-q+p}^{-s',*} u_n^-)] + \text{c.c.}
 \end{aligned} \tag{C3}$$

From here it is noted that the second and third velocity triple-product differences are equal to the first times  $s'$  and  $s''$ , respectively, that is,

$$\begin{aligned}
 &u_{n-q}^{s',*} u_{n-q+p}^{+,*} u_n^{s''} - u_{n-q}^{-s',*} u_{n-q+p}^{-,*} u_n^{-s''} \\
 &= s' (u_{n-q}^{+,*} u_{n-q+p}^{s',*} u_n^{s''} - u_{n-q}^{-,*} u_{n-q+p}^{-s',*} u_n^{-s''})
 \end{aligned} \tag{C4}$$

$$\begin{aligned}
 &u_{n-q}^{s'',*} u_{n-q+p}^{s',*} u_n^+ - u_{n-q}^{-s'',*} u_{n-q+p}^{-s',*} u_n^- \\
 &= s'' (u_{n-q}^{+,*} u_{n-q+p}^{s',*} u_n^{s''} - u_{n-q}^{-,*} u_{n-q+p}^{-s',*} u_n^{-s''}),
 \end{aligned} \tag{C5}$$

thus allowing the triple-product differences to be moved outside the square brackets. A similar calculation may be done for  $H^{(\beta)}$ , yielding a positive sign between the velocity triple products, implying that all three triple-product sums are similar. Tidying up by defining correlators as

$$\Delta_{n,p,q}^{\pm,s',s''} \equiv 2k_{n-q} \text{Re} [u_{n-q}^{+,*} u_{n-q+p}^{s',*} u_n^{s''} \pm u_{n-q}^{-,*} u_{n-q+p}^{-s',*} u_n^{-s''}] \tag{C6}$$

the generalized energy and helicity equations become

$$d_t|_{\text{N.L.}} E^{(\alpha)} = \sum_{\substack{p,q \\ 0 < p < q \\ k_n + k_{n+p} \geq k_{n+q}}} G_{p,q} \sum_{s',s''} g_{p,q}^{s',s''} \mathcal{E}_{p,q}^{s',s''} \sum_{n=q}^N k_{n-q}^\alpha \Delta_{n,p,q}^{-,s',s''} \tag{C7}$$

$$d_t|_{\text{N.L.}} H^{(\beta)} = \sum_{\substack{p,q \\ 0 < p < q \\ k_n + k_{n+p} \geq k_{n+q}}} G_{p,q} \sum_{s',s''} g_{p,q}^{s',s''} \mathcal{H}_{p,q}^{s',s''} \sum_{n=q}^N k_{n-q}^\beta \Delta_{n,p,q}^{+,s',s''} \tag{C8}$$

where the three correlator prefactors in (C3) (and correspondingly for the helicity) have been grouped together

$$\Pi_n^{E^{(\alpha)}} = \sum_{\substack{p,q \\ 0 < p < q \\ k_n + k_{n+p} \geq k_{n+q}}} G_{p,q} \sum_{s',s''} g_{p,q}^{s',s''} \left[ \mathcal{E}_{p,q}^{s',s''} \sum_{m=q}^n k_{m-q}^\alpha \Delta_{m,p,q}^{-,s',s''} + \sum_{m=n+1}^{n+q} k_{m-q}^\alpha \Delta_{m,p,q}^{-,s',s''} - s' \epsilon_{p,q}^{s',s''} \sum_{m=n+1}^{n+q-p} k_{m-q+p}^\alpha \Delta_{m,p,q}^{-,s',s''} \right], \tag{D1}$$

where summation over the shared range  $q \leq m \leq n$  has been grouped together in the first term. This term, however, vanishes since  $\mathcal{E}_{p,q}^{s',s''}(\lambda^\alpha) = 0$  for  $E^{(\alpha)}$  to be an invariant. Going through similar calculations for  $\Pi_n^{H^{(\beta)}}$  one finally finds that the spectral

by

$$\mathcal{E}_{p,q}^{s',s''}(\lambda^\alpha) = 1 - s'(\lambda^\alpha)^p \epsilon_{p,q}^{s',s''} + s''(\lambda^\alpha)^q \xi_{p,q}^{s',s''}, \tag{C9}$$

$$\mathcal{H}_{p,q}^{s',s''}(\lambda^\beta) = 1 - (\lambda^\beta)^p \epsilon_{p,q}^{s',s''} + (\lambda^\beta)^q \xi_{p,q}^{s',s''}. \tag{C10}$$

Equations (C9) and (C10) are in fact equal to the generalized conservation constraints, (6) and (7), imposed by the NSE by noting that  $\{k, k', k''\} = \{k_n, k_{n+p}, k_{n+q}\}$ .

The conservation of  $E^{(\alpha)}$  and  $H^{(\beta)}$  thus requires  $\mathcal{E}_{p,q}^{s',s''}(\lambda^\alpha) = 0$  and  $\mathcal{H}_{p,q}^{s',s''}(\lambda^\beta) = 0$ . Plugging  $\alpha = 0$  into  $\mathcal{E}_{p,q}^{s',s''}(\lambda^\alpha)$  one finds that the energy is always conserved independently of the triad shape  $(\{\lambda, p, q\})$  and submodel  $(\{s', s''\})$ . Other solutions to  $\mathcal{E}_{p,q}^{s',s''}(\lambda^\alpha) = 0$ , however, depend on the specific submodel and triad shape resolved. Since these solutions are not shared across triad shapes or submodels, the remaining invariants can be considered triad shape- and submodel-specific invariants, or *pseudoenergy invariants*, because they are broken when mixing triad shapes and/or submodels, just as in the NSE. In a similar fashion, each submodel inviscidly conserves the helicity ( $\beta = 1$ ) separately for every triad shape since  $\mathcal{H}_{p,q}^{s',s''} = 0$  by substituting (A11) and (A12) in. The remaining helicity-like invariants behave similarly to the energy-like invariants and are thus denoted *pseudohelicity invariants*.

Note that because of the polynomial structure of (C9) and (C10), any triad shape configuration given by  $\{\lambda, p, q\}$  will have  $q - 1$  pseudoenergy invariants and  $q - 1$  pseudohelicity invariants.

#### APPENDIX D: SPECTRAL FLUXES

Nonlinear spectral fluxes of  $E^{(\alpha)}$  and  $H^{(\beta)}$  through the  $n$ th shell are given as the transfers from all wave numbers less than  $k_n$  to wave numbers greater than  $k_n$ , that is,  $\Pi_n^{E^{(\alpha)}} = d_t|_{\text{N.L.}} \sum_{m=0}^n k_m^\alpha (|u_m^+|^2 + |u_m^-|^2)$  and  $\Pi_n^{H^{(\beta)}} = d_t|_{\text{N.L.}} \sum_{m=0}^n k_m^\beta (|u_m^+|^2 - |u_m^-|^2)$ . Following the calculations through, one finds that (C3) becomes (breaking the sum at  $n$  instead of  $N$ )

fluxes are given by

$$\Pi_n^{E^{(\alpha)}} = \sum_{\substack{p,q \\ 0 < p < q \\ k_n + k_{n+p} \geq k_{n+q}}} G_{p,q} \sum_{s',s''} g_{p,q}^{s',s''} \left[ \sum_{m=n+1}^{n+q} k_{m-q}^{\alpha} \Delta_{m,p,q}^{-,s',s''} - s' \epsilon_{p,q}^{s',s''} \sum_{m=n+1}^{n+q-p} k_{m-q+p}^{\alpha} \Delta_{m,p,q}^{-,s',s''} \right], \quad (\text{D2})$$

$$\Pi_n^{H^{(\beta)}} = \sum_{\substack{p,q \\ 0 < p < q \\ k_n + k_{n+p} \geq k_{n+q}}} G_{p,q} \sum_{s',s''} g_{p,q}^{s',s''} \left[ \sum_{m=n+1}^{n+q} k_{m-q}^{\beta} \Delta_{m,p,q}^{+,s',s''} - \epsilon_{p,q}^{s',s''} \sum_{m=n+1}^{n+q-p} k_{m-q+p}^{\beta} \Delta_{m,p,q}^{+,s',s''} \right]. \quad (\text{D3})$$

- 
- [1] F. Waleffe, The nature of triad interactions in homogeneous turbulence, *Phys. Fluids A* **4**, 350 (1992).
- [2] L. Biferale, S. Musacchio, and F. Toschi, Inverse Energy Cascade in Three-Dimensional Isotropic Turbulence, *Phys. Rev. Lett.* **108**, 164501 (2012).
- [3] E. B. Gledzer, System of hydrodynamic type admitting two quadratic integrals of motion, *Soviet Physics Doklady* **18**, 216 (1973).
- [4] V. S. L'vov, E. Podivilov, A. Pomyalov, I. Procaccia, and D. Vandembroucq, Improved shell model of turbulence, *Phys. Rev. E* **58**, 1811 (1998).
- [5] P. D. Ditlevsen, Symmetries, invariants, and cascades in a shell model of turbulence, *Phys. Rev. E* **62**, 484 (2000).
- [6] L. Biferale and R. M. Kerr, Role of inviscid invariants in shell models of turbulence, *Phys. Rev. E* **52**, 6113 (1995).
- [7] R. Benzi, L. Biferale, R. M. Kerr, and E. Trovatore, Helical shell models for three-dimensional turbulence, *Phys. Rev. E* **53**, 3541 (1996).
- [8] L. Biferale, D. Pierotti, and F. Toschi, Helicity transfer in turbulent models, *Phys. Rev. E* **57**, R2515 (1998).
- [9] L. Biferale, D. Pierotti, and F. Toschi, Helicity advection in turbulent models, *J. Phys. IV France* **08**, Pr6-131 (1998).
- [10] M. De Pietro, L. Biferale, and A. A. Mailybaev, Inverse energy cascade in nonlocal helical shell models of turbulence, *Phys. Rev. E* **92**, 043021 (2015).
- [11] A. Brissaud, U. Frisch, J. Leorat, M. Lesieur, and A. Mazure, Helicity cascades in fully developed isotropic turbulence, *Phys. Fluids (1958–1988)* **16**, 1366 (1973).
- [12] P. D. Ditlevsen and I. A. Mogensen, Cascades and statistical equilibrium in shell models of turbulence, *Phys. Rev. E* **53**, 4785 (1996).
- [13] R. Kraichnan and D. Montgomery, Two-dimensional turbulence, *Rep. Prog. Phys.* **43**, 547 (1980).
- [14] T. Gilbert, V. S. L'vov, A. Pomyalov, and I. Procaccia, Inverse Cascade Regime in Shell Models of Two-Dimensional Turbulence, *Phys. Rev. Lett.* **89**, 074501 (2002).

### 7.3 Outlook

The partitioning of the energy cascade between symmetrized helical triad interactions (different from G1–G4) was recently investigated by Alexakis (2017) in a direct numerical simulation of the spectral-helical NSE. Like here, it was found that the energy cascade partitions itself into constant-flux components within the inertial range — an intriguing result since energy conservation implies only the total flux needs to be constant.

Alexakis (2017) furthermore found the partitioning to be unaffected by helicity pumping, suggesting it might be universal. The partitioning was however considered across the entire set of (average of) resolved triad shapes, making it unclear whether the partitioning universality is valid on a per triad shape basis too (i.e. not just a net property of coupled systems). In order to test the partitioning universality, additional shell models simulations could therefore be conducted in which both triad shape and helicity pumping are varied (the latter being in contrast to the two extreme cases considered in study #3, i.e. no helicity and maximal helically forced).

In the popular nearest-neighbour limit of shell models (figure 6.9), however, triad shapes are relatively local (close to equilateral) since the middle and largest triangle sides are merely  $\lambda$  and  $\lambda^2$  times larger than the smallest, respectively, where  $1 < \lambda \leq g$  and  $g$  is the golden ratio. The shell model presented in this paper is meanwhile nonlocal, thereby extending the range of possible relative leg sizes to  $\lambda^p$  and  $\lambda^q$ , respectively, for integers  $1 < p < q$ . The triad interactions resolved by the new shell model can therefore have unrestricted shapes for small enough  $\lambda$  and large enough  $p, q$  (figure 7.1), which is useful for the further investigating the energy cascade partitioning between G1–G4 according to the above ideas.

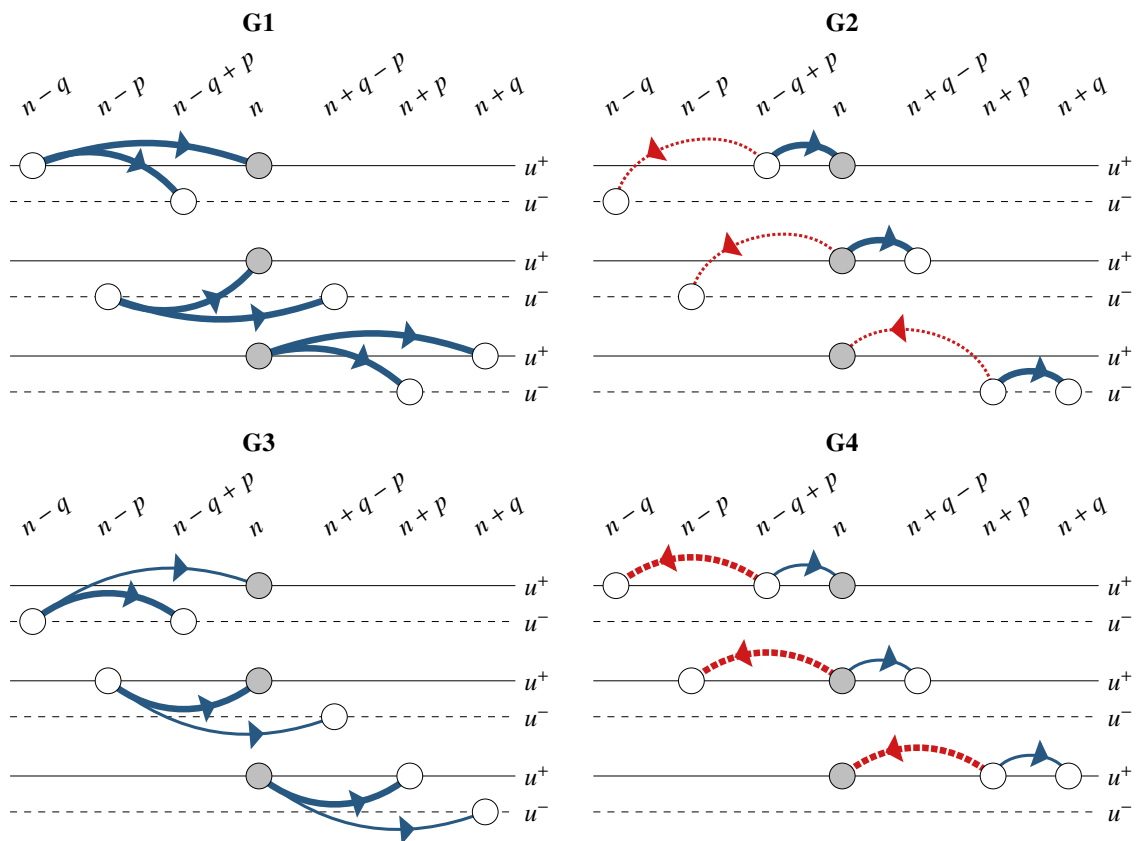


Figure 7.1: Nonlocal helical shell model, consisting of the three helical triad interactions per interaction group (G1–G4) coupling to  $u_n^+$  (filled gray circles). Complementary interactions coupling to  $u_n^-$  are given by similar but sign-flipped interactions (not shown). The arrows indicate the average energy transfer direction within each decoupled triadic interaction (showing the same as in figure 6.7, but from a shell model’s perspective) resulting from a linear stability analysis (Waleffe, 1992): solid blue (dashed red) arrows denote forward (reverse) energy transfers, while thick (thin) arrows represent dominant (subordinate) transfers. In each panel, the left (right) direction corresponds to larger (smaller) scales.

# Chapter 8

## Study #4

### 8.1 Introduction

Quadratic invariants play a fundamental role in the understanding of turbulent cascade dynamics, such as enstrophy effectively blocking the forward energy cascade in 2D. Recently, it was found that G4 triad interactions conserve a hidden enstrophy-like quantity capable of reversing the 3D forward energy cascade in analogy to enstrophy in 2D (Biferale et al., 2012), thus providing a clearer physical explanation for the reverse (R-class) contribution predicted from a linear stability analysis (G4 in figure 6.7).

In this work, we show that G2 interactions also conserve an enstrophy-like invariant capable of reversing the energy cascade, but that the conservation depends on triad geometry, thus making the cascade reversal dependant on triad geometry too. Remarkably, this result coincides with predictions based on a linear stability analysis and from studying the energy flux equation assuming an infinite Kolmogorov scaling (Waleffe, 1992). The standing problem of explaining why the dominant transfer direction in G2 shifts from forward to reverse depending on triad geometry (G2 in figure 6.7) is therefore proposed to be explained by the existence of a new quadratic quantity. This study does thus not only suggests a novel physical explanation for the behaviour of G2 triads, but has important ties to the traditional view that quadratic invariants are important for the directionality of the energy cascade.

## **8.2 The paper**

(intentionally blank)

## Pseudo-invariants contributing to inverse energy cascades in three-dimensional turbulence

Nicholas M. Rathmann\* and Peter D. Ditlevsen†

*Niels Bohr Institute, University of Copenhagen, Copenhagen, Denmark*

(Received 11 October 2016; published 26 May 2017)

Three-dimensional (3D) turbulence is characterized by a dual forward cascade of both kinetic energy and helicity, a second inviscid flow invariant besides energy, from the integral scale of motion to the viscous dissipative scale. In helical flows, however, such as strongly rotating flows with broken mirror symmetry, an inverse (reversed) energy cascade can be observed analogous to that of two-dimensional turbulence (2D) where enstrophy, a second positive-definite flow invariant, unlike helicity in 3D, effectively blocks the forward cascade of energy. In the spectral-helical decomposition of the Navier-Stokes equation, it has previously been shown that a subset of three-wave (triad) interactions conserve helicity in 3D in a fashion similar to enstrophy in 2D, thus leading to a 2D-like inverse energy cascade in 3D. In this work, we show, both theoretically and numerically, that an additional subset of interactions exist, conserving a new pseudo-invariant in addition to energy and helicity, which contributes either to a forward or an inverse energy cascade depending on the specific triad interaction geometry.

DOI: [10.1103/PhysRevFluids.2.054607](https://doi.org/10.1103/PhysRevFluids.2.054607)

### I. INTRODUCTION

Fully developed three-dimensional (3D) turbulence is characterized by a forward cascade of kinetic energy from the large integral scale of motion to the small Kolmogorov scale  $\eta$  of viscous dissipation. In the large Reynolds number limit,  $\eta \rightarrow 0$ , the production of enstrophy, the integral of the vorticity squared, by the stretching and bending term in the incompressible Navier-Stokes equations (NSE) permits the viscous dissipation of energy at the Kolmogorov scale. In two-dimensional (2D) turbulence, the stretching and bending term is absent, and enstrophy is, in addition to energy, also an inviscid invariant [1]. In this case, the dissipation of enstrophy prevents dissipation of energy at the Kolmogorov scale, effectively blocking the forward cascade of energy. The dual inviscid conservation of both quantities,  $\int E(k)dk$  and  $\int k^2 E(k)dk$ , the integrals over the spectral energy and enstrophy densities, respectively, consequently implies a reversal of the energy cascade to larger scales, hereafter referred to as a reverse cascade, following Waleffe [2] (synonymous to an inverse or upscale cascade). In 3D turbulence, helicity, the integral of the scalar product of velocity and vorticity, is also an inviscid invariant [3]. Similar to the enstrophy spectrum, the helicity spectrum,  $H(k) \sim kE(k)$ , dominates over the energy spectrum at small scales (large  $k$ ), but unlike enstrophy, helicity is not sign definite. As a consequence, the increased dissipation (of both signs) of helicity compared to energy can be obtained without a net helicity production as long as the dissipation of both positive and negative helicities balance [4]. Inviscid conservation of helicity therefore does not prevent a forward cascade of energy [5].

In helical flows, such as strongly rotating flows with broken mirror symmetry, a simultaneous forward helicity cascade and reverse energy cascade can however be observed [6]. In the spectral decomposition of the NSE, energy and helicity (and enstrophy in 2D) are conserved within each three-wave interaction (triad interaction). It was recently proposed that reverse energy cascades might generally exist in 3D turbulence [7], caused by a specific subset of triad interactions among

---

\*rathmann@nbi.ku.dk

†pditlev@nbi.ku.dk

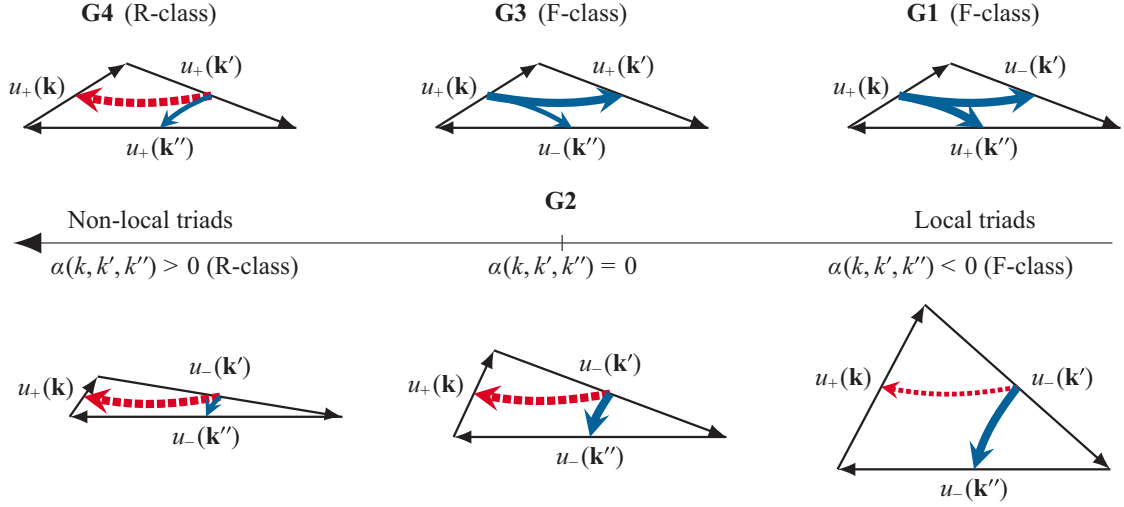


FIG. 1. G1–G4 helical triad interactions classified by behavior (F and R classes). The behavior of G2 triads is here proposed to be determined by the conservation of a new geometry-dependant enstrophy-like quantity,  $E^{(\omega)}$ . The arrows indicate the average energy transfer directions based on a linear stability analysis [2]: Blue/solid (red/dashed) arrows denote forward (reverse) energy transfers while thick (thin) arrows represent the dominant (subordinate) transfers.

helical wave components [2] of the same sign which render helicity enstrophy-like. The relative roles played by the different subsets of helical triad interactions would depend specifically on the symmetries and boundary conditions of the turbulent flow [8,9].

By applying the helical decomposition [2] to the NSE, triad interactions are split into four distinct groups of interactions between helical modes of different signs (depending on the relative weights of interchange of energy and helicity among the three waves). Within each helical interaction group, we show that an additional either helicity- or enstrophy-like quantity is conserved. Here, we conjecture that it is the spectral properties of this triad-specific invariant that governs the dual cascade of energy and helicity in 3D turbulence. Our conjecture is confirmed in the case of a shell model (reduced wave space model) which obeys the same conservations as the NSE [8].

In the helical decomposition [2] of the NSE for incompressible flows, each complex spectral velocity component,  $\mathbf{u}(\mathbf{k})$ , is decomposed into helical modes,  $\mathbf{h}_{\pm}(\mathbf{k})$  (using  $\mathbf{k} \cdot \mathbf{u}(\mathbf{k}) = 0$ ), which are eigenmodes of the curl operator, i.e.,  $i\mathbf{k} \times \mathbf{h}_{\pm} = \pm k\mathbf{h}_{\pm}$ , where  $k = |\mathbf{k}|$ . In this basis, velocity components are given by  $\mathbf{u}(\mathbf{k}) = u_{+}(\mathbf{k})\mathbf{h}_{+} + u_{-}(\mathbf{k})\mathbf{h}_{-}$ , and energy and helicity are given by  $E = \sum_{\mathbf{k}} (|u_{+}(\mathbf{k})|^2 + |u_{-}(\mathbf{k})|^2)$  and  $H = \sum_{\mathbf{k}} k(|u_{+}(\mathbf{k})|^2 - |u_{-}(\mathbf{k})|^2)$ , respectively. The spectral NSE become [2]

$$(d_t + \nu k^2)u_s(\mathbf{k}) = -1/4 \sum_{\mathbf{k}+\mathbf{k}'+\mathbf{k}''=0} \sum_{s',s''} (s'k' - s''k'') \mathbf{h}_{s'}^*(\mathbf{k}') \times \mathbf{h}_{s''}^*(\mathbf{k}'') \cdot \mathbf{h}_s^*(\mathbf{k}) u_{s'}^*(\mathbf{k}') u_{s''}^*(\mathbf{k}''), \quad (1)$$

where  $\{s, s', s''\} = \pm 1$  are the helical signs of the interacting modes and  $(s'k' - s''k'') \mathbf{h}_{s'}^*(\mathbf{k}') \times \mathbf{h}_{s''}^*(\mathbf{k}'') \cdot \mathbf{h}_s^*(\mathbf{k})$  is the coupling coefficient of the helical triad interaction involving velocity components  $\{u_s(\mathbf{k}), u_{s'}(\mathbf{k}'), u_{s''}(\mathbf{k}'')\}$ . Each triad interaction in the spectral NSE is thus split into four helical triad interactions by the inner sum over helical signs in (1) when sorted against shared coupling coefficients:  $\{s, s', s''\} = \pm\{+, -, +\}, \pm\{+, -, -\}, \pm\{+, +, -\}, \pm\{+, +, +\}$ , hereafter referred to as groups G1, . . . , G4 respectively; see Fig. 1.

By isolating terms in (1) involving only three wave vectors  $\{\mathbf{k}, \mathbf{k}', \mathbf{k}''\}$  (a single triad) and defining the shorthand notation  $g = \mathbf{h}_{s'}^*(\mathbf{k}') \times \mathbf{h}_{s''}^*(\mathbf{k}'') \cdot \mathbf{h}_s^*(\mathbf{k})$ , one finds, using the cyclic property

of  $g$ ,

$$\begin{aligned}
 d_t u_s(\mathbf{k}) &= (s'k' - s''k'') g u_{s'}^*(\mathbf{k}') u_{s''}^*(\mathbf{k}''), \\
 d_t u_{s'}(\mathbf{k}') &= (s''k'' - sk) g u_s^*(\mathbf{k}) u_{s''}^*(\mathbf{k}''), \\
 d_t u_{s''}(\mathbf{k}'') &= (sk - s'k') g u_s^*(\mathbf{k}) u_{s'}^*(\mathbf{k}').
 \end{aligned} \tag{2}$$

This simple form of the helically decomposed NSE triad dynamics is the basis of our analysis. Note that the cyclic symmetry of (2) implies that one may assume  $k \leq k' \leq k''$  without loss of generality. By multiplying by  $u_s^*(\mathbf{k}), u_{s'}^*(\mathbf{k}')$  and  $u_{s''}^*(\mathbf{k}'')$ , respectively, in the three equations (2), it immediately follows that energy is conserved within each triad interaction, and similarly for helicity by multiplication of  $sk u_s^*(\mathbf{k}), s'k' u_{s'}^*(\mathbf{k}')$  and  $s''k'' u_{s''}^*(\mathbf{k}'')$ , respectively [2]. The energy flux between the three triad legs is fixed for a given triad and is determined by the terms  $(s'k' - s''k''), (s''k'' - sk)$ , and  $(sk - s'k')$  in (2), while the average flux direction (to or from a leg) is determined by the sign of the three-wave correlator  $\langle u_s^*(\mathbf{k}) u_{s'}^*(\mathbf{k}') u_{s''}^*(\mathbf{k}'') \rangle + \text{c.c.}$

Waleffe [2] suggested that a linear instability analysis would predict the average energy flux direction within helical triad interactions by assuming that energy, on average, flows out of the most unstable wave mode and into the other two. By evaluating the stability of the fixed points  $\{u_s(\mathbf{k}), u_{s'}(\mathbf{k}'), u_{s''}(\mathbf{k}'')\} = \{U_0, 0, 0\}, \{0, U_0, 0\}, \{0, 0, U_0\}$  using (2), the unstable wave mode may be identified as the one with the largest absolute coefficient value in (2). This criterion implies that the smallest leg (largest scale) is unstable in G1 and G3 interactions, suggesting that these interactions contribute with a forward energy cascade (F-class interactions), while for G2 and G4 the middle leg is unstable, suggesting part of the energy flux is reversed. In G4, only same-signed helical modes interact, implying both positive and negative helicities,  $H^+ = \sum_{\mathbf{k}} k |u_+(\mathbf{k})|^2$  and  $H^- = \sum_{\mathbf{k}} k |u_-(\mathbf{k})|^2$ , are separately conserved. As such, G4 interactions can be regarded as analogous to enstrophy-conserving 2D interactions, and, consequently, should contribute with a reversed energy cascade (R-class interactions). This was recently indeed found to be the case numerically [7]. Note that the 2D analogy argument for why G4 interactions should exhibit a reversed energy cascade is different from that of the instability assumption. Lastly, in G2 interactions, positive and negative helicity components do interact, thus breaking the helicity-enstrophy analogy for explaining the mixed F- and R-class nature of G2 [2].

## II. THE PSEUDO-INVARIANT

Here we argue that the mixed F- and R-class nature of G2 interactions is determined by a new quantity different from energy and helicity, which too is conserved within a single triad interaction (2), but depends on triad shape. This new ‘‘pseudo-invariant’’ is thus, unlike energy and helicity, not a globally conserved quantity (across all triad interactions) because of its shape dependency. We therefore conjecture that the energy cascade, within subsets of identically shaped triads, should transition from forward (F-class) to reverse (R-class) depending on whether energy or the pseudo-invariant is dominant at the dissipation scale. To realize this, consider the spectral pseudo-invariant quantity defined as

$$E^{(\alpha)}(\mathbf{k}) = k^\alpha (|u_+(\mathbf{k})|^2 + |u_-(\mathbf{k})|^2), \quad \alpha \in \mathbb{R}, \tag{3}$$

which is analogous to the spectral energy density  $E(\mathbf{k}) = |u_+(\mathbf{k})|^2 + |u_-(\mathbf{k})|^2$ . This quantity is conserved by triad interactions governed by (2) if  $d_t(E^{(\alpha)}(\mathbf{k}) + E^{(\alpha)}(\mathbf{k}') + E^{(\alpha)}(\mathbf{k}'')) = 0$ , implying

$$\left(s' \frac{k'}{k} - s'' \frac{k''}{k}\right) + \left(\frac{k'}{k}\right)^\alpha \left(s'' \frac{k''}{k} - s\right) + \left(\frac{k''}{k}\right)^\alpha \left(s - s' \frac{k'}{k}\right) = 0, \tag{4}$$

which is trivially fulfilled for any triad when  $\alpha = 0$  (i.e., energy). As a function of triad shape, given by the relative leg sizes  $k'/k$  and  $k''/k$ , the left-hand side of (4) consists of a constant term and two monotonically increasing or decreasing terms. The existence of a nontrivial, real solution ( $\alpha \neq 0$ )

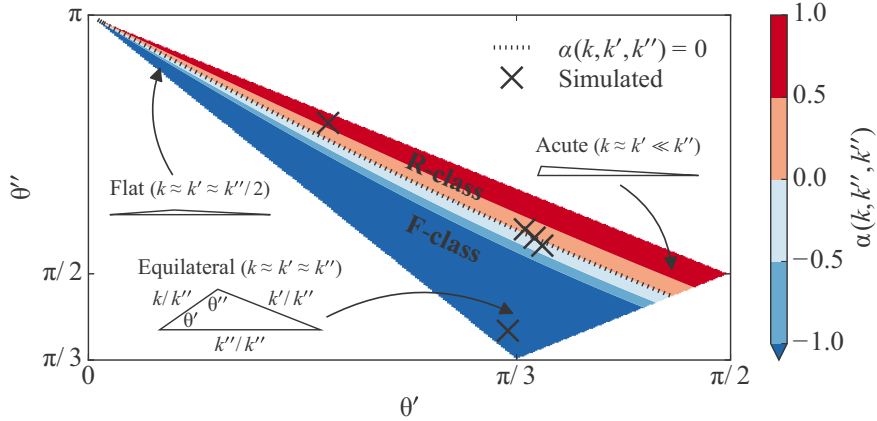


FIG. 2. G2  $\alpha$  solutions as a function of triad shape given by the two interior angles  $\theta'$  and  $\theta''$ . Overlaid are the  $\alpha = 0$  contour using Eq. (5) (dotted line) and the specific triad geometries simulated in this study (crosses).

for a given triad shape  $\{k, k', k''\}$  and interaction group  $\{s, s', s''\}$  therefore requires the signs of the coefficients of the two last terms in (4) to be opposite. Note that no more than *one* nontrivial, real solution can exist. It follows that only G2 and G4 interactions can have nontrivial solutions to (4). For G4,  $\alpha = 1$  is the solution for any triad, corresponding to the global inviscid conservation of helicity, as expected. For G2, the solution  $\alpha = \alpha(k, k', k'')$  is triad shape dependent.

Figure 2 shows the numerically solved G2 solutions for all possible (noncongruent) triad geometries (colored area in Fig. 2) by expressing each triad in terms of the two interior angles  $\theta'$  and  $\theta''$  using the sine rule:  $k'/k = \sin(\theta')/\sin(\pi - \theta' - \theta'')$  and  $k''/k = \sin(\theta'')/\sin(\pi - \theta' - \theta'')$ .

For G2 triads fulfilling

$$\frac{\log k''/k}{1 + k''/k} = \frac{\log k'/k}{1 + k'/k}, \quad (5)$$

[taking  $d/d\alpha|_{\alpha=0}$  of Eq. (4)], the trivial and nontrivial solutions collapse to the single solution  $\alpha = 0$ . Because the ratio of the spectral pseudo-invariant density to energy scales as  $k^\alpha$  (growing with  $k$  for  $\alpha > 0$ ), the subset of G2 triad interactions having  $\alpha > 0$  (red in Fig. 2) may be regarded analogous to enstrophy-conserving interactions in 2D turbulence. Note that these triad interactions correspond to nonlocal interactions.

In addition to a stability analysis, Waleffe [2] also estimated the behaviors of G1–G4 by studying the spectral energy flux equation. Assuming an infinite Kolmogorov scaling, the analysis suggested, to leading order, that triad geometries for which

$$\frac{\log k/k'}{1 + k/k'} + \frac{\log k''/k'}{k''/k' - 1} \quad (6)$$

is positive (negative) should contribute with forward (reverse) energy cascades. Noting that  $1 \leq k''/k' \leq k/k' + 1$  (triangle inequality), it follows that G2 triads with  $k/k' > 0.318$  contribute to a forward cascade, whereas  $k/k' < 0.278$  contribute reversely. That is, a band of triad geometries exist,  $0.278 < k/k' < 0.318$ , outside which the energy cascade is either forward or reverse. Here, however, we argue that retaining the original expression (6) contains more information on the G2 F/R transition since (i) setting it equal to 0 can be shown to be identical to (5), which has a clearer physical interpretation, and (ii) provides the exact F/R-transition line as a function of triad geometry (Fig. 2).

### III. NUMERICAL TEST

In order to test our conjecture, we apply our newly constructed helical shell model [8] (source available at <https://github.com/nicholasmr/rdshellmodel>). Shell models are a class of fixed-triad-shape and reduced-wave-space models, allowing for very long inertial ranges to be resolved. Benzi *et al.* [10] did the pioneering work on constructing helical shell models, which, since then, has inspired other helical shell models and led to important insights on helically decomposed triad dynamics [4,8,11–17]. The shell model used here [8], which is related to the Sabra model [15] by the transformation  $u_s(k_n) \rightarrow -isu_s(k_n)$  except for a sign change in G1 and G3 (relevant only when coupling G1–G4), additionally provides a natural coupling between the four interaction groups (G1–G4) and multiple triad shapes through coupling weights derived directly from (1).

In helical shell models, it is straight forward to perform “spectral surgery” as proposed [7,15,18,19] in order to investigate the (isolated/uncoupled) behavior of G2 interactions. Considering only fixed-shaped G2 interactions, the shell model takes the form

$$\begin{aligned} (d_t + \nu k_n^2 + \nu_L k_n^{-2})u_s(k_n) = & sk_n \left[ u_{-s}^*(k_{n+p})u_{-s}(k_{n+q}) - \frac{\epsilon_{p,q}}{\lambda^p} u_{-s}^*(k_{n-p})u_s(k_{n+q-p}) \right. \\ & \left. + \frac{1 + \epsilon_{p,q}}{\lambda^q} u_{-s}(k_{n-q})u_s(k_{n-q+p}) \right] + f_s(k_n), \end{aligned} \quad (7)$$

where  $\epsilon_{p,q} = (1 + \lambda^q)/(\lambda^p - \lambda^q)$ ,  $f_s(k_n)$  is the forcing at wave number  $k_n$ , and the linear terms  $\nu k_n^2 u_s(k_n)$  and  $\nu_L k_n^{-2} u_s(k_n)$  are viscous dissipation and a drag term, respectively; the latter is added in the usual way to remove energy at large scales. The scalars  $k_n = k_0 \lambda^n$ , where  $n = 0, \dots, N$ , represent the exponentially distributed shell wave numbers resolved,  $\{p, q\} \in \mathbb{N}$  where  $1 < p < q$ ,  $k_0 \in \mathbb{R}_+$ , and  $\lambda \in ]1, (1 + \sqrt{5})/2] = ]1, \varphi]$ . The golden ratio  $\varphi$  is the upper limit such that any set of nearest neighbor waves fulfills the triangle inequality as required by the NSE.

The integers  $\{p, q\}$  can be related to any triangular shape through the sine rule. The possible resolved triad shapes depend therefore on the combination of  $\{\lambda, p, q\}$ : For  $\lambda \rightarrow 1$  any triad geometry may be constructed for sufficiently large or small values of  $\{p, q\}$ , while for  $\{\lambda, p, q\} = \{\varphi, 1, 2\}$  triads collapse to a line. Thus, for each chosen set of  $\{\lambda, p, q\}$ , the shell model consists, independently of scale  $k_n$ , only of fixed-shaped triad interactions.

The nonlinear terms in (7) conserve both energy  $E = \sum_{n=0}^N (|u_+(k_n)|^2 + |u_-(k_n)|^2)$  and helicity  $H = \sum_{n=0}^N k_n (|u_+(k_n)|^2 - |u_-(k_n)|^2)$ . Each  $\{p, q\}$  configuration of the model ( $\lambda$  hereafter assumed fixed) additionally conserves the pseudo-invariants  $E^{(\alpha)} = \sum_{n=0}^N k_n^\alpha (|u_+(k_n)|^2 + |u_-(k_n)|^2)$  in complete analogy to (4) for the NSE [8].

The nonlinear spectral energy flux through the  $n$ th shell is given by [8]

$$\Pi(k_n) = \sum_{m=n+1}^{n+q} \Delta_{m,p,q} + \epsilon_{p,q} \sum_{m=n+1}^{n+q-p} \Delta_{m,p,q}, \quad (8)$$

where  $\Delta_{m,p,q} = 2k_{m-q} \operatorname{Re}[u_+^*(k_{m-q})u_-^*(k_{m-q+p})u_-(k_m) - u_-^*(k_{m-q})u_+^*(k_{m-q+p})u_+(k_m)]$ .

Simulations were conducted with  $\lambda = 1.1$ ,  $k_0 = 1$ , and  $N = 223$  for both high and low Reynolds number configurations  $\{\nu, \nu_L\} = \{1 \times 10^{-12}, 1 \times 10^2\}$ ,  $\{1 \times 10^{-11}, 1 \times 10^4\}$ , respectively. Five different sets of  $\{p, q\}$  were chosen:  $p = \{1, 12, 13, 14, 22\}$  with  $q = p + 1$ , corresponding to  $\alpha = \{-30.9, -0.15, 0.01, 0.15, 0.69\}$  (crosses in Fig. 2). In all simulations, the forcing  $f_\pm(k_{n_f}) = (1 + i)/u_\pm^*(k_{n_f})$  was applied to both helical components at shell  $n_f = 108$ , supplying a constant energy input of  $\epsilon_{\text{in}} = 4$ .

Figure 3 shows the simulated spectral energy fluxes. The blue curves show the resulting energy fluxes for the model configured with triad shapes having  $\alpha < 0$ , in which case energy should exhibit a forward cascade. The red curves show the opposite with  $\alpha > 0$ , namely a 2D-like reversed energy cascade and a forward cascade of the enstrophy-like pseudo-invariant (latter not shown). As the

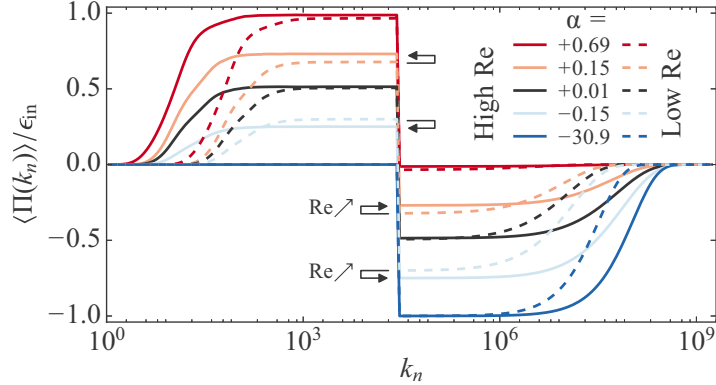


FIG. 3. Simulated spectral energy fluxes of the G2 triad geometries ( $\alpha$  values) considered. Solid (dashed) lines correspond to high (low) Reynolds number configurations.

cascade directions for the energy and the pseudo-invariant interchange at  $\alpha = 0$ , we expect a split forward and reversed energy cascade to develop, which is indeed found to be the case (black curve in Fig. 3). Furthermore, because the ratio of the spectral pseudo-invariant density to energy scales as  $k^\alpha$ , one would expect with increasing Reynolds numbers a narrowing of the  $\alpha$  interval over which the F- to R-class transition occurs, which is also found to be the case (solid versus dashed lines in Fig. 3).

#### IV. DISCUSSION

De Pietro *et al.* [15] gave an alternative explanation for the F to R transition in the case of a shell model by studying the energy flux equation (8). Their work suggested that if time-averaged triple correlators,  $\langle \Delta_{n,p,q} \rangle$ , are asymptotically constant (independent of  $k_n$ ), Eq. (8) may be written as  $\langle \Pi(k_n) \rangle = (q + (q - p)\epsilon_{p,q})\langle \Delta_{n,p,q} \rangle = F_{p,q}\langle \Delta_{n,p,q} \rangle$ . Thus, the sign of  $F_{p,q}$ , which depends on triad geometry, would indicate the flux direction, assuming the sign of  $\langle \Delta_{n,p,q} \rangle$  is fixed and given by a stability analysis [2, 15]. However, even though this prediction is in agreement with our conjecture for the triad geometries considered here, it is important to note that  $\langle \Delta_{n,p,q} \rangle$  cannot necessarily be assumed asymptotically constant in the nonlocal triad limit [8].

The importance of the “hidden” reverse energy cascade carried by G2 R-class interactions ( $\alpha > 0$ ), which are mostly nonlocal, depends (i) on the number of G2 R-class triads compared to the number of G2 F-class triads, and (ii) the magnitude of the G2 coupling coefficients in (1) compared to those of G1, G3, and G4. To estimate (i), consider the continuous version of (1) where the triad sum becomes an integral over  $dk' dk''$ . In terms of  $\theta'$  and  $\theta''$ , the corresponding density of triads within the element  $dk' dk''$  is given by the transformation  $dk' dk'' = |\det J| d\theta' d\theta''$ , where  $J = \partial\Phi$  is the Jacobian of the transformation  $k' = \Phi'(\theta', \theta'')$  and  $|\det J| = k^2 \sin(\theta') \sin(\theta'') [1 + \cos(\theta' + \theta'')]^2 / \sin(\theta' + \theta'')^4$ . Thus, the number of G2 R-class triads far exceeds the number of G2 F-class triads in the limit of large inertial ranges ( $\text{Re} \rightarrow \infty$ ) since the acute triad limit  $k', k'' \rightarrow \infty$  implies  $\sin(\theta' + \theta'') \rightarrow 0$  and therefore a large density of nonlocal triads. To estimate (ii), consider the relative (normalized) magnitudes of the G2 coupling coefficients given by  $I_{-, -} / \sum_{s', s''} I_{s', s''}$ , where  $I_{s', s''} = |(sk + s'k' + s''k'')(s'k' - s''k'')|$ . That is,  $I_{s', s''}$  is the part of the total coupling weight unique to each of G1–G4, which originates from (1) by noting  $|(s'k' - s''k'')g| = I_{s', s''} Q / (2kk'k'')$ , where  $Q = (2k^2k'^2 + 2k'^2k''^2 + 2k''^2k^2 - k^4 - k'^4 - k''^4)^{1/2}$  [2]. Figure 4 shows the relative G2 coupling magnitudes (solid black lines), suggesting G2 R-class interactions should, overall, play an important role in the helically decomposed dynamics of flat and semi-acute triads. In addition, assuming  $k = 1$  without loss of generality, the colored contours in Fig. 4 show the triad density,  $|\det J|$ , is also large for such flat and semi-acute triads, suggesting G2 R-class interactions

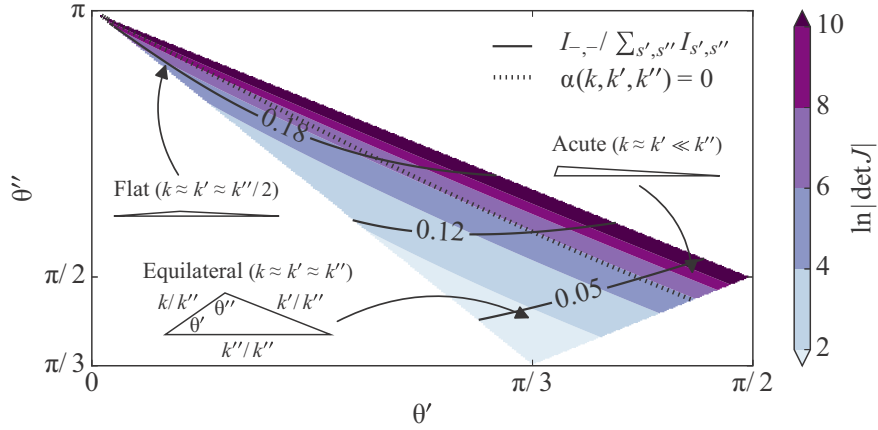


FIG. 4. G2 relative coupling weight (solid black contours) and triad densities (coloured contours) as a function of triad shape.

become increasingly important to the extent that the inertial range is long enough for them to be resolved.

## V. SUMMARY

In conclusion, we presented an alternative classification to linear triad stability analysis [2] for explaining the nature of the four elementary nonlinear interactions of the spectral Navier-Stokes equation in the helical basis. By showing a subset of interactions conserve new enstrophy-like blocking quantities depending on triad geometry, the apparent complicated nature of the second group (G2) of helical interactions (Fig. 1) may be explained in terms of physically conserved quantities analogous to enstrophy in 2D turbulence.

- 
- [1] R. H. Kraichnan, Inertial ranges in two-dimensional turbulence, *Phys. Fluids* **10**, 1417 (1967).
  - [2] F. Waleffe, The nature of triad interactions in homogeneous turbulence, *Phys. Fluids* **4**, 350 (1992).
  - [3] H. K. Moffatt, The degree of knottedness of tangled vortex lines, *J. Fluid Mech.* **35**, 117 (1969).
  - [4] P. D. Ditlevsen and P. Giuliani, Dissipation in helical turbulence, *Phys. Fluids* **13**, 3508 (2001).
  - [5] A. Brissaud, U. Frisch, J. Leorat, M. Lesieur, and A. Mazure, Helicity cascades in fully developed isotropic turbulence, *Phys. Fluids* **16**, 1366 (1973).
  - [6] P. D. Mininni, A. Alexakis, and A. Pouquet, Scale interactions and scaling laws in rotating flows at moderate rossby numbers and large reynolds numbers, *Phys. Fluids* **21**, 015108 (2009).
  - [7] L. Biferale, S. Musacchio, and F. Toschi, Inverse Energy Cascade in Three-Dimensional Isotropic Turbulence, *Phys. Rev. Lett.* **108**, 164501 (2012).
  - [8] N. M. Rathmann and P. D. Ditlevsen, Role of helicity in triad interactions in three-dimensional turbulence investigated by a new shell model, *Phys. Rev. E* **94**, 033115 (2016).
  - [9] A. Alexakis, Helically decomposed turbulence, *J. Fluid Mech.* **812**, 752 (2017).
  - [10] R. Benzi, L. Biferale, R. M. Kerr, and E. Trovatore, Helical shell models for three-dimensional turbulence, *Phys. Rev. E* **53**, 3541 (1996).
  - [11] P. D. Ditlevsen and P. Giuliani, Cascades in helical turbulence, *Phys. Rev. E* **63**, 036304 (2001).
  - [12] T. Lessinnes, F. Plunian, and D. Carati, Helical shell models for MHD, *Theor. Comput. Fluid Dyn.* **23**, 439 (2009).
  - [13] T. Lessinnes, F. Plunian, R. Stepanov, and D. Carati, Dissipation scales of kinetic helicities in turbulence, *Phys. Fluids* **23**, 035108 (2011).

- [14] R. Stepanov, P. Frick, and I. Mizeva, Joint inverse cascade of magnetic energy and magnetic helicity in mhd turbulence, [Astrophys. J. Lett. \*\*798\*\*, L35 \(2015\)](#).
- [15] M. De Pietro, L. Biferale, and A. A. Mailybaev, Inverse energy cascade in nonlocal helical shell models of turbulence, [Phys. Rev. E \*\*92\*\*, 043021 \(2015\)](#).
- [16] G. Sahoo, M. De Pietro, and L. Biferale, Helicity statistics in homogeneous and isotropic turbulence and turbulence models, [Phys. Rev. Fluids \*\*2\*\*, 024601 \(2017\)](#).
- [17] M. De Pietro, A. A. Mailybaev, and L. Biferale, Chaotic and regular instantons in helical shell models of turbulence, [Phys. Rev. Fluids \*\*2\*\*, 034606 \(2017\)](#).
- [18] L. Biferale, S. Musacchio, and F. Toschi, Split energy–helicity cascades in three-dimensional homogeneous and isotropic turbulence, [J. Fluid Mech. \*\*730\*\*, 309 \(2013\)](#).
- [19] G. Sahoo, F. Bonaccorso, and L. Biferale, Role of helicity for large- and small-scale turbulent fluctuations, [Phys. Rev. E \*\*92\*\*, 051002\(R\) \(2015\)](#).

### 8.3 Outlook

Having studied G2 interactions in isolation, it is not immediately clear whether the G2 cascade reversal persistently carries over to coupled triad configurations; that is if coupling-induced effects change the behaviour of G2 triads. An important next step would therefore be to couple G1–G4 systematically for many different triad geometries, where the sampled geometries cross  $\alpha(k, k', k'') = 0$  too. This would allow to determine whether the reversal persists even as the cascade partitioning possibly changes as a function of coupling weights (related to the outlook of study #3). If so, the robustness of pseudo-invariants could arguably be important for understanding the behaviour of large coupled systems too, or even the spectral-helical NSE.

Another potential implication of pseudo-invariants is that they might exist in magnetohydrodynamical turbulence too. A central problem in astrophysics is how magnetic fields are generated by astrophysical bodies at spatial scales much larger than the outer scale of the bodies. A popular explanation is that a large-scale dynamo action occurs, by which the magnetic field is amplified through turbulent, nonlinear interactions between the velocity field and the magnetic field in the electroconducting fluid inside the body. Specifically, the upscale cascade of the inviscid invariant magnetic helicity in magnetohydrodynamical (MHD) turbulence, defined as the inner product between the magnetic field and the magnetic potential,

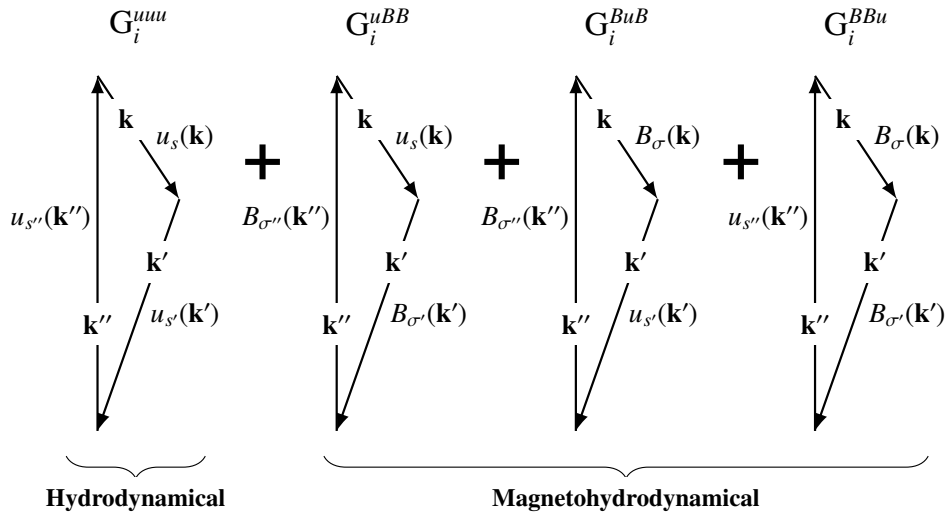


Figure 8.1: The minimal set of triad interactions (MTI) required to conserve all three magnetohydrodynamical invariants: energy, magnetic helicity, and cross-helicity. For a given triad of waves,  $\{\mathbf{k}, \mathbf{k}', \mathbf{k}''\}$ , the MTI consists of one hydrodynamical triad interaction group ( $G_i^{uuu}$ ) and three magnetohydrodynamical groups ( $G_i^{uBB}$ ,  $G_i^{BuB}$ ,  $G_i^{BBu}$ ). Each MTI is uniquely defined by the helical signs of the interacting modes,  $\{s, s', s'', \sigma, \sigma', \sigma''\} = \pm$ , or, equivalently, by group indices  $i$  in analogy to the notation used for hydrodynamical turbulence and in this thesis.

has been proposed as an explanation (Frisch et al., 1975). In this respect, it is important to study the dynamical mechanisms by which inviscid invariants are transferred across spatial scales in order to cast light on the evolution of planetary and stellar magnetic fields.

Since both velocity and magnetic fields are solenoidal in MHD turbulence, both fields may be expressed in the helical basis as

$$\begin{aligned}\mathbf{u}(\mathbf{k}) &= u_+(\mathbf{k})\mathbf{h}_+ + u_-(\mathbf{k})\mathbf{h}_- \\ \mathbf{B}(\mathbf{k}) &= B_+(\mathbf{k})\mathbf{h}_+ + B_-(\mathbf{k})\mathbf{h}_-.\end{aligned}$$

Applying this decomposition to the MHD equations (Lessinnes et al., 2009), one finds that each triad of waves  $\{\mathbf{k}, \mathbf{k}', \mathbf{k}''\}$  conserve all ideal MHD invariants: energy (kinetic+magnetic), magnetic helicity and cross-helicity. Unlike hydrodynamical turbulence, however, four distinct triad interactions (for each triad of waves) is required to conserve all invariants — constituting a minimal set of triad interactions (MTI) [figure 8.1]. Because the magnetic components have their own associated helical signs ( $\{\sigma, \sigma', \sigma''\}$  for legs  $\{\mathbf{k}, \mathbf{k}', \mathbf{k}''\}$ ), a total of  $2^6 = 64$  distinct MTIs exist.

Similarly to the hydrodynamical case (6.12), by picking out terms from the spectral-helical MHD equations involving a single triad of waves, the simplified dynamics governing a single MTI falls out. Considering then the enstrophy-like pseudo-invariant

$$E^{(\alpha)}(\mathbf{k}) = k^\alpha (|u_+(\mathbf{k})|^2 + |u_-(\mathbf{k})|^2 + |B_+(\mathbf{k})|^2 + |B_-(\mathbf{k})|^2)$$

and applying the MTI equations, a subset of triad interactions might be found to conserve hidden enstrophy-like quantities in analogy to G2 and G4 for hydrodynamical turbulence. If a further subset of these triads additionally have magnetic components as the smallest triad leg (largest spatial scale), such triads could, potentially, contribute with an upscale transfer of magnetic energy and thereby to large-scale dynamo action.

# Bibliography

- Alexakis, A. Helically decomposed turbulence. *Journal of Fluid Mechanics*, 812: 752–770, 2017.
- Alnæs, M. S., Logg, A., Mardal, K.-A., Skavhaug, O., and Langtangen, H. P. Unified Framework for Finite Element Assembly. *International Journal of Computational Science and Engineering*, 4(4):231–244, 2009. doi: 10.1504/IJCSE.2009.029160.
- Alnæs, M. S., Logg, A., Ølgaard, K. B., Rognes, M. E., and Wells, G. N. Unified Form Language: A domain-specific language for weak formulations of partial differential equations. *ACM Transactions on Mathematical Software*, 40(2), 2014. doi: 10.1145/2566630.
- Alnæs, M. S., Blechta, J., Hake, J., Johansson, A., Kehlet, B., Logg, A., Richardson, C., Ring, J., Rognes, M. E., and Wells, G. N. The FEniCS Project Version 1.5. *Archive of Numerical Software*, 3(100), 2015. doi: 10.11588/ans.2015.100.20553.
- André, J. and Lesieur, M. Influence of helicity on the evolution of isotropic turbulence at high Reynolds number. *Journal of Fluid Mechanics*, 81(01):187–207, 1977.
- Aravas, N. Finite-strain anisotropic plasticity and the plastic spin. *Modelling and Simulation in Materials Science and Engineering*, 2(3A):483, 1994.
- Arnold, D. N., Brezzi, F., and Fortin, M. A stable finite element for the Stokes equations. *Calcolo*, 21(4):337–344, 1984.
- Azuma, N. A flow law for anisotropic ice and its application to ice sheets. *Earth and Planetary Science Letters*, 128(3-4):601–614, 1994.
- Azuma, N. A flow law for anisotropic polycrystalline ice under uniaxial compressive deformation. *Cold regions science and technology*, 23(2):137–147, 1995.
- Azuma, N. and Goto-Azuma, K. An anisotropic flow law for ice-sheet ice and its implications. *Annals of Glaciology*, 23:202–208, 1996.
- Barnes, P., Tabor, D., and Walker, J. The friction and creep of polycrystalline ice. *Proc. R. Soc. Lond. A*, 324(1557):127–155, 1971.

- Batchelor, G. K. Computation of the energy spectrum in homogeneous two-dimensional turbulence. *The Physics of Fluids*, 12(12):II-233, 1969.
- Batchelor, G. K. *The theory of homogeneous turbulence*. Cambridge university press, 1953.
- Bercovier, M. and Pironneau, O. Error estimates for finite element method solution of the Stokes problem in the primitive variables. *Numerische Mathematik*, 33(2): 211–224, 1979.
- Biferale, L. Shell models of energy cascade in turbulence. *Annual review of fluid mechanics*, 35(1):441–468, 2003.
- Biferale, L., Musacchio, S., and Toschi, F. Inverse energy cascade in three-dimensional isotropic turbulence. *Physical review letters*, 108(16):164501, 2012.
- Brissaud, A., Frisch, U., Leorat, J., Lesieur, M., and Mazure, A. Helicity cascades in fully developed isotropic turbulence. *Physics of Fluids (1958-1988)*, 16(8): 1366–1367, 1973.
- Bunge, H.-J. *Texture analysis in materials science: mathematical methods*. Elsevier, 2013.
- Castelnau, O. and Duval, P. Simulations of anisotropy and fabric development in polar ices. *Annals of Glaciology*, 20:277–282, 1994.
- Castelnau, O., Duval, P., Lebensohn, R. A., and Canova, G. R. Viscoplastic modeling of texture development in polycrystalline ice with a self-consistent approach: Comparison with bound estimates. *Journal of Geophysical Research: Solid Earth*, 101(B6):13851–13868, 1996.
- Christianson, K., Peters, L. E., Alley, R. B., Anandkrishnan, S., Jacobel, R. W., Riverman, K. L., Muto, A., and Keisling, B. A. Dilatant till facilitates ice-stream flow in northeast Greenland. *Earth and Planetary Science Letters*, 401:57–69, 2014.
- Courtney, T. H. *Mechanical behavior of materials*. Waveland Press, 2005.
- Cuffey, K. M. and Paterson, W. S. B. *The physics of glaciers*. Academic Press, 2010.
- Dahl-Jensen, D. and Gundestrup, N. Constitutive properties of ice at Dye 3, Greenland. *International Association of Hydrological Sciences Publication*, 170:31–43, 1987.
- Davidson, P. A. *Turbulence: an introduction for scientists and engineers*. Oxford University Press, 2004.

- De Pietro, M., Biferale, L., and Mailybaev, A. A. Inverse energy cascade in nonlocal helical shell models of turbulence. *Phys. Rev. E*, 92:043021, Oct 2015. doi: 10.1103/PhysRevE.92.043021. URL <http://link.aps.org/doi/10.1103/PhysRevE.92.043021>.
- Ditlevsen, P. D. Symmetries, invariants, and cascades in a shell model of turbulence. *Physical Review E*, 62(1):484, 2000.
- Ditlevsen, P. D. *Turbulence and Shell Models*. Cambridge University Press, 2010. ISBN 9780511919251. URL <http://dx.doi.org/10.1017/CBO9780511919251>. Cambridge Books Online.
- Duval, P. and Castelnau, O. Dynamic recrystallization of ice in polar ice sheets. *Le Journal de Physique IV*, 5(C3):C3–197, 1995.
- Duval, P., Ashby, M., and Anderman, I. Rate-controlling processes in the creep of polycrystalline ice. *The Journal of Physical Chemistry*, 87(21):4066–4074, 1983.
- Fjørtoft, R. On the changes in the spectral distribution of kinetic energy for twodimensional, nondivergent flow. *Tellus*, 5(3):225–230, 1953.
- Fossen, H. *Structural Geology*, 463 pp, 2010.
- Frisch, U. *Turbulence: the legacy of AN Kolmogorov*. Cambridge university press, 1995.
- Frisch, U., Pouquet, A., Léorat, J., and Mazure, A. Possibility of an inverse cascade of magnetic helicity in magnetohydrodynamic turbulence. *Journal of Fluid Mechanics*, 68(4):769–778, 1975.
- Fukuda, A., Hondoh, T., and Higashi, A. Dislocation mechanisms of plastic deformation of ice. *Le Journal de Physique Colloques*, 48(C1):C1–163, 1987.
- Gillet-Chaulet, F., Gagliardini, O., Meyssonier, J., Montagnat, M., and Castelnau, O. A user-friendly anisotropic flow law for ice-sheet modeling. *Journal of glaciology*, 51(172):3–14, 2005.
- Glen, J. W. The creep of polycrystalline ice. *Proc. R. Soc. Lond. A*, 228(1175): 519–538, 1955.
- Gödert, G. and Hutter, K. Induced anisotropy in large ice shields: theory and its homogenization. *Continuum Mechanics and Thermodynamics*, 10(5):293–318, 1998.
- Goldsby, D. and Kohlstedt, D. Superplastic deformation of ice: Experimental observations. *Journal of Geophysical Research: Solid Earth*, 106(B6):11017–11030, 2001.

- Gow, A. J. and Williamson, T. Rheological implications of the internal structure and crystal fabrics of the West Antarctic ice sheet as revealed by deep core drilling at Byrd Station. *Geological Society of America Bulletin*, 87(12):1665–1677, 1976.
- Greve, R., Zwinger, T., and Gong, Y. On the pressure dependence of the rate factor in Glen's flow law. *Journal of Glaciology*, 60(220):397–399, 2014.
- Gudmundsson, G. H., Krug, J., Durand, G., Favier, L., and Gagliardini, O. The stability of grounding lines on retrograde slopes. *The Cryosphere*, 6(6):1497–1505, 2012. doi: 10.5194/tc-6-1497-2012. URL <http://www.the-cryosphere.net/6/1497/2012/>.
- Herron, S. L. and Langway, C. C. A comparison of ice fabrics and textures at Camp Century, Greenland and Byrd Station, Antarctica. *Annals of glaciology*, 3: 118–124, 1982.
- Hood, P. and Taylor, C. Navier-Stokes equations using mixed interpolation. *Finite element methods in flow problems*, pages 121–132, 1974.
- Hooke, R. L. Structure and flow in the margin of the Barnes Ice Cap, Baffin Island, NWT, Canada. *Journal of Glaciology*, 12(66):423–438, 1973.
- Hutter, K. *Theoretical Glaciology: Material Science of Ice and the Mechanics of Glaciers and Ice Sheets (Mathematical Approaches to Geophysics)*, 1983.
- Jensen, M., Paladin, G., and Vulpiani, A. Intermittency in a cascade model for three-dimensional turbulence. *Physical Review A*, 43(2):798, 1991.
- Johnson, A. Creep characterization of transversely-isotropic metallic materials. *Journal of the Mechanics and Physics of Solids*, 25(2):117–126, 1977.
- Jones, S. and Glen, J. The effect of dissolved impurities on the mechanical properties of ice crystals. *Philosophical Magazine*, 19(157):13–24, 1969.
- Jun, L., Jacka, T., and Budd, W. Deformation rates in combined compression and shear for ice which is initially isotropic and after the development of strong anisotropy. *Annals of Glaciology*, 23:247–252, 1996.
- Kamb, B. and Echelmeyer, K. A. Stress-gradient coupling in glacier flow: IV. Effects of the “T” term. *Journal of Glaciology*, 32(112):342–349, 1986.
- Kearsley, E. A. and Fong, J. Linearly independent sets of isotropic Cartesian tensors of ranks up to eight. *J. Res. Natl Bureau of Standards Part B: Math. Sci. B*, 79: 49–58, 1975.
- Kirby, R. C. Algorithm 839: FIAT, a New Paradigm for Computing Finite Element Basis Functions. *ACM Transactions on Mathematical Software*, 30(4):502–516, 2004. doi: 10.1145/1039813.1039820.

- Kirby, R. C. and Logg, A. A Compiler for Variational Forms. *ACM Transactions on Mathematical Software*, 32(3), 2006. doi: 10.1145/1163641.1163644.
- Kolmogorov, A. N. Dissipation of energy in locally isotropic turbulence. In *Dokl. Akad. Nauk SSSR*, volume 32, pages 16–18, 1941a.
- Kolmogorov, A. N. The local structure of turbulence in incompressible viscous fluid for very large Reynolds numbers. In *Dokl. Akad. Nauk SSSR*, volume 30, pages 299–303, 1941b.
- Kraichnan, R. and Montgomery, D. Two-dimensional turbulence. *Rep. Prog. Phys.*, 43, 1980.
- Kraichnan, R. H. Inertial ranges in two-dimensional turbulence. Technical report, DTIC Document, 1967.
- Kraichnan, R. H. Inertial-range transfer in two- and three-dimensional turbulence. *Journal of Fluid Mechanics*, 47(03):525–535, 1971.
- Landau, L. and Lifshitz, E. *Course of theoretical physics. vol. 6: Fluid mechanics*. London, 1959.
- Langtangen, H. P. and Mardal, K.-A. Introduction to Numerical Methods for Variational Problems. 2016.
- Lautrup, B. Physics of continuous matter. *Exotic and Everyday Phenomena in the Macroscopic World*, IOP, 2005.
- Le Meur, E., Gagliardini, O., Zwinger, T., and Ruokolainen, J. Glacier flow modelling: a comparison of the Shallow Ice Approximation and the full-Stokes solution. *Comptes Rendus Physique*, 5(7):709–722, 2004.
- Leith, C. Atmospheric predictability and two-dimensional turbulence. *Journal of the Atmospheric Sciences*, 28(2):145–161, 1971.
- Lessinnes, T., Plunian, F., and Carati, D. Helical shell models for MHD. *Theoretical and Computational Fluid Dynamics*, 23(6):439–450, 2009.
- Lile, R. The effect of anisotropy on the creep of polycrystalline ice. *Journal of Glaciology*, 21(85):475–483, 1978.
- Lliboutry, L. Anisotropic, transversely isotropic nonlinear viscosity of rock ice and rheological parameters inferred from homogenization. *International journal of plasticity*, 9(5):619–632, 1993.
- Logg, A. and Wells, G. N. DOLFIN: Automated Finite Element Computing. *ACM Transactions on Mathematical Software*, 37(2), 2010. doi: 10.1145/1731022.1731030.

- Lorenz, E. N. Atmospheric predictability as revealed by naturally occurring analogues. *Journal of the Atmospheric sciences*, 26(4):636–646, 1969.
- MacAyeal, D. R. Large-scale ice flow over a viscous basal sediment: Theory and application to ice stream B, Antarctica. *Journal of Geophysical Research: Solid Earth*, 94(B4):4071–4087, 1989.
- Meyssonnier, J. and Philip, A. A model for the tangent viscous behaviour of anisotropic polar ice. *Annals of Glaciology*, 23:253–261, 1996.
- Mises, R. v. Mechanik der plastischen Formänderung von Kristallen. *ZAMM-Journal of Applied Mathematics and Mechanics/Zeitschrift für Angewandte Mathematik und Mechanik*, 8(3):161–185, 1928.
- Morland, L. Unconfined ice-shelf flow. In *Dynamics of the West Antarctic Ice Sheet*, pages 99–116. Springer, 1987.
- Morlighem, M., Rignot, E., Mouginot, J., Seroussi, H., and Larour, E. Deeply incised submarine glacial valleys beneath the Greenland ice sheet. *Nature Geoscience*, 7(6), 2014.
- Mouginot, J., Rignot, E., Scheuchl, B., Fenty, I., Khazendar, A., Morlighem, M., Buzzi, A., and Paden, J. Fast retreat of Zachariæ Isstrøm, northeast Greenland. *Science*, 350(6266):1357–1361, 2015.
- Naumenko, K. and Altenbach, H. *Modeling of creep for structural analysis*. Springer Science & Business Media, 2007.
- Nye, J. F. The distribution of stress and velocity in glaciers and ice-sheets. *Proc. R. Soc. Lond. A*, 239(1216):113–133, 1957.
- Odqvist, F. K. G. *Mathematical theory of creep and creep rupture*. Oxford University Press, 1974.
- Pattyn, F. A new three-dimensional higher-order thermomechanical ice sheet model: Basic sensitivity, ice stream development, and ice flow across subglacial lakes. *Journal of Geophysical Research: Solid Earth*, 108(B8), 2003.
- Pouryazdan, M., Kaus, B. J., Rack, A., Ershov, A., and Hahn, H. Mixing instabilities during shearing of metals. *Nature Communications*, 8(1):1611, 2017.
- Rathmann, N. M. and Ditlevsen, P. D. Role of helicity in triad interactions in three-dimensional turbulence investigated by a new shell model. *Physical Review E*, 94(3):033115, 2016.
- Rathmann, N. M. and Ditlevsen, P. D. Pseudo-invariants contributing to inverse energy cascades in three-dimensional turbulence. *Physical Review Fluids*, 2(5): 054607, 2017.

- Rathmann, N., Hvidberg, C., Solgaard, A., Grinsted, A., Gudmundsson, G. H., Langen, P. L., Nielsen, K., and Kusk, A. Highly temporally resolved response to seasonal surface melt of the Zachariae and 79N outlet glaciers in northeast Greenland. *Geophysical Research Letters*, 44(19):9805–9814, 2017.
- Rose, H. and Sulem, P. Fully developed turbulence and statistical mechanics. *Journal de Physique*, 39(5):441–484, 1978.
- Sergienko, O., Creyts, T. T., and Hindmarsh, R. Similarity of organized patterns in driving and basal stresses of Antarctic and Greenland ice sheets beneath extensive areas of basal sliding. *Geophysical Research Letters*, 41(11):3925–3932, 2014.
- Shames, I. H. *Elastic and inelastic stress analysis*. CRC Press, 1997.
- Shapero, D. R., Joughin, I. R., Poinar, K., Morlighem, M., and Gillet-Chaulet, F. Basal resistance for three of the largest Greenland outlet glaciers. *Journal of Geophysical Research: Earth Surface*, 121(1):168–180, 2016.
- Shoji, H. and Langway, C. Flow-law parameters of the Dye 3, Greenland, deep ice core. *Annals of Glaciology*, 10:146–150, 1988.
- Shoji, H. and Langway Jr, C. C. Mechanical properties of fresh ice core from Dye 3, Greenland. *Greenland ice core: geophysics, geochemistry, and the environment*. Washington, DC, American Geophysical Union, pages 39–48, 1985.
- Staroszczyk, R. and Gagliardini, O. Two orthotropic models for strain-induced anisotropy of polar ice. *Journal of Glaciology*, 45(151):485–494, 1999.
- Svendsen, B. and Hutter, K. A continuum approach for modelling induced anisotropy in glaciers and ice sheets. *Annals of Glaciology*, 23:262–269, 1996.
- Svensson, A., Schmidt, K. G., Dahl-Jensen, D., Johnsen, S. J., Wang, Y., Kipfstuhl, S., and Thorsteinsson, T. Properties of ice crystals in NorthGRIP late-to middle-Holocene ice. *Annals of glaciology*, 37:113–118, 2003.
- Thorsteinsson, T. An analytical approach to deformation of anisotropic ice-crystal aggregates. *Journal of Glaciology*, 47(158):507–516, 2001.
- Van der Veen, C. and Whillans, I. Development of fabric in ice. *Cold regions science and technology*, 22(2):171–195, 1994.
- Van Der Veen, C. J. and Whillans, I. Force budget: I. Theory and numerical methods. *Journal of Glaciology*, 35(119):53–60, 1989.
- Waleffe, F. The nature of triad interactions in homogeneous turbulence. *Physics of Fluids A: Fluid Dynamics (1989-1993)*, 4(2):350–363, 1992.
- Weertman, J. On the sliding of glaciers. *Journal of glaciology*, 3(21):33–38, 1957.

Weertman, J. Creep deformation of ice. *Annual Review of Earth and Planetary Sciences*, 11(1):215–240, 1983.

Ziegler, H. Some extremum principles in irreversible thermodynamics, with application to continuum mechanics. *Progress in solid mechanics*, vol. 4, pages 93–193, 1963.